

DISSERTATION

SYNTHESIS, POSTSYNTHETIC MODIFICATION, AND INVESTIGATION OF
METAL-ORGANIC FRAMEWORKS FOR ENVIRONMENTAL AND BIOLOGICAL
APPLICATIONS

Submitted by

Heather N. Rubin

Department of Chemistry

In partial fulfillment of the requirements

For the Degree of Doctor of Philosophy

Colorado State University

Fort Collins, Colorado

Fall 2018

Doctoral Committee:

Advisor: Melissa Reynolds

Eugene Chen

Richard Finke

Alan Van Orden

Susan James

Copyright by Heather N. Rubin 2018

All Rights Reserved

ABSTRACT

SYNTHESIS, POSTSYNTHETIC MODIFICATION, AND INVESTIGATION OF METAL-ORGANIC FRAMEWORKS FOR ENVIRONMENTAL AND BIOLOGICAL APPLICATIONS

Metal-organic frameworks (MOFs) are unique porous coordination polymers having record-high surface areas, and tunability at both the organic linkers and metal ions. As such, MOFs are advantageous for various applications including electronics, gas adsorption, and separations amongst others. Despite the advantages associated with MOFs, there are several key challenges that must be addressed in order to broadly expand the practicality of these materials. Such challenges include synthetic pitfalls, structural instability, selectivity, and inefficient heterogeneous catalysis. For instance, most MOFs are not stable in moisture-rich environments, which leads to structural collapse even in the open atmosphere. This instability poses a serious limitation for useful applications. In addition, the synthesis of MOF-related ligands is underdeveloped, which can lead to costly or inaccessible materials. To overcome these challenges, one goal of this research is to develop a solution to enhance the kinetic stability of MOFs to water and another is to execute an efficient and cost-effective synthetic strategy to generate the MOFs used herein. CuBTC (copper benzene-1,3,5-tricarboxylate), a commercially available MOF that has been well-studied and designated as having great potential for many applications, undergoes rapid degradation in humid atmospheres. Therefore, a novel synthetic approach was developed to efficiently access NH₂BTC on gram-scale. Postsynthetic modification to the amine of the MOF powder material enhances the kinetic stability of the MOF to water. A distinct linear relationship

between the number of carbons in the modification and observed water contact angle is described for the first time. This facilitates the first report of reliable access to mixed-ligand frameworks with predictable, calculated wettability and tunable kinetic stability to water. This work is also the first report of functionalizing copper MOFs as well as MOFs containing a benzene-1,3,5-tricarboxylate ligand to alter hydrophobic characteristics. That initial work inspired further exploration of CuNH₂BTC as an antibacterial surface when synthetically grown on the surface of carboxymethylated cotton. The resultant material is capable of tunable Cu²⁺ ion release (via postsynthetic modification) and exceeds current industry standards for antibacterial agents, exhibiting a log-3 or greater reduction in bacteria both on the surface and in solution.

As the scientific community continues to explore and understand MOFs, the implementation of these materials for various applications is dramatically increasing. As such, the second part of this research was devoted to applying and manipulating MOFs to better understand the interactions of MOFs with small molecules and ions. The photophysical properties of CuNH₂BTC were investigated and specific interactions between anions and metal ions with MOFs were identified, encouraging the strategic design of MOFs to detect target-analytes via changing fluorescence emission properties in dimethylformamide (quenching or enhancing emission intensity or changing emission wavelength). This work provides a prerequisite study towards the development of improved next-generation MOF chemosensors. In addition, the open coordination site of thermodynamically stable porphyrin-based MOFs was exploited for simultaneous heavy metal detection and metal ion removal from aqueous solutions. Lastly, to better understand heterogeneous catalysis with MOFs in biologically relevant media water, a ¹H NMR method with solvent suppression was implemented and allows for kinetic and mechanistic studies of biologically relevant MOF-catalyzed decomposition of GSNO with thermodynamically stable

MOF CuBTri in H₂O and eventually in blood. As a whole this research provides valuable insights as to how MOFs may be strategically designed, manipulated, and utilized for sensing, catalysis, and antibacterial applications.

ACKNOWLEDGEMENTS

I am undeniably grateful for the relationships that I have fostered throughout graduate school. I have met some incredible minds and spent time with those, if even for only one conversation and unannounced to them, have forever changed my perspective of the world and outlook for science. From UNCW I acknowledge Professor Jeremy Morgan and others there who have inspired me, pushed me, and supported me throughout my graduate career. Thank you for teaching me that no matter what happens, it is remarkable to be a part of the scientific community and together, *in support of one another* we can accomplish great things.

At CSU I have been privileged to have worked with Professor Tomislav Rovis and former colleagues in his research group. I feel the most indebted to Professor Melissa Reynolds for my research experience and personal growth here at CSU. As my advisor, Melissa not only saw me through some of my most challenging life experiences to date, but also gave me the support and freedom to be creative, fostering innovation in research as well as independence to take a project from the imagination to impactful publication. Melissa was influential and necessary for my personal transformation into a successful independent scientist. Thank you to other faculty as well at CSU who have helped me along this journey including those in the CIF, admin, and my committee members.

While I realize I am ultimately the one responsible for earning this PhD, I cannot help but feel as though there were others who share in this accomplishment as those who contributed some sort of gear or guidance to help me persevere to climb this mountain. Jonathan, Chris, Kim, and Amy thank you for the personal and scientific support. To my Reynolds group colleagues (past and present) you are remarkable; good luck to you all and thank you for the opportunity to grow

with you. To the triad – I see you. Jesus and Bella, thank you both for your professional guidance and even more so for your friendship.

To my family (Rubin and Henry): I apologize for all of the birthdays, holidays, memorials and other life events I have unfortunately had to miss. I am so grateful to have had your support and patience throughout this experience. Mom – we made it to the stars, thank you for *always* being there when I needed you and showing me just how strong a woman can be. Dad – cheers, I am so grateful for such a supportive best friend. My grandparents – thank you for the push to carry on, especially in times that I needed it most and for being my greatest cheerleaders. Paul – I could not imagine anyone else by my side (and Bella’s) over the past few years, you inspire me.

My grandmother once told me “you are never too old to learn something new”. Thus, I know this is really the end of one opportunity and just the beginning of something new. I am grateful to all the remarkable women who have fought for my right to be here, for my family, my true friends, and I am overwhelmed with excitement for my new beginning as Dr. Heather N. Rubin, PhD.

TABLE OF CONTENTS

| | |
|---|----|
| ABSTRACT..... | ii |
| ACKNOWLEDGEMENTS..... | v |
| CHAPTER 1 – INTRODUCTION..... | 1 |
| 1.1 Introduction and Background to Metal-Organic Frameworks (MOFs)..... | 1 |
| 1.2 Dissertation Overview..... | 9 |
| REFERENCES..... | 14 |
| CHAPTER 2 – POSTSYNTHETIC MODIFICATION OF METAL-ORGANIC FRAMEWORKS TO ACHIEVE CONTROLLABLE WETTABILITY | |
| 2.1 Summary..... | 17 |
| 2.2 Introduction..... | 18 |
| 2.3 Experimental..... | 21 |
| 2.3.1 Materials..... | 21 |
| 2.3.2 Characterization..... | 21 |
| 2.3.3 Synthetic Methods..... | 22 |
| 2.3.4 Synthesis of MOF $\text{Cu}_3(\text{NH}_2\text{BTC})_2$ | 24 |
| 2.3.5 Post-synthetic Modification (PSM) of MOF $\text{Cu}_3(\text{NH}_2\text{BTC})_2$ | 24 |
| 2.3.6 Wettability Studies..... | 25 |
| 2.3.7 Structural Stability in Water Studies..... | 26 |
| 2.3.8 Data Analysis..... | 26 |

| | |
|--|----|
| 2.4 Results and Discussion | 27 |
| 2.4.1 Synthesis and Characterization | 27 |
| 2.4.2 Post-synthetic Modification..... | 29 |
| 2.4.3 Post-synthetic Modification to Alter Wettability. | 33 |
| 2.4.4 Enhanced Stability to Water | 38 |
| 2.5 Conclusions..... | 40 |
| REFERENCES | 41 |

CHAPTER 3 – SURFACE ANCHORED METAL-ORGANIC FRAMEWORK-COTTON MATERIAL FOR TUNABLE ANTIBACTERIAL COPPER DELIVERY

| | |
|---|----|
| 3.1 Summary..... | 45 |
| 3.2 Introduction..... | 46 |
| 3.3 Experimental Section..... | 50 |
| 3.3.1 Materials | 50 |
| 3.3.2 Characterization | 51 |
| 3.3.3 Carboxymethylation of Cotton Swatch..... | 52 |
| 3.3.4 Layer-by-layer Growth Process of $\text{Cu}_3(\text{NH}_2\text{BTC})_2$ on Modified Cotton | 53 |
| 3.3.5 Post-synthetic modification of $\text{Cu}_3(\text{NH}_2\text{BTC})_2$ on Modified Cotton..... | 54 |
| 3.3.6 Copper Releasing Studies | 54 |
| 3.3.7 Bacteria Studies | 55 |
| 3.3.8 Antibacterial Activity Under Wet Conditions | 56 |
| 3.3.9 Antibacterial Activity Under Dry Conditions..... | 57 |
| 3.4 Results and Discussion | 57 |
| 3.4.1 Development of the MOF-Cotton Material. | 57 |

| | |
|---|----|
| 3.4.2 Characterization of the MOF-Cotton Material | 59 |
| 3.4.3 Postsynthetic Modification of the MOF-Cotton Material. | 63 |
| 3.4.4 Copper Delivery Performance | 66 |
| 3.4.5 Bacteria Studies | 69 |
| 3.4.6 Antibacterial Activity Under Wet Conditions | 70 |
| 3.4.7 Antibacterial Activity Under Dry Conditions | 72 |
| 3.5 Conclusions..... | 74 |
| REFERENCES | 76 |

CHAPTER 4 – AMINO-INCORPORATED TRICARBOXYLATE METAL–ORGANIC FRAMEWORK FOR THE SENSITIVE FLUORESCENCE DETECTION OF HEAVY METAL IONS WITH INSIGHTS TO THE ORIGIN OF PHOTOLUMINESCENCE RESPONSE

| | |
|---|----|
| 4.1 Summary..... | 79 |
| 4.2 Introduction..... | 80 |
| 4.3 Experimental..... | 84 |
| 4.3.1 Materials and Methods..... | 84 |
| 4.3.2 Synthesis of MOF $\text{Cu}_3(\text{NH}_2\text{BTC})_2$ and Postsynthetic Modification | 85 |
| 4.3.3 Photophysical Studies | 85 |
| 4.3.4 Fluorescence $[\text{M}^{n+}]$ Sensing Experiments | 86 |
| 4.3.5 Anion Sensing..... | 87 |
| 4.4 Results and Discussion | 87 |
| 4.4.1 Metal Ion Detection | 93 |
| 4.4.2 Photophysical Properties and Structural Details of $\text{Cu}_3(\text{NH}_2\text{BTC})_2$ | 93 |
| 4.4.3 Solvent Interactions | 95 |

| | |
|--|-----|
| 4.4.4 Anion Influence on Sensing | 96 |
| 4.4.5 Investigation and Insights of the Emission Changing Pathways | 98 |
| 4.5 Conclusions..... | 100 |
| REFERENCES | 102 |

CHAPTER 5 – PORPHYRIN-BASED METAL-ORGANIC FRAMEWORK NU-902 FOR FLORESCENCE SENSING AND REMOVAL OF DIVALENT METAL IONS FROM WATER

| | |
|--|-----|
| 5.1 Summary..... | 105 |
| 5.2 Introduction..... | 106 |
| 5.3 Experimental..... | 108 |
| 5.3.1 Materials and Methods..... | 108 |
| 5.3.2 Characterization | 108 |
| 5.3.3 Synthesis of Tetrakis(4-carboxyphenyl)porphine (TCPP)..... | 109 |
| 5.3.4 Synthesis of MOF NU-902 | 110 |
| 5.4 Results and Discussion | 110 |
| 5.5 Conclusions and Future Directions..... | 112 |
| REFERENCES | 114 |

CHAPTER 6 – ¹H NMR WITH WATER SOLVENT SUPPRESSION TO DETERMINE STOICHIOMETRY, KINETICS, AND MECHANISM OF Cu²⁺ VS. WATER-STABLE METAL–ORGANIC FRAMEWORK (CuBTri) HETEROGENOUS CATALYSIS IN WATER

| | |
|-----------------------|-----|
| 6.1 Summary..... | 116 |
| 6.2 Introduction..... | 118 |
| 6.3 Experimental..... | 120 |

| | |
|--|-----|
| 6.3.1 Reagents..... | 120 |
| 6.3.2 Water Suppression ¹ H NMR Method | 121 |
| 6.3.3 Syntheses..... | 122 |
| 6.3.4 Reaction Setup | 122 |
| 6.4 Results and Discussion | 123 |
| 6.4.1 Ex-Situ ¹ H NMR Reaction Monitoring | 123 |
| 6.4.2 Cu ²⁺ Catalyzed GSNO Decomposition | 126 |
| 6.4.3 Cu-MOF Catalyzed GSNO Decomposition | 129 |
| 6.4.4 Balanced Reaction Stoichiometry | 133 |
| 6.5 Conclusions..... | 135 |
| REFERENCES | 138 |

CHAPTER 7 – SUMMARY AND FUTURE FOR MOFs

| | |
|---|-----|
| 7.1 Summary..... | 141 |
| 7.2 Postsynthetic Modification (PSM) and Future Design Principles | 146 |
| 7.3 Emerging Real-World Applications of MOFs | 146 |
| 7.4 Final Comments | 147 |
| REFERENCES | 150 |

APPENDIX A. SUPPORTING INFORMATION FOR CHAPTER 2

| | |
|---|-----|
| A.1 Synthesis Characterization | 153 |
| A.1.1 Characterization of <i>N</i> -mesitylacetamide | 153 |
| A.1.2 Characterization of 2-amino-1,3,5-tricarboxylate | 154 |
| A.2 Post-synthetic modification (PSM) of Cu ₃ (NH ₂ BTC) ₂ | 155 |

| | |
|--|-----|
| A.2.1 ¹ HNMR of Modified Ligands | 155 |
| A.2.2 MS of Modified Ligands | 160 |
| A.3 Thermal gravimetric analysis | 163 |
| A.4 IR..... | 164 |
| A.5 Wettability..... | 165 |
| A.5.1 Water Contact Angles | 165 |
| A.5.2 Water Contact Angle vs. Number of Carbons in Amide | 166 |
| A.6 Water Stability PXRD | 167 |
| A.7 3-D Drawings of MOF | 168 |
| A.8 SEM images of MOF | 168 |
| REFERENCES | 169 |

APPENDIX B. SUPPORTING INFORMATION FOR CHAPTER 3

| | |
|---|-----|
| B.1 Ligand Details | 170 |
| B.2 Carboxymethylation of natural cotton | 170 |
| B.3 Layer-by-layer growth of MOF Cu ₃ (NH ₂ BTC) ₂ on carboxymethylated cotton | 172 |
| B.4 Postsynthetic modification of MOF with valeric anhydride: AM-5 | 172 |
| B.5 PXRD after NBM exposure | 174 |
| REFERENCES | 175 |

APPENDIX C. SUPPORTING INFORMATION FOR CHAPTER 4

| | |
|--|-----|
| C.1 PXRD Characterization of Cu ₃ (NH ₂ BTC) ₂ used in Metal Ion Detection..... | 176 |
|--|-----|

APPENDIX D. SUPPORTING INFORMATION FOR CHAPTER 6

| | |
|---|-----|
| D.1 Additional Characterization Methods | 177 |
| D.2 PXRD Characterization of CuBTTri..... | 177 |
| D.3 ¹ H NMR Peak Assignments of GSH | 178 |
| D.4 CuBTTri Drawings | 178 |
| D.5 Calibration ¹ H NMR Spectra and Resulting Calibration Curves | 179 |
| D.6 GSNO after 16 h (no catalyst)..... | 179 |
| D.7 GSNO and GSH (no catalytic copper species) | 180 |
| D.8 GSNO (2 mM) and GSH (2 mM) with no Cu-BTTri | 180 |
| D.9 Cu-BTTri Reactions Under Open Atmospheric Conditions | 181 |
| D.10 Incomplete Cu ²⁺ Reactions with Excess GSH | 181 |
| | |
| APPENDIX E. NITRIC OXIDE DONORS IN NERVE REGENERATION..... | 182 |
| REFERENCES | 217 |

CHAPTER 1

INTRODUCTION

1.1 Introduction and Background to Metal-Organic Frameworks (MOFs)

The field of porous solid materials having large surface area to volume ratio has expanded rapidly over the past several decades. Zeolites are nanoporous materials often with TO_4 tetrahedra (T usually = Si or Al)¹ found in nature and subsequently synthesized in the laboratory. Zeolites have been widely used since they were discovered in 1765 by Cronstedt,² and in a wide array of applications from small molecule separation to catalysis owing to their inherent high thermal and hydrothermal stability under processible conditions.^{2,3} In search of materials capable of fine-tuning to meet the demands of various applications for porous solids, metal-organic frameworks (MOFs), a relatively new class of ordered crystalline microporous solids comprised of inorganic metal ion or cluster nodes networked together with organic coordinating linkers, have emerged and may also be referred to as porous coordination polymers (PCPs, Figure 1.1). Unlike zeolites, the interaction between the metal-based nodes and linkers are not covalent but coordinative or ionic. Additionally, MOFs exhibit the largest surface area of any known solid material (up to $7000 \text{ m}^2\text{g}^{-1}$) to date with predicted capabilities to reach approximately $14,600 \text{ m}^2\text{g}^{-1}$ or greater.⁴ The near infinite possibilities to optimize the physical and chemical properties of MOFs for target specific applications, simply by careful selection of the organic linkers or metal ions or late stage modifications, makes these materials attractive for gas storage, sensing, drug delivery, separations, amongst others. As such, MOFs have been referred to as “designer zeolites”.⁵

A direct consequence of the tunability of MOFs is the ability to engineer specificity for target applications – something not possible with their homogeneous counterparts nor with

alternative porous materials, a feature which expands their overall utility. For example, postsynthetic modification of MOF UiO-67 and UiO-68 with proline reverses diastereoselectivity of a catalytic aldol addition.⁶ The use of chiral ligands in the structure of MOFs leads to chiral porous materials that are promising as stationary phases for the chiral separation of small molecules.⁷ MOFs also show great potential for drug eluting,⁸ biological imaging,⁹ gas storage,¹⁰ and chemical sensing¹¹ as a direct outcome of the unmatched surface area of MOFs. Such high surface area can concentrate guest molecules within the pores of the MOF, effectively maximizing interactions of small molecules with the MOF surface. The resultant increase in molecular interactions is highly advantageous for sensing, gas storage and catalytic applications. High tunability coupled with a recent emphasis on understanding the interaction of small molecules with these materials broadens possibilities for MOFs in emerging applications ranging from porous and/or inorganic-organic hybrid materials.¹²

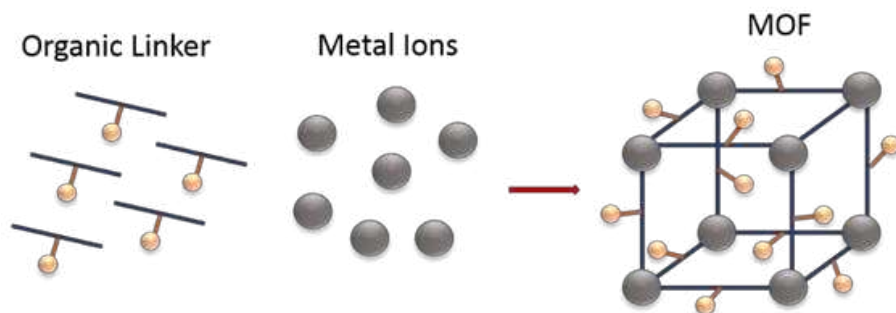


Figure 1.1 Simplified representation of a metal-organic framework, whereby organic linkers and metal ions assemble into porous coordination networks.

While MOFs show promise for a variety of applications, there are several associated challenges which undermine the full potential and prevents the practical wide-spread use of MOFs. A few key drawbacks addressed herein include synthetic challenges, structural instability,

selectivity, and inefficient heterogeneous catalysis. In order to advance the practical applicability and overall usefulness of MOFs, efforts to understand and address such challenges are necessary.

Synthetic challenges can be categorized into two parts: (1) a lack of affordable syntheses and purification of available MOF ligands, and (2) limited scalability and reproducibility of MOF syntheses. To design ligands for MOFs one must consider the structural complexity and vast possible topologies and compositions that are conceivable.¹³ Transition-metal ions or lanthanide ions are most commonly used for the metal nodes, whereby many possible coordination geometries are achievable. The organic linkers are classically bi-coordinating or multi-coordinating as anionic or neutral donor ligands. The ligands are also typically highly-conjugated resulting in robust and rigid linkers that ensure crystallinity and prevent multiple ligand conformers. More recently, more complex functional ligands that have useful characteristics as chemical species (outside of the MOFs) are incorporated into the ligand scaffolds of MOFs. Functionality associated with the independent ligand can be present in the resultant MOF. Accordingly, fluorescent ligands may yield fluorescent MOFs, catalytic ligands may yield catalytic MOFs, and chiral ligands may yield chiral MOFs. Alternatively, the ligands may hold potential for new functionality when aggregated in the framework, as seen for tetraphenylethylene-based MOFs which exhibit aggregation-induced fluorescence emission once concentrated in the structure, rigidifying the ligand within the framework.^{14,15} Unfortunately, scalable, affordable syntheses for many ligands of interest are scarce. The ability to postsynthetically modify and chemically react small molecules with ligands of MOFs via the incorporation of free and accessible moieties for late stage-functionalization (commonly free-amines, thiols, or hydroxyl groups) is powerful for tuning properties such as hydrophobicity and catalytic or sensing selectivity. However, such ligands also have limited availability. Limited synthetic routes of ligands leads to increased costs, and lengthy procedures

to synthesize these materials, rendering MOFs irrelevant for industrial applications. As such, new synthetic strategies to affordable ligands requires attention for practical scalability.

While various synthetic strategies are available, the specific route used to generate a MOF introduces a level of complexity as it influences the crystallinity, purity, and reproducibility of the material. MOFs are classically synthesized under hydrothermal/solvothermal conditions, requiring increased pressure and heat in sealed vessels (relatively mild conditions for solid porous materials). Syntheses requiring more excessive heat (greater than 120 °C), typically necessitate an autoclave reactor, which in turn limits practical scalability and introduces impurities or structural variabilities to the synthesized MOF due to reactor contaminants. For example, residual acid that is released during synthesis from a contaminated reaction vessel may impact the nucleation and growth kinetics of the MOF. As such, it is critical to prepare all reaction reservoirs identically for the reproducible synthesis of MOFs. Autoclave reaction vessels are advantageous for MOF syntheses, and aid in formation of highly crystalline MOFs. When using common glassware, such as round bottom flasks or glass vials, the final MOF structure and crystallinity can be influenced by minor scratches or defects in the glass surface, which result in preferred nucleation sites. Subsequent, epitaxial growth of the MOF from the surface of glass may influence the crystal orientation. Some frameworks require the aid of a nucleating agent to facilitate MOF growth (often benzoic acid or formic acid). MOFs containing zirconium oxide nodes, for instance, typically necessitate acid modifiers.^{16,17} In summary, while the synthesis of MOFs is often acknowledged as a “self-assembly” process, many parameters including temperature, solvent, heat, modifiers, and reaction vessel all impact the resultant crystallinity of the material, and thus must be clearly defined and documented to develop MOFs with batch to batch consistencies.

Despite the availability of nearly 75,000 MOF structures in the Cambridge Structural Database (CSD) to date,¹⁸ most of these materials have structural instability to humidity, pressure, or thermal evacuation. On one hand, structural instabilities can be exploited for applications such as tunable drug release upon slow and controlled degradation of the MOF. On the other hand, structural instability limits the ability to isolate, store, and reuse MOFs. As such, developing and modifying MOFs to enhance their stability is highly advantageous and necessary for broadening practicality. MOFs may intrinsically have kinetic and/or thermodynamic stability to water.²⁰ Kinetic stability of MOFs is influenced by factors such as hydrophobicity and steric hindrance, which would prevent hydrolysis due to unfavorable high transition state energies associated with water-ligand exchange or preventing water from accessing metal sites. A MOF may be characterized as having kinetic stability if structurally stable to highly humid conditions and short exposure times to water (minutes to hours). Thermodynamic stability is influenced by the metal-ligand bond strength and inertness to water, which makes hydrolysis unfavorable. A MOFs may be characterized as thermodynamically stable if structurally stable to long-term exposure to aqueous solutions (days to weeks).

Increased kinetic stability can be achieved in MOFs by increasing the hydrophobicity and/or sterics of the MOF via techniques including postsynthetic modification or hydrophobic coating deposition (like perfluorohexane) to the surface of the MOF. To develop more thermodynamically stable MOFs one must consider the interaction between the ligand and metal nodes (M-L interactions). One common trend is MOFs having 6-coordinate metal ions that are more thermodynamically stable and less susceptible to ligand exchange with water compared to 4-coordinate metal ions.²⁰ Commonly, ions with relatively small radii and high charge, like Zr^{4+} , rather than divalent transition metals like Cu^{2+} or Zn^{2+} , tend to generate more thermodynamically

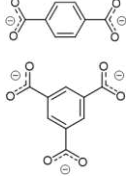
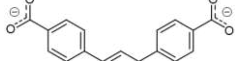
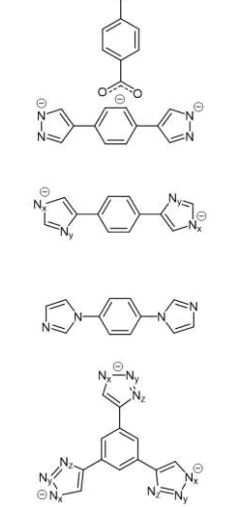
stable MOFs. The pK_a and electron density associated with the conjugated acids of ligands provides information about the coordinating strength of the ligand.²¹ Increasing M-L coordination strength results in increasing the resultant thermal and water stability of MOFs. For example, the MOF CuBTC with Cu^{2+} ions and carboxylate-based ligands (pK_a approximately 4.7 and natural bond orbital (NBO) charge -0.813) is not stable to water; however, CuBTTri with Cu^{2+} ions and triazole ligands (pK_a 11.10 and NBO -0.412) is stable in water, even at elevated temperatures (boiling) (Table 1, Compounds **2** and **7**). Plainly, ligands having higher pK_a values and greater natural bond orbital electron density are more likely to yield stronger M-L coordinating strength than those with lower pK_a values and lower natural bond orbital electron density. M-L strength may also be predicted using hard and soft acid/base theory, whereby soft metal cations create stronger bonds with soft donor ligands and hard metal ions create stronger bonds with hard donor ligands. For example, carboxylate ligands which have hard oxygen donors form more stable frameworks with hard metal cations like Zr^{4+} or Al^{3+} ,^{22,23} whereas soft N-donor ligands like triazoles generate more stable frameworks when paired with softer low-valent cations like Cu^{2+} .²⁴ In summary, the key to designing more thermodynamically stable and useful MOFs is to maximize the M-L interaction strength via careful pairing of metal ions with ligands.

The pore sites within MOFs provide unique chemical environments. The ability to tune both the size and electronics of the pore spaces offers the opportunity to impart selectivity with MOFs for various applications including sensing, separations, and catalysis. By contracting or expanding MOF linkers, one may ensure size selective interactions occur with small molecules. For example, hydrogenation of a mixture of 4 olefins or imines demonstrates the use of this strategy to molecularly sieve and produce selective hydrogenated olefins or imines.²⁵ Metal ions may impact selectivity by preferentially interacting with target small molecules by selective

pairing. Such selective pairing can be seen most commonly when MOFs are implemented for catalysis, whereby the specific MOF used is often electronically similar, if not the same as, its homogeneous counterpart.²⁶ Additionally, the organic linkers may be tailored such that they selectively react with targeted small molecules. For instance, selective recognition and sensing of biothiols has recently been reported in response to 2,4-dinitrosulfonyl chloride cleavage that takes place in the presence of biothiols.²⁷ In conclusion, the future of MOF design strategies should reflect the ability to tune the materials to impart selectivity for catalytic or other desired application.

Table 1.1 pK_a and electron density values for common metal-organic framework ligands

| Ligand Name | Structure in MOF | pK_a^1 | pK_a^1 | pK_a^1 | NBO Charges ² |
|---|------------------|----------|----------|----------|--------------------------|
| | | 1 | 2 | 3 | |
| 1 BDC - 1,4- benzene dicarboxylic acid | | 3.54 | 4.34 | - | O: -0.798 |
| 2 BTC - Benzene-1,3,5-tricarboxylic acid | | 3.12 | 3.89 | 4.70 | O: -0.813 |
| 3 BTB - 1,3,5-Tris(4-carboxyphenyl)benzene | | 6.72 | - | - | O: -0.788 |
| 4 4,4'-(1,4-Phenylene)bis(1H-pyrazole) | | 18.15 | 19.66 | - | N: -0.403 |

| | | | | | | |
|---|---|---|-------|-------|---|-------------------------|
| 5 | 2,2'-(1,4-Phenylene)bis(1H-imidazole) |  | 17.20 | 17.94 | - | N _x : -0.615 |
| 6 | 1,4-di(1H-imidazol-1-yl)benzene |  | - | - | - | N _y : -0.587 |
| 7 | BTTri - 1,3,5-tri(1H-1,2,3-triazol-4-yl)benzene |  | 11.10 | - | - | N _x : -0.358 |
| | | | | | | N _y : -0.223 |
| | | | | | | N _z : -0.412 |

¹*pK_a* values taken from the 92nd CRC Handbook of Chemistry and Physics. ²Reported by Lu et al. as natural bond orbital (NBO) charges of the coordinating atoms of the ligands.²¹

A final challenge when using MOFs addressed herein, is the difficulty in achieving efficient heterogeneous catalysis. The insoluble nature of MOFs is attractive for recycling and reusing the material, particularly in packed column separations as well as in high throughput catalysis. The use of MOFs for such applications eliminates the necessity for complex re-isolation steps or additional solid-support additives like silica. The catalytic potential of MOFs has also found utility in a wide range of applications including biomaterials and MOFs truly bridge the gap between fundamental chemical research and materials discovery. Many MOFs, however, are not as efficient as their homogenous counterparts. As such, the development of more efficient MOF catalysts is a necessity. Unfortunately, understanding of how small molecules interact with MOFs is currently limited, thwarting the possibility of strategically designing MOF catalysts. En route to develop

more efficient catalysts, the community first must develop a fundamental understanding with mechanistic insights as to how small molecules interact with MOFs.

1.2 Dissertation Overview

The following dissertation contains two manuscripts previously published in peer-reviewed chemistry journals including one full-paper article in *Inorganic Chemistry* as chapter 2 and another in *Applied Materials & Interfaces* as chapter 3. Chapters 4 and 5 are included as communications, prepared for submission. A modified version of chapter 6 is in the submission process. The overall purpose of this dissertation is to address several challenges associated with MOFs (synthesis, wettability, stability), to develop studies to better understand how small molecules interact with MOFs (catalysis and sensing) and to advance practical applications of MOFs (antibacterial and environmental).

In chapter 2, postsynthetic modification to enhance the kinetic stability of a tri-coordinating metal-organic framework to achieve controllable wettability is described. The ability to control wettability is very challenging especially with regard to microporous materials. As such, controlling the degree of hydrophobicity is not well-documented nor understood. The research goals in chapter 2 were to address (a) if $\text{NH}_2\text{H}_3\text{BTC}$ can be accessed with a scalable, cost-effective synthesis to provide a tricarboxylate MOF for PSM, (b) if MOFs with sterically hindered constituents can undergo covalent PSM with long chained and branched hydrocarbons, and (c) if such PSM can expand functionality of the material by providing an isostructural system with improved hydrophobicity. Chapter 2 achieves covalent postsynthetic modification (PSM) of a metal-organic framework (MOF), $\text{Cu}_3(\text{NH}_2\text{BTC})_2$, to manipulate the degree of hydrophobic character and the kinetic stability to water of the MOF. A distinct linear relationship between the

number of carbons in the modification and observed water contact angle is described. This facilitates reliable access to mixed-ligand frameworks with predictable, calculated wettability and tunable water stability. Chapter 2 reports on functionalizing copper MOFs as well as MOFs containing a benzene-1,3,5-tricarboxylate ligand to achieve hydrophobic characteristics. The work in this chapter enables further exploration of using tunable organic-inorganic hybrid materials in a variety of applications and foreshadows the ability to capitalize on structural bias to finely tune nanomaterials.

We hypothesized that the tunability and control over the physical and chemical properties determined for $\text{Cu}_3(\text{NH}_2\text{BTC})_2$ in chapter 2, would be valuable for antibacterial applications. Based on findings in the chapter 2, chapter 3 utilized PSM of surface anchored $\text{Cu}_3(\text{NH}_2\text{BTC})_2$ as an antibacterial surface capable of tunable antibacterial copper delivery. Thus, the research goal was to develop a $\text{Cu}_3(\text{NH}_2\text{BTC})_2$ MOF-cotton composite that could be tuned with PSM to deliver antibacterial copper. By postsynthetically modifying the material, we hypothesized that the resulting changes to the kinetic stability of the MOF to water would result in variable release rates of Cu^{2+} ions in solution. We hypothesized that (1) the presence of copper on the surface of the MOF-cotton material would yield an antibacterial surface and (2) the release of Cu^{2+} ions into solution would kill planktonic bacteria in solution. The resultant MOF-cotton materials developed meet and, in some cases, exceed current industry standards for antibacterial agents and exhibit a log-3 or greater reduction in bacteria both on the surface of cotton and in solution. Testing the ability for the materials to inhibit bacterial attachment under multiple conditions (wet and dry) strongly supports the potential application as antibacterial surfaces. Chapter 3 reports synthetically tunable copper ion release from the surface of a textile with MOFs. Additionally, the protocol for carboxymethylation of cotton used enables increased nucleation sites for MOF growth, a process

which will prove important for future surface immobilized MOFs. Overall chapter 3 reports the synthesis of tunable materials and surfaces, the design of a functional inorganic material, and the development of a new antibacterial material and surface.

A MOF was used in chapter 4 as a fluorescent metal ion sensor. Highly conjugated, carboxylate-based MOF $\text{Cu}_3(\text{NH}_2\text{BTC})_2$ is capable of exhibiting fluorescence and of having multiple conceivable modes of ion interaction (via the free amine, open coordination sites on Cu^{2+} nodes, labile carboxylate ligand). Thus, chapter 4 was developed to test the hypothesis that a change in emission spectra (intensity or wavelength) may be possible with $\text{Cu}_3(\text{NH}_2\text{BTC})_2$ upon the introduction of metal-ion analytes. Chapter 4 additionally focused on the research question of how different ions may interact with the MOF. The MOF $\text{Cu}_3(\text{NH}_2\text{BTC})_2$ is indeed, highly sensitive for the detection of divalent metal ions following a hard-soft acid-base theory trend. Additional metal ions and anions were explored as well indicating that depending on the specific analyte, the interaction to elicit a photoluminescent response from the MOF, varied. The resultant sensor is highly sensitive, exhibiting fluorescence turn-off for Fe^{3+} and Fe^{2+} ions likely interacting via the carboxylate of the MOF ligand. Cr^{7+} as $\text{Cr}_2\text{O}_7^{2-}$ proved to be a fluorescence quencher, the Cr^{7+} likely interacting with the free amine. Isorecticular MOF $\text{Cu}_3(\text{BTC})_2$ and postsynthetically modified $\text{Cu}_3(\text{NH}_2\text{BTC})_2$ (blocking access of ions to the amine) were also used to further elucidate the pathway of Cr^{7+} ion interaction with the MOF. The findings in chapter 4 contribute to the overall understanding of how ions interact with the MOF, enabling future strategic engineering of MOFs to selectively detect target analytes.

While the use of $\text{Cu}_3(\text{NH}_2\text{BTC})_2$ as a metal ion sensor revealed valuable information regarding how metal ions interact with MOFs, the MOF $\text{Cu}_3(\text{NH}_2\text{BTC})_2$ is not thermodynamically stable, which leads to significant instability to water and limits its use in sensing devices. In

response, a research goal in chapter 5 was to utilize a thermodynamically stable, and ultimately water-stable, metal-organic framework for divalent metal-ion sensing and metal-ion removal from water. Thus, the synthesis and application of a tetracarboxylate porphyrin-containing zirconium-based MOF NU-902 is reported in chapter 5. NU-902 is a water-stable fluorescent MOF capable of metal ion detection via postsynthetic metalation to the nitrogen-donor center of the porphyrin ligand. The intended application is the detection and removal of heavy metal ions from the environment and this study is currently ongoing for the detection and/or removal of metal ions from water.

In chapter 6, a fundamental mechanistic study of MOF-catalyzed (CuBTTri) and copper ion-catalyzed (CuCl₂) decomposition of *S*-nitrosoglutathione in water is provided. Prior to this study, methods to simultaneously monitor multiple reaction components were not developed. Thus, a central research goal of this chapter was to develop a method that would allow for monitoring multiple reaction components and to determine the stoichiometry of the reaction. This work represents the first fundamental study of a biologically-relevant, MOF-catalyzed reaction carried out in the blood-relevant solvent, water. The MOF, CuBTTri, was used in part because the presence of Cu²⁺ induces GSNO decomposition and the Cu-triazole coordination yields a thermodynamically stable MOF that is stable to boiling in water (100 °C, 72 h), cell media, and blood. Importantly, the ¹H NMR method developed and implemented allows for the determination of the stoichiometry of a biologically relevant MOF-catalyzed reaction in H₂O. Future mechanistic studies in blood, should therefore be possible. Mechanistic understanding of both Cu²⁺ and copper-MOF catalyzed *S*-nitrosoglutathione (GSNO) decomposition will enable the directed design of improved future MOF catalysts for GSNO decomposition. The nitric oxide release reaction from GSNO carries great importance in medicine and biomedical engineering (due to the catalytic

release of nitric oxide). The complete reaction stoichiometry for solvated Cu^{2+} and for MOF Cu-BTtri catalyzed GSNO decomposition in H_2O is reported. The work in chapter 6 identifies a variable dependence of solvated homogeneous Cu^{2+} versus heterogeneous Cu-BTtri catalyzed systems on the presence of a reducing agent (glutathione), indicating these catalysts likely operate through different mechanistic pathways.

All supporting information and when appropriate additional details corresponding to each chapter are included as Appendixes at the end of this dissertation.

REFERENCES

1. E. M. Flanigen, in *Studies in Surface Science and Catalysis*, eds. H. van Bekkum, E. M. Flanigen, P. A. Jacobs and J. C. Jansen, Elsevier, 2001, vol. 137, pp. 11-35.
2. Zimmermann, N. E. R.; Haranczyk, M. *Crystal Growth & Design*, **2016**, *16*, 3043-3048.
3. Klinowski, J. *Chem. Rev.*, **1991**, *91*, 1459-1479.
4. Farha, O. K.; Eryazici, I.; Jeong, N. C.; Hauser, B. G.; Wilmer, C. E.; Sarjeant, A. A.; Snurr, R. Q.; Nguyen, S. T.; Yazaydin, A. O.; Hupp, J. T. *J. Am. Chem. Soc.*, **2012**, *134*, 15016-15021.
5. Ward, M. D. *Nature*, **1995**, *374*, 764-765.
6. Kutzscher, C.; Nickerl, G.; Senkowska, I.; Bon V.; Kaskel, S. *Chem. Mater.*, **2016**, *28*, 2573-2580.
7. Peng, Y.; Gong, T.; Zhang, K.; Lin, X.; Liu, Y.; Jiang, J.; Cui, Y. *Nat. Commun.*, **2014**, *5*, 4406.
8. Huxford, R. C.; Rocca, J. D.; Lin, W. *Curr. Opin. Chem. Bio.*, **2010**, *14*, 262-268.
9. Della Rocca, J.; Lin, W. *Eur. J. Inorg. Chem.*, **2010**, 3725-3734.
10. Li, H.; Wang, K.; Sun, Y.; Lollar, C. T.; Li, J.; Zhou, H.-C. *Mater. Today*, **2018**, *21*, 108-121.
11. Kreno, L. E.; Leong, K.; Farha, O. K.; Allendorf, M.; Van Duyne, R. P.; Hupp, J. T. *Chem. Rev.*, **2012**, *112*, 1105-1125.
12. Ricco, R.; Pfeiffer, C.; Sumida, K.; Sumbly, C. J.; Falcaro, P.; Furukawa, S.; Champness, N. R.; Doonan, C. J. *CrystEngComm*, **2016**, *18*, 6532-6542.

13. Hendon, C. H.; Rieth, A. J.; Korzyński, M. D.; Dincă, M. *ACS Central Science*, **2017**, *3*, 554-563.
14. Shustova, N. B.; Ong, T.-C.; Cozzolino, A. F.; Michaelis, V. K.; Griffin, R. G.; Dincă, M. *J. Am. Chem. Soc.*, **2012**, *134*, 15061-15070.
15. Shustova, N. B.; McCarthy, B. D.; Dincă, M. *J. Am. Chem. Soc.*, **2011**, *133*, 20126-20129.
16. H. J. Park, J. K. Jang, S.-Y. Kim, J.-W. Ha, D. Moon, I.-N. Kang, Y.-S. Bae, S. Kim and D.-H. Hwang, *Inorganic Chemistry*, 2017, **56**, 12098-12101. MOD HERE!
17. Y. Bai, Y. Dou, L.-H. Xie, W. Rutledge, J.-R. Li and H.-C. Zhou, *Chemical Society Reviews*, 2016, **45**, 2327-2367.
18. How many MOFs are there in the CSD?, <https://www.ccdc.cam.ac.uk/support-and-resources/support/case/?caseid=9833bd2c-27f9-4ff7-8186-71a9b415f012>, (accessed August 7, 2018, 2018).
19. N. C. Burtch, H. Jasuja, and K. S. Walton, *Chem. Rev.*, **2014**, *114*, 10575–10612.
20. J. J. Low, A. I. Benin, P. Jakubczak, J. F. Abrahamian, S. A. Faheem and R. R. Willis, *Journal of the American Chemical Society*, 2009, **131**, 15834-15842.
21. P. Lu, Y. Wu, H. Kang, H. Wei, H. Liu and M. Fang, *Journal of Materials Chemistry A*, 2014, **2**, 16250-16267.
22. B. Wang, X.-L. Lv, D. Feng, L.-H. Xie, J. Zhang, M. Li, Y. Xie, J.-R. Li and H.-C. Zhou, *Journal of the American Chemical Society*, 2016, **138**, 6204-6216.
23. H. Li, X. Feng, D. Ma, M. Zhang, Y. Zhang, Y. Liu, J. Zhang and B. Wang, *ACS Applied Materials & Interfaces*, 2018, **10**, 3160-3163.
24. T. M. McDonald, D. M. D'Alessandro, R. Krishna and J. R. Long, *Chemical Science*, 2011, **2**, 2022-2028.

25. Z. Li, R. Yu, J. Huang, Y. Shi, D. Zhang, X. Zhong, D. Wang, Y. Wu and Y. Li, *Nature Communications*, 2015, **6**, 8248.
26. L. Zhu, X.-Q. Liu, H.-L. Jiang and L.-B. Sun, *Chemical Reviews*, 2017, **117**, 8129-8176.
27. S. Sharma and S. K. Ghosh, *ACS Omega*, 2018, **3**, 254-258.

CHAPTER 2

POSTSYNTHETIC MODIFICATION OF METAL–ORGANIC FRAMEWORKS TO ACHIEVE CONTROLLABLE WETTABILITY¹

2.1 Summary

The overall versatility of a material can be immensely expanded by the ability to controllably tune its hydrophobicity. Herein we took advantage of steric bias to demonstrate tri-carboxylate metal–organic frameworks (MOFs) can undergo covalent post-synthetic modification to confer various degrees of hydrophobicity by tuning the kinetic stability of the MOF. MOF copper 2-aminobenzene-1,3,5-tricarboxylate ($\text{Cu}_3(\text{NH}_2\text{BTC})_2$) was modified with varying-length aliphatic carbon chains. Unmodified $\text{Cu}_3(\text{NH}_2\text{BTC})_2$ degrades in minutes upon contact with water, whereas modification as low as 14% results in powders that show significantly enhanced hydrophobic character with contact angles up to 147° . The modified material is capable of withstanding direct contact with water for 30 minutes with no visual evidence of altered surface characteristics. A linear relationship was observed between the length of the tethered chain and the water contact angle. These results reveal a predictable method for achieving a range of desirable sorption rates and highly controllable hydrophobic character. This work thereby expands the possibilities of rationally modifying MOFs for a plethora of target-specific applications.

¹ This dissertation chapter was adapted with permission from Rubin, H. N.; Reynolds, M. M. Functionalization of Metal–Organic Frameworks to Achieve Controllable Wettability. *Inorg. Chem.* **2017**, 56, 9, 5266-5274. Copyright 2015 American Chemical Society. This work was supported by the National Science Foundation (NSF/DMR) Career Grant CBET-1351909. We thank Jesus Tapia for help acquiring mass spectrometry data, Dr. Morgan Hawker and Michelle Mann for help with the contact angle goniometer, and Dr. Patrick McCurdy for assistance using the scanning electron microscope.

2.2 Introduction

The ability to predictably tune the properties of a material expands the overall usefulness, leading to enhanced functionality for target-specific applications. Hybrid materials are comprised of two or more constituents and inherently possess a high degree of tunability attributable to the ability to manipulate each individual component.¹ Metal–organic frameworks (MOFs) are a distinct class of organic-inorganic hybrid nanomaterials with intricate porous networks. The unique chemical environments at the pore sites has led to the investigation of MOFs for applications such as gas adsorption, catalysis, drug delivery, electronics, and luminescence.²⁻⁴ Wettability is a characteristic that attracts significant attention in the practical applicability of materials, including MOFs.⁵⁻⁷ Engineering the wettability of a material presents a rational, yet complex solution to combat failure related to water absorptivity in biomedical, energy, environmental and industrial systems. The ability carefully and predictably to tune MOF wettability would enhance potential applications and provide a material with controlled, desirable characteristics.

Currently counted among the most-studied frameworks, copper benzene-1,3,5-tricarboxylate ($\text{Cu}_3(\text{BTC})_2$), has shown a range of notable applications; however, water instability presents a significant obstacle for practical use.⁸⁻¹⁰ A method to control interaction of a MOF with water would permit this instability to be circumvented or exploited for a specific application. For example, rendering the material more stable in aqueous environments would significantly impact long-term applications, while tunable degradation rates would hold potential for drug carriers with tunable drug release.^{11,12} Post-synthetic modification (PSM) provides a method of obtaining new physical and chemical characteristics with preexisting MOFs via late stage functionalization of the material including altering the hydrophobicity.¹³⁻¹⁷ While changing the overall wettability of

material from hydrophilic to hydrophobic is valuable, control over the degree of hydrophobicity holds even more promise for expanding the overall usefulness of a material.^{18,19} Tricarboxylate ligands have an increased level of steric hindrance, which may change the rate of PSM and enable fine tuning of the amount of functionalization. These systems have yet to be thoroughly investigated with a covalent post-synthetic functionalization strategy. This is partially attributable to concerns that steric hindrance may impede access to the functional handle intended for modification. Moreover, tricarboxylate ligands with useful functional handles (such as primary amines) have limited availability. Thus, the present study was conducted to determine (a) if $\text{NH}_2\text{H}_3\text{BTC}$ can be accessed with a scalable, cost-effective synthesis to provide a tricarboxylate MOF for PSM, (b) if MOFs with sterically hindered constituents can undergo covalent PSM with long chained and branched hydrocarbons, and (c) if such PSM can expand functionality of the material by providing an isostructural system with improved hydrophobicity.

We report a practical 2-step synthetic route to 2-aminobenzene-1,3,5-tricarboxylic acid for tri-coordinate MOFs. The ensuing synthesis of the MOF $\text{Cu}_3(\text{NH}_2\text{BTC})_2$ produced a highly uniform, crystalline green powder that was subsequently functionalized with various anhydrides. The reported synthetic process yields a series of modified frameworks having mixed-ligands. Based on equivalents of anhydride added, the percent modification is varied. Remarkable reliability and reproducibility to obtain mixed-ligand ratios is observed, while drastic changes in the hydrophobic character of the material were simultaneously achieved even at low conversion quantities. The wettability of the modified MOFs was carefully evaluated for each sample with a method outlined herein that allows for comparison of water sorption rates into MOF powders. With 7% conversion using valeric anhydride, water sorption rates decreased from 8.8 $\mu\text{L}/\text{sec}$ to 0.46 $\mu\text{L}/\text{sec}$. Furthermore, this type of modification resulted in $\text{Cu}_3(\text{NH}_2\text{BTC})_2$ derivatives

demonstrating hydrophobic to nearly superhydrophobic water contact angles (120 – 150°). As a whole, this work presents a new approach to access $\text{NH}_2\text{H}_3\text{BTC}$, a reliable covalent PSM with long chained and branched hydrocarbons, and, notably, also PSM that results in altered physical and chemical properties that provide an isostructural system with tunable hydrophobicity and enhanced stability to water. The type and percentage of modification is results in significant variations to the wettability of the material in this 3D MOF system.

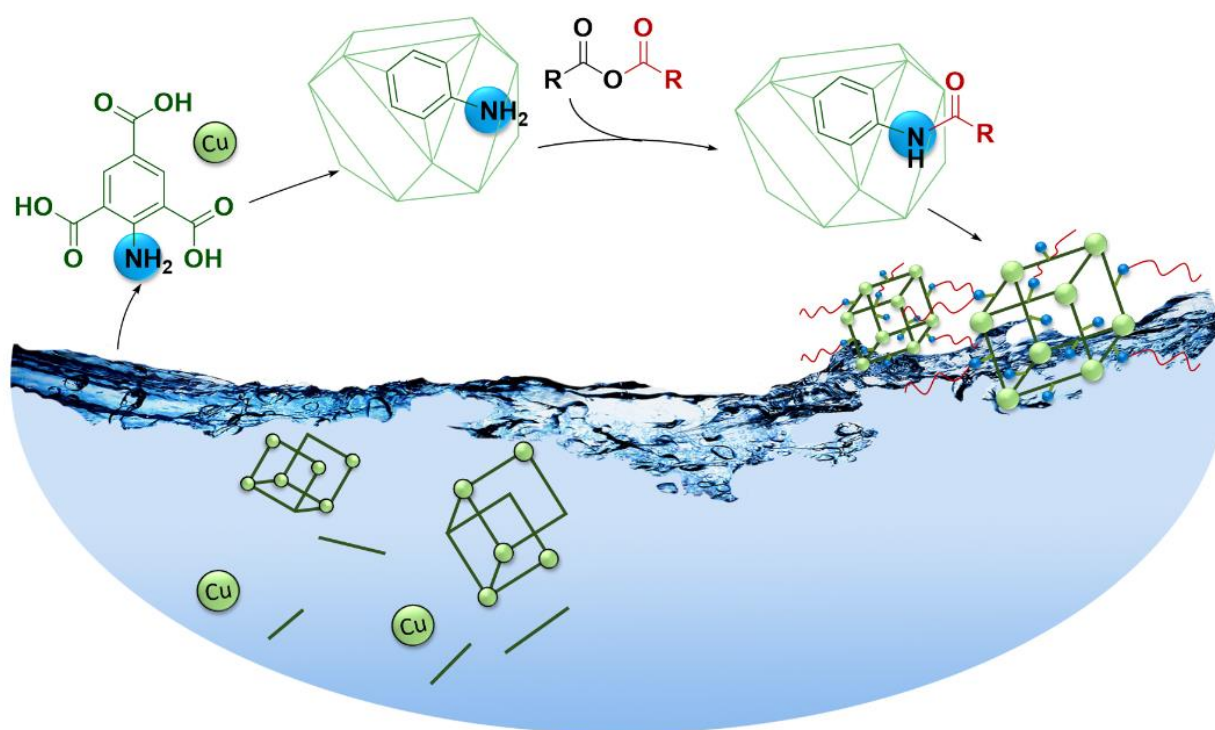


Figure 2.1. We report here the synthesis and characterization of ligand 2-aminobenzene-1,3,5-tricarboxylic acid ($\text{H}_3\text{NH}_2\text{BTC}$) for copper metal-organic framework $\text{Cu}_3(\text{NH}_2\text{BTC})_2$ and subsequent post-synthetic modification. Functionalization of $\text{Cu}_3(\text{NH}_2\text{BTC})_2$ changes the physicochemical properties of the material, resulting in various degrees of hydrophobicity and stability to water. A linear relationship observed between the length of the functionalized moiety and the water contact angle facilitates a predictable method for achieving a range of desirable sorption rates and controllable wettability.

2.3 Experimental Section

2.3.1 Materials.

Syntheses sensitive to air and moisture were performed using standard Schlenk techniques under an atmosphere of inert nitrogen or argon. Anhydrous dimethylformamide (DMA), and anhydrous methanol (MeOH) were purchased through Sigma Aldrich. Anhydrous chloroform (CHCl_3) was obtained from Fisher Scientific. $\text{Cu}_3(\text{BTC})_2$ was purchased as Basolite C300 from Sigma Aldrich. Additional solvents and reagents were obtained from TCI, Aldrich, and Alfa Aesar, and used without further purification. The synthesis of the MOF $\text{Cu}_3(\text{NH}_2\text{BTC})_2$ herein is previously described in the literature.¹⁸ A Millipore purification system set at 18 M Ω was used for all water submersion experiments.

2.3.2 Characterization.

All NMR experiments were performed using an Agilent (Varian) 400MR equipped with automated tuning and a 7600 sample changer at room temperature. All NMR spectra were analyzed using MestReNova NMR software. In order to verify and quantify modification to each ligand after the above PSM procedure, all samples were digested in acid to analyze the individual components. For NMR analysis approximately 5 mg of modified MOF was added to an NMR tube followed by 0.8 mL DMSO and 3 drops of DCl. NMR tubes were vortexed briefly and sonicated for 1 minute, whereby the solution took on a fluorescent green hue. The material was allowed to settle for 10 minutes and ^1H NMR spectra was acquired. For mass spectrometry (MS) data approximately 1 mg of each modified sample was added to a 2 mL Agilent vial followed by 1 mL of MeOH and 1 drop of HCl. The vials were shaken by hand until all particulate was fully dissolved (approximately 5 minutes) and mass spectra was acquired using an Agilent 6224 Accurate Mass

TOF LC/MS with electrospray and multi-mode (ESI/APCI) sources in negative or positive ion mode by direct injection in methanol. For each sample $[M - H]^-$ or $[M + H]^+$ was detected for both the unmodified and modified ligands. Thermal stability was evaluated using thermal gravimetric analysis (TGA) acquired with a TGA Q500 V20.13 Build 39 instrument with a ramp rate of 20 °C/min under an inert flow of nitrogen from 25 °C to 800 °C, and analyzed with TA Universal Analysis. Sample mass was approximately 1-5 mg. Powder X-Ray diffraction (PXRD) patterns were obtained using a Bruker D8 Discover DaVinci Powder X-ray Diffractometer with $CuK\alpha$ radiation operated at 40 kV and 40 mA. A 0.6 mm divergent slit was placed on the primary beam side and a high-resolution energy-dispersive LYNXEYE-XE-T detector on the diffracted beam side during the XRD studies. The instrument alignment was tested using the NIST 1976b SRM. A typical scan rate was 0.1 sec/step with a step size of 0.02 deg. Infrared (IR) data was acquired on a Nicolet 6700 FTIR spectrometer with all samples prepared as pressed potassium bromide (KBr) pellets. In short, approximately 5 – 10 mg of gently ground MOF was added to a clean 10 mL beaker followed by approximately 200 mg of FTIR grade potassium bromide. After thoroughly mixing samples were pressed to obtain sample-containing KBr pellets.

2.3.3 Synthetic Methods.

N-mesitylacetamide was synthesized in two steps beginning with 2,4,6-trimethylaniline via modifications to a known literature procedure.²¹ Under Argon atmosphere 2,4,6-trimethylaniline (10.5 mL, 75 mmol, 1 equiv) was added to a flame dried 500 mL round bottom flask equipped with a Teflon stir bar. Dichloromethane (100 mL) was added while stirring and the flask was cooled to 0 °C. Acetyl chloride (5.64 mL, 79 mmol, 1.05 equiv) was added dropwise via addition funnel, followed by triethylamine (11.01 mL, 79 mmol, 1.05 equiv). The reaction was monitored

by TLC. When little to no starting material remained (approximately 2 hours), the reaction mixture was filtered. The solid was suspended in water for 30 minutes, collected by filtration, and dried overnight *in vacuo* to yield 9.5 grams, 72%. Crude material was carried on without further purification. ^1H NMR: (CDCl_3 , 400 MHz, δ): 6.93, s, 2H; 2.29, s, 3H; 2.25, s, 6H; 1.73, s, 3H. ^{13}C NMR: (CDCl_3 , 101 MHz, δ): 169.0, 137.1, 136.3, 135.3, 129.2, 128.9, 23.18, 20.90, 19.75, 18.33. MS ESI-APCI found $M+1 = 178.12$. IR: (KBr pellet) ν (cm^{-1}) = 3147, 3097, 2914, 2852, 2764, 2534, 2447, 1896, 1716, 1676, 1483, 1414, 1225, 766.

2-aminobenzene-1,3,5-tricarboxylic acid was synthesized from crude *N*-mesitylacetamide, in a one-pot oxidation of the methyl substituents² and removal of the acetyl group. *N*-mesitylacetamide (5.0 g, 28.2 mmol, 1 equiv) was added to a 500 mL round bottom flask equipped with a Teflon stir bar and condenser followed by 165 mL deionized H_2O . NaOH was added (0.55 g, 14 mmol, 0.5 equiv) slowly in approximately 0.1 g portions over 5 minutes. KMnO_4 was added last (34 g, 215 mmol, 7.8 equiv) in approximately 5 g portions over 2 hours at room temperature. Once the KMnO_4 addition was complete, the reaction was stirred for 1 hour at room temperature and then heated to reflux at 85°C for 72 hours. The resultant brown slurry was filtered through filter paper to remove MnO_2 , and rinsed with 200 mL hot water. The clear filtrate was acidified with 20 mL concentrated HCl while stirring to a pH of 1–2. The mixture was refluxed overnight at 100°C . Upon cooling to room temperature the product crystallized in solution as a white solid. The solid was filtered and rinsed with 200 mL ice cold water yielding 3 grams, 40% of the product. ^1H NMR: (DMSO-d_6 , 400 MHz, δ): 13.27 (s, 3H); 8.56 (s, 2H); 8.55 (s, 2H). ^{13}C NMR: (DMSO-d_6 , 101 MHz, δ): 169.1, 166.6, 155.6, 138.7, 115.1, 112.0. MS ESI-APCI found $M+1 = 226.03$. IR (KBr pellet) ν (cm^{-1}) 3418, 3291, 3074, 1716, 1678, 1446, 1570, 1292, 1252, 1114, 1084, 883, 813, 694.

2.3.4 Synthesis of MOF $\text{Cu}_3(\text{NH}_2\text{BTC})_2$.

The MOF was synthesized following modification to a known literature procedure.¹⁰ In brief, 2-aminobenzene-1,3,5-tricarboxylic acid (510 mg, 2.65 mmol, 1 equiv) was added to a 100 mL Pyrex glass container followed by $\text{Cu}(\text{NO}_3)_2 \cdot 3\text{H}_2\text{O}$ (1.03 g, 4.26 mmol, 1.61 equiv). Next, 5 mL H_2O and 40 mL DMA were added by syringe and the solution was mixed via sonication for 10 minutes. The homogeneous solution was then heated to 85°C for 42 hours and slowly cooled to room temperature. The resulting green/teal crystalline MOF material was collected by filtration and dried in air overnight. The MOF was then loaded into a cellulose thimble and was treated by Soxhlet extraction with ethanol for 20 hours to exchange the solvent. Lastly, the MOF was thermally activated in a vacuum oven at 120°C for 20 hours yielding a dark green powder.

2.3.5 Post-synthetic modification (PSM) of MOF $\text{Cu}_3(\text{NH}_2\text{BTC})_2$.

For each modification $\text{Cu}_3(\text{NH}_2\text{BTC})_2$ (75 mg, 0.2 mmol relative to the amine) was added to a 2-dram vial followed by 4 mL of CHCl_3 and soaked overnight. After 12 hours each vial was dosed with 1, 10, 20 or 40 equivalents of the desired anhydride. The heterogeneous mixtures were mixed via vortex for 3 seconds at 3000 RPM. Vials were then heated to 45°C for 24 hours in a heating block. Upon cooling, the vials were centrifuged at 3000 RPM for 10 minutes. Solvent was decanted with a pipette and 4 mL clean CHCl_3 was added. The vials were vortexed once again, centrifuged, and the solution decanted. This was repeated 2 times. Once more CHCl_3 was added and soaked overnight. After 12 hours the vials were centrifuged and solvent decanted. The MOFs were dried in open atmosphere for 12 hours followed by 12 hours in the oven at 100°C . To remove residual chloroform, the material can be rinsed with methanol as described above; however, rinsing with methanol bears no impact on the hydrophobic effects observed, nor does it remove any

additional byproduct observed. All modifications were performed three times using three independent $\text{Cu}_3(\text{NH}_2\text{BTC})_2$ samples. Various batches of the MOF were used for each modification to confirm that the percent conversions were independent of the different batches of MOF used. The values given represent the average and standard deviation of three independent trials. The percent conversions were calculated by comparing the ratio of the aromatic chemical shifts associated with the unmodified and modified ligands in the ^1H NMR spectra of each independent acid digested material.

2.3.6 Wettability Studies.

Contact Angle Goniometry (CAG) was performed to analyze the interaction of the materials with water using a Krüss DSA30 goniometer with ultrapure water. Approximately 10 mg of each MOF powder was gently ground and added to a glass slide. Using another glass slide the material was carefully pressed to 2 mm in height. Videos were collected at 25 frames per second for 10 seconds. All water contact angles (WCA) were determined with a 6 – 8 μL droplet of water, whereby contact angles were calculated at 1 second after deposition. For less hydrophobic materials, measuring a static WCA was not possible. Therefore, water sorption rates were determined using 1 μL droplets of water. The time which the water droplet made contact with the material was subtracted from the time at which the entire water droplet went into the material. This value in milliseconds was used to determine the rate that 1 μL took to sorb into the material and is reported as the sorption rate in $\mu\text{L}/\text{s}$. The values given represent the average and standard deviation of three independent trials. It is vital to prep the samples consistently to ensure that the packing, particle size, roughness, thickness, and amount of material is consistent from sample to sample, as all may influence the WCA observed. Thus, while the change in hydrophobicity likely leads to the

observed change in WCA herein, packing, particle size, roughness, thickness, and amount of material may also contribute to the observed WCAs.

2.3.7 Structural Stability in Water Studies.

To test the stability of the MOF in water, approximately 10 mg of $\text{Cu}_3(\text{NH}_2\text{BTC})_2$, or the modified MOF was added to a 20 mL glass vial. Slowly, 5 mL of millipore water was poured into each vial. Vials sat undisturbed for 30 minutes, after which Kimwipes were used to absorb the water. The material was dried for 1 hour in open atmosphere, followed by 1 hour in the oven at 100°C and immediately analyzed with PXRD and Scanning electron microscope (SEM) imaging. SEM imaging was performed using a JEOL JSM-6500F microscope prior to and after water exposure. An accelerating voltage of 15.0 kV and a working distance of 10.0 mm were used. All samples were placed under vacuum and coated with 10 nm gold prior to imaging. Five to six representative images were taken at three different magnifications for each sample.

2.3.8 Data Analysis.

All postsynthetic modifications were performed three times using three independent $\text{Cu}_3(\text{NH}_2\text{BTC})_2$ samples. Various batches of the MOF were used for each modification to confirm that the percent conversions were independent of the different batches of MOF used. The percent conversions were calculated by comparing the ratio of the aromatic chemical shifts associated with the unmodified and modified ligands in the ^1H NMR spectra of each independent acid-digested material. The data reported in Table 1 represents the average of the three modified samples and the standard deviation associated with those averages. In the CAG experimentation the standard deviation shown is associated with the average of the three separate rates acquired for the sample.

When contact angles could be determined, 6–8 μL droplets were used. The contact angles reported are the average of three independent droplet contact angles after 1 second of water deposition, and the standard deviations reported are the respective calculated standard deviations. Contact angles were plotted versus the number of carbons in the PSM amide modification. A linear fit was plotted with an equation of $y = 5.7x + 89.5$, $R^2 = 0.97$. Each data point represents the average of three trials. Error bars represent the standard deviation of 3 separate water droplets. By inserting a desired number of carbons in the carbon chain length for x , one can solve for the observed contact angle, y . Alternatively, if a desired contact angle is inserted for y , an estimated number of carbons needed in the amide chain can be deduced by solving for x .

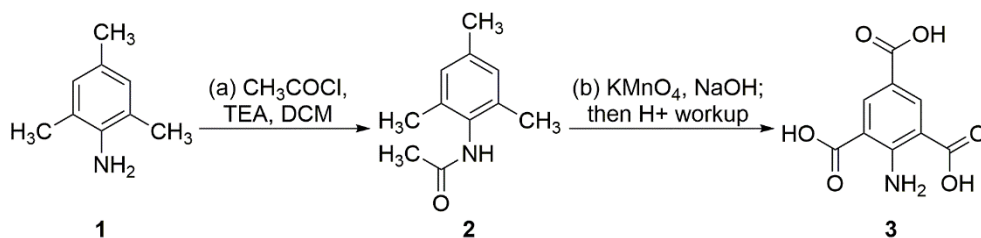
2.4 Results and Discussion

2.4.1 Synthesis and Characterization.

Having direct and efficient access to a benzene-1,3,5-tricarboxylate ligand containing a functional group for late-stage modification enables the modification of isostructural MOFs. Tricarboxylate ligands with useful functional handles (such as primary amines) have limited availability. An amine functional handle is particularly attractive from a PSM perspective due to its susceptibility to an assortment of potential chemical modifications.¹⁴ The only existing preparation of the amine-functionalized tricarboxylate ligand 2-aminobenzene-1,3,5-tricarboxylic acid ($\text{NH}_2\text{H}_3\text{BTC}$) involves an expensive synthesis with 2-fluoromesitylene (\$45.70/g AA) achieved in low to moderate yields.^{20, 23} Thus, initial efforts were focused on devising a more efficient synthetic route. Protection and deprotection steps are minimized in our 2-step approach followed by an HCl workup to **3** in 30% overall yield on gram scale (Scheme 2.1). Using 2,4,6-

trimethylaniline **1** decreased the cost of synthesis more than 120-fold as compared to previous reports (\$0.36/g AA).²³

Scheme 2.1. Synthesis of 2-aminobenzene-1,3,5-tricarboxylic acid (NH₂H₃BTC).



Reagents: (a) **1** (1.0 equiv), CH₃COCl (1.05 equiv), TEA (1.05 equiv), DCM, 0 → 25 °C, 2 h, 72% yield; (b) **2** (1.0 equiv), KMnO₄ (7.8 equiv), 1 M aq NaOH (0.5 equiv), H₂O, 25 → 85 °, 72 h; then 12 M aq HCl, pH = 1, reflux, 12 h, 40% yield; 30% overall yield. Abbreviations: TEA = triethylamine; DCM = dichloromethane.

The amine was first protected as an amide using acetyl chloride and subsequently oxidized with KMnO₄ over 3 days. After filtering to remove unwanted oxidized manganese products, the desired product was simultaneously deprotected and protonated in a hydrochloric acid workup. Upon cooling, the product crystallized as a pure white powder and was isolated by filtration. This approach was found to be a remarkably straightforward method of accessing this compound. NH₂H₃BTC was then used for the synthesis of the MOF Cu₃(NH₂BTC)₂ under hydrothermal conditions in DMF.²⁰ The resultant green crystalline material was thoroughly rinsed and solvent exchanged with ethanol. Thermal activation of the material results in a much darker green color (almost black). Overall this route to NH₂H₃BTC requires the use of minimal purification steps, reduces the number of protection and deprotection steps, and is accomplished with significant economical improvements, yielding an attractive efficient synthesis of the ligand and the MOF Cu₃(NH₂BTC)₂. This approach enables practical exploration of Cu₃(NH₂BTC)₂ for post-synthetic

modification including amidation, alkylation, diazonium salt formation, enamine formation, and carbamate formation, amongst others.

2.4.2 Post-synthetic modification.

PSM of $\text{Cu}_3(\text{BTC})_2$ is limited to dative modification, and modification of the carboxylate moiety.²⁴⁻²⁶ There is one example of covalent PSM with the isostructural system $\text{Cu}_3(\text{NH}_2\text{BTC})_2$ that showed $\text{Cu}_3(\text{NH}_2\text{BTC})_2$ can successfully undergo modification with acetic anhydride, while maintaining porosity.²⁰ Thus, the present study aimed to modify $\text{Cu}_3(\text{NH}_2\text{BTC})_2$ with a variety of anhydrides containing inherent hydrophobic moieties to confer greater hydrophobicity and altered wettability.

In each PSM procedure $\text{Cu}_3(\text{NH}_2\text{BTC})_2$ was soaked in chloroform overnight and subsequently dosed with 1, 10, 20, or 40 equivalents of the desired anhydride with respect to the amount of free amine (Table 1). After 24 h, solvent was removed and successive rinsing and drying steps afforded the modified MOFs. Little to no effect on conversion was achieved when increasing equivalents beyond 40, increasing reaction time, or with increasing the temperature of the reaction. The mass $[\text{M} - \text{H}]^-$ of both the unmodified and modified linkers was abundant in the digested mass spectrum of each modification, confirming the mixed-ligand functionalization. The appearance and intensity of a chemical shift within the ^1H NMR spectra at 8.39 ppm of the digested MOF samples is indicative of the aromatic protons on the modified amino tricarboxylate ligands (Figure 2.2). The unmodified ligand peaks are denoted with a black square and appear slightly downfield of the modified ligands denoted with red circles. The two peaks in the aromatic region were used to quantify the conversion ratio of modified to unmodified ligands after PSM.

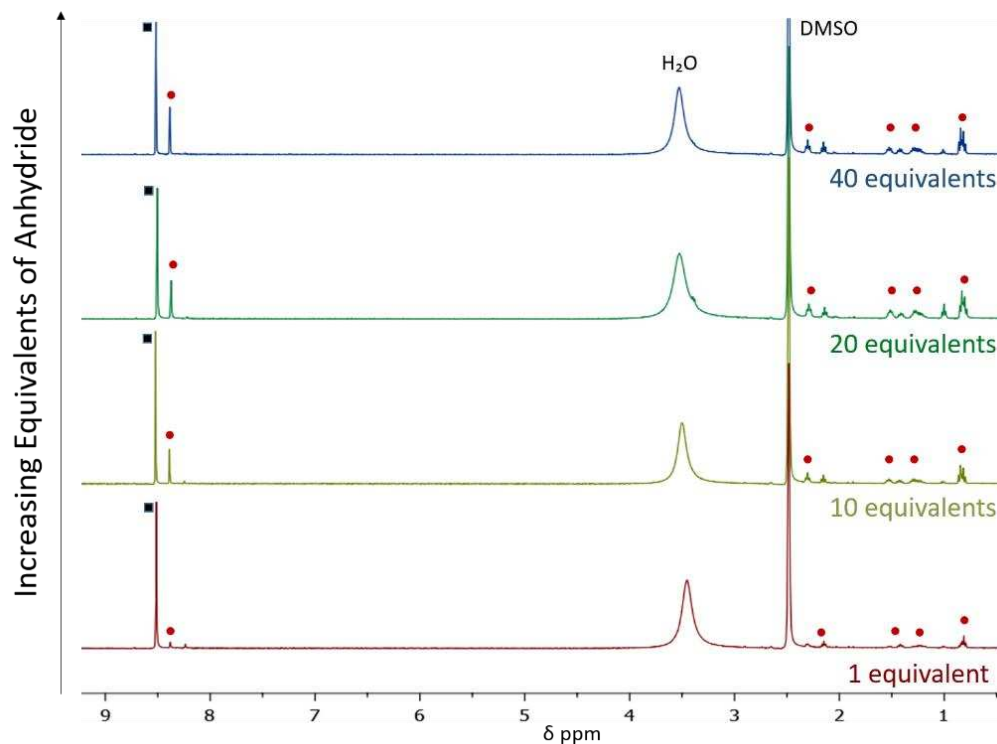


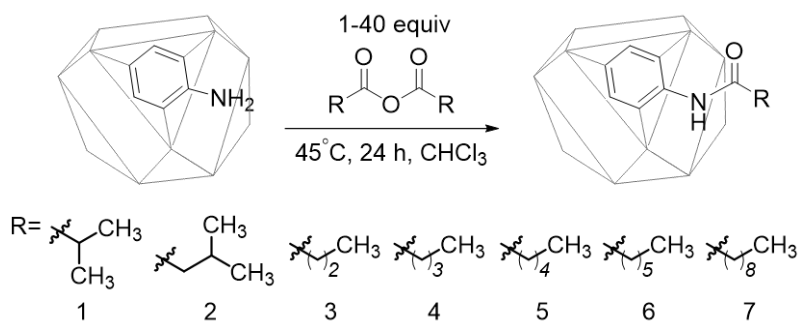
Figure 2.2. ^1H NMR spectra after acid digestion with DCl in DMSO- d_6 of modified $\text{Cu}_3(\text{NH}_2\text{BTC})_2$ with valeric anhydride to confirm synthesis of $\text{Cu}_3(\text{NH-AM5-BTC})_2$. All samples were dried at 100°C for 12 h and digested in 0.8 mL DMSO with 2 drops of DCl. The unmodified ligand peaks are denoted with a black square and appear slightly downfield of the modified ligands denoted with red circles. The appearance and intensity of a chemical shift within the ^1H NMR spectra of the digested MOF samples at 8.39 ppm, indicative of the aromatic protons on the modified amino tricarboxylate ligands, was identified. The aromatic region (8 ppm – 9 ppm) was used to quantify percent conversion to the desired amides. As the equivalents of anhydride increases, so does the percentage of modification, denoted by the peak in the aromatic region with the red circle.

Reproducible control of a range of percent conversions was accomplished for each different anhydride used (Table 2.1). As the carbon chain of the PSM amide increases in linear aliphatic chain length, a decrease in the maximum percent conversion is observed. Overall, this trend is consistent with reports of PSM with NH_2BDC ; however, these reports indicate that amide chains with 8 or less carbons led to near complete conversion (>90%). In our study with NH_2BTC , chains as low as 4 carbons in length result in maximum conversions of 50%. Modifications with

branched chain functionalities do not seem to fit this trend. We hypothesize that these observations may be due to steric hindrance, preventing access and diffusion of the anhydrides used for these reactions to the intended modification sites.

Complete conversion of $\text{Cu}_3(\text{NH}_2\text{BTC})_2$ with anhydrides containing carbon lengths of 4 or more does not appear to be possible; however, this provides a unique opportunity to control mixed-ligand ratios within this framework and may be attributable to the decrease in disorder of the BTC system due to the increased substitution of the ligand. This is often not the case with mixed-ligand syntheses, wherein the ratio of mixed-ligands added to form the desired MOF does not predictably impact the percent incorporation of each ligand present in the resultant MOF formulation.²⁷

Table 2.1. Percent Modification of $\text{Cu}_3(\text{NH}_2\text{BTC})_2$ with Anhydrides^a



| Entry | MOF | % Conversion | | | |
|-------|---|--------------|------------|------------|------------|
| | | 1 equiv | 10 equiv | 20 equiv | 40 equiv |
| 1 | $\text{Cu}_3(\text{NH-AM}i\text{Pr-BTC})_2$ | 6 ± 1 | 10 ± 6 | 11 ± 2 | 20 ± 6 |
| 2 | $\text{Cu}_3(\text{NH-AM}i\text{Bu-BTC})_2$ | 11 ± 0 | 28 ± 1 | 37 ± 0 | 43 ± 0 |
| 3 | $\text{Cu}_3(\text{NH-AM}4\text{-BTC})_2$ | 14 ± 1 | 31 ± 1 | 43 ± 0 | 50 ± 3 |
| 4 | $\text{Cu}_3(\text{NH-AM}5\text{-BTC})_2$ | 7 ± 4 | 20 ± 6 | 25 ± 8 | 32 ± 3 |
| 5 | $\text{Cu}_3(\text{NH-AM}6\text{-BTC})_2$ | 13 ± 2 | 20 ± 5 | 27 ± 7 | 32 ± 1 |

| | | | | | |
|---|-------------------------------------|-----------|------------|------------|------------|
| 6 | $\text{Cu}_3(\text{NH-AM7-BTC})_2$ | 9 ± 1 | 18 ± 2 | 22 ± 2 | 26 ± 4 |
| 7 | $\text{Cu}_3(\text{NH-AM10-BTC})_2$ | 6 ± 1 | 10 ± 1 | 11 ± 1 | 13 ± 1 |

^aAll values are the average and standard deviations of three independent experiments.

The ability to reliably access mixed-ligand frameworks yields materials that have multiple distinctive pore environments with different chemical properties within the same material.²⁸ This type of control could permit multi-selective gas adsorption (among other multifunctional applications) due to the ability to tune a percentage of the ligands, and by default affect the properties of a desired percentage of pore sites within the same material.²⁹

Conversion limitations may also be advantageous for the retention of MOF crystallinity. Using acetic anhydride (2 carbons in amide), up to 92% conversion can be achieved, however, after 73% conversion substantial loss of crystallinity is observed.²⁰ In this study, when using butyric anhydride with a 4 carbon chain, the maximum conversion is limited to 50% and the same degradation concerns are not observed. A close examination of the ¹H NMR spectra obtained from the digested modified MOFs shows that minor peaks are present, consistent with carboxylic acid byproduct generated during the formation of the amide. The presence of this byproduct may suggest that it is simply trapped within the MOF. Alternatively, the byproduct may be coordinating to the copper metal ions, replacing the labile ethanol ligands.³⁰ This byproduct provides insight to a plausible mechanism for modification-related degradation. Nevertheless, even at maximum levels of modification, thermal gravimetric analysis indicates that the modified materials in this study maintain thermal stability compared to the unmodified material (Supporting information, APPENDIX A.3). Additionally, PXRD reveals crystallinity is retained after each modification with 40 equivalents of anhydride to amine as evidenced by patterns having matching 2 θ reflections (Figure 2.3). Thus, we have developed a covalent PSM approach with $\text{Cu}_3(\text{NH}_2\text{BTC})_2$ that allows

reliable access to mixed-ligand frameworks having conversions ranging from 6–50% with a retention of structural integrity.

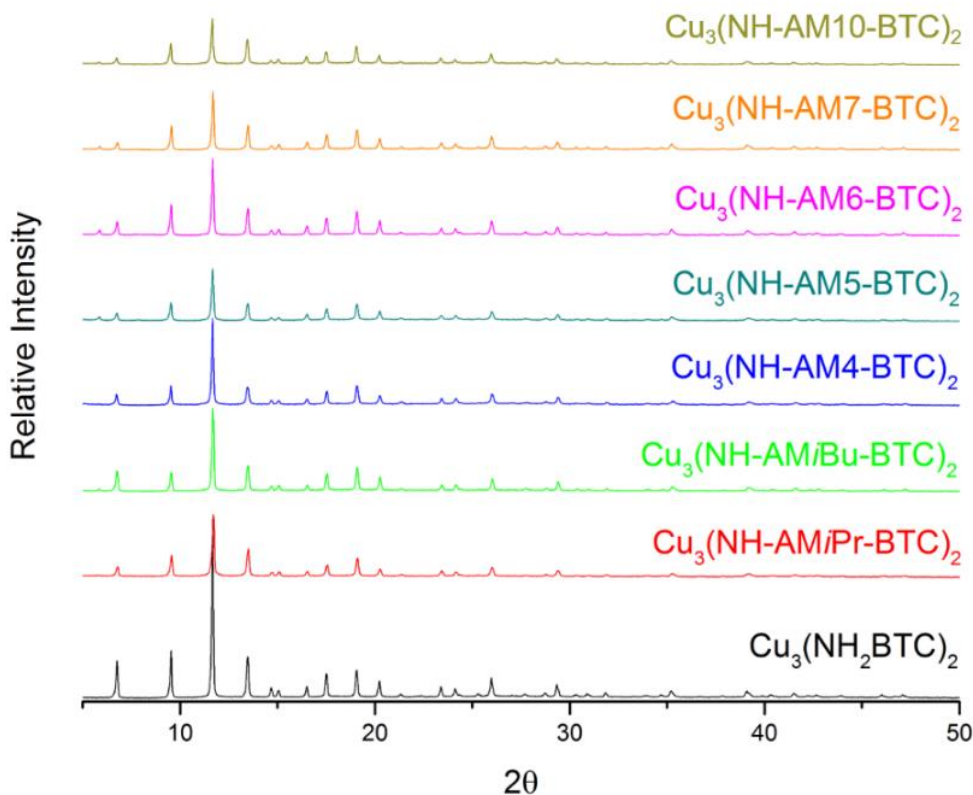


Figure 2.3. Powder X-ray diffraction patterns for unmodified $\text{Cu}_3(\text{NH}_2\text{BTC})_2$ (black) and all modified samples with 40 equivalents of anhydride, showing little to no loss of crystallinity after modification. All samples were dried at 100°C gently ground and pressed onto a zero-diffraction silicon plate.

2.4.3 Post-synthetic Modification to Alter Wettability.

We anticipated that modifying $\text{Cu}_3(\text{NH}_2\text{BTC})_2$ would increase the overall hydrophobicity of the material, leading to improved water stability. Contact angle goniometry (CAG) has previously been used with PSM to show hydrophobic and super hydrophobic properties of zinc MOFs.¹⁶ We expanded upon this technique to use CAG to not only observe contact angles achieved after maximum modification, but also to compare the sorptive rates of the materials at varying

amounts of conversion. According to Krüss Scientific, when the contact angle of a liquid on a porous solid is less than the critical angle for spontaneous capillary or pore wetting at 90° , the CAG water contact angle method cannot accurately be obtained; therefore, in this study sorptive rates are reported.

The MOF material was gently ground and pressed using a glass slide to nearly 2 mm thick onto a separate glass slide. Water sorption rates were calculated using 1 μL droplets and the total time necessary to completely sorb 1 μL of water into the powder was used to determine a relative sorption rate for the resultant material after minimum and maximum conversions. As samples increased in hydrophobic character, water droplets of 1 μL would not deposit on the surface of the material; for these samples 6–8 μL water droplets were dispensed and contact angles were calculated 1 second after the droplet made contact with the MOF material. Table 2 shows the results of the CAG experimentation from averaging three independent water droplet experiments being reported as the corresponding average.

The hydrophobicity of the material closely correlates to the modification and overall percent of modification. $\text{Cu}_3(\text{NH}_2\text{BTC})_2$ exhibits a similar sorption rate as $\text{Cu}_3(\text{BTC})_2$ at 8.8 $\mu\text{L}/\text{s}$ (Table 2.2). All of the modified material has slower sorption rates than the unmodified material, demonstrating that all of the modifications made increase the hydrophobic character of the MOF, albeit to different extents. For instance, $\text{Cu}_3(\text{NH-AMiBu-BTC})_2$ with 11 % conversion results in nearly half the sorption rate of the unmodified material, sorbing water at a rate of $4.1 \pm 1.6 \mu\text{L}/\text{s}$. Additionally, nearly all materials exhibit greater hydrophobicity with slower sorption rates or contact angles achieved using 40 equiv of anhydride versus 1 equiv. Materials displaying contact angles from 90° – 150° are considered hydrophobic.³¹ Maximum percent modifications with 5 or more carbons in the alkyl chain result in contact angles from 95° – 147° , rendering these new mixed-

ligand systems hydrophobic (Table 2, Figure 2.4C and 2.4D). Upon increasing modification to nearly 32% with valeric anhydride, sorption rates are significantly decreased so that after 1 s, a water contact angle of $118 \pm 4^\circ$ is achieved. Unexpectedly, as little as 6 % modification with decanoic anhydride led to a contact angle of $66 \pm 6^\circ$. At 13 % conversion an impressive hydrophobic effect was achieved where the material exhibited an observed contact angle of $147 \pm 6^\circ$.

Over the course of these experiments, several intriguing trends unique to the $\text{Cu}_3(\text{NH}_2\text{BTC})_2$ system were identified. Increased hydrophobicity and slower sorption rates are achieved with straight-chain versus branched moieties. This trend holds true for both 4 and 5 carbon modifications; such as valeric versus isovaleric, and butyric versus isobutyric anhydrides. The modified samples displayed distinctive hydrophobic properties, whereby with the MOF powder spread over the entire surface of the water droplet during the CAG experiments (Figure 2.4C). This observation may indicate a change in adhesion properties or electrostatic charge in the modified materials. These observations may be a consequence of changes in mechanical interlocking, inter-particulate forces of cohesion, liquid bridging, or moisture-induced particle adhesion, or reduced particle stiffness.³²⁻³⁵ These properties are not observed with the unmodified materials, further supporting the capability of late-stage functionalization to tune the chemical properties of the material. Superhydrophobic materials are characterized by contact angles $>150^\circ$, accordingly modification of $\text{Cu}_3(\text{NH}_2\text{BTC})_2$ yielded near superhydrophobic powders ($\sim 147^\circ$). These data indicate modifications have a relatively significant impact on the hydrophobicity of this material, resulting in varied sorption rates.

Table 2.2. Effect of PSM on Wettability^{a,b}

| Entry | MOF | % Conversion | Sorption ($\mu\text{L/s}$) | Contact Angle |
|-------|---|--------------|------------------------------|-----------------|
| 1 | $\text{Cu}_3(\text{NH}_2\text{BTC})_2$ | 0 | 8.8 ± 0 | n/a |
| 2 | $\text{Cu}_3(\text{NH-AM}i\text{Pr-BTC})_2$ | 6 ± 1 | 1.8 ± 0.1 | n/a |
| | | 20 ± 6 | 1.5 ± 0.3 | n/a |
| 3 | $\text{Cu}_3(\text{NH-AM}i\text{Bu-BTC})_2$ | 11 ± 0 | 4.1 ± 1.6 | n/a |
| | | 43 ± 0 | n/a | 94.9 ± 1.3 |
| 4 | $\text{Cu}_3(\text{NH-AM}4\text{-BTC})_2$ | 14 ± 1 | 7.8 ± 1.9 | n/a |
| | | 50 ± 3 | 1.02 ± 0.4 | n/a |
| 5 | $\text{Cu}_3(\text{NH-AM}5\text{-BTC})_2$ | 7 ± 4 | 0.46 ± 0.1 | n/a |
| | | 32 ± 3 | n/a | 118.2 ± 0.9 |
| 6 | $\text{Cu}_3(\text{NH-AM}6\text{-BTC})_2$ | 13 ± 2 | 0.63 ± 0.2 | n/a |
| | | 32 ± 1 | n/a | 126 ± 5 |
| 7 | $\text{Cu}_3(\text{NH-AM}7\text{-BTC})_2$ | 9 ± 1 | 1.21 ± 0.2 | n/a |
| | | 26 ± 4 | n/a | 127 ± 6 |
| 8 | $\text{Cu}_3(\text{NH-AM}10\text{-BTC})_2$ | 6 ± 1 | n/a | 66 ± 6 |
| | | 13 ± 1 | n/a | 147 ± 6 |

^a Measurements are the average of three independent experiments. Percent conversions shown for each modification are for modifications using 1 equiv and 40 equiv of anhydride to free amine. The average and standard deviation of the three trials are reported. ^bFor samples in which the water droplet was completely taken into the material after 1 second of deposition a WCA could not be determined. Therefore, sorption rates are reported instead for these samples.

When the material is modified at maximum conversion, a linear relationship is observed where the contact angle increases in proportion to the number of carbons in the amide (Figure 2.4D). The resultant linear relationship allows for deliberate modification to access the desired level of hydrophobic character. This observation may suggest either the entire surface or a

particular pore is modified on the MOF leading to predictable contact angles. Using the linear fit, one or two more carbons to the alkyl chain may produce superhydrophobic material with calculated contact angles approximately 152–158°. Thus, this is the first report of using late stage functionalization with a metal–organic framework that allows for control of the hydrophobic properties of the material. Using ANOVA the data in Figure 2.4D was statistically significant at the 95% confidence interval; however, each individual value was not statistically significantly different from one another. At the 95% confidence interval, AM10 (147°) is statistically significantly different from all other values. Efforts to manipulate materials to attain tunable degradation and release is especially appealing for the delivery of therapeutics, among other biomedical applications.³⁶

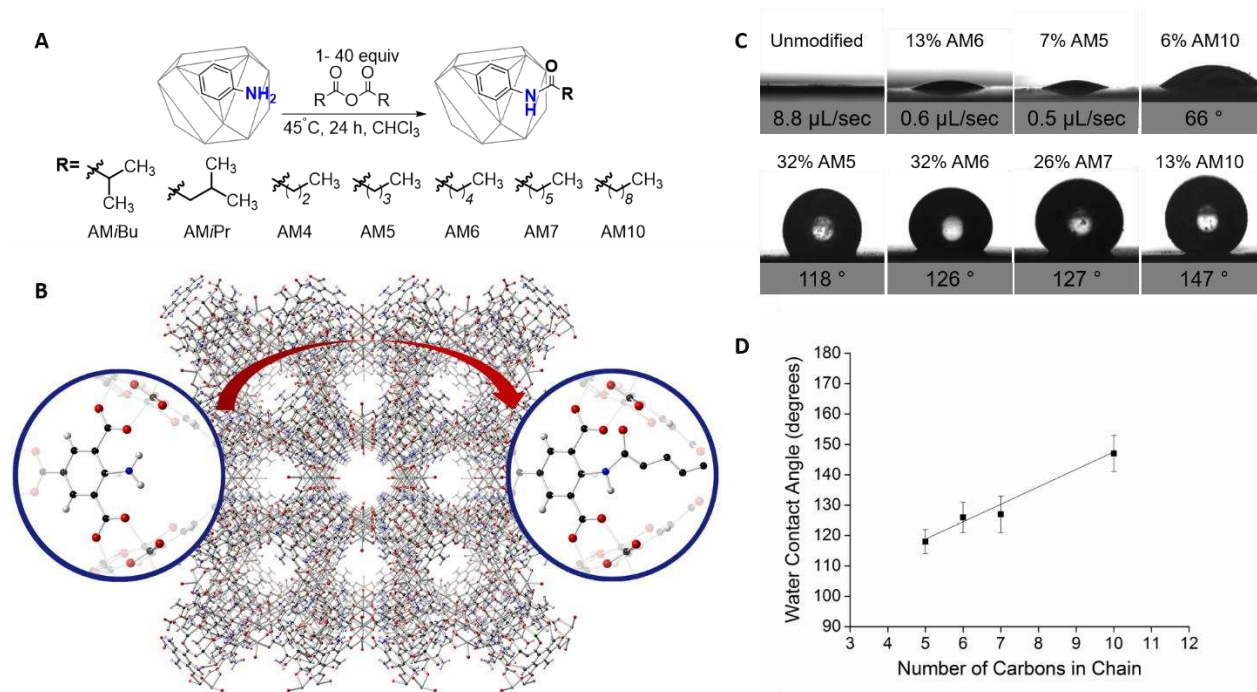


Figure 2.4. (A) PSM of the MOF with various anhydrides, (B) 3D image showing the MOF and potential sites for modification (carbon black, hydrogen white, oxygen red, nitrogen blue, copper green), (C) CAG images of water on the surface of the MOF shows tunable wettability with different modification and percentage, (D) Water contact angle increases as the number of carbons in the linear chain increase. Values and standard deviation shown are the average of three independent experiments.

2.4.4 Enhanced Stability to Water.

Since this is the first report of synthetic functionalization of a copper MOF to control hydrophobicity, we probed the limitations of water stability with the modified MOFs. $\text{Cu}_3(\text{NH}_2\text{BTC})_2$ as well as $\text{Cu}_3(\text{NH-AMiBu-BTC})_2$ and $\text{Cu}_3(\text{NH-AM10-BTC})_2$ with maximum conversions were added to 3 separate 20 mL glass vials and 5 mL of water was added to each for 30 minutes. The modified materials did not remain at the bottom of the vial and were dispersed around and at the surface of the water, demonstrating enhanced hydrophobic character (Figure 2.5A). This was especially apparent with $\text{Cu}_3(\text{NH-AM10-BTC})_2$ (Figure 2.5A, far right). Upon removal of the water and adequate drying, the powder was analyzed. The PXRD pattern of $\text{Cu}_3(\text{NH-AM10-BTC})_2$ showed a crystalline material was present after water submersion (Figure 2.5B). Conversely, $\text{Cu}_3(\text{NH}_2\text{BTC})_2$ no longer exhibited well resolved diffraction peaks after water submersion. These results demonstrate that modifying the MOF with 14 % decanoic anhydride renders this material significantly more stable in aqueous environments.

$\text{Cu}_3(\text{BTC})_2$ is known to rapidly degrade in water-rich environments.¹⁰ As such we would expect similar degradation observations with unmodified $\text{Cu}_3(\text{NH}_2\text{BTC})_2$. We evaluated this by analyzing the MOF's surface characteristics before and after water submersion. SEM imaging shows that $\text{Cu}_3(\text{NH}_2\text{BTC})_2$ is comparable to $\text{Cu}_3(\text{BTC})_2$ with regard to surface deterioration upon water submersion (Figures 2.5C and 2.5D). Prior to water submersion, the surface of $\text{Cu}_3(\text{NH}_2\text{BTC})_2$ appears smooth and uniform. After submersion there is significant change to the morphology of the MOF; pores are expanded and the original octahedral crystals are nearly impossible to distinguish. $\text{Cu}_3(\text{NH-AMiBu-BTC})_2$ still appears to undergo minor surface alteration exhibiting a more roughly textured morphology with breaks and cracks, albeit much less severe than in the unmodified material (Figure 2.5E and 2.5F). $\text{Cu}_3(\text{NH-AM10-BTC})_2$ on the other

hand, showed little to no impact to the surface characteristics after being submerged in water (Figure 2.5G and 2.5H). PXRD patterns of $\text{Cu}_3(\text{NH-AM10-BTC})_2$ and $\text{Cu}_3(\text{NH}_2\text{BTC})_2$ on the material after water submersion verified that the modified material retained crystallinity after water submersion (Supporting Information, APPENDIX Figure A23). The water submersion results indicate that tunable degradation rates are achievable by modifying $\text{Cu}_3(\text{NH}_2\text{BTC})_2$. These results suggest the stability of the material correlates with the relative amount of hydrophobicity observed. This technique can be used with other modifications made herein to assess stability to water after modification. Taken together, these data showcase the elevated hydrophobic character of the modified material and its immunity to moisture damaging effects present with $\text{Cu}_3(\text{BTC})_2$.

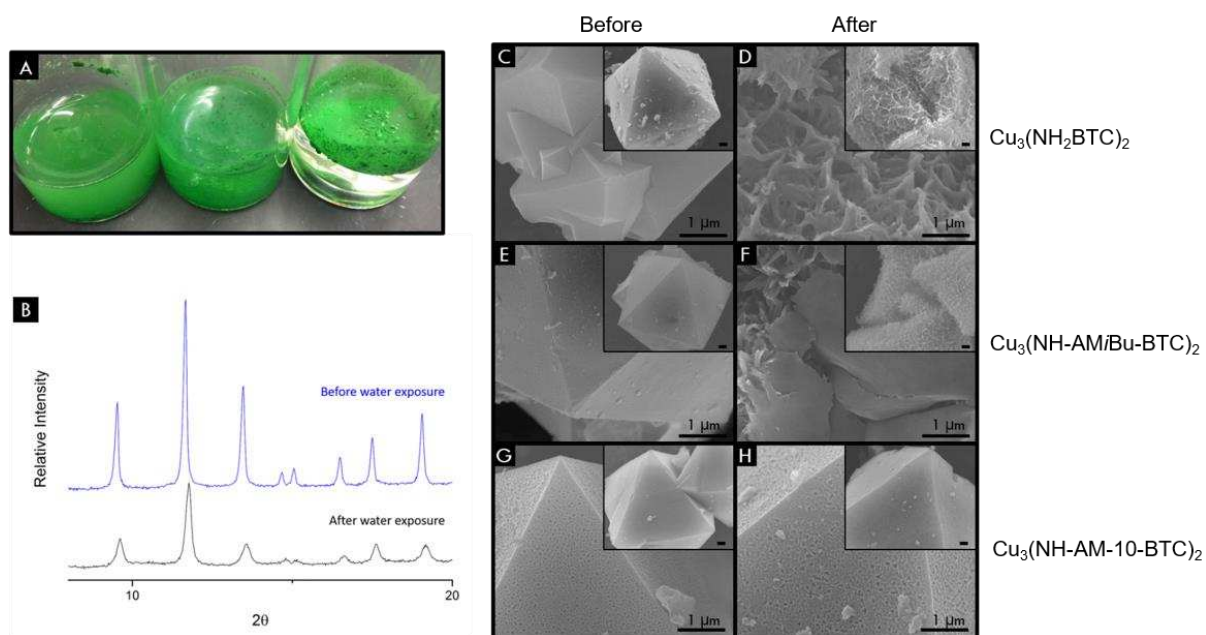


Figure 2.5. Results after water submersion. (A) (left to right) $\text{Cu}_3(\text{NH}_2\text{BTC})_2$, $\text{Cu}_3(\text{NH-AMiBu-BTC})_2$, and $\text{Cu}_3(\text{NH-AM10-BTC})_2$ in vials with 5 mL of Millipore water. (B) Powder X-ray diffraction patterns of $\text{Cu}_3(\text{NH-AM10-BTC})_2$ before and after 30 minutes of submersion in water. (C) & (D) SEM images of $\text{Cu}_3(\text{NH}_2\text{BTC})_2$ before/after water submersion, (E) & (F) SEM images of $\text{Cu}_3(\text{NH-AMiBu-BTC})_2$ before/after water submersion. (G) & (H) SEM images of $\text{Cu}_3(\text{NH-AM10-BTC})_2$ before/after water submersion. All images shown are representative of 4000X (small) and 20,000X (large) magnifications; the black bar represents 1 μm .

2.5 Conclusions

In summary, we have determined that modifying a sterically hindered MOF like $\text{Cu}_3(\text{NH}_2\text{BTC})_2$ serves as an excellent approach to improve functionality of these materials. In this study we designed a new synthesis of 2-aminobenzene-1,3,5-tricarboxylic acid affording a rapid, inexpensive route to MOF $\text{Cu}_3(\text{NH}_2\text{BTC})_2$. The new synthesis allowed for late stage functionalization with a series of anhydrides containing greasy aliphatic hydrocarbon chains. Importantly, controlled access to new mixed-ligand copper MOFs that are isostructural to $\text{Cu}_3(\text{NH}_2\text{BTC})_2$ can now be obtained without effecting the overall stability of the system. Lastly, these modifications result in tunable changes to the chemical and physical properties of the system, specifically herein leading to control over the stability of the MOF to water, the hydrophobic properties and wettability of the MOF. The results of this study expand the methods for the covalent PSM of MOFs to include copper MOFs and also opens the possibilities to PSM other BTC ligand-containing MOFs. This work foreshadows new capabilities for the same finely-tuned hybrid material to be employed in many diverse applications including biological, gas storage, and electronics, previously impeded by instability to water.

REFERENCES

1. Wang, C.; Liu, D.; Lin, W. *J. Am. Chem. Soc.* **2013**, *135*, 13222-13234.
2. Parola, S.; Julián-López, B.; Carlos, L. D.; Sanchez, C. *Adv. Funct. Mater.* **2016**, *26*, 6506.
3. Li, J.-R.; Kuppler, R. J.; Zhou, H.-C. *Chem. Soc. Rev.* **2009**, *38*, 1477-1504.
4. Furukawa, H.; Cordova, K. E.; O’Keeffe, M.; Yaghi, O. M. *Science* **2013**, 341.
5. Li, B.; Wen, H.-M.; Cui, Y.; Zhou, W.; Qian, G.; Chen, B. *Adv. Mater.* **2016**, *28*, 8819-8860.
6. Sow, P. K.; Prass, S.; Mérida, W. *Inorg. Chem.*, **2017**, DOI: 10.1021/acs.inorgchem.6b02840.
7. Jeong, H.; Kim, J. *ACS Appl. Mater. Interfaces*, **2015**, *7*, 7129–7135.
8. Sezginel, K.; Keskin, S.; Uzun, A. *Langmuir* **2016**, *32*, 1139-1147.
9. Burch, N. C.; Jasuja, H.; Walton, K. S. *Chem. Rev.* **2014**, *114*, 10575-10612.
10. Horcajada, P.; Serre, C.; Vallet-Regí, M.; Sebban, M.; Taulelle, F.; Férey, G. *Angew. Chem. Int. Ed.* **2006**, *45*, 5974.
11. Sun, K.; Li, L.; Yu, X. L.; Liu, L.; Meng, Q.; Wang, F.; Zhang, R. *Journal of Colloid and Interface Science* **2017**, *486*, 128.
12. DeCoste, J. B.; Peterson, G. W.; Schindler, B. J.; Killops, K. L.; Browe, M. A.; Mahle, J. J. *J. of Mater. Chem. A* **2013**, *1*, 11922-11932.
13. Burrows, A. D.; Frost, C. G.; Mahon, M. F.; Richardson, C. *Angew. Chem. Int. Ed.* **2008**, *47*, 8482-8486.

14. Garibay, S. J.; Wang, Z.; Tanabe, K. K.; Cohen, S. M. *Inorg. Chem.* **2009**, *48*, 7341-7349.
15. Tanabe, K. K. Z., W., and Cohen, S. M. *J. Am. Chem. Soc.* **2008**, 8508–8517.
16. Nguyen, J. G.; Cohen, S. M. *J. Am. Chem. Soc.* **2010**, *132*, 4560-4561.
17. Wittmann, T.; Siegel, R.; Reimer, N.; Milius, W.; Stock, N.; Senker, J. *Chem. Euro. J.* **2015**, *21*, 314-323.
18. Rodriguez-Hermida, S.; Tsang, M. Y.; Vignatti, C.; Stylianou, K. C.; Guillerm, V.; Perez-Caravajal, J.; Teixidor, F.; Vinas, C.; Choquesillo-Lazarte, D.; Verdugo-Escamilla, C.; Peral, I.; Juanhuix, J.; Verdaguer, A.; Imaz, I.; MasPOCH, D.; Planas, J. G. *Angew. Chem. Int. Ed.* **2016**, *128*, 16283-16287.
19. Sun, Q.; He, H.; Gao, W.-Y.; Aguila, B.; Wojtas, L.; Dai, Z.; Li, J.; Chen, Y.-S.; Xiao, F.-S.; Ma, S. *Nat. Comm.* **2016**, *7*, 13300.
20. Peikert, K.; Hoffmann, F.; Froba, M. *Chem. Commun.* **2012**, *48*, 11196-11198.
21. Cai, Y.; Kulkarni, A.; Huang, Y.-G.; Sholl, D.; Walton, K. *Crystal growth & design* **2014**, *14*, 6122-6128.
22. Tanabe, K. K.; Cohen, S. M. *Chem. Soc. Rev.* **2011**, *40*, 498-519.
23. Data accessed on March 20, 2016 at www.alfa.com and reported price per gram. All values are based on the lowest quantity available.
24. Chui, S. S.-Y. L., S. M.-F.; Charmant, J. P. H. ; Orpen, A. G.; Williams, I. D. *Science* **1999**, *283*, 1148-1150.

25. Al-Janabi, N.; Deng, H.; Borges, J.; Liu, X.; Garforth, A.; Siperstein, F. R.; Fan, X. *Ind. Eng. Chem. Res.* **2016**, *55*, 7941.
26. Mohideen, M. I. H.; Xiao, B.; Wheatley, P. S.; McKinlay, A. C.; Li, Y.; Slawin, A. M. Z.; Aldous, D. W.; Cessford, N. F.; Düren, T.; Zhao, X.; Gill, R.; Thomas, K. M.; Griffin, J. M.; Ashbrook, S. E.; Morris, R. E. *Nat. Chem.* **2011**, *3*, 304-310.
27. Yin, Z.; Zhou, Y.-L.; Zeng, M.-H.; Kurmooc, M. *Dalton Trans.*, **2015**, *44*, 5258.
28. Chen, D.-M.; Xu, N.; Qiu, X.-H.; Cheng, P. *Cryst. Growth Des.* **2015**, *15*, 961.
29. Burrows, A. D. *Cryst. Eng. Comm.* **2011**, *13*, 3623-3642.
30. Bordiga, S.; Regli, L.; Bonino, F.; Groppo, E.; Lamberti, C.; Xiao, B.; Wheatley, P. S.; Morris, R. E.; Zecchina, A. *Phys. Chem. Chem. Phys.* **2007**, *9*, 2676-2685.
31. Hawker, M. J.; Pegalajar-Jurado, A.; Fisher, E. R. *Plasma Processes and Polymers* **2015**, *12*, 846-863.
32. Lumay, G.; Boschini, F.; Traina, K.; Bontempi, S.; Remy, J. C.; Cloots, R.; Vandewalle, N. *Powder Technology* **2012**, *224*, 19-27.
33. Gregory, J.: *Particles in water properties and processes*; IWA Pub Taylor & Francis: London, **2006**.
34. Sandler, N.; Reiche, K.; Heinämäki, J.; Yliruusi, J. *Pharmaceutics* **2010**, *2*, 275.
35. Armstrong, B. B., K.; Clayton, J. *AIChE Journal* **2014**, *110*, 25-30.

36. Sankaranarayanan, J.; Mahmoud, E. A.; Kim, G.; Morachis, J. M.; Almutairi, A. *ACS Nano* **2010**, *4*, 5930-5936.

CHAPTER 3

SURFACE-ANCHORED METAL–ORGANIC FRAMEWORK–COTTON MATERIAL FOR TUNABLE ANTIBACTERIAL COPPER DELIVERY²

3.1 Summary

In the present study, a new copper MOF-cotton material was strategically fabricated to be exploited for its antibacterial properties and postsynthetic modification (PSM) to introduce a free amine to tune the physicochemical properties and the kinetic stability of the material. A modified methodology for carboxymethylation of natural cotton was utilized to enhance the number of nucleation sites for MOF growth. Subsequently, MOF $\text{Cu}_3(\text{NH}_2\text{BTC})_2$ was synthesized into a homogenous surface supported film via a layer-by-layer dip coating process. The resultant materials contained uniformly distributed $1\ \mu\text{m} \times 1\ \mu\text{m}$ octahedral MOF crystals around each carboxymethylated fiber. Importantly, the accessible free-amine of the MOF ligand allowed for PSM of the MOF-cotton surface with valeric anhydride, yielding $23.5 \pm 2.2\%$ of the amines being modified. The Cu^{2+} ion releasing performance of the materials was probed under biological conditions per submersion in complex nutrient broth media at $37\ ^\circ\text{C}$. Indeed, PSM induces a

² The following was adapted with permission from Rubin, H. N.; Neufeld, B. N.; Reynolds, M. M. Surface-Anchored Metal–Organic Framework–Cotton Material for Tunable Antibacterial Copper Delivery. *ACS Appl. Mater. Interfaces* **2018**, *17*, 15189-15199. Copyright 2018 American Chemical Society. We acknowledge financial support from the National Science Foundation Division of Biomaterials (DMR-1352201), the National Institutes of Health (1R21EB016838-021). We thank the central instrument facility, in particular Dr. Patrick McCurdy for assistance using the SEM and Dr. Roy Geiss for assistance with the TEM. We would like to thank the MIN at CSU, particularly Kim Vanderpool for aid with attaining sample cross-sections and additional help with TEM imaging. We thank the Soil, Water and Plant Testing Laboratory at CSU for ICP-OES analysis. We would also like to thank the Prieto Lab at CSU for access to their robotics. All bacteria studies with the materials were performed and plotted by coauthor Bella Neufeld specifically sections 3.3.7, 3.3.8, 3.3.9, 3.4.6, and 3.4.7. All other experimentation was performed by Heather Rubin.

change in the copper flux of the material over the first 6 h. The materials continue to slowly release Cu^{2+} ions beyond the 24 h tested at a flux of $0.22 \pm 0.003 \mu\text{mols}\cdot\text{cm}^{-2}\cdot\text{h}^{-1}$ with the unmodified MOF-cotton and at $0.25 \pm 0.004 \mu\text{mols}\cdot\text{cm}^{-2}\cdot\text{h}^{-1}$ with the modified MOF-cotton. The antibacterial activity of the material was explored using *Escherichia coli* by testing the planktonic and attached bacteria under a variety of conditions. MOF-cotton materials elicit antibacterial effects, yielding a log-4 or greater reduction, of bacteria after 24 h of exposure. Additionally, the MOF-cotton materials inhibit the attachment of bacteria, under both dry and wet conditions. A MOF-cotton material of this type would be ideal for clothing, bandages, and other textile applications. As such, this work provides precedence towards developing uniform, tunable MOF-composite textile materials that can kill bacteria and prevent the attachment of bacteria to the surface.

3.2 Introduction

The development of antibacterial surfaces to prevent the spread and growth of bacteria, remains a materials necessity of high priority to combat a pressing global health concern.^{1,2} Bacteria may thrive for weeks to months upon common surfaces including bandages, clothing, and blankets.³ Once materials of this type are compromised with microbial attachment, it is likely for the bacteria to advance to biofilm formation, in which microbial cells become increasingly impenetrable to traditional antibiotics, making treatment extremely difficult.⁴ Due to the emergence of “superbugs”, multidrug-resistant organisms, new antibacterial agents with decreased likelihood for resistance are needed.⁵ An optimal strategy is to develop efficient antimicrobial coatings, metals, and fabric materials which kill or prevent the attachment of bacteria altogether. Using small molecules which kill bacteria via multiple mechanisms is a relatively well-established route with excellent success rates for avoiding bacterial resistance.⁶⁻⁸ On the other hand, it is easier

to prevent than treat biofilms. Thus, materials with surfaces that *prevent* the attachment of bacteria altogether would minimize the spread of bacteria and, in turn, lessen the necessity for traditional antibiotics. Towards this goal, antimicrobial materials, which kill or inhibit the growth of microorganisms have become an important focus for materials science.

Nano-antimicrobial materials offer the unique opportunity to fill the void associated with current antibiotic treatment failure. While traditional antibiotics target inhibition of DNA replication, cell wall synthesis, or protein synthesis, all of which primarily due to resultant secondary oxidative species, materials containing nanoparticles, on the other hand, may be unaffected by most resistance mechanisms as they display multiple modes of action. Several modes of action of nanoparticles to kill bacteria include the direct interaction of the nanoparticles with the bacterial cell membranes to kill bacteria and prevent biofilm formation, induce metal-redox species which causes oxidative stress to damage bacterial cell components, and disrupt critical permeability into or out of the cell.^{9,10} Nanomaterials also serve as excellent drug carriers, materials which would support and strengthen traditional antibiotic treatments.¹¹ Moreover, release of small molecules or metal ions with antibacterial properties has shown promise for strategically developing antibacterial materials.

Metal-organic frameworks (MOFs) are a unique subclass of nanomaterials consisting of tunable coordination networks. Manipulation at both the metal ion centers or organic linkers yields seemingly infinite possibilities to control the physicochemical properties of the MOF-based materials. Minor adjustments to synthetic conditions permits synthetic regulation of the size and shape of the MOF crystals. Since greater surface area is associated with increased antibacterial efficacy of nanoparticles, control over particle size is valuable.¹² The unprecedented porosity achieved with MOFs gives these particular systems unique properties due to increased surface

area-to-mass ratio over other nanomaterials. This characteristic effectively increases interactions with cells in biological mediums, adversely affecting bacterial cell membranes. Additionally, controlled release and decomposition kinetics of the MOF itself or guest molecules pre-loaded into the pores yields effective synergistic therapeutic delivery systems. As such, MOFs are excellent candidates for incorporation into materials and devices to exhibit antibacterial activity.

Under controlled conditions, copper ions have proven nontoxic yet highly effective at killing bacteria and preventing the formation of biofilms.¹³ Ancient civilizations used copper to sterilize wounds and drinking water.¹⁴ More recently, antimicrobial copper alloys have been approved by the United States Environmental Protection Agency and implemented as antibacterial surfaces for a multitude of common items from electronic cases, to handles, and countertops at healthcare facilities, community facilities, residential buildings, and mass transit facilities.¹⁵ Copper is suspected to elicit antibacterial action due to multiple mechanisms including inducing intracellular leakage, cell wall accumulation causing reduced permeability, disrupting the DNA structure, damaging critical enzymes, and causing cellular internalization.¹⁶ Therefore, copper-containing MOFs present a promising opportunity to develop useful and effective antibacterial materials.

While release of Cu^{2+} ions has been observed with non-porous copper containing materials, manipulation of ion release rates is limited to the surface area of the material or specialized coatings.^{17,18} Thus, few successful attempts to synthetically control the rate of the release of Cu^{2+} ions have been reported. Tunable ion release, however, is advantageous and necessary for various environmental and biomedical applications, as this would provide an opportunity to control ion-delivery rates. CuBTC is a well-known, commercially available copper-containing MOF, which when attached to surfaces, increases antimicrobial activity at the interface.¹⁹ By utilizing a similar

ligand scaffold that contains a functional handle for postsynthetic modification (PSM) of the material, a MOF-system capable of releasing antibacterial agents would become amenable to fine tuning. Tuning of MOF-based materials would offer the exclusive opportunity to manipulate the physicochemical properties of such materials, offering control over the stability to aqueous environments using late-stage synthetic functionalization. The low temperatures associated with MOF syntheses, as compared to other copper containing synthetic processes, allows for MOF incorporation into more sensitive, flexible materials, such as polymers and textiles. Such surfaces, including bandages, curtains, and garments all serve as proponents for bacteria to attach, proliferate, and spread. Thus, PSM of MOFs on commonly used textiles for such applications, like cotton, may yield new, useful antibacterial fabric materials with controllable Cu^{2+} ion release. This would have far reaching consequences for textile applications including medical supplies, apparel, and common fabrics in shared facilities that would then be able to prevent the attachment and therefore spread of deadly bacteria.

In the present study, we engineered a new MOF-cotton material for antibacterial applications that can undergo PSM. MOF $\text{Cu}_3(\text{NH}_2\text{BTC})_2$ was grown using a layer-by-layer process on the surface of carboxymethylated cotton fabric. The resultant MOF-cotton material was uniformly coated with distinct octahedral MOF crystals to yield a robust, flexible composite. PSM to the MOF grown on cotton changes the rate at which the material delivers Cu^{2+} ions when fully submerged in nutrient broth media at $37\text{ }^\circ\text{C}$ over 24 h, as a model for extreme biological conditions. The antibacterial efficacy of the cotton swatches was demonstrated against *Escherichia coli* (*E. coli*) over 24 hours, as a proof of concept for the intended application, such as a wound dressing. Importantly, not only did the release of Cu^{2+} from the modified materials kill bacteria in solution, the materials were also able to significantly reduce the attachment of bacteria to the surface as

compared to plain cotton under both wet and dry conditions, demonstrating the usefulness of the MOF-cotton to impede biofilm formation and act as antibacterial surfaces.

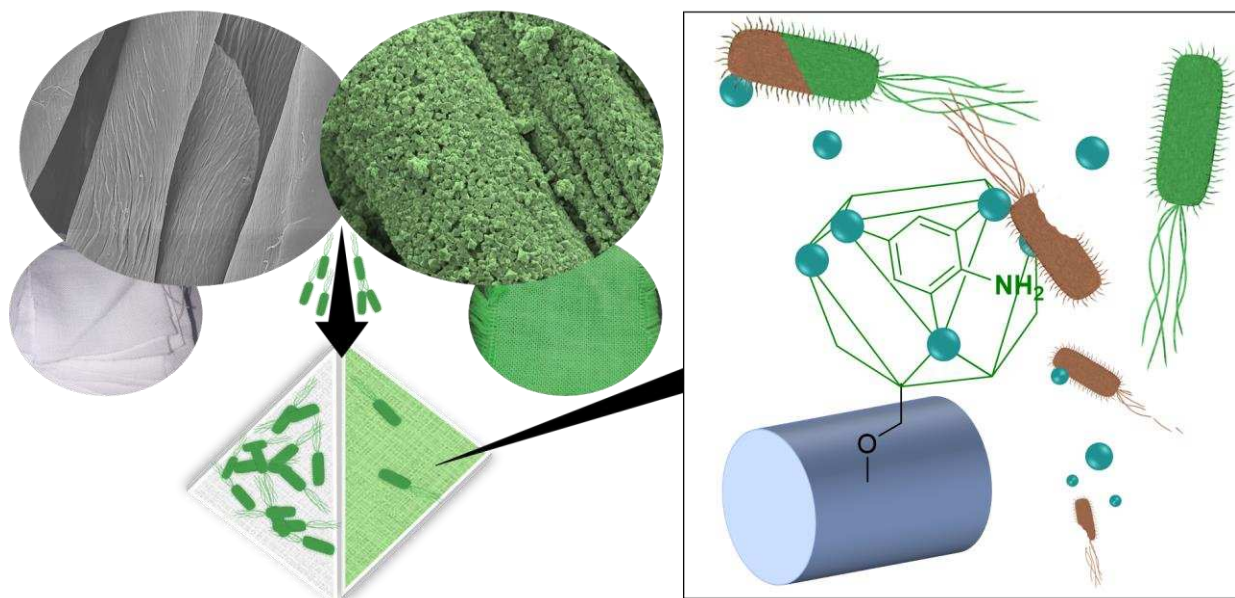


Figure 3.1. Summary image showing growth of a MOF on the surface (SURMOF) of $\text{Cu}_3(\text{NH}_2\text{BTC})_2$ onto the surface of carboxymethylated cotton. When exposed to bacteria, less bacteria is observed on the surface of the material. Additionally, the slow release of copper ions into aqueous solutions kills bacteria in solution.

3.3 Experimental Section

3.3.1 Materials.

Absolute ethanol was attained via Pharmco-Aaper. anhydrous dimethylacetamide (DMA), anhydrous chloroform (CHCl_3), dimethylsulfoxide (DMSO), sodium hydroxide, and copper (II) nitrate were purchased through Sigma Aldrich. Deuterium chloride (DCI) was purchased from Acros Organics. Anhydrides were purchased from TCI. Natural resized and bleached cotton was purchased via SDL Atlas. Sodium chloroacetate was purchased through Ark Pharm Inc. All materials were used as provided, without further purification. For experiments requiring water, a

Millipore purification system set at 18 M Ω was used. OxoidTM nutrient broth media (NBM, OXCM0001B), OxoidTM nutrient agar (NA, OXCM0003B), and sodium chloride were purchased from Fisher Scientific. *Escherichia coli* (*E. coli*, ATCC 25922) was purchased from the American Type Culture Collection (ATCC).

3.3.2 Characterization.

An Agilent (Varian) 400MR equipped with automated tuning and a 7600 sample changer at room temperature was used for all NMR experiments. The attained FID was processed using MestReNova NMR software. To quantify PSM, a small portion of the modified fiber was added to a vial with 0.8 mL dimethylsulfoxide (DMSO) and 3 drops of DCl. The solution was vortexed or shaken until the cotton returned to its original white color and the solution was transferred to an NMR tube for analysis of the ligand component. Powder X-ray diffraction (PXRD) patterns were obtained to verify MOF crystallinity with a Bruker D8 Discover DaVinci Powder X-ray diffractometer with Cu K α radiation operated at 40 kV and 40 mA. A 0.6 mm divergent slit was placed on the primary beam side, and a high-resolution energy dispersive LYNXEYE-XE-T detector was placed on the diffracted beam side during the XRD studies. The instrument alignment was tested using the NIST 1976b SRM. A typical scan rate was 0.1 s/step with a step size of 0.02°. Infrared (IR) data were acquired on a Nicolet 6700 Fourier transform infrared (FTIR) spectrometer under a nitrogen flow. Diffuse reflectance UV-Vis spectroscopy was performed using a Nicolet Evolution 300 UV-Vis Spectrophotometer equipped with a Praying Mantis diffuse reflectance accessory. To access MOF coverage of the cotton fibers, scanning electron microscopy (SEM) imaging was performed using a JEOL JSM-6500F microscope. An accelerating voltage of 5.0 kV and a working distance of 10.0 mm were used. All samples were placed under vacuum and coated

with 20 nm gold prior to imaging. Five to six representative images were taken at three different magnifications for each sample. Cross-sectional transmission electron microscopy (TEM) imaging was performed to analyze the MOF crystals around individual cotton fibers using a JEOL JEM2100F microscope. For cross-sectioned TEM imaging samples were first embedded. In brief, samples were heated under vacuo at 22 psi and 70 °C for 30 min, embedded in a mixture of 70% resin, 30% acetone for 40 min on the rotator, followed by 100% resin for 1 h on the rotator, and finally transferred to flat embedding molds and heated under vacuo at 22 psi and 70 °C for 20 h. Sections were then cut on Reichert Ultracut E at 70 nm thick, and imaged. Additional TEM imaging was performed by isolating 1 cotton fiber. The fiber was drop casted using ethanol between 2 copper grids prior to imaging. This imaging includes bright field transmission electron microscopy (BFTEM), high angle annular dark field scanning transmission electron microscopy (HAADF-STEM), and high resolution TEM (HRTEM).

3.3.3 Carboxymethylation of Cotton Swatch.

To increase nucleation sites for the growth of the MOF, the appendant hydroxyl moieties of the cotton fabric were first modified to yield available surface carboxylates (Figure 3.2). In a typical modification procedure, a 15 wt % NaOH (15 g per swatch) solution was prepared with 100 mL of 2:1 absolute ethanol/deionized water per swatch. Precut cotton swatches with dimensions 4.5 cm x 2 cm were added and gently stirred for 30 min. The swatches were removed and sodium chloroacetate added to the original solution to attain a 1 M solution (11.6 g). After complete dissolution, the swatches were added back to the solution and gently stirred for 1 h. The resultant modified cotton was soaked for 30 min in Millipore water and rinsed with 100 mL

Millipore water, followed by 100 mL ethanol. After drying in open atmosphere, the modified swatches were dried in an oven for 1 h at 60 °C.

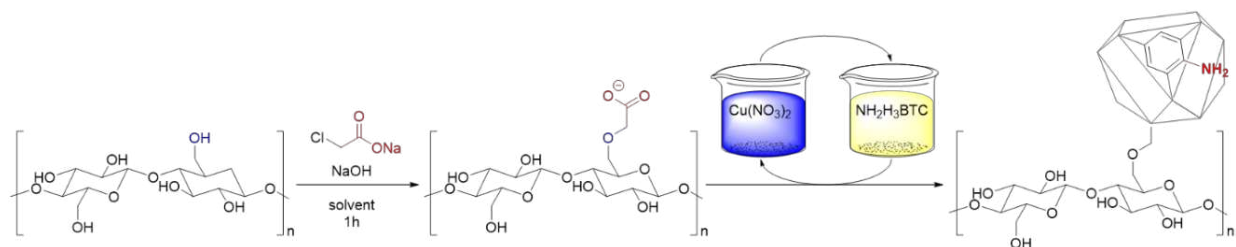


Figure 3.2. Schematic of the process to carboxymethylate and grow the MOF $\text{Cu}_3(\text{NH}_2\text{BTC})_2$ using a layer-by-layer process on the surface of cotton fabric. First cotton swatches were modified under basic conditions with sodium chloroacetate. Resultant nucleation sites enabled the immobilization of the MOF chemically bound to the cotton fibers via a layer-by-layer growth process using repetitive dipping into solutions of copper nitrate or ligand $\text{NH}_2\text{H}_3\text{BTC}$.

3.3.4 Layer-by-layer Growth Process of $\text{Cu}_3(\text{NH}_2\text{BTC})_2$ on Modified Cotton.

Uniform growth of the MOF onto the cotton fibers was achieved via layer-by-layer dip coating process using a mechanical dip coater (Figure 3.2). Each swatch was dipped into independently prepared copper and ligand containing solutions. In a typical procedure, 20 mL scintillation vials were first filled with 20 mL of solution. Copper containing **solution A** was prepared using 1:1:1 dimethylacetamide (DMA), ethanol, Millipore water and 1.90 g copper (II) nitrate. The ligand, 2-aminobenzene-1,3,5-tricarboxylic acid, was synthesized following our previously reported procedure.²⁰ The ligand containing **solution B** was prepared using 2:1:1 DMA, ethanol, Millipore water and 675 mg of the ligand. All solutions were vortexed, shaken, and sonicated (10 min) to ensure all compounds were completely dissolved. The solutions were transferred to 20 mL beakers. Carboxymethylated cotton swatches trimmed to 1.7 cm x 3.8 cm were loaded to a mechanical dip coater and hydrated with absolute ethanol. The materials were then dipped into **solution A** for 17 min, a solution of ethanol for 5 sec, **solution B** for 17 min, followed by ethanol for 5 sec. The process was repeated for a total of 15 cycles (30 total layers, 15

of each **solution A** and **B**). To remove any residual nonbonded copper or ligand, swatches were soaked in 20 mL of ethanol overnight. After this time, each swatch was added to a new solution of ethanol, washed and vortexed six times with new solvent in a new vial each time.

3.3.5 Postsynthetic Modification of $\text{Cu}_3(\text{NH}_2\text{BTC})_2$ on Modified Cotton.

After the MOF-cotton composites were characterized, the swatches were subjected to PSM with valeric anhydride (designated AM-5 modified MOF, Figure 3.3). Modification of the MOF on cotton was optimized when a swatch was submerged in a 1.5 M solution of valeric anhydride in CHCl_3 for 24 h. The MOF-cotton composites were added to 20 mL scintillation vials followed by 12 mL CHCl_3 and 3.55 mL valeric anhydride and vortexed to mix. After 24 h of soaking, the cotton swatch was removed, rinsed several times with CHCl_3 , and soaked overnight. Each swatch was subsequently soaked in ethanol for 24 h, after which time the solution was decanted, swatches rinsed with 100 mL ethanol, and then swatches dried in the oven at 60 °C for 1 h.

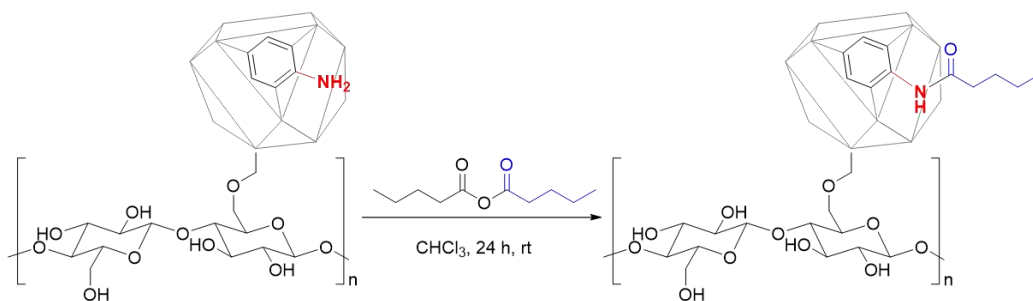


Figure 3.3. Postsynthetic modification of MOF $\text{Cu}_3(\text{NH}_2\text{BTC})_2$ with valeric anhydride to yield AM-5 Modified MOF.

3.3.6 Copper Release Studies.

Soaking studies were performed to test the rate at which the materials released copper into aqueous environments under biologically relevant conditions. MOF-cotton composites were first

cut to 0.7 cm x 0.7 cm individual pieces and placed into 4-dram vials. Next, 1 mL of NBM solution was added and the materials were incubated at 37 °C for various timepoints. After the intended time, the solutions were pipetted into a new vial, diluted with 4 mL Millipore water and analyzed by inductively coupled plasma optical emission spectroscopy (ICP-OES) detection. Each data point reported is representative of 3 trials from 3 independent swatches with the standard deviation.

3.3.7 Bacteria Studies.

Antibacterial efficacy of the MOF-cotton materials was evaluated against *E. coli* using a standard broth dilution agar plating method. Stock cultures of *E. coli* were obtained by first streaking onto agar plates and placing in a 37 °C incubator until formation of colony-forming units (CFUs). A colony was removed from the agar plate, placed in NBM, and allowed to grow at 37 °C under shaking conditions until reaching an O.D._{600nm} ~1.0. Aliquots of the culture were mixed with 30% (v/v) glycerol solution in a 1:1 fashion before being stored at -80 °C until use for future bacteria studies. To perform the antibacterial kill rate studies, the stock culture was thawed on the benchtop and subsequently centrifuged at 4700 rpm for 10 min. The supernatant was discarded and the remaining pellet was resuspended using 5 mL warmed NBM. An additional 45 mL NBM was added to the culture and placed under incubated and shaking conditions overnight, until reaching an O.D._{600nm} ~1.0.

3.3.8 Antibacterial Activity Under Wet Conditions.

After overnight growth of the stock culture, the *E. coli* solution was diluted using NBM to a working concentration associated with an O.D._{600nm} ~0.35. The cotton materials were placed in a 24-well plate before the addition of 1 mL of the diluted *E. coli* culture. The well plate was placed

in a 37 °C incubator and 100 µL aliquots were pulled from each well at 1, 6, and 24 h after exposure to the cotton materials. At each time point, the aliquots underwent 10-fold serial dilutions using 0.85% NaCl solution and subsequently plated on agar using 50 µL. At the end of the total 24 h exposure period, all remaining solution was removed, the wells were washed once with warmed NBM, all swatches were moved to a new well, and 1 mL NBM was added. The plate was sonicated for 5 min (100 W power, 42 kHz frequency) to liberate any bacteria that were adhered to the cotton materials. Aliquots were then taken from the sonicated wells and plated on agar following the above protocol. The agar plates were placed in a 37 °C incubator and CFUs were counted the following day. The assessed CFUs were normalized by the dilution factor and volume by Equation 1. All kill rates by the MOF-cotton swatches are relative to clean natural cotton swatches without MOF present.

Equation 1:
$$\frac{CFU}{mL} = \frac{No.of\ CFUs}{(Dilution\ Factor)*(Vol.Plated)}$$

3.3.9 Antibacterial Activity Under Dry Conditions.

The overnight stock culture of *E coli* (O.D._{600nm} ~1.0) was used to assess bacterial attachment onto the cotton swatches under dry conditions. The three types of swatches were placed in a 24-well plate and 10 µL aliquot of the concentrated bacterial solution was added to each swatch. The plate was placed in a 37 °C incubator for 5 min before being assessed for bacterial attachment. The plate was removed after the 5 min exposure period, 1 mL of warmed NBM added, and the plate was sonicated for 5 min. Viable bacteria were plated for CFUs and assessed via Equation 1.

3.4 Results and Discussion

3.4.1 Development of the MOF-Cotton Material.

MOF coatings on surfaces often result in nonuniform coverage with heterogeneous crystal formation. The resultant polycrystallinity and/or inhomogeneity, may interfere with the materials final performance leading to substantial batch-to-batch inconsistencies. An alternative approach is to synthetically grow MOF crystals or films bound to the surface. This commonly includes using a layer-by-layer growth method or liquid-phase epitaxy. These techniques result in more consistent, homogeneous surface supported, highly oriented MOFs, known as SURMOFs.²¹ Firstly, the material is synthetically manipulated to provide a nucleation site which mimics that of the ligands within the desired MOF. To this end, natural cotton was first functionalized with sodium chloroacetate under basic conditions to yield available carboxylate on the surface of the fabric. Initial immobilization of the MOF on cotton efforts were attempted utilizing previously reported methodology, whereby cotton carboxymethylation occurs in 100% water.²² However, using 100% water led to minimal surface coverage of the MOF $\text{Cu}_3(\text{NH}_2\text{BTC})_2$. Thus, a new protocol for carboxymethylation was employed to optimize surface coverage of the cotton fibers. Recent advances in the understanding of carboxymethylation suggest that an increased degree of substitution, yielding a greater percentage of carboxylate moieties on the surface of the cotton, can be achieved by adding alcohol to the carboxymethylation solution. A 100% water carboxymethylation solution yields a degree substitution of just 0.13, whereas a 2:1 ethanol to water solution has been shown to exhibit a degree of substitution of 0.39, 3 times that of using water alone.²³ Knowing this, the cotton swatches were carboxymethylated in 2:1 ethanol to water solutions to increase the available nucleation sites for subsequent MOF growth. To verify carboxymethylation was successful, IR spectroscopy was performed of both the natural cotton and

the carboxymethylated material (Figure 3.4). In the chemically modified cotton spectra the appearance of a peak at 1630 cm^{-1} indicates the presence of the C=O bond stretch associated with the carboxylate moiety. Additionally, a decrease in the intensity and peak shape of the OH stretch at 3380 cm^{-1} is observed, consistent with carboxymethylation.

To ensure consistent results across batches of material, the carboxymethylated cotton swatches were attached to a mechanical robot and subjected to dip-coating to generate the MOF particles chemically bound to the cotton fibers. First, the swatches were introduced into a concentrated solution of copper nitrate for 17 min. After which time, the material exhibits a characteristic blue color associated with copper coordination to the carboxymethylated cotton. The material was briefly rinsed with ethanol and then introduced into a concentrated solution containing the $\text{NH}_2\text{H}_3\text{BTC}$ ligand for 17 min. Immediately upon submerging the material, a distinct color shift to green is observed. This change in color is attributable to the interaction of the ligand (having an electron donating amine) with the copper layer on the surface of the cotton. After 15 total cycles, the material has a uniformly green appearance, characteristic of the MOF $\text{Cu}_3(\text{NH}_2\text{BTC})_2$ (Figure 3.5). To remove any unattached MOF particles, the MOF-cotton material was thoroughly rinsed and agitated. The MOF-cotton material was then dried in open atmosphere for several hours and then in the oven at $60\text{ }^\circ\text{C}$ to remove any remaining ethanol.

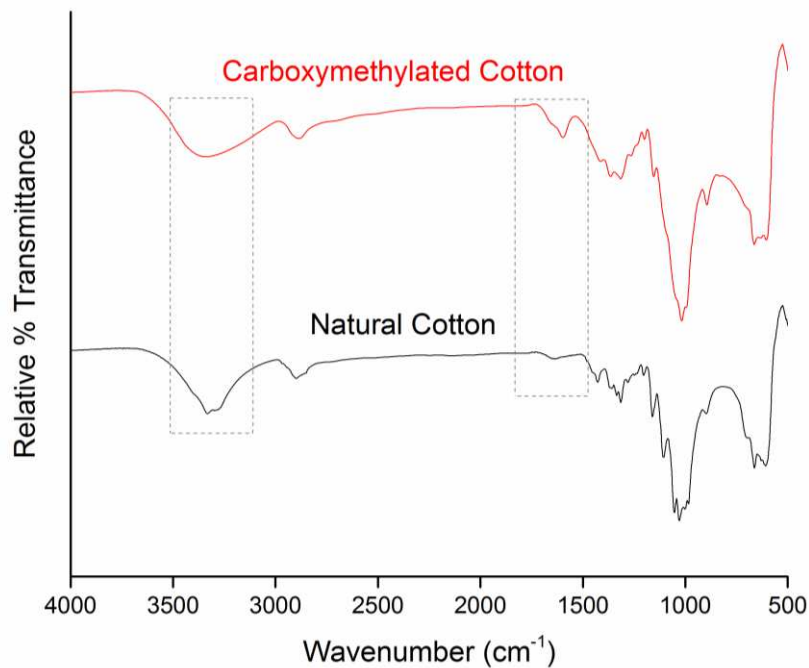


Figure 3.4. IR spectrum of carboxymethylated cotton (red) and natural cotton (black). Verification of carboxymethylation highlighted at 3380 cm^{-1} indicates the functionalization of free alcohol to carboxylate ion as well as the appearance of a new C=O shift at 1630 cm^{-1} .



Figure 3.5. Images of natural cotton used (left) and the uniformly grown MOF on cotton material (right).

3.4.2 Characterization of the MOF-Cotton Material.

Diffuse reflectance UV-Vis and PXRD were performed to confirm the presence and orientation of the crystalline MOF on the surface of carboxymethylated cotton.

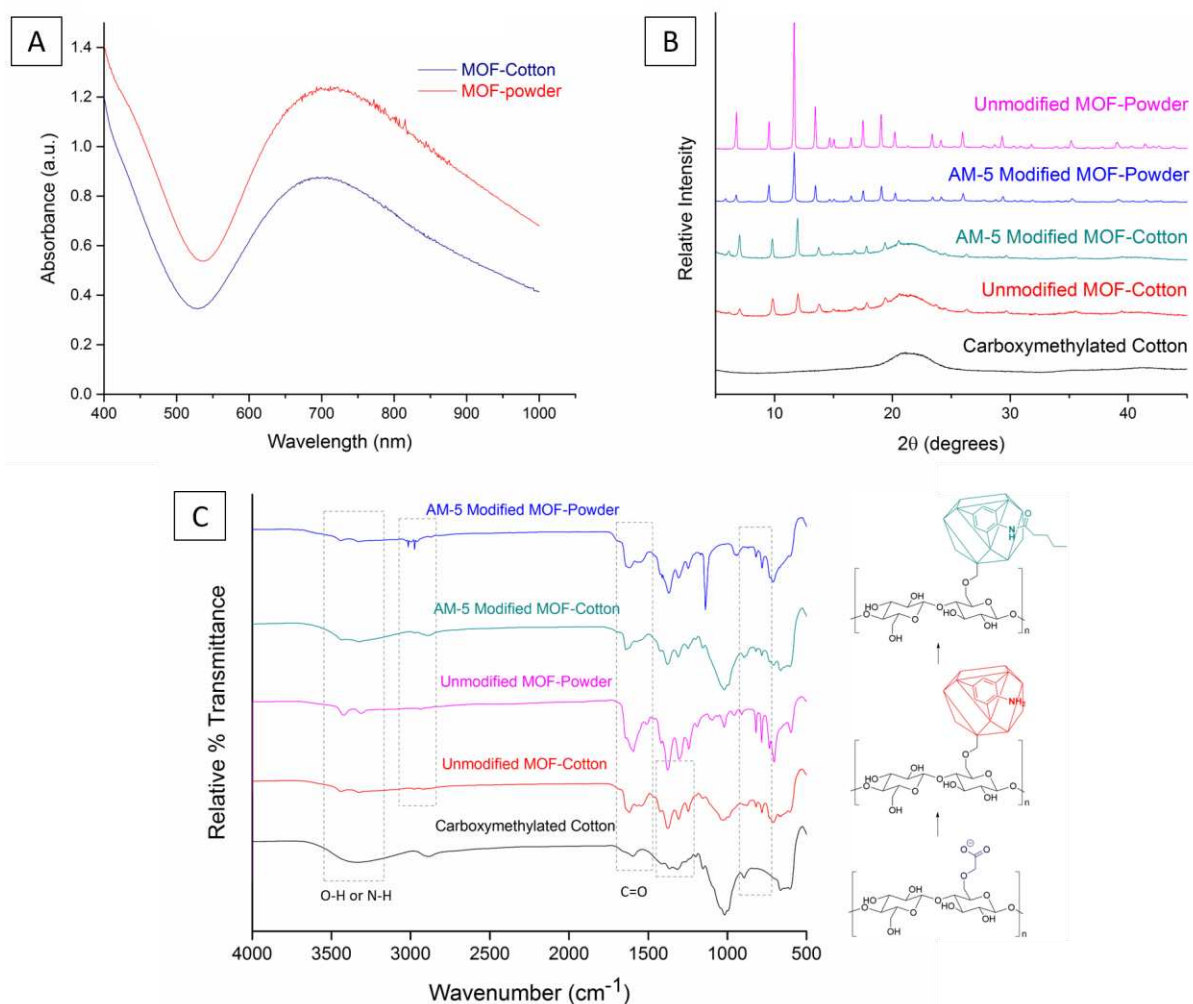


Figure 3.6. (A) Diffuse reflectance UV-Vis of the MOF-powder (red) and MOF-cotton (blue) materials, showing the presence of the MOF on cotton. (B) PXRD data of all relevant samples indicating the crystalline MOF on the surface of carboxymethylated cotton. Postsynthetically modifying the materials does not impact the structural integrity or morphology of the MOF crystals. (C) IR spectroscopy of the MOF-powder and MOF-cotton samples with relevant features noted.

In the UV-Vis spectra, a characteristic absorbance peak around 700 nm is observed, indicating the MOF grown on cotton exhibits nearly the same diffuse reflectance of dispersed light inside the crystalline lattice as the MOF powder (Figure 3.6A). This suggests the MOF is indeed present on the surface of the carboxymethylated cotton and, hence, is expected to behave electronically like the MOF powder itself. Furthermore, the diffractogram of the unmodified MOF-

cotton composite supports that the crystallinity of the carboxymethylated cotton is retained and that the MOF particles on cotton have the same morphology and orientation as the MOF powder materials, as evidenced by sharp Bragg reflections at relevant 2Θ (Figure 3.6B) with matching relative peak intensities. Lastly, IR spectroscopy shows a clear difference between the carboxymethylated cotton and the MOF grown on cotton (Figure 3.6C). The unmodified MOF cotton contains several characteristic features of the MOF, as observed by comparison with the MOF powder. With MOF present, a distinct 3400 cm^{-1} band shows the presence of an amine, a new feature at 1640 cm^{-1} is representative of the C=O stretch associated with the MOF, and features within the thumbprint region between 750 cm^{-1} and 850 cm^{-1} are also present. Taken together these data indicate that the cotton contains crystalline MOF crystals uniformly on the surface.

Surface coverage of the MOF onto cotton fibers was investigated and analyzed using SEM and TEM imaging. Initial experiments demonstrated a significant increase in MOF growth on the cotton fibers that were carboxymethylated in 2:1 ethanol/water rather than previous protocols with 100% water (Supporting Information, APPENDIX Figure B2). As a result, these materials were carried on for further optimization. Coverage of cotton surface was optimized by varying the number of layers made and the allowed deposition time. Complete and consistent coverage of the cotton fibers was accomplished with 17 min in each solution and with at least 30 total layers (i.e. 15 times in each copper or ligand solution). As previously mentioned, the use of a mechanical dip coater ensured uniformity between individual MOF-cotton swatches. Shown in figure 3.7, The MOF crystals individually appear to be approximately $1\text{ }\mu\text{m}$ in diameter with little twinning of the crystallites. In conclusion, SEM imaging reveals that the resultant materials contain consistent full coverage of the surface of the cotton swatches with abutting MOF crystals of uniform size and morphology.

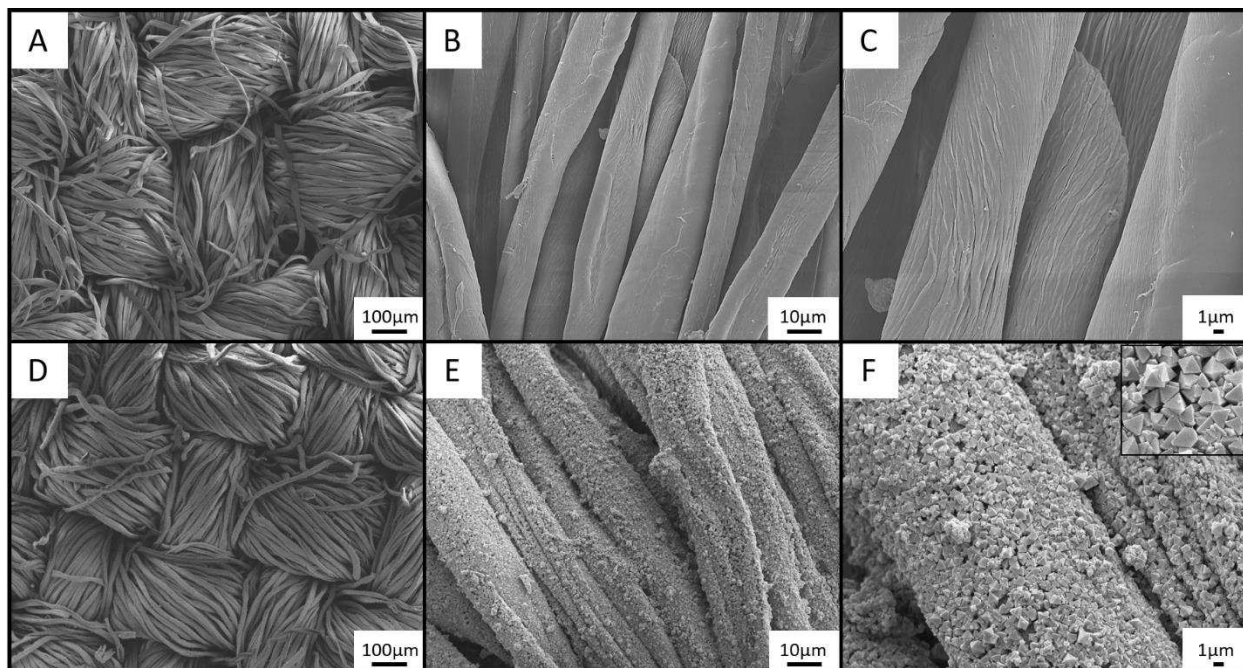


Figure 3.7. SEM images taken at 5 kV of the MOF-cotton materials showing excellent surface coverage of the MOF fibers. A-C are images of natural cotton. D-F are images of the MOF immobilized onto the cotton fibers under optimized conditions. All cotton swatches were imaged over at least 3 different sites (not shown).

To analyze MOF coverage around the entire cotton fiber, the material was cross-sectioned and analyzed with SEM and TEM imaging (Figure 3.8). SEM imaging coupled with EDS mapping of a cross section of the MOF-cotton material shows copper is present around the entire surface of the individual cotton fibers (Figure 3.8A). TEM imaging of the cross sectioned material reveals that the optimized conditions generate a single uniform layer of adjoining crystallites around each cotton fiber roughly $1\ \mu\text{m} \times 1\ \mu\text{m}$ in size (Figure 3.8B). The TEM data indicate that the detailed growth parameters maximize the surface area and size of each individual MOF crystal attached, as opposed to increasing the number of MOF crystals on the surface. Upon further magnification, the individual MOF crystals displayed distinct ligand and copper layers as light and dark layered regions of the BFTEM images (Figure 3.8C). TEM imaging allows for detailed monitoring of

individual MOF components, a critical microscopic technique for characterizing MOF interactions including future studies with biological systems or MOF loading. Such studies with MOFs are limited due to the instability of MOFs to the high energy electrons associated with using TEM.²⁴ Using HAADF-STEM, however, images of the MOF-cotton materials were successfully imaged (Figure 3.8D-F). Figure 3.7D shows a single fiber of material, whereby the surface appears entirely covered with MOF crystals. Higher magnification, further supports this conclusion, showing 2 crystals attached to the cotton surface (Figure 3.8E). The crystals appear to show copper striations attributed to the layers of copper in the materials (Figure 3.8F). To further assess the crystallinity and orientation of the crystals, free particles liberated during isolation of a single MOF-cotton fiber were imaged using HRTEM (Figure 3.8G). Magnification of the framed regions are shown with insets of the associated Fourier transforms. Several crystal orientations are shown depicting clear lattice fringes throughout the crystals. Taken together, the imaging data suggest that the detailed methodology is advantageous for ensuring that natural cotton is sufficiently carboxymethylated to yield increased crystalline MOF growth around the entire surface of individual modified cotton fibers. Additionally, this method results in the uniform growth of MOF $\text{Cu}_3(\text{NH}_2\text{BTC})_2$ octahedral crystals on the surface of each individual cotton fiber.

3.4.3 Postsynthetic Modification of the MOF-Cotton Material.

PSM of surfaces allows access to tunable and biocompatible surfaces with far reaching applications including wound dressings, nanomedicine, and antifouling surfaces.²⁵ Previously reported PSM to the free-amine moiety of the powdered MOF achieves a controllable change in the stability to water of the material.²⁰ This premise suggests functionalizing the MOF-cotton composite may also yield control of the stability of the material to biologically relevant NBM.

Ultimately, this would enable the unprecedented tunable release of Cu^{2+} ions into aqueous environments.

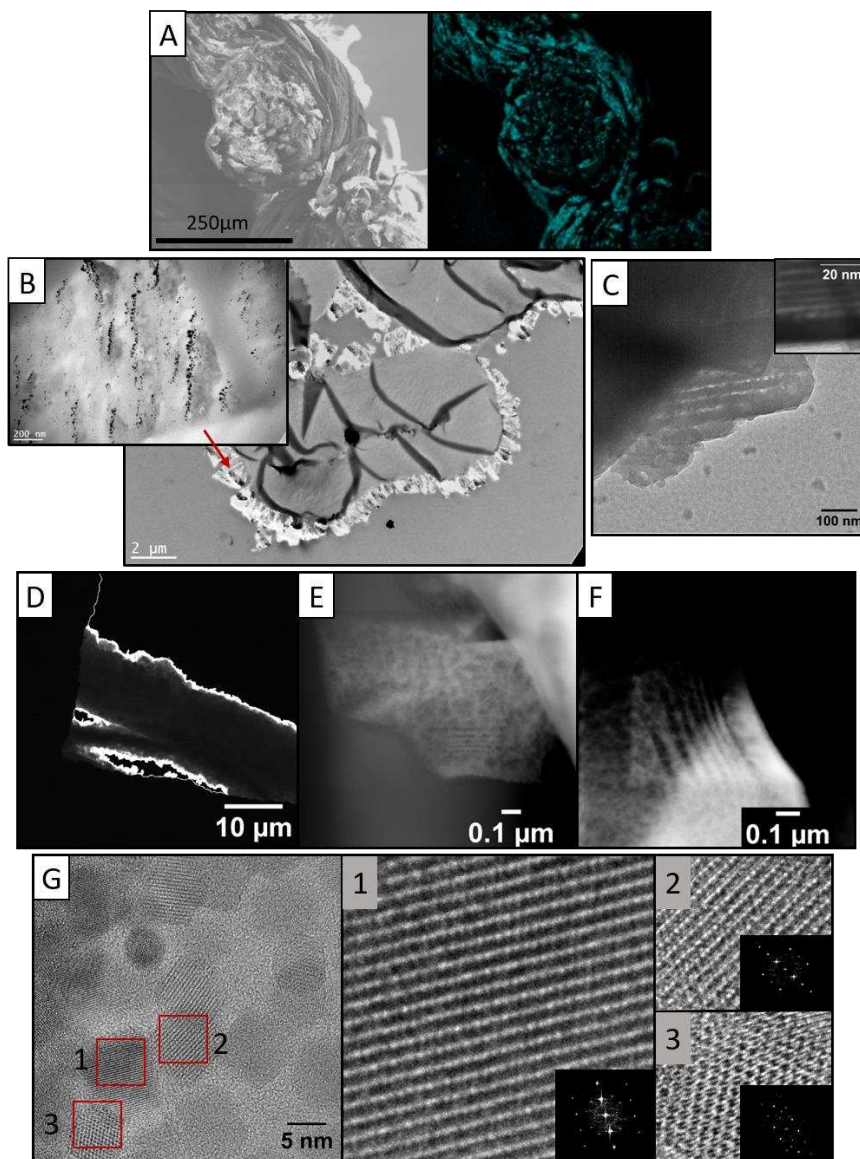


Figure 3.8. (A) SEM image of the cross-sectioned MOF-cotton material and EDS mapping of copper. (B) TEM images of embedded and cross-sectioned MOF-cotton material showing coverage around the entire cotton fiber. (C) BFTEM image of a MOF crystal anchored on cotton material. (D) HAADF-STEM image of MOF crystals on the surface of a single fiber of MOF-cotton material. (E) HAADF-STEM image of MOF crystals on MOF-cotton material. (F) HAADF-STEM image of a MOF crystal on MOF-cotton material, lines of copper are visible. (G) HRTEM image of a MOF crystals from MOF-cotton material liberated during isolation of a single fiber of material. Framed sections 1, 2, and 3 are magnified and shown with associated Fourier transform.

Tunable release of Cu^{2+} ions would be of great value for various applications including as an antibacterial agent. Thus, the materials were postsynthetically modified with valeric anhydride to determine the resultant impact to the stability of the composite material to NBM before and after modification. IR spectroscopy of the AM-5 modified MOF on cotton is consistent with modified MOF powder. An increase in sp^3 C-H at 3005 cm^{-1} further verifies the presence of the valeric anhydride carbon chain. A small section of the modified swatches was cut and digested in acidic dimethylsulfoxide- D_6 and examined by ^1H NMR to quantify the percentage of modification achieved. The average observed percent modification with valeric anhydride was $23.5 \pm 2.2\%$ ($n = 3$). After modification, the total amount of copper per cm^2 section of material measured $6.65 \pm 0.30\ \mu\text{mols}\cdot\text{cm}^{-2}$, while the unmodified material contained $9.56 \pm 0.66\ \mu\text{mols}\cdot\text{cm}^{-2}$. Therefore, modification under these conditions does lead to a slight depreciation of the MOF on the surface. These results are consistent with those previously observed using anhydrides to modify $\text{Cu}_3(\text{NH}_2\text{BTC})_2$, whereby a loss in copper is attributed to the byproduct carboxylate released during modification.²⁰ For these studies, PSM was maximized relative to the total amount of MOF to ensure maximum modification possible; however, to retain more SURMOF a less concentrated solution may be used. To analyze any changes the MOF may have underwent during the modification process, PXRD and SEM imaging were performed following modification. The retention of diffraction pattern after PSM suggests that the crystallinity of the MOF does not change upon modification (Figure 5B). The SEM images indicate there is no visual damage to the structural integrity of the MOF crystals, morphology, nor to the overall size (Supporting Information APPENDIX Figure B4). In all, the PSM procedure employed slightly reduces the amount of MOF remaining on the cotton; however, it does not cause any detectable change to the morphology or size of the MOF crystals.

3.4.4 Copper Delivery Performance.

While having surfaces which prevent the growth of biofilms is extremely critical and a central goal of this study, we also recognize the advantages associated with a material that may slowly release Cu^{2+} ions into solution. Slow and controlled release of Cu^{2+} ions would be of significance for biomedical applications, agricultural applications, and shape the future for nano-antibacterial materials. As such, using PSM to tune the copper release rate of the material was investigated. Specifically, modified and unmodified MOF-cotton materials were subjected to extreme biological conditions, in which the materials were submerged in complex media at elevated temperatures. $\text{Cu}_3(\text{NH}_2\text{BTC})_2$ on cotton is resistant to detectable damage due to sonication and washing with organic solvents including ethanol, methanol, and chloroform. However, when submerged in aqueous environments, the MOF may undergo slow structural collapse and release of Cu^{2+} ions.²⁰ The rate of copper release from the materials was carefully monitored over various time points. The modified materials were found to release less copper into solution within the first 6 h than the unmodified materials (Table 3.1). The unmodified MOF-cotton initially releases Cu^{2+} ions into solution most quickly over the first 6 h. After which time copper release remains slow and consistent. If the material is postsynthetically modified, initially slower release of Cu^{2+} ions is observed than the unmodified material. After 6 h, the modified material releases Cu^{2+} ions at a faster rate than the unmodified material. Clearly, modification of the MOF yields interesting changes to the releasing capabilities of the material. Importantly, both modified and unmodified materials continue to slowly release Cu^{2+} ions beyond the 24 h tested. At 24 h, the modified material has released ~90% of the total copper content, while the unmodified material has released just ~54% of the total copper content. These results suggest that these materials may be advantageous for slow and controlled release of Cu^{2+} ions.

To better understand the copper releasing performance of these materials, the copper flux of each was determined and plotted for the first 6 h (Figure 3.9). The rate of copper flux of the unmodified material at 30 min is significantly greater than that for the modified MOF. At 1 h, the MOF-cotton material still exhibits a greater flux than the unmodified material. After 2.5 h, the materials begin to behave similarly and slowly release Cu^{2+} ions. After 6 h, copper ions are continually released for both materials at a flux less than or equal to $0.9 \mu\text{mol}\cdot\text{cm}^{-2}\cdot\text{h}^{-1}$. Based on previous reports of PSM yielding more stable materials, we anticipated the modified materials would release copper ions slower than the unmodified material. Conversely, the results of PSM to the materials leads to an increase in the copper flux. While the results with valeric anhydride are not what was hypothesized, they excitingly suggest that this strategy does indeed yield tunable materials. As such, these findings serve as sufficient precedent to encourage further exploration using PSM of MOFs in textile materials for controllable ion release.

Table 3.1. Copper in solution after soaking 0.49 cm^2 swatch in 1 mL NBM at $37 \text{ }^\circ\text{C}$, average and standard deviation displayed (n=3).

| Time (h) | MOF-Cotton ($\mu\text{mol}\cdot\text{cm}^{-2}$) | AM-5 Modified Cotton ($\mu\text{mol}\cdot\text{cm}^{-2}$) |
|----------|---|---|
| 0.5 | 3.21 ± 0.21 | 2.55 ± 0.08 |
| 1 | 3.70 ± 0.42 | 3.07 ± 0.10 |
| 2.5 | 4.10 ± 0.11 | 3.85 ± 0.20 |
| 6 | 5.28 ± 0.36 | 5.16 ± 0.22 |
| 12 | 5.01 ± 0.11 | 5.76 ± 0.17 |
| 24 | 5.18 ± 0.07 | 6.15 ± 0.10 |

PXRD of the MOF-cotton materials after 1 h of being submerged in NBM at room temperature revealed that while these materials are releasing copper, the MOF retains crystallinity (Supporting Information, APPENDIX Figure B5). These results are particularly interesting when compared to previous reports investigating the biocompatibility of MOF coatings on solid Au surfaces and the stability to water and complex media of the materials.²⁶ Notably, similar copper-SURMOF (HKUST-1) releases Cu^{2+} ions due to dissolution of the MOF, most rapidly in cell culture media. Complete structural collapse is observed within 30 min of HKUST-1 submersion in water. Herein, the materials retain crystallinity after 1 hour of submersion in NBM. In addition, the materials continue to release Cu^{2+} ions beyond the 24 hours tested. Retention of crystallinity may directly enhance the overall efficacy of using a MOF for antibacterial applications. The direct interaction of marine bacterium with copper-MOF surfaces has been reported to lead to the decomposition of SURMOF crystallinity and release of Cu^{2+} ions.²⁷ Taken together, the data suggests that the particular solid support to which the MOF is bound, the MOF growth process, and PSM may all contribute to the stability and overall copper releasing activity observed with the materials and therefore, should be carefully considered for the desired application. Since the Cu^{2+} ions are toxic to microorganisms including bacteria, $\text{Cu}_3(\text{NH}_2\text{BTC})_2$ -cotton materials warrant further investigation of antimicrobial efficacy.

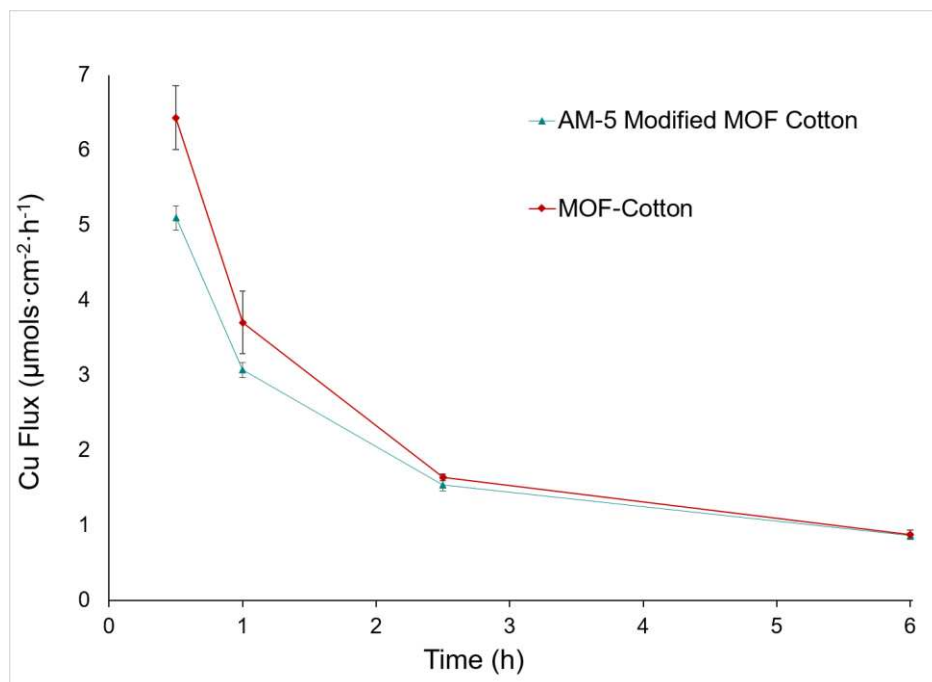


Figure 3.9. Copper ion releasing flux data of the MOF-cotton materials soaked in NBM solution for 6 h at 37 °C. The modified MOF cotton materials exhibit a different copper releasing flux, which is most substantial over the first 6 h. Data presented as the average with the associated standard deviation, n=3.

3.4.5 Bacteria Studies.

The antibacterial efficacy of the unmodified and modified MOF-cotton swatches was tested against *E. coli* both under wet conditions (over a 24 h period) and under dry conditions (5 min exposure period). Bacteria strains that are naturally present on skin (including *E. coli*) can readily attach onto textile surfaces, leading to potentially lethal bloodstream infections.²⁸ To determine the extent of cellular viability after exposure to the materials, a broth dilution, agar plating method was employed. This allows for extremely sensitive measurements to be attained, with a LOD of 1 CFU/mL.^{29,30} This agar plating method works not only for planktonic bacteria (where aliquots can be removed at the desired time points), but it also allows for quantification of the viable bacteria remaining on the swatches after the exposure period. A 5 min sonication period of the cotton swatches liberates the bacteria that was previously attached to the surface without causing any loss

of cellular viability in the process. Once the sonication period is complete, aliquots can be removed and plated in an identical fashion as the planktonic bacteria.³¹

3.4.6 Antibacterial Activity Under Wet Conditions.

Given the application of cotton swatches as wound dressings, it is useful to determine the remaining cellular viability after exposure to the cotton at varying time points, especially because it has been shown that the relative amount of bacteria present at a wound site is directly attributable to the potential to alter the normal wound healing process.^{32,33} Therefore, the remaining viable *E. coli* cells were assessed after 1, 6, and 24 h exposure to the cotton swatches. Indeed, 6 h is considered the ideal time necessary for bacteria to colonize a wound; however, it is also necessary to test the cellular viability after 24 h to ensure no regrowth of the bacteria has occurred.³⁴ This is considered “wet” experimental conditions, as the materials are fully submerged in the bacteria solution for the entire challenge period. Additionally, both the planktonic bacteria (in solution) were assessed as well as the viable bacteria that attached to the cotton swatches after the 24 h exposure period. This gives insight into both the antibacterial efficacy of the Cu²⁺ ions being released from the MOF-cotton swatches and the ability for the MOF-cotton swatches to impede bacterial attachment while performing as an antibacterial surface.

Figure 3.10 shows the results from the *E. coli* kill rate study over the entire 24 h challenge period. The results show that the cotton swatches alone have no effect on the cellular viability of *E. coli* at any tested point. Indeed, the *E. coli* cells assessed in the presence of both the cotton and carboxymethylated cotton swatches were not statistically different when compared to *E. coli* without any cotton present. As an additional control, the cellular viability of *E. coli* in the presence of the ligand was assessed (at equal amounts that are present on MOF-cotton swatches) and

demonstrated very little antibacterial effect (10^7 CFUs/mL after 24 h exposure). After the initial h of exposure to the MOF-cotton swatches, there does not appear to be any significant decrease in viability. However, after 6 h of exposure to both the unmodified and modified MOF-cotton swatches, a decrease in planktonic viability is apparent. Both MOF grown surfaces result in a log-3 reduction in cellular viability when compared to the cotton swatch alone. This is a substantial reduction to achieve given the current industry standard is considered a log-3 reduction (equivalent to 99.9% reduction in viable cells). After 24 h of exposure, the reduction in viability is even greater, resulting in a log-4 for the modified MOF and log-5 for the unmodified MOF. This assessment after 24 h is critical as reports have shown significant regrowth of bacteria after initial efficacy was determined.^{35,36}

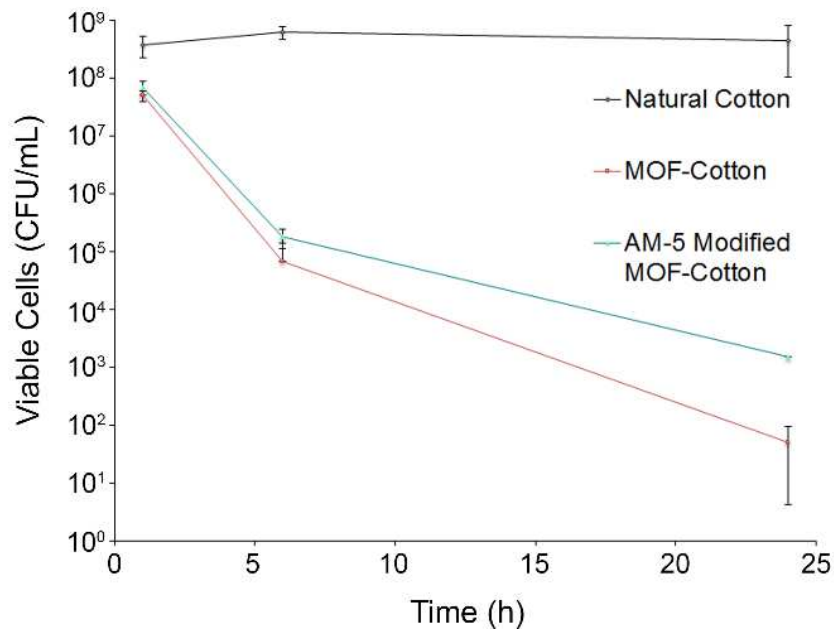


Figure 3.10. Bacteria kill rate of *E. coli* in the presence of the three cotton swatches, with viable cells versus time displayed. The graph shows the average and standard deviation, n=6.

In addition to the planktonic kill rate achieved using both the modified and unmodified MOF surfaces, the bacterial attachment onto the cotton was depleted in the presence of the MOF-cotton swatches when compared with cotton on its own. Figure 3.9 shows the results of this study, where there is a massive log-3 reduction in viable bacteria attached to the MOF-surfaces compared to the cotton surface. Bacterial attachment is the first step in biofilm formation and, hence, becomes the critical step to ensuring this detrimental effect does not occur.^{37,38} The observed reduction in attachment after 24 h indicates that these MOF-cotton materials could indeed act as antibacterial surfaces, particularly through additional tuning of Cu²⁺ ion release to increase the reduction in bacterial attachment. It is also interesting to note that there is no statistical difference between the reduction in attachment between the modified and unmodified MOF, given their unique behavior against planktonic bacteria. This suggests that the remaining MOF (and subsequent copper) that is still present on both types of MOF-swatches is within the threshold to elicit these impressive effects.

3.4.7 Antibacterial Activity Under Dry Conditions.

To understand how these materials behave as antibacterial surfaces under circumstances more similar to a pure copper surface application, dry conditions were also employed. Dry conditions examine the efficacy of the materials without a direct contribution to metal ions releasing into solution and killing planktonic bacteria. The dry method is also more representative of the wound healing model, where there is not a continuous solution of bacteria surrounding the materials. A 5 min exposure period was chosen based off previous bacteria studies using metal surfaces.^{39,40} The results from this study (and the wet attachment study) is shown in Figure 3.11, where there is a further enhanced reduction in attachment onto the unmodified swatches under dry

conditions then what was observed under wet conditions (log-4 versus log-3), and a similar reduction in attachment observed for the modified swatch. The reduction in bacterial attachment is remarkable to achieve using a minimal 5 min exposure period. This indicates that the inability for *E. coli* cells to begin the biofilm process is near immediate, representing an attractive option for biofilm impediment. It is also fascinating that the total amount of attached cells onto the natural cotton is the same, regardless of exposure time or wet versus dry conditions.

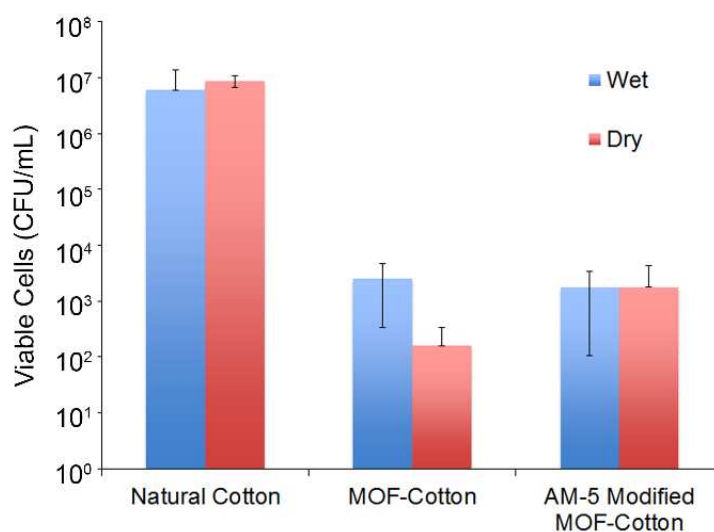


Figure 3.11. Attachment of *E. coli* onto the three cotton swatches under wet and dry conditions, with viable bacteria versus the type of swatch displayed. Wet conditions indicate the films were submerged in bacteria solution for 24 h before assessment of viability; dry conditions indicate an aliquot of bacteria solution was added to each swatch for 5 mins before assessment of viability. Data shows the average standard deviation, n=6.

While there has been preliminary work reporting copper-based MOFs as antibacterial agents, the results achieved in this work represent the most promising to date towards utilizing MOFs in an antibacterial surface fashion. Abbasi *et al.* use Cu-BTC grown on silk fibers to test the growth inhibition of *E. coli* and *Staphylococcus aureus*, but did not attempt to quantify the antibacterial efficacy of their MOF materials.¹⁹ Rodriguez et al. expose *E. coli* cells to Cu-BTC

grown on cellulose fibers, but the quantification method (resazurin) lacks the sensitivity to achieve the reductions seen in the present work.⁴¹ Most importantly, however, is the determination of the cotton swatches to act as an antibacterial surface, a property that has not been tested in any of the mentioned literature. It is critical to test the surviving bacteria not only in solution (where it is known to be most susceptible to antibacterial agents) but also in bacteria's ability to attach to a surface.³⁸ The ability to impede bacterial attachment is indeed the most promising avenue for novel biomaterials, making this work particularly powerful in its ability to inhibit *E coli* attachment under both wet and dry conditions.

3.5 Conclusions

This work demonstrates the use of surface mounted MOF containing materials to control the copper flux from materials and exploit the antibacterial properties of the metal ions in MOFs for antibacterial effects. The carboxymethylation process implemented establishes a new standard for increasing the amount of modification of cotton to improve the number of nucleation sites on cotton fibers for MOF growth. The layer-by-layer growth process utilized herein leads to highly uniform and evenly dispersed MOF around each entire cotton fiber. Importantly, this MOF permits PSM to the free amine to tune the physicochemical properties of the resultant material. By manipulating the stability of the MOF-cotton material to complex nutrient broth media at biologically relevant conditions, the overall flux of the material may be changed over the first 6 h. This work demonstrates that the MOF-cotton materials prevent the attachment of bacteria to the surface and kill bacteria in solution. Future studies will also analyze the compatibility of the MOF-cotton surfaces with other cell lines. Taken together, the antibacterial activity with cell compatibility will lead to a surface that can be used in the clinical arena. This study serves as a

critical precedent to enable synthetic control demonstrating the potential power of PSM to tune antibacterial textile surfaces.

REFERENCES

1. Wei, T.; Tang, Z.; Yu, Q.; Chen, H. *ACS Appl. Mater. Interfaces* **2017**, *9*, 37511-37523.
2. He, L.; Li, S.; Chung, C. T. W.; Gao, C.; Xin, J. H. *Scientific Reports* **2016**, *6*, 36327.
3. Neely, A. N.; Maley, M. P. *J. of Clin. Microbiol.* **2000**, *38*, 724-726.
4. Wu, H.; Moser, C.; Wang, H.-Z.; Høiby, N.; Song, Z.-J. *Int. J. Oral Sci.* **2015**, *7*, 1-7.
5. Szycher, M.: Antimicrobial Materials for Medical Devices. In *Kirk-Othmer Encyclopedia of Chemical Technology*; John Wiley & Sons, Inc., 2000.
6. Aiken, S. S.; Cooper, J. J.; Florance, H.; Robinson, M. T.; Michell, S. *Surgical Infections* **2015**, *16*, 54-61.
7. Schairer, D. O.; Chouake, J. S.; Nosanchuk, J. D.; Friedman, A. J. *Virulence* **2012**, *3*, 271-279.
8. Vincent, M.; Hartemann, P.; Engels-Deutsch, M. *Int. J. Hyg. Environ. Health* **2016**, *219*, 585-591.
9. Wang, L.; Hu, C.; Shao, L. *Int. J. of Nanomedicine* **2017**, *12*, 1227-1249.
10. Kohanski, M. A.; Dwyer, D. J.; Collins, J. J. *Nat. Rev. Microbiol.* **2010**, *8*, 423-435.
11. Du, X.; Fan, R.; Qiang, L.; Xing, K.; Ye, H.; Ran, X.; Song, Y.; Wang, P.; Yang, Y. *ACS Appl. Mater. Interfaces* **2017**, *9*, 28939-28948.
12. Kinnear, C.; Moore, T. L.; Rodriguez-Lorenzo, L.; Rothen-Rutishauser, B.; Petri-Fink, A. *Chem. Rev.* **2017**, *117*, 11476-11521.
13. Baker, J. S., S.; Sengupta, M.; Johnson, M.; Jayaswal, R. K.; Morrissey, J. A. *Appl. Environ. Microbiol.* **2010**, *76*, 150-160.
14. Grass, G. R., C.; and Solioz, M. *Appl. Environ. Microbiol.* **2011**, *77*, 1541-1547.

15. Watkins, E. EPA Reg. No. 82012-1.
16. Dalecki, A. G.; Crawford, C. L.; Wolschendorf, F. Chapter Six - Copper and Antibiotics: Discovery, Modes of Action, and Opportunities for Medicinal Applications. In *Advances in Microbial Physiology*; Poole, R. K., Ed.; Academic Press, 2017; Vol. 70; pp 193-260.
17. Yang, Z.; Xie, C.; Cai, S.; Xia, X. *Mater. Lett.* **2008**, *62*, 4226-4228.
18. Liu, Y.; Suo, X.; Wang, Z.; Gong, Y.; Wang, X.; Li, H. *Mater. Des.* **2017**, *130*, 285-293.
19. Abbasi, A. R.; Akhbari, K.; Morsali, A. *Ultrason. Sonochem.* **2012**, *19*, 846-852.
20. Rubin, H. N.; Reynolds, M. M. *Inorg. Chem.* **2017**, *56*, 5266-5274.
21. Gliemann, H.; Wöll, C. *Mater. Today* **2012**, *15*, 110-116.
22. da Silva Pinto, M.; Sierra-Avila, C. A.; Hinestroza, J. P. *Cellulose* **2012**, *19*, 1771-1779.
23. Zhao, J.; Tang, Y.; Liu, Y.; Cui, L.; Xi, X.; Zhang, N.; Zhu, P. *Mater. Des.* **2015**, *87*, 238-244.
24. Wiktor, C.; Meledina, M.; Turner, S.; Lebedev, O. I.; Fischer, R. A. *J. Mater. Chem. A* **2017**, *5*, 14969-14989.
25. Schmitt, S.; Hümmer, J.; Kraus, S.; Welle, A.; Grosjean, S.; Hanke-Roos, M.; Rosenhahn, A.; Bräse, S.; Wöll, C.; Lee-Thedieck, C.; Tsotsalas, M. *Adv. Funct. Mater.* **2016**, *26*, 8455-8462.
26. Hanke, M.; Arslan, H. K.; Bauer, S.; Zybaylo, O.; Christophis, C.; Gliemann, H.; Rosenhahn, A.; Wöll, C. *Langmuir* **2012**, *28*, 6877-6884.
27. Arpa Sancet, M. P.; Hanke, M.; Wang, Z.; Bauer, S.; Azucena, C.; Arslan, H. K.; Heinle, M.; Gliemann, H.; Wöll, C.; Rosenhahn, A. *Biointerphases* **2013**, *8*:29.
28. Bajpai, V. B., S.; Jha, M.K.; Dey, A.; Ghosh, S. *J. Environ. Res. Develop.* **2011**, *5*, 666-672.

29. ASTM D5465-16 Standard Practices for Determining Microbial Colony Counts from Waters Analyzed by Plating Methods, ASTM International, West Conshohocken, PA, 2016.
30. Sutton, S. J. *Validation Technol.* **2011**, *17*, 42.
31. Ceri, H.; Olson, M. E.; Stremick, C.; Read, R. R.; Morck, D.; Buret, A. *J. Clin. Microbiol.* **1999**, *37*, 1771-1776.
32. Robson, M. C. *Ann. Emerg. Med.* **1988**, *17*, 1274-1278.
33. Robson, M. C. *Surg. Clin. North Am.* **1997**, *77*, 637-650.
34. Poelstra, K. A.; Barekzi, N. A.; Rediske, A. M.; Felts, A. G.; Slunt, J. B.; Grainger, D. W. *J. Biomed. Mater. Res.* **2002**, *60*, 206-215.
35. May, J.; Chan, C. H.; King, A.; Williams, L.; French, G. L. *J. Antimicrob. Chemother.* **2000**, *45*, 639-643.
36. Pegalajar-Jurado, A.; Easton, C. D.; Styan, K. E.; McArthur, S. L. *J. Mater. Chem. B* **2014**, *2*, 4993-5002.
37. Hall-Stoodley, L.; Costerton, J. W.; Stoodley, P. *Nat. Rev. Microbiol.* **2004**, *2*, 95-108.
38. Cloutier, M.; Mantovani, D.; Rosei, F. *Trends in Biotechnol.* **2015**, *33*, 637-652.
39. Santo, C. E.; Lam, E. W.; Elowsky, C. G.; Quaranta, D.; Domaille, D. W.; Chang, C. J.; Grass, G. *Appl. Environ. Microbiol.* **2011**, *77*, 794-802.
40. Noyce, J. O.; Michels, H.; Keevil, C. W. *Appl. Environ. Microbiol.* **2006**, *72*, 4239-4244.
41. Rodríguez, H. S.; Hinestroza, J. P.; Ochoa-Puentes, C.; Sierra, C. A.; Soto, C. Y. *J. Appl. Polym. Sci.* **2014**, *131*, 40815.

CHAPTER 4

AMINO-INCORPORATED TRICARBOXYLATE METAL–ORGANIC FRAMEWORK FOR THE SENSITIVE FLUORESCENCE DETECTION OF HEAVY METAL IONS WITH INSIGHTS TO THE ORIGIN OF PHOTOLUMINESCENCE RESPONSE³

4.1 Summary

Metal-organic frameworks (MOFs) can be powerful chemosensors. This work contributes to the overall understanding and characterization of metal ion interactions with MOFs to elicit detectable changes in optical properties, such as fluorescence, a necessary step en route to developing more sensitive and selective systems for metal ion sensing. MOFs offer the opportunity to selectively detect and remove heavy metals from environmental sources such as soil and water. The photophysical properties of tricarboxylate $\text{Cu}_3(\text{NH}_2\text{BTC})_2$ were investigated. The MOF was ultra-sensitive for the detection of Fe^{2+} and Fe^{3+} exhibiting the most intense fluorescence quenching as low as 1.55 ppm, 27.8 μM at room temperature in under 2 min. Pb^{2+} , Cu^{2+} , Mn^{2+} , Ni^{2+} and Co^{2+} were also detectable at 5.7, 12, 3.0, 1.6 and 0.2 ppm respectively. A fluorescence enhancement phenomenon was observed when Lewis acids ZrCl_4 and AlCl_3 were introduced to the MOF solution and significant fluorescence quenching was observed in the presence of anions CO_3^{2-} , OAc^- , and $\text{Cr}_4\text{O}_7^{2-}$. As a means to elucidate the mechanism of detection, isoreticular Cu_3BTC_2 and postsynthetically modified $\text{Cu}_3(\text{NH}_2\text{BTC})_2$ (to hinder access to the free-amine moiety) were also investigated, revealing that the free amine is essential for the detection of the anions and is involved in the detection of several divalent metal ions, which is consistent with hard

³ The present chapter has been developed in full and is currently prepared for submission with author Melissa M. Reynolds. The work presented in this chapter was performed by Heather Rubin.

soft acid/base theory. The metal ion on the other hand, Fe^{2+} likely induces an emission change by interaction with the carboxylate of the MOF ligand or the Cu^{2+} sites. Taken together, this report demonstrates that $\text{Cu}_3(\text{NH}_2\text{BTC})_2$ has unique photoluminescent properties and likely elicits sensitive detection of potentially harmful ions (ppm, μM) via multiple photoluminescent mechanisms. As such, MOFs with free accessible functional handles (such as an amine) can be strategically modified to selectively detect specific metal ions.

4.2 Introduction

Metals are prevalent in varying concentrations around the world in different geological regions.¹ Some metals are vital to ecological health and growth. Others, namely heavy metals, in the environment can be detrimental to the health of virtually all living organisms including plants, animals, and humans.² Transition metal ions in particular including Fe^{2+} , Fe^{3+} , Cu^{1+} , Cu^{2+} , Co^{2+} , Cr^{5+} , Cr^{7+} , Hg^{2+} , Ni^{2+} , V^{4+} , V^{5+} , and Pb^{2+} impose deleterious health effects attributed to oxidative species formed in the body resulting in enhanced lipid peroxidation, DNA damage, and overall damage to renal, reproductive, or central nervous systems.^{3,4} Ions Cd^{2+} , Cr^{4+} , and Be^{2+} are all identified as human carcinogens.⁵ Divalent metal ions are common drinking water contaminants, all of which are deemed unsafe at relatively low concentrations.⁶ Copper in the ionic form of Cu^{2+} is commonly found in drinking water yet recommended by the Environmental Protecting Agency (EPA) not to exceed 1.3 ppm, as it can lead to negative respiratory, gastrointestinal, or hematological effects.^{7,8} Divalent lead (Pb^{2+}) is the stable species of lead found in the environment, and is recommended by the EPA not to exceed 0.015 ppm in drinking water, as it can cause significant delays in physical or mental development in children and gastrointestinal, hematologic,

and/or neurologic symptoms in adults.⁹ As such, it is vital to have the capability to identify and quantify the presence of such metal ions at low concentrations.

Current methods for quantifying metal ion contaminants include inductively coupled plasma optical emission spectrometry (ICP-OES),¹⁰ electrochemical detection,¹¹ or atomic absorption spectrophotometry (AAS),¹² largely owing to the ability to accurately detect metal ions at low ppb level concentrations. However, these methods often require large sample quantities (5 mL or more), necessitating costly stationary equipment. Additionally, these methods are not viable strategies to attain rapid quantification in the field. Thus, developing low-cost materials for immediate metal ion detection remains a fundamental analytical challenge.

To overcome these challenges, luminescence sensing is an alternative optical method attracting significant attention for rapid (less than 10 min),^{13,14} sensitive (ppb level),^{15,16} and facile detection of various analytes.¹⁷ Luminescent metal-organic frameworks (MOFs) have recently been recognized as attractive chemosensing materials. MOFs are highly tunable, crystalline porous coordination networks of metal ions or clusters with coordinating organic linkers. The record-high porosity of MOFs concentrates analytes at greater levels than achievable by nonporous materials. Maximizing analyte interactions between the surface of the MOF and target-analytes can result in greater sensitivity.

MOF linkers often contain highly conjugated moieties, yielding materials that are apt to fluoresce.¹⁸ Fluorescence is a subset of luminescence whereby a compound enters an excited state by absorbing light at a given wavelength, and emits light at a longer wavelength upon relaxation to the ground state. Fluorescence in MOFs can be quite sensitive to changes in solvent and analyte loading, leading to detectable changes in fluorescent intensity or emission wavelengths.¹⁹ As a result, MOFs as chemosensors can be highly sensitive and useful for detecting various analytes of

environmental concern, such as heavy metals,²⁰ nitroaromatics,²¹ and volatile organic carbons.²² Additionally, the near infinite possibilities to tune the structures of the material by varying the metal ions or linkers renders MOFs ideal for strategically engineering analyte selectivity. For example, postsynthetic modification, whereby a framework contains a free and accessible functional handle, may yield selective desirable reactivity with a target analyte to induce detectable PL changes (Figure 4.1).²³ For instance, free-amine decorated UiO-66 ($\text{NH}_2\text{-UiO-66}$) containing $[\text{Zr}_6\text{O}_4(\text{OH})_4]$ clusters with 1,4-benzodicarboxylic acid struts, selectively and rapidly (less than 5 min) undergoes a significant reduction in fluorescence intensity in the presence of Cu^{2+} ions.²⁴ As such, MOFs with fluorescing ligands and free accessible functional handles show promise for selectively detecting metal ions and other analytes, warranting further investigation.

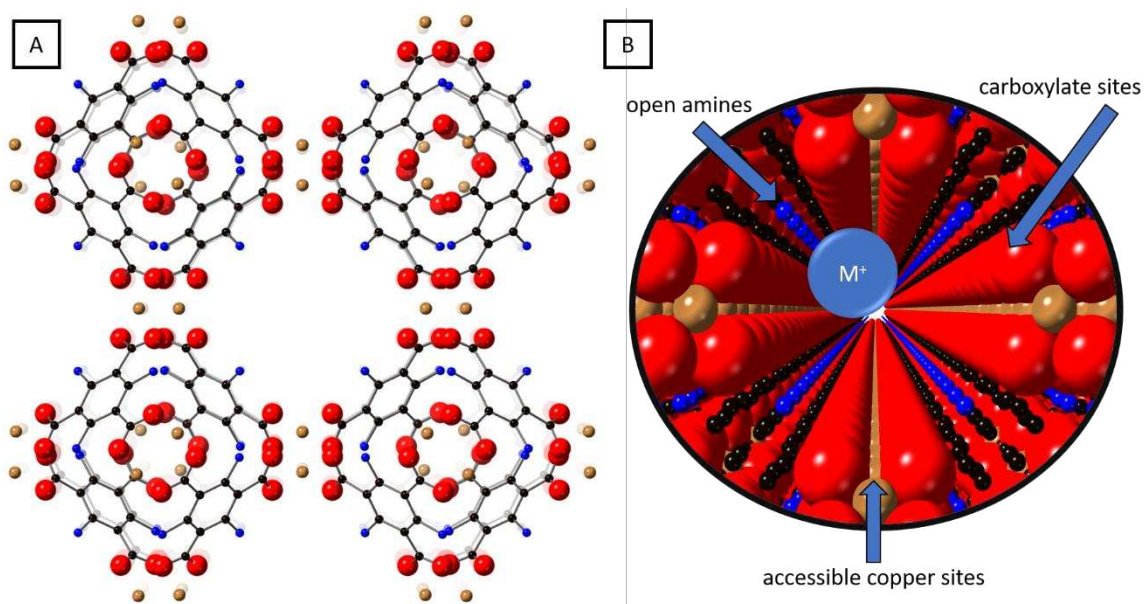


Figure 4.1. CrystalMaker drawings of $\text{Cu}_3(\text{NH}_2\text{BTC})_2$. A. showing a secondary binding unit of the framework with accessible amines (blue), oxygen (red), copper (tan), and carbon (black) including B. a space-filling model indicating where a metal ion may access the MOF.

The ligand NH_2BTCH_3 is highly fluorescent in solution as well as in the MOF structure. Herein, the photophysical properties of tricarboxylate copper 2-aminobenzene-1,3,5-tricarboxylate ($\text{Cu}_3(\text{NH}_2\text{BTC})_2$) were investigated and probed for metal-ion sensing capabilities. The present PL investigations were performed to assess if $\text{Cu}_3(\text{NH}_2\text{BTC})_2$ could undergo detectable changes in fluorescence with various metal ion analytes. A primary goal was to study the mechanism of analyte interaction with the MOF towards understanding the interactions between ions and MOFs. Excitingly, $\text{Cu}_3(\text{NH}_2\text{BTC})_2$ interacts selectively with various metal ions detailed herein. The material is highly sensitive for the detection of Fe^{2+} and Fe^{3+} . Our investigations suggest that the mechanism of analyte detection may vary depending upon the analyte of interest. For example, anions appear to elicit a fluorescence quenching response by interacting directly through the free amine. Interaction with the amine is potentially responsible for the observed fluorescence quenching of the MOF with most divalent metal ions. Fe^{2+} , is one exception and likely elicits a fluorescence quenching response by interaction with the carboxylate sites of the linker and/or the open coordination sites of the Cu^{2+} within the MOF structure. Additionally, our results indicate that metal-ion detection with MOFs can be both rapid (less than 2 min) and highly sensitive (1.55 ppm for Fe^{2+}). Taken together, the studies herein demonstrate that MOFs such as $\text{Cu}_3(\text{NH}_2\text{BTC})_2$ having multiple opportunities to interact and detect ions (anions, acids, and metal ions) may be tuned to have selectivity for target-analytes. As such, tunable MOFs are attractive materials to address the fundamental analytical challenge of enabling access to sensitive, selective, and rapid detection of metal ions (visible with a UV bulb).

Photoluminescent Ion-Induced Changes

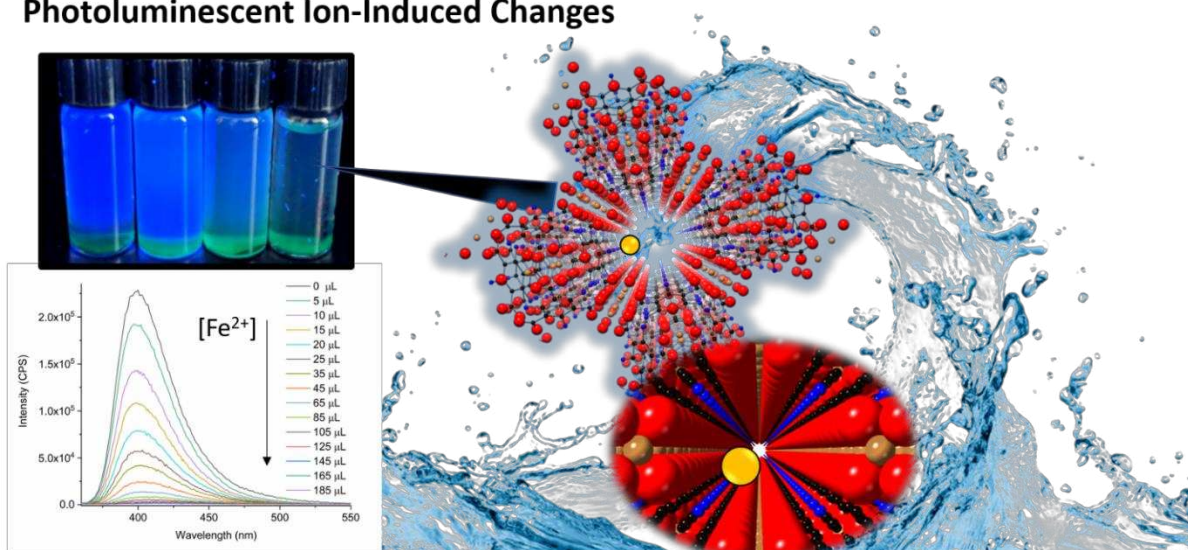


Figure 4.2. Summary image of chapter 4, whereby fluorescence intensity changes are apparent due to ion interactions with MOF $\text{Cu}_3(\text{NH}_2\text{BTC})_2$.

4.3 Experimental

4.3.1 Materials and methods.

Dimethylacetamide (DMA), dimethylformamide (DMF), anhydrous chloroform (CHCl_3), dimethylsulfoxide (DMSO), acetonitrile (ACN), diethyl ether (Et_2O), ethanol (EtOH), toluene (MePh), benzene (PhH), Basolite C300, and ionic compounds: NaCl, KBr, NaI, Na_2CO_3 , $\text{Na}_2\text{Cr}_2\text{O}_7$, NaOAc, CuCl_2 , ZnCl_2 , $\text{Ni}(\text{NO}_3)_2$, CoCl_2 , FeCl_2 , CdCl_2 , MnCl_2 , PbCl_2 , FeCl_3 , AlCl_3 , CrCl_3 , ZrCl_4 , CuI, BiNO_3 , CsNO_3 , CaNO_3 , SrNO_3 , and RbNO_3 were purchased from Sigma Aldrich. All materials were used as provided without further purification. For experiments requiring water, a Millipore purification system set at 18 M Ω was used. An Agilent (Varian) 400MR equipped with automated tuning and a 7600 sample changer at room temperature was used for all NMR experiments. The attained FID was processed using MestReNova NMR software. Powder X-ray diffraction (PXRD) patterns were obtained to verify MOF crystallinity with a Bruker D8 Discover DaVinci Powder X-ray diffractometer with Cu $\text{K}\alpha$ radiation operated at 40

kV and 40 mA. A 0.6 mm divergent slit was placed on the primary beam side, and a high-resolution energy dispersive LYNXEYE-XE-T detector was placed on the diffracted beam side during the XRD studies. The instrument alignment was tested using the NIST 1976b SRM. A typical scan rate was 0.1 s/step with a step size of 0.02°. Infrared (IR) data were acquired on a Nicolet 6700 Fourier transform infrared (FTIR) spectrometer under a nitrogen flow. Diffuse reflectance UV-Vis spectroscopy was performed using a Nicolet Evolution 300 UV-Vis Spectrophotometer equipped with a Praying Mantis diffuse reflectance accessory. Fluorescence experiments were performed on a Horiba Jobin-Yvon FluoroLog-3 Spectrofluorometer using a UV-Quartz cuvette with a 1 cm pathlength.

4.3.2 Synthesis of MOF $\text{Cu}_3(\text{NH}_2\text{BTC})_2$ and Postsynthetic Modification.

The MOF was synthesized as previously reported in the literature.²⁵ The modified samples were synthesized with postsynthetic modification (PSM) of MOF $\text{Cu}_3(\text{NH}_2\text{BTC})_2$ following a previously reported procedure.²⁶ The identity and purity was determined and matches previously reported analyses (IR, pXRD, and NMR).

4.3.3 Photophysical Studies.

Fluorescence experiments were designed to minimize light scattering due to the insolubility of the MOF. To achieve minimal light scattering and optimize the fluorescent signal, in a typical experiment 2-3 mg of finely ground MOF was added to a 2 mL vial, followed by 2 mL of solvent. The MOF was soaked in the solvent overnight. Then, the vial was shaken thoroughly by hand for 30 s and sonicated for 1 h. Subsequently, the solution containing the suspended MOF was decanted and added to a UV-Quartz cuvette with a 10 mm pathlength for analysis. Emission spectra were

acquired from 355 nm to 600 nm using an excitation wavelength of 350 nm. Following an initial solvent screen, DMF was used for photophysical studies.

4.3.4 Fluorescence [M^{n+}] Sensing Experiments.

Sensing experiments were designed to minimize the impact of dilution and solvent effects upon adding aliquots of metal ion solutions. Solutions at a concentration of 10 mM were prepared in DMF using M^{2+} solutions $CuCl_2$, $ZnCl_2$, $Ni(NO_3)_2$, $CoCl_2$, $FeCl_2$, $CdCl_2$, $MnCl_2$, and $PbCl_2$. Additional solutions include $FeCl_3$, $AlCl_3$, $CrCl_3$, $ZrCl_4$, CuI , $BiNO_3$, $CsNO_3$, $CaNO_3$, $SrNO_3$, and $RbNO_3$. For these experiments, 2 mg of finely ground MOF was added to a 2 mL vial followed by 2 mL DMF, shaken for 30 s, sonicated for 1 h, and the suspended MOF carefully pipetted into a new vial and stored until further use. Upon decanting, 0.53 ± 0.07 mg of MOF remain in the sample solution. The sample was shaken for 30 s by hand to resuspend the MOF for metal ion detection studies. Next, 1.8 mL of the MOF suspended in DMF was added to the cuvette. For each emission spectrum obtained the metal solutions were titrated in at the following aliquots: 5, 10, 15, 25, 35, 45, 65, 85, 105, 125, 145, 165, 185, 205, 225, 275, 325, or 375 μ L and immediately agitated using a pipette. The entire process of adding an aliquot, agitation, and sample detection took 2 min, assume the detection occurs in less than 2 min. To ensure fluorescence emission data was not changing over time, for several aliquots of each metal, emission spectra was reacquired after 10 min of solution aging. In all cases unless otherwise noted, the fluorescence intensity was unchanging between 1 min and 30 min after detection.

4.3.5 Anion Sensing.

Solutions at concentrations of 10 mM were prepared in DMF with minimal (less than 200 μL) water to aid in dissolving the salts: NaCl, KBr, NaI, Na_2CO_3 , $\text{Na}_2\text{Cr}_2\text{O}_7$, and NaOAc. For these experiments, 2 mg of finely ground MOF was added to a 2 mL vial followed by DMF, shaken for 30 s, sonicated for 1 h, and the suspended MOF carefully pipetted into a new vial and stored until further use. The sample was shaken for 30 s by hand to resuspend the MOF prior to the following ion detection studies. Next, 1.8 mL of the MOF suspended in DMF was added to the cuvette. The ion containing solutions were titrated in at the following aliquots: 5, 10, 20, 50, 100, 150, or 200 μL . Each solution was immediately agitated using a pipette following introduction of a titration and emission spectra were taken. The process of adding an aliquot, agitation, and sample detection took less than 2 min.

4.4 Results and Discussion

4.4.1 Metal Ion Detection.

$\text{Cu}_3(\text{NH}_2\text{BTC})_2$ exhibits unique photophysical properties and contains numerous MOF-analyte interaction opportunities (free-amine, open coordination sites at Cu^{2+} nodes, flexible carboxylate linkers). As such, the ligand and the photoluminescence (PL) of the MOF were explored herein. The conjugated aromatic ligand, NH_2BTCH_3 , is fluorescent when excited at a wavelength of 350 nm, exhibiting an emission wavelength at 400 nm (Figure 4.3). When incorporated into the copper MOF, the material is highly fluorescent, also exhibiting fluorescent emission at 400 nm when excited at 350 nm. In addition, the quantum efficiency is greater for the MOF $\text{Cu}_3(\text{NH}_2\text{BTC})_2$, than the ligand as the free lumiphore species in solution. As such, fluorescence emission from $\text{Cu}_3(\text{NH}_2\text{BTC})_2$ is likely ligand-based emission which may be

responsive and undergo PL changes (shifts in emission intensity or emission wavelength) upon interactions with metal ions.

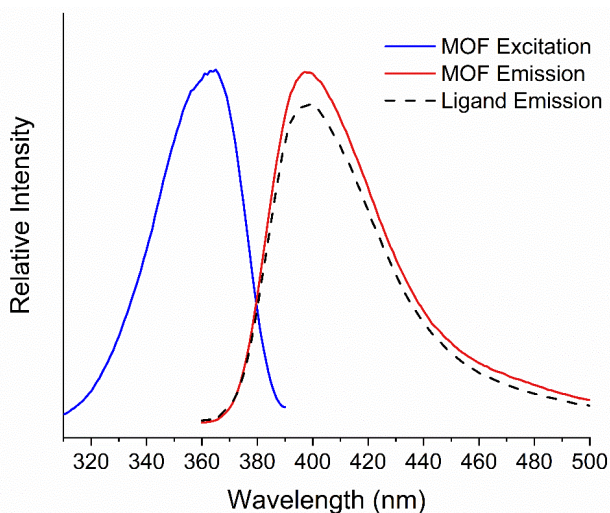


Figure 4.3. Excitation (blue) and emission (red) spectra of $\text{Cu}_3(\text{NH}_2\text{BTC})_2$ and the emission spectra of ligand NH_2BTCH_3 in DMF.

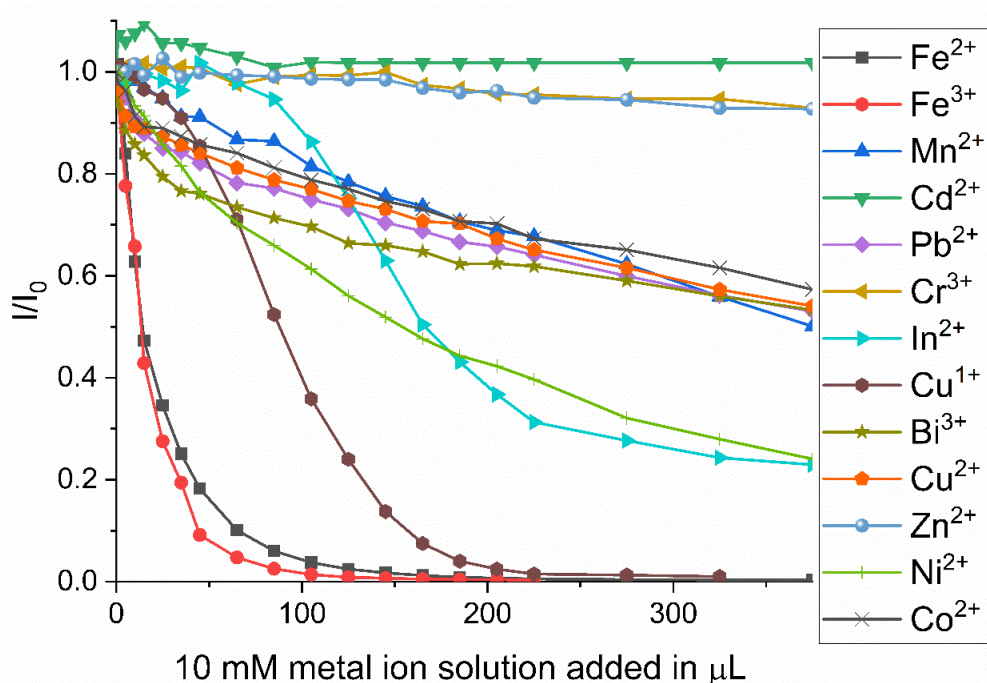


Figure 4.4. Normalized fluorescence intensity (I/I_0) of $\text{Cu}_3(\text{NH}_2\text{BTC})_2$ using emission wavelength at 400 nm upon the addition of varying 10mM metal ion containing aliquots excited at 350 nm. The photoluminescent quenching response is most sensitive to the addition of Fe^{2+} (grey) and Fe^{3+} (red). Detectable fluorescence quenching was also observed with the addition of divalent ions Mn^{2+} , Pb^{2+} , Co^{2+} , Ni^{2+} , Cu^{2+} , and In^{2+} and also ions Cu^{1+} and Bi^{3+} .

Because heavy metals may be toxic to humans they often require detection and removal from drinking water. Furthermore, because many heavy metals are in the M^{2+} oxidation state, various M^{2+} ions were introduced to the MOF in aliquots and the resultant emission recorded within 2 min of exposure (Figure 4.4). The data presented in Figure 3 shows the normalized fluorescence intensity (I/I_0), whereby I represents the resultant intensities after aliquot additions and I_0 represents the initial intensity before ion addition. Ions such as Cd^{2+} and Zn^{2+} have nearly no impact to the fluorescence emission of the MOF. The MOF is somewhat sensitive to fluorescence quenching with Mn^{2+} , Fe^{2+} , Co^{2+} , Ni^{2+} , Cu^{2+} , In^{2+} , and Pb^{2+} and undergoes more intense fluorescence quenching with In^{2+} and Ni^{2+} . The fluorescence of the MOF was quenched most rapidly in the presence of Fe^{2+} . Importantly, $Cu_3(NH_2BTC)_2$ can detect several M^{2+} ions at ppm levels: Pb^{2+} , Cu^{2+} , Mn^{2+} , Ni^{2+} and Co^{2+} at 5.7, 12, 3.0, 1.6 and 0.2 ppm, respectively. Complete fluorescence quenching with Fe^{2+} and Fe^{3+} metals from 1.5 to 56 ppm, whereby detection limits reported are the concentration of metal ions in solution to yield a detectable change in fluorescence intensity. Thus, the MOF is highly responsive to most M^{2+} ions and therefore a versatile chemosensing material. In general, the MOF seems to follow hard-soft acid and base theory (HSAB), which postulates that hard-acids prefer interaction with hard-bases and soft-acids prefer interacting with soft-bases.²⁷ The core motif of the MOF contains aniline, formally considered to be a borderline soft base. Therefore, the nitrogen of the ligand likely interacts with borderline soft acidic metals. Additional metal ions were tested to elucidate the interaction which may be responsible for the fluorescence quenching. Fluorescence quenching in MOFs can occur via the formation of a non-luminescent complex in the ground state (static), de-excitation of the lumiphore (ligand) in the excited state while interacting with an acceptor (metal ion), or energy transfer (de-

excitation of the lumiphore by energy transfer from the excited state to another molecule in the ground state).²⁸

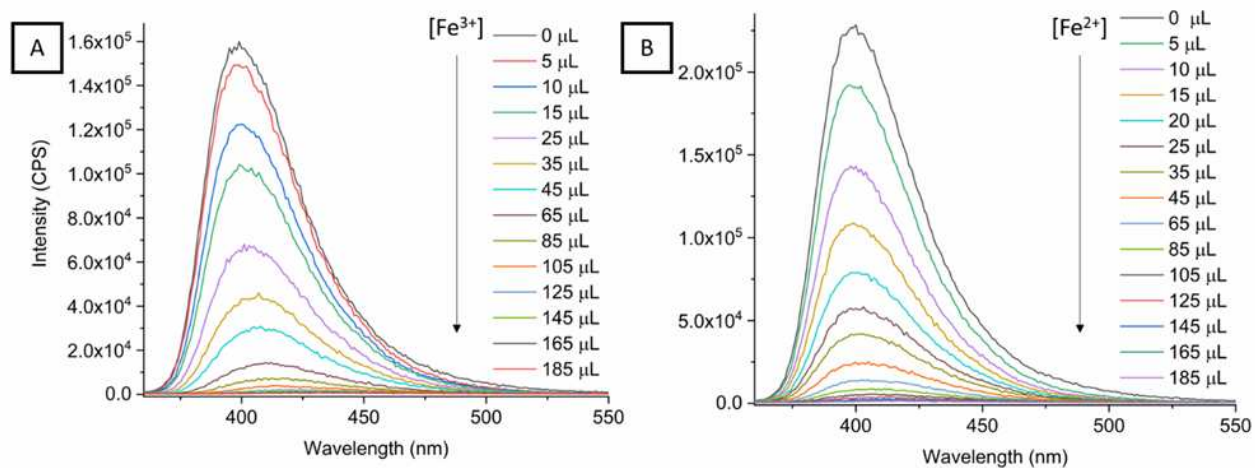


Figure 4.5. Fluorescence intensity changes of Cu₃(NH₂BTC)₂ using emission wavelength at 400 nm, excited at 350 nm upon the addition of varying aliquots of (A) Fe³⁺ (left) or (B) Fe²⁺ (right).

Continuing with the HSAB trend, the MOF was also sensitive to borderline hard metal Bi³⁺. When soft acid Cu¹⁺ was tested, however, the MOF displayed rapid fluorescence quenching. Fe³⁺ was also investigated, revealing the MOF is highly sensitive to both Fe³⁺ and Fe²⁺, undergoing complete fluorescence quenching with 56 ppm Fe²⁺ or Fe³⁺ present in solution (Figure 4.5). When FeCl₂ was added to Cu₃BTC₂ (with ligand 1,3,5-benzenetricarboxylate), similar fluorescence quenching was observed, albeit less intense (Figure 4.6). A likely hypothesis for the observed PL (fluorescence quenching) with Fe²⁺ is energy transfer from an excited state of the ligand to an electron-deficient region induced by carboxylate and or amine electron donation to the Fe²⁺ ion.

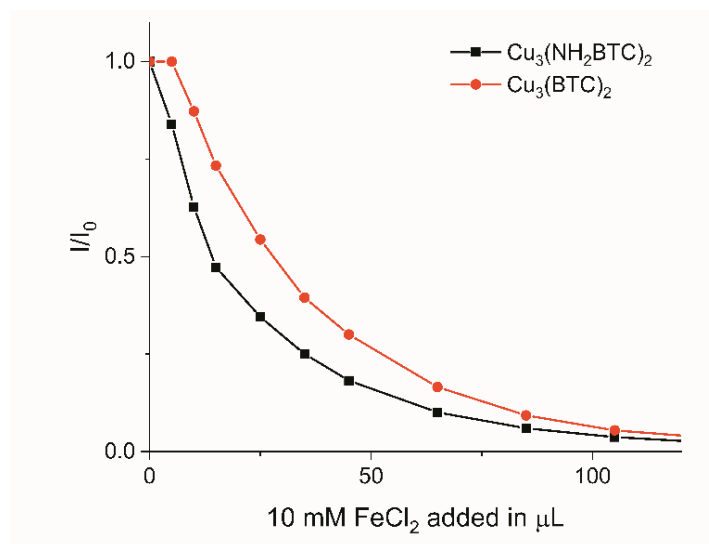


Figure 4.6. Normalized fluorescence intensity (I/I_0) of $\text{Cu}_3(\text{NH}_2\text{BTC})_2$ (black) and $\text{Cu}_3(\text{NH}_2\text{BTC})_2$ (red) upon the addition of 10 mM FeCl_2 solution. Both MOFs undergo significant PL quenching with Fe^{2+} , albeit $\text{Cu}_3(\text{NH}_2\text{BTC})_2$ is slightly more sensitive.

This donor-acceptor relationship was hypothesized to occur during the fluorescence quenching of Fe^{3+} ions with Zn-MOFs UMCM-1 and UMCM-1- NH_2 (with 1,3,5-tris(4-carboxyphenyl)benzene ligand (BTB) and 1,4-benzenedicarboxylate (BDC) or 2-amino-1,4-benzenedicarboxylate (NH_2BDC)).²⁹ $\text{NH}_2\text{-UiO66}$ (with NH_2BDC ligand) undergoes significant fluorescence enhancement in the presence of Cr^{3+} , attributed to its chelation to the free amine and an oxygen of the ligand to form a six-membered chelating ring that may rigidify the structure.³⁰ Conversely, when the hard acid Cr^{3+} was utilized herein, the MOF underwent little to no change in fluorescence. Despite having the same chelation possibilities with the NH_2BTC ligand as NH_2BDC , it appears that the MOF $\text{Cu}_3(\text{NH}_2\text{BTC})_2$ used herein either does not form the suggested chelate or is a more rigid framework before metal ion addition, and therefore does not have the same outcome as rigidifying the more flexible BDC-based MOF. Alternatively, ion detection may not occur via the suggested chelate with the carboxylate and amine.

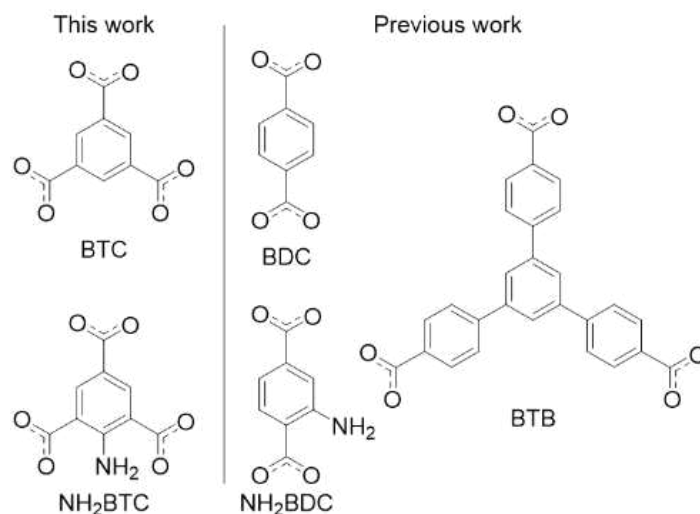


Figure 4.7. Common carboxylate-based ligands for MOFs that exhibit fluorescence.

For a complete picture of the metal ion detection capabilities of $\text{Cu}_3(\text{NH}_2\text{BTC})_2$, experiments were performed with 200 μL of 10 mM alkali metals Na^+ , K^+ , Rb^+ and Ca^+ and alkaline earth metals Sr^{2+} and Ca^{2+} (Figure 4.8). Little to no change in fluorescence is observed upon the addition of alkali metals; however, the addition of alkaline earth metals quenches the fluorescence by nearly 50%. To our knowledge this is one of few reports demonstrating the ability for MOFs to sense Ca^{2+} . In addition, a new peak at 475 nm is detected. Taken together, these data suggest that the alkaline earth metals are interacting with the MOF to reduce the fluorescence efficiency of the material.

In summary, $\text{Cu}_3(\text{NH}_2\text{BTC})_2$ demonstrates potential to rapidly, selectively and sensitively react with many metal ions. The ions Fe^{2+} and Fe^{3+} elicit the most intense fluorescence quenching response; however, the MOF is also responsive to several other divalent metal ions as consistent with HSAB theory (specifically Pb^{2+} , Cu^{2+} , Mn^{2+} , Ni^{2+} , In^{2+} and Co^{2+}). The $\text{Cu}_3(\text{NH}_2\text{BTC})_2$ system is also capable of detecting alkaline earth metals via a fluorescence quenching response. By further

exploring how ions interact with the MOF, tuning the MOF for specific metal ion detection may be realized.

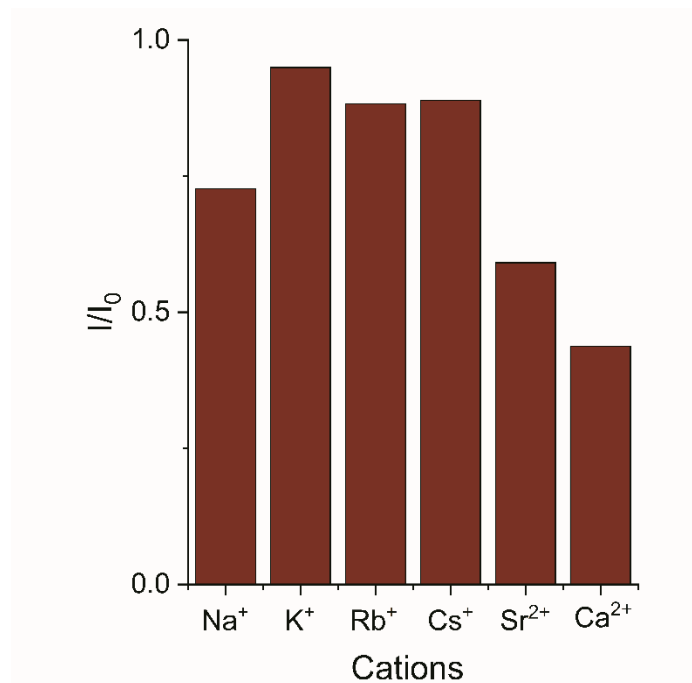


Figure 4.8. Normalized fluorescence intensity (I/I_0) changes of $\text{Cu}_3(\text{NH}_2\text{BTC})_2$ following excitation at 350 nm monitoring emission wavelength at 400 nm, following the addition of 200 μL of 10 mM in DMF solutions of the reported alkali (Na^+ , K^+ , Rb^+ and Cs^+) and alkaline earth metals (Sr^{2+} and Ca^{2+}). Fluorescence intensity is quenched to nearly half its initial in the presence of the alkaline earth metals.

4.4.2 Photophysical Properties and Structural Details of $\text{Cu}_3(\text{NH}_2\text{BTC})_2$.

Ligand-based luminescence is commonly associated with MOFs containing d^{10} metal ions having no d-d or f-f transitions and is marked by inefficient ligand-to-metal charge-transfer (LMCT) because of the full metal-based orbitals.²⁸ In such cases, where there is little to no electronic interaction between the organic linkers and metal ion nodes, ligand-based emission prevails recognizable by emission akin to emission for the free ligand in solution.¹⁸ On the other hand, MOFs with a BTC ligand often exhibit LMCT-based emission. Thus, $\text{Cu}_3(\text{NH}_2\text{BTC})_2$ may

exhibit a mixture of ligand-based emission and LMCT. One can assume $\text{Cu}_3(\text{NH}_2\text{BTC})_2$ is analogous to isoreticular MOF Cu_3BTC_2 , having Cu^{2+} ions with d^9 electronic configuration and having two coordinatively unsaturated Cu sites per paddlewheel secondary building units (SBUs).³¹ Consequently, $\text{Cu}_3(\text{NH}_2\text{BTC})_2$ offers the opportunity to impart detectable changes to the emission properties of the MOF (shifts in emission intensity or emission wavelength) by infiltrating the material with analytes that are or form bimolecular excited states with energy transfer from donor to acceptor, bimolecular excited states via interactions of an excited molecule with proximal non-excited molecules, or quenchers that absorb energy transferred from a fluorophore (ligand).³² The nanoporosity combined with the unique flexible properties of carboxylate-based MOFs allows for various possible interactions between $\text{Cu}_3(\text{NH}_2\text{BTC})_2$ and small molecules or metal ions (Figure 4.9). Changes in emission spectra may arise as a consequence of metal insertion (Figure 4.9A) between the open amine and the carboxylate linker, direct monodentate coordination of the metal ions to the amine (Figure 4.9B), structural collapse by metal insertion and coordination to form a chelating bidentate interaction (Figure 4.9C), postsynthetic cation exchange (Figure 4.9D), or alternatively via metal to metal interactions (Figure 4.9E). Thus, $\text{Cu}_3(\text{NH}_2\text{BTC})_2$ is an attractive material to use for sensing and investigating photoluminescent changes of MOFs by interactions with metal ions and small molecules.

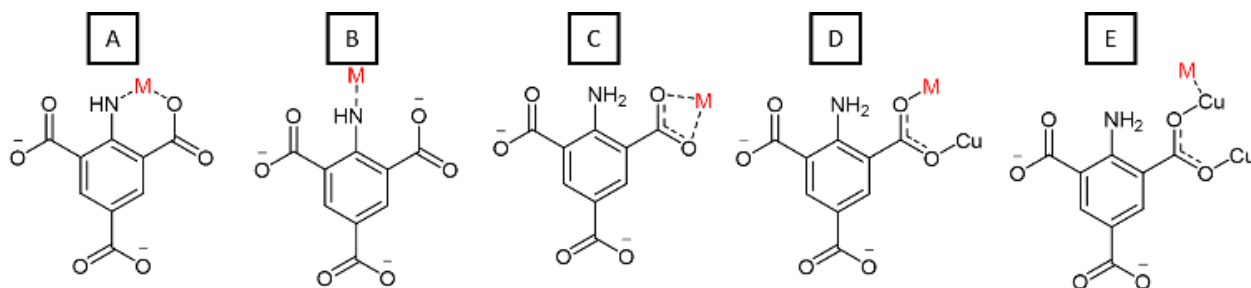


Figure 4.9. Possible mechanisms of metal ion interactions with $\text{Cu}_3(\text{NH}_2\text{BTC})_2$. A. metal insertion between the open amine and the carboxylate linker; B direct monodentate coordination of the metal ions to the amine; C. metal insertion and coordination to form a chelating bidentate interaction; D. postsynthetic metal cation exchange; E. metal to metal interactions.

4.4.3 Solvent Interactions.

Sensing various volatile organic carbons (VOCs) has been achieved with MOFs that have open coordination sites, whereby the material may display unique emission wavelengths specific to the coordination of different solvents.^{33,34} Additionally, the fluorescence emission spectra of fluorophores are often sensitive to the polarity of their environment.³⁵ Therefore, the impact to emission of $\text{Cu}_3(\text{NH}_2\text{BTC})_2$ was initially analyzed herein after the MOF was soaked in various organic solvents for 24 h to identify an optimal solvent for metal-ion detection and to determine if the solvent environment has a significant effect on the observed MOF emission properties (Figure 4.10). Unexpectedly, when dispersed in DCM, MePh, PhH or CHCl_3 the emission spectra all contained four distinct emission wavelengths at 391 nm, 410 nm, 435 nm, and 467 nm.

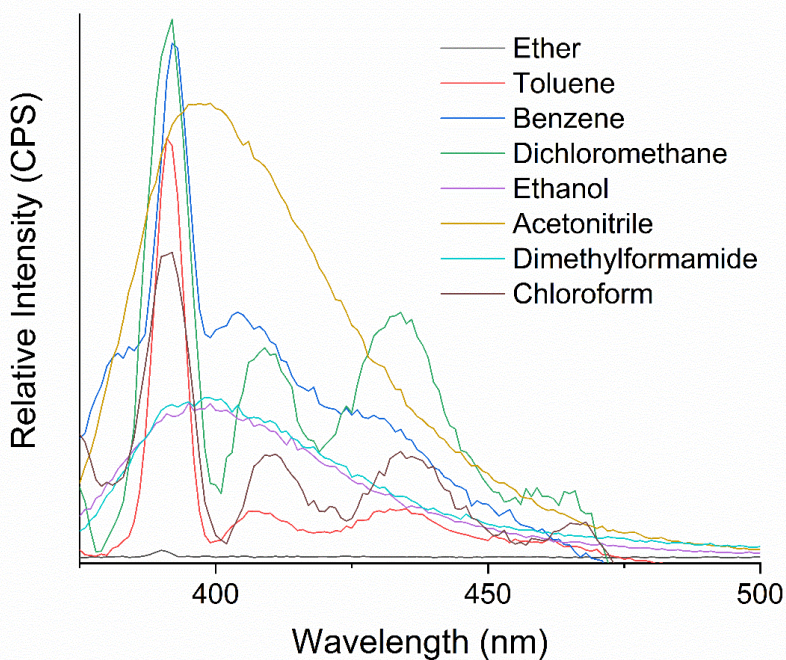


Figure 4.10. Emission spectra of $\text{Cu}_3(\text{NH}_2\text{BTC})_2$ excited at 350 nm after submersion in organic solvents for 24 h. The emission properties of the MOF vary in the presence of the solvents shown. Benzene (blue), dichloromethane (green), chloroform (brown) and toluene (red) all exhibit 4 distinct emission peaks at 391 nm (the most intense), 410 nm, 435 nm, and 467 nm. In order of decreasing intensity, acetonitrile (yellow), dimethylformamide (black), ethanol (purple), and ether (orange) all exhibit a single emission peak at 400 nm.

These results support that the fluorescence associated with the MOF occurs via multiple emission pathways, which is visible in these solvents. This is further supported by previously reported molecular simulations with isostructural $\text{Cu}_3(\text{BTC})_2$ suggesting that size, configuration, polarity, and entropic factors of the solvent effect the adsorption of solvent to the framework.³⁶ The emission wavelength of $\text{Cu}_3(\text{NH}_2\text{BTC})_2$ occurred solely at 400 nm in solvents capable of hydrogen-bonding or strongly coordinating including ACN, DMF, EtOH and Et₂O. While the emission intensity was most intense in ACN, the MOF was most well-dispersed in DMF. As such, the solvent choice impacts the emission properties of $\text{Cu}_3(\text{NH}_2\text{BTC})_2$ as well as the MOFs ability to be evenly suspended in solution for ion detection. DMF results in 1 observed relatively intense emission peak and evenly dispersed particles in solution for up to 10 min (yielding the same fluorescence intensity at this time) and was therefore used for all ion interaction studies herein.

4.4.4 Anion Influence on Sensing.

To ensure the observed fluorescence quenching was indeed a consequence of metal-ion detection and not the associated counterion, several sodium or potassium salts were investigated (Figure 4.11). When 200 μL of 10 mM solutions of Cl^- , Br^- , I^- , or NO_3^- were introduced to the MOF, little to no significant difference in fluorescence intensity was observed. Amino-decorated MOF Zn-NH₂BDC demonstrates strong fluorescent turn-on response to oxidizing agents such as chromium anions.⁹⁵ Thus, we anticipated similar behaviour with $\text{Cu}_3(\text{NH}_2\text{BTC})_2$ if the fluorescence quenching was in response to interactions of the anion with the ligand. Indeed, fluorescence was strongly impacted by the addition of dichromate ($\text{Cr}_2\text{O}_7^{2-}$); however, the fluorescence was not increased, but rather significantly quenched at 400 nm. Furthermore, CO_3^{2-} and OAc^- also significantly quenched the fluorescence of the MOF. These anions are likely

interacting directly with the free amine (via hydrogen bonding, or ion-dipole intermolecular forces) and/or coordinating to the open coordination sites at the Cu^{2+} nodes.

Studies with isorecticular MOF Cu_3BTC_2 suggest that anions may indeed strongly interact with the Cu^{2+} of a MOF, resulting in lengthening of Cu-O bond between the Cu^{2+} nodes and the carboxylate linkers, effectively decreasing the frequency of its vibrational mode.³⁷ A decrease in vibrational mode of a MOF may ultimately result in fluorescence quenching. In summary, common counterions including nitrate and halides have no significant impact to the PL of the MOF, whereas CO_3^{2-} , $\text{Cr}_2\text{O}_7^{2-}$, and OAc^- significantly quench the fluorescence. Interestingly, $\text{Cu}_3(\text{NH}_2\text{BTC})_2$ is unlike structurally similar MOFs in exhibiting a quenching response with all 3 of the aforementioned anions, suggesting that the open copper sites may be responsible for the observed anion quenching observations or alternatively the NH_2BTC ligand is involved in anion coordination likely through direct interaction with the amine moiety.

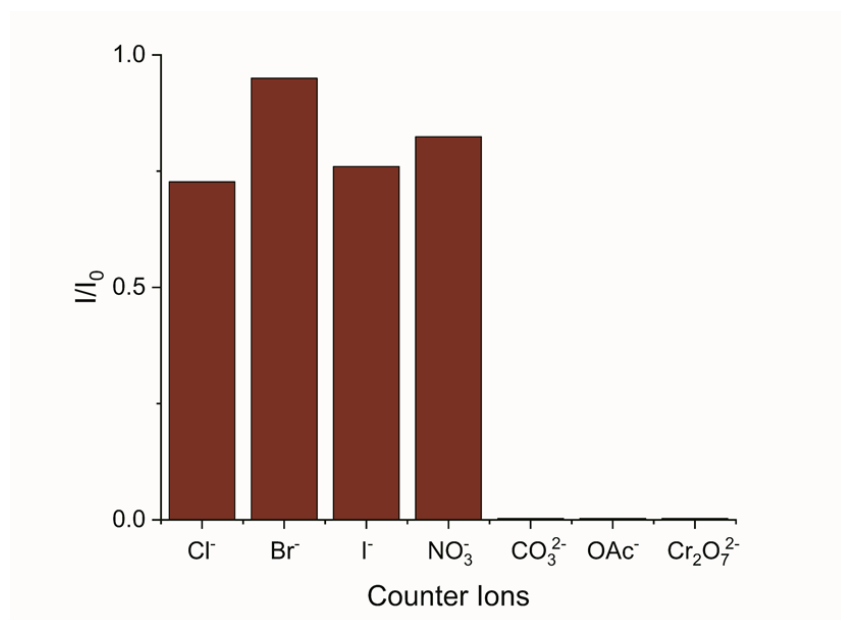
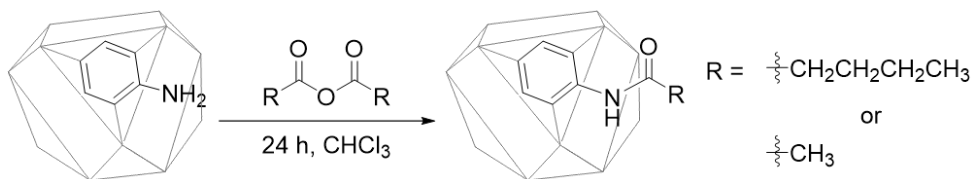


Figure 4.11. Normalized fluorescence intensity (I/I_0) changes of $\text{Cu}_3(\text{NH}_2\text{BTC})_2$ using emission wavelength at 400 nm 1 mM (upon the addition of 200 μL 10mM) ion containing aliquots excited at 350 nm focused on anion detection.

4.4.5 Investigation and Insights into the Changing Emission Pathways.

If the amine was undergoing hydrogen bonding or directly coordinating with the metal-ions or anions detected, one would expect the addition of acid to disrupt this interaction, resulting in a reversal of fluorescence quenching and yield a fluorescence turn-on response. 20 μL of 10 mM HCl in DMF was added to a solution of $\text{Cu}_3(\text{NH}_2\text{BTC})_2$ ($I/I_0 = 1$) partially quenched with 20 μL 10 mM NaOAc ($I/I_0 = 0.4$). In turn, the fluorescence intensity indeed was recovered, exceeding the initial intensity ($I/I_0 = 2.8$). Moreover, when 20 μL of 10 mM HCl in DMF was added to MOF in solution, the fluorescence intensity increased 10-fold. These ions may be interacting through the free amine moiety or coordinating at the open coordination sites to copper.³⁸

Scheme 4.1. Postsynthetic modification of $\text{Cu}_3(\text{NH}_2\text{BTC})_2$ with valeric or acetic anhydride.



To further understand the fluorescence quenching phenomenon, access to the free amine of the MOF ligand was blocked by postsynthetically modifying the free amine to an amide using acetic or valeric anhydrides (Scheme 4.1). In both cases the initial fluorescence intensity of the modified MOF samples was significantly less relative to the unmodified material $\text{Cu}_3(\text{NH}_2\text{BTC})_2$. Furthermore, a second emission peak at 475 nm was observed. As such, one can deduce that the presence of a second peak at 475 nm (also observed with Ca^{2+} , Ca^{2+} , CO_3^{2-} , OAc^- , $\text{Cr}_2\text{O}_7^{2-}$, Cl^- , and I^- quenching) suggests that, in part, the fluorescence may be quenched via directly interacting with the amine moiety (Figure 4.12).

When 50 μL of CaCl_2 was added to a solution of $\text{Cu}_3(\text{NH}_2\text{BTC})_2$, the observed change in fluorescence intensity ($I/I_0 = 0.50$) was much greater than with $\text{Cu}_3(\text{NHAcBTC})_2$ ($I/I_0 = 0.77$). The partial quenching of $\text{Cu}_3(\text{NHAcBTC})_2$ also supports the hypothesis of multiple quenching mechanisms taking place. In addition, the fluorescence intensity of isorecticular MOF Cu_3BTC_2 was also investigated. The ligand of Cu_3BTC_2 is identical to that of $\text{Cu}_3(\text{NH}_2\text{BTC})_2$, except for the absence of a free amine. When 200 μL of 10 mM NaOAc in DMF was added to Cu_3BTC_2 , the fluorescence intensity did not change, further suggesting that the anions are resulting in fluorescence quenching of $\text{Cu}_3(\text{NH}_2\text{BTC})_2$ at least in part by interacting directly with the free amine.

When 20 μL of 10 mM HCl in DMF was added, as with $\text{Cu}_3(\text{NH}_2\text{BTC})_2$, the fluorescence intensity of Cu_3BTC_2 also increased (2-fold). Thus, H^+ is likely, at least in part, interacting with the carboxylate ligands or Cu^{2+} ion nodes to elicit a fluorescent turn-on response in these materials. Fluorescence turn-on response was also observed when Lewis acids ZrCl_4 and AlCl_3 were introduced to the MOF $\text{Cu}_3(\text{NH}_2\text{BTC})_2$. Conceivably, these Lewis acids may rigidify the MOF³⁹ or form a new exciplex resulting in the observed fluorescence turn-on event. In all, this data suggests that $\text{Cu}_3(\text{NH}_2\text{BTC})_2$ is a sensitive fluorescence sensor which likely produces either a turn-off or turn-on response as a result of more than one metal- or ion-MOF interaction dependent upon the particular analyte ion.

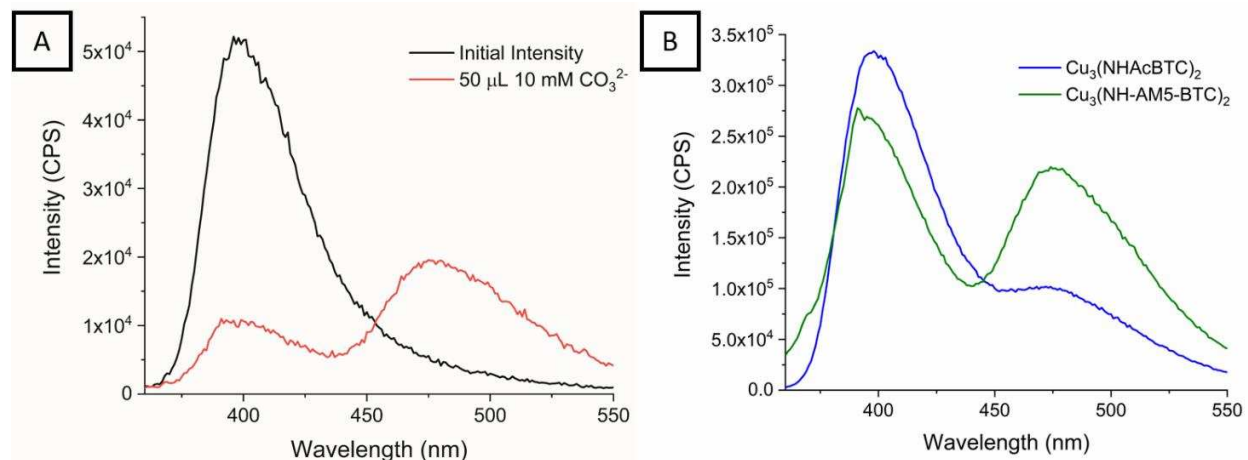


Figure 4.12. (A) Emission spectra before (black) and after (red) the addition of 50 μL of 10 mM Na_2CO_3 . Upon the addition of the anion, the peak at 400 nm is significantly quenched and a new peak at 475 nm is present. (B) Emission spectra of postsynthetically modified MOF with acetic anhydride ($\text{Cu}_3(\text{NHAcBTC})_2$, blue) and valeric anhydride ($\text{Cu}_3(\text{NH-AM5-BTC})_2$, green), with a peak at 400 nm and another at 475 nm.

4.5 Conclusions

The photoluminescent properties of amino-incorporated MOF $\text{Cu}_3(\text{NH}_2\text{BTC})_2$ were thoroughly investigated and undergo unique fluorescence responses, markedly different from NH_2BDC -containing MOFs. Importantly, $\text{Cu}_3(\text{NH}_2\text{BTC})_2$ was shown for the first time to detect several M^{2+} ions (Pb^{2+} , Cu^{2+} , Mn^{2+} , Ni^{2+} and Co^{2+} at 5.7, 12, 3.0, 1.6 and 0.2 ppm respectively) and undergoes complete fluorescence quenching with Fe^{2+} and Fe^{3+} metals from 1.5 to 56 ppm. Alkaline earth metals are also detectable via fluorescence quenching of $\text{Cu}_3(\text{NH}_2\text{BTC})_2$. Conversely, little to no fluorescence response is observed when adding alkali metals. Additionally, this work demonstrates that MOFs having free and accessible function handles (like an amine) yield a complex chemosensing system which likely undergoes fluorescence turn-off responses as a result of more than one mechanism depending on the specific analyte. Anions, for instance, likely interact via the free amine moiety, whereas metal ions likely interact via the free amine and/or the

carboxylate of the ligand. Dichromate, one of the most carcinogenic forms of chromium,⁴⁰ is detected at 1.65 ppm. To our knowledge this is the lowest report for MOF detection of chromium. Moreover, metal ion detection herein with $\text{Cu}_3(\text{NH}_2\text{BTC})_2$ is rapid (< 2 min). As such, $\text{Cu}_3(\text{NH}_2\text{BTC})_2$ is an ideal candidate for use as a fluorescence responsive metal ion chemosensor.

The experimental design principles herein used to investigate the pathways of ion interactions with the MOF, demonstrate the potential use of postsynthetic modification to probe the interaction of MOFs with small molecules and to manipulate selectively. For instance, postsynthetically modifying the free amine directs reactivity at the open coordination sites of the metal nodes and the carboxylate functionality. A better understanding of how MOFs interact with ions is needed to enable future strategic design of MOFs for various applications with ions and small molecules. The design of powerful chemosensors with strategically engineered selectively is a viable end goal.

REFERENCES

1. Tchounwou, P. B.; Yedjou, C. G.; Patlolla, A. K.; Sutton, D. J. *EXS*, 2012, **101**, 133-164.
2. Jaishankar, M.; Tseten, T.; Anbalagan, N.; Mathew, B. B.; Beeregowda, K. N. *Interdisciplinary Toxicology*, **2014**, *7*, 60-72.
3. Stohs S. J.; Bagchi, D. *Free Radical Biology and Medicine*, **1995**, *18*, 321-336.
4. Flora, G.; Gupta, D.; Tiwari, A. *Interdisciplinary Toxicology*, **2012**, *5*, 47-58.
5. Kim, H. S.; Kim, Y. J.; Seo, Y. R. *Journal of Cancer Prevention*, **2015**, *20*, 232-240.
6. U. S. E. P. Agency, <https://www.epa.gov/enviro/drinking-water-contaminants>, (accessed July 27, 2018).
7. U. S. E. P. Agency, <https://www.epa.gov/ground-water-and-drinking-water/national-primary-drinking-water-regulations#Inorganic>, (accessed July, 27, 2018).
8. ATSDR, *Agency for Toxic Substances & Disease Registry*, **2004**, 105-109.
9. Agency for Toxic Substances & Disease Registry, <https://www.atsdr.cdc.gov/toxprofiles/tp13-c6.pdf>.
10. Martin, C. A. B. T.D.; Creed, J.T.; EMMC Methods Work Group, *Journal*, 1994.
11. Bansod, B.; Kumar, T.; Thakur, R.; Rana, S.; Singh, I. *Biosensors and Bioelectronics*, **2017**, *94*, 443-455.
12. Sanders, J. *Agilent Technologies, Inc*, **2012**.
13. Yang, J.; Wang, Z.; Hu, K.; Li, Y.; Feng, J.; Shi, J.; Gu, J. *ACS Applied Materials & Interfaces*, **2015**, *7*, 11956-11964.
14. Long, F.; Zhu, A.; Shi, H.; Wang, H.; Liu, J. *Scientific Reports*, **2013**, *3*, 2308.

15. Srinivasan, K.; Subramanian, K.; Murugan, K.; Dinakaran, K. *Analyst*, **2016**, *141*, 6344-6352.
16. Shah, M. T.; Balouch, A.; Alveroglu, E. *J. Mater. Chem. C*, **2018**, *6*, 1105-1115.
17. W. P. Lustig, S. Mukherjee, N. D. Rudd, A. V. Desai, J. Li and S. K. Ghosh, *Chem. Soc. Rev.* **2017**, *46*, 3242-3285.
18. Cui, Y.; Yue, Y.; Qian, G.; Chen, B. *Chem. Rev.* **2012**, *112*, 1126-1162.
19. Kreno, L. E.; Leong, K.; Farha, O. K.; Allendorf, M.; Van Duyne, R. P.; Hupp, J. T. *Chem. Rev.* **2012**, *112*, 1105-1125.
20. Rudd, N. D.; Wang, H.; Fuentes-Fernandez, E. M. A.; Teat, S. J.; Chen, F.; Hall, G.; Chabal, Y. J.; Li, J. *ACS Applied Materials & Interfaces*, **2016**, *8*, 30294-30303.
21. Du, J.-L.; Zhang, X.-Y.; Li, C.-P.; Gao, J.-P.; Hou, J.-X.; Jing, X.; Mu, Y.-J.; Li, L.-J. *Sensors and Actuators B: Chemical*, **2018**, *257*, 207-213.
22. Takashima, Y.; Martínez, V.; Furukawa, M. S.; Kondo, M.; Shimomura, S.; Uehara, H.; Nakahama, M.; Sugimoto, K.; Kitagawa, S. *Nature Communications*, **2011**, *2*, 168.
23. Wen, L.; Zheng, X.; Lv, K.; Wang, C.; Xu, X. *Inorganic Chemistry*, **2015**, *54*, 7133-7135.
24. Wu, L.; Zhang, X.-F.; Li, Z.-Q.; Wu, F. *Inorganic Chemistry Communications*, **2016**, *74*, 22-25.
25. Peikert, K.; Hoffmann, F.; Froba, M. *Chem Commun (Camb)*, **2012**, *48*, 11196-11198.
26. Rubin, H. N.; Reynolds, M. M. *Inorganic Chemistry*, **2017**, *56*, 5266-5274.
27. Pearson, R. G. *Journal of the American Chemical Society*, **1963**, *85*, 3533-3539.
28. *Metal-Organic Frameworks*, Wiley-VCH Verlag & Co., Weinheim, Germany, 2011.
29. Xiang, Z.; Fang, C.; Leng, S.; Cao, D. *Journal of Materials Chemistry A*, **2014**, *2*, 7662-7665.

30. Lv, R.; Wang, J.; Zhang, Y.; Li, H.; Yang, L.; Liao, S.; Gu, W.; Liu, X. *Journal of Materials Chemistry A*, **2016**, *4*, 15494-15500.
31. Hendon, C. H.; Walsh, A. *Chemical Science*, **2015**, *6*, 3674-3683.
32. Kalinowski, J. *Materials Science-Poland*, **2009**, *27*, 735-756.
33. Lin, R. B.; Liu, S. Y.; Ye, J. W.; Li, X. Y.; Zhang, J. P. *Advanced Science*, **2016**, *3*, 1500434.
34. Zhang, M.; Feng, G.; Song, Z.; Zhou, Y.-P.; Chao, H.-Y.; Yuan, D.; Tan, T. T. Y.; Guo, Z.; Hu, Z.; Tang, B. Z.; Liu, B.; Zhao, D. *Journal of the American Chemical Society*, **2014**, *136*, 7241-7244.
35. Lakowicz, J. R. in *Principles of Fluorescence Spectroscopy*, Springer US, Boston, MA, 1983, DOI: 10.1007/978-1-4615-7658-7_7, pp. 187-215.
36. Gutiérrez-Sevillano, J. J.; Vicent-Luna, J. M.; Dubbeldam, D.; Calero, S. *The Journal of Physical Chemistry C*, **2013**, *117*, 11357-11366.
37. Liu, D.; Zhong, C. *The Journal of Physical Chemistry Letters*, **2010**, *1*, 97-101.
38. Dhumal, N. R.; Singh, M. P.; Anderson, J. A.; Kiefer, J.; Kim, H. J. *The Journal of Physical Chemistry C*, **2016**, *120*, 3295-3304.
39. Wei, Z.; Gu, Z.-Y.; Arvapally, R. K.; Chen, Y.-P.; McDougald, R. N.; Ivy, J. F.; Yakovenko, A. A.; Feng, D.; Omary, M. A.; Zhou, H.-C. *Journal of the American Chemical Society*, **2014**, *136*, 8269-8276.
40. U. S. D. o. H. a. H. Services, *Agency for Toxic Substances and Disease Registry* 2012.

CHAPTER 5

PORPHYRIN-BASED METAL-ORGANIC FRAMEWORK NU-902 FOR FLORESCENCE SENSING AND REMOVAL OF DIVALENT METAL IONS FROM WATER⁴

5.1 Summary

Metal ion contamination of drinking water and ground water further depletes the works already scare supply of clean water. Existing techniques are too often costly and time-consuming to detect and remove such ions from water. As such, the develop of new materials and techniques to detect and remove metal ions from water is a persistent necessity. The present study uses NU-902, a water stable zirconium porphyrin-based metal-organic framework (MOF) for the eventual detection and removal of divalent metal ions from water. The ligand of the MOF is highly selective for the detection of several divalent metal ions and is therefore an ideal candidate for incorporation into a MOF scaffold. The present study indicates that the material is fluorescent and preliminary data indicates that the MOF undergoes a change in photoluminescent emission properties in the presence of Cd²⁺ ions. Future work will focus on determining the efficacy of the material for metal ion detection by changes fluorescence (quenching or enhancing) or absorbance properties (UV-Vis, colorimetric), as well as the ability for the material to remove metal ions from aqueous solutions.

⁴ This dissertation chapter reflects research and experiments performed by Heather Rubin. Undergraduate researcher Jack Miera assisted with the initial photophysical studies as well as the MOF-polymer composites for this project. Hailey Hibbard also assisted with acquiring photophysical data of the MOF-powder for metal ion detection.

5.2 Introduction

Wide spread use of heavy metal ions primarily via anthropological activities including industrial, agricultural, and technological applications has led to their unwanted prevalence in the environment posing a serious threat to the health and well-being of the earth's ecosystems.¹ When metal ions contaminate drinking water and ground water there is a risk of human exposure.² Human consumption is a primary mode of exposure for people to metal ions.³ Moreover, according to the World Health Organization (WHO) nearly 80 % of the global population is challenged with a serious water supply risk. A significant increase in water contamination has therefore become a major world-wide concern for humanity with only 0.036 % of earth's 3% available fresh water (the most critical resource) usable.⁴ As such, it is vital to be able to remove and detect metal ion environmental contaminants from water sources.

Metal-organic frameworks (MOFs) offer a relatively new technological approach towards the development of new chemosensors capable of detecting and removing target analytes including metal ions from water.^{5,6} MOFs are highly porous crystalline organic-inorganic materials with metal ion or cluster nodes with organic ligand linkers. These materials are highly tunable, offering a unique opportunity to engineer selectivity and reactivity into the porous material for preferential interactions with target analytes, like metal ions, via strategic ligand design or metal node selection. Furthermore, MOFs often contain highly conjugated organic linkers, which are apt to fluoresce upon excitation or be ultra-violet (UV) active. Moreover, upon interaction of the ligands with target-analytes, a detectable optical response such as a change in emission properties (emission intensity or emission wavelength) or colorimetric change (absorbance wavelength) renders these materials attractive for chemosensing with fluorescence and/or UV-Vis detection.^{7,8}

Porphyrins are excellent metal ion chelators and are therefore an ideal scaffold to incorporate into MOF ligands for metal ion sensing.⁹⁻¹¹ Porphyrins are rigid, stable highly conjugated square-planar organic class of compounds that are prevalent in nature capable of complexing metals by way of 4-center facing nitrogens. Hemoglobin for instance, is a biological transporter of oxygen, containing an iron metallated porphyrin moiety. Another example is chlorophyll, having a key porphyrin motif metallated with magnesium. Porphyrins may also be easily diversified to tune the electronics of the material by using pre-functionalized pyrroles and aldehydes during synthesis. Incorporating such moieties into the ligands of MOFs produces materials likely capable of metal ion sensing.

The compound tetrakis(4-carboxyphenyl)porphine (TCPP) has been well characterized and is commercially available as a chelating reagent for the selective trace heavy metal detection for Pb^{2+} , Ni^{2+} , Cu^{2+} , Cd^{2+} , and Mn^{2+} , determinable with high performance liquid chromatography (HPLC).¹² Complexation occurs in 20 min at room temperature. One hypothesis for achieving efficient divalent metal ion detection is thus to incorporate a porphyrin into the ligand of a MOF. Increased surface area within MOFs concentrates analytes to the surface (ligands) of the MOF and often result in enhanced reactivity with little solvent necessary, a result that is not feasible with the corresponding individual homogeneous components.¹³⁻¹⁵ This would ultimately lead to faster reactions times and subsequent ion detection. In addition, the interconnected structure of MOFs may lead to enhanced detection signal yielding a highly sensitive material. The ability for the porphyrin to undergo optical changes (fluorescence and/or UV-Vis) is also advantageous for sensing, as these techniques are highly sensitive (ppb). Thus, the present study was performed to develop and apply a metal ion sensing water-stable MOF material that can remove metal ions from water via complexation within the center of a porphyrin-based ligand. This study also reveals

challenges associated with porphyrin-based MOF syntheses and outlines future directions for these versatile materials.

5.3 Experimental

5.3.1 Materials and Methods.

Syntheses sensitive to air and moisture were performed using standard Schlenk techniques under an atmosphere of inert nitrogen or argon. Anhydrous dimethylformamide (DMF), and anhydrous methanol (MeOH) were purchased through Sigma Aldrich. When tetrakis(4-carboxyphenyl)porphine (TCPP) was purchased it was obtained via TCI. Additional solvents and reagents were obtained from TCI, Aldrich, and Alfa Aesar, and used without further purification. The synthesis of the MOF herein is previously described in the literature. A Millipore purification system set at 18 M Ω was used for all experiments requiring water (synthesis, fluorescence).

5.3.2 Characterization.

All NMR experiments were performed using an Agilent (Varian) 400MR equipped with automated tuning and a 7600 sample changer at room temperature. All NMR spectra were analyzed using MestReNova NMR software. Mass spectra was acquired using an Agilent 6224 Accurate Mass TOF LC/MS with electrospray and multi-mode (ESI/APCI) sources in negative or positive ion mode by direct injection in methanol. Powder X-Ray diffraction (PXRD) patterns were obtained using a Bruker D8 Discover DaVinci Powder X-ray Diffractometer with CuK α radiation operated at 40 kV and 40 mA. A 0.6 mm divergent slit was placed on the primary beam side and a high-resolution energy-dispersive LYNXEYE-XE-T detector on the diffracted beam side during the XRD studies. The instrument alignment was tested using the NIST 1976b SRM. A typical scan

rate was 0.2 sec/step with a step size of 0.02 deg. Infrared (IR) data was acquired on a Nicolet 6700 FTIR spectrometer. SEM imaging was performed using a JEOL JSM-6500F microscope prior to and after water exposure. An accelerating voltage of 15.0 kV and a working distance of 10.0 mm were used. Fluorescence measurements were obtained on a Horiba Jobin-Yvon FluoroLog-3 Spectrofluorometer.

5.3.3 Synthesis of tetrakis(4-carboxyphenyl)porphine (TCPP).

Multiple attempts to synthesize the ligand were made. The ligand was synthesized either by method (A) or (B). In method (A) 4-formylbenzoic acid (1.5 g, 10 mmol) was dissolved in 50 mL propionic acid. After heating to 80 °C, pyrrole (0.7 mL, 10 mmol) was added dropwise. The mixture refluxed for 2 h, cooled to rt, and placed in a 0 °C freezer for 12 h. The resultant precipitate was isolated by filtration and rinsed with DCM. In method (B) methyl 4-formylbenzoate (5g, 30.45 mmol) was dissolved in 30 mL propionic acid. The flask was kept dark and out of light until workup. The solution was heated to 50 °C and pyrrole (2.11 mL, 30.45 mmol) added dropwise. The reaction flask was refluxed for 12 h at 80 °C, after which time the reaction mixture was slowly cooled to rt and placed in a refrigerator at 5 °C for 3 h. The resultant precipitate was collected by filtration and washed with 30 mL propionic acid and 50 mL cold water. The product contained impurities and was further purified by recrystallization using trituration with DCM and MeOH yielding a purple solid of esterified TCPP (TCPPOMe). The esters were hydrolyzed to yield the desired TCPP ligand. 2 g of KOH was added dissolved in 10 mL water. TCPPOMe was dissolved in 1:1 MeOH/THF (20 mL total). The solutions were combined in a 100 mL round bottom flask and refluxed at 80 °C for 12 h. Upon cooling to rt, the pH was adjusted to 4 with 1.0 M HCl and

the liberated TCPP solid precipitate was collected by filtration. To purify, the solid was dissolved in THF, precipitated with hexanes, and isolated by filtration.

5.3.4 Synthesis of MOF NU-902.

The MOF was synthesized with minor variations to a published literature procedure.¹⁶ In brief, zirconyl-chloride octahydrate (25 mg, 0.075 mmol) was added to a 22 mL glass vial followed by (675 mg, 5.50 mmol). 12 mL of DMF was added and the sealed mixture was sonicated for 10 minutes and placed in a preheated 80 °C oven for 1.5 h. The mixture cooled to rt over 1.5 h and TCPP added. The vial was sealed and sonicated to 10 min prior to adding to a preheated oil bath at 95 °C. After 20 h the reaction mixture was allowed to slowly cool to rt. The MOF NU-902 began precipitating out of solution after several hours of heating. Once at rt, the heterogeneous mixture was transferred to a large test tube, centrifuged and the solution carefully decanted. The solid was then rinsed 3 times each with 10 mL DMF by a process of adding solvent, vortex mixing for 30 s, centrifuging for 10 min, followed by decanting the solvent. 10 mL of DMF was added for 24 h, and the MOF rinsed for 2 more days. Then, the MOF was rinsed 3 more times with acetone. The acetone was also added for 24 h before a final decant. The MOF was then dried to open atmosphere and heated at 100 °C for 12 h to remove residual solvent.

5.4 Results and Discussion

Multiple attempts to synthesize porphyrin-based MOFs were performed, yielding a wide array of unexpected results. Initial efforts were directed at synthesizing two alternative zirconium-containing porphyrin-based MOFs to NU-902, MOF-525 and PCN-222 (Figure 5.1). However,

after many attempts (varying reaction vessel, modifier, modifier concentration, temperature, time, and sonication intervals) no successful reproducible MOF was synthesized in-house.

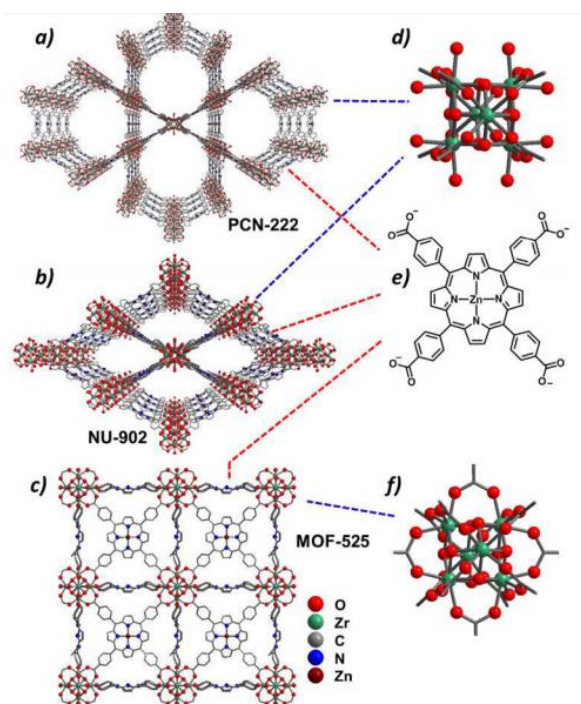


Figure 5.1. MOFs (a) PCN-222, (b) NU-902, and (c) MOF-525. Corresponding Zr₆-oxo nodes (d, f) and the linker (e) carboxylate form of Zn-TCPP are presented on the right. NU-902 was used in the present study for metal ion detection at the position occupied by Zn in this drawing. Adapted with permission from Deria, P.; Gómez-Gualdrón, D. A.; Hod, I.; Snurr, Randall Q.; Hupp, J. T.; and Farha, O. K. *J. Am. Chem. Soc.* **2016**, *138*, (43) 14449-14457. Copyright 2016 American Chemical Society.

In response, the purity of the MOF ligand was reexamined, hence the reported 2 methods of ligand synthesis herein to rule out the possibility of ligand impurities, yielding inconsistent syntheses of the MOF. The impact of the ligand purity was further ruled unlikely, as the purchased pure ligand also did not yield reproducible crystalline MOF. Conversely, the synthesis of NU-902 was highly reproducible (>10 times) yielding a dark purple crystalline MOF (>70 mg each). Accordingly, NU-902 was used for the future development of a photoluminescent responsive porphyrin-based MOF metal ion chemosensor.

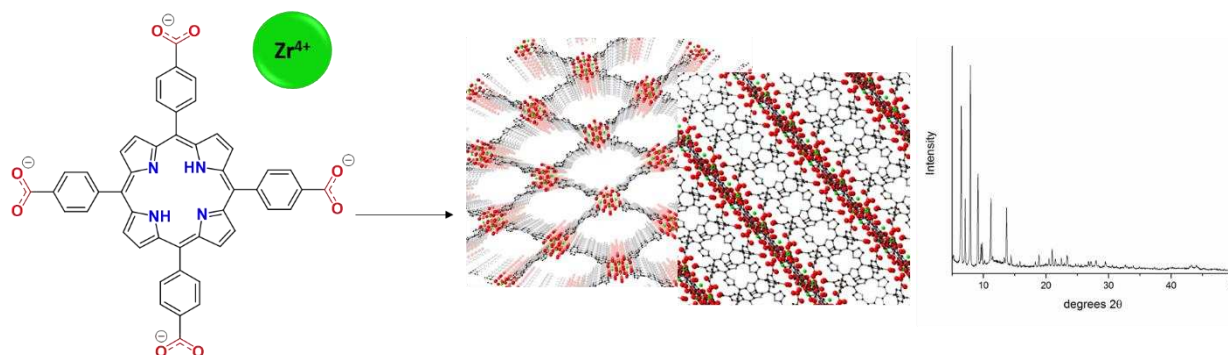


Figure 5.2. MOFs NU-902 synthesis and PXRD characterization.

NU-902 is a thermodynamically stable zirconium (IV) – carboxylate coordination bonds. The material has high surface area ($1580 \text{ m}^2\text{g}^{-1}$) and importantly is stable to water.¹⁷ Additional preliminary studies reveal the MOF is fluorescent.¹⁶ As such, NU-902 warrants further investigation for the optical detection of divalent metal ions. Towards this the photoluminescent (PL) properties of the MOF were investigated. Excitingly, in this study the MOF was found to exhibit fluorescence emission in multiple solvents when excited by a UV-lamp (365 nm), including environmentally relevant solvent water. The fluorescence is also detectable by eye, displaying an emitted bright pink color. The material displays an emission peak at X nm when excited at X nm. Preliminary data from the present study suggests that the material is indeed responsive to the presence of Cd^{2+} displaying fluorescence quenching.

5.5 Conclusions and Future Directions

In summary, water-stable porphyrin-based MOF NU-902 was synthesized for the detection of metal ions in aqueous environments. The MOF is water-stable and shows promise for detecting divalent metal ions. The next step currently underway is to perform a full and reproducible fluorescence study to assess the efficacy of the MOF for metal ion sensing. In order to use the

material in real-world applications (in-field detection) a necessary first step is to develop a useful solid support form of the material. One route is to synthetically modify and grow a MOF on the surface (SURMOF) of a material such as cotton, aluminum, or silicon. Alternatively, MOF-polymer blended composites are promising materials for such applications. FeBTC-polydopamine for instance, shows recent precedence for the utility of MOF-polymer composites to selectively and efficiently remove heavy metals from water.¹⁸ Unique to the proposed study herein, is that the porphyrin-based NU-902 MOF is potentially capable of not only removing metals (to be determined by ICP-OES), but also detecting them via changes in optical properties (fluorescence or UV-Vis). Initial studies are ongoing whereby the MOF has been blended in polyvinylchloride (a non-fluorescing polymer) for metal ion detection and removal studies. Future outcomes from this study include efforts to optimize metal ion detection, which may require tuning of the MOFs electronics, achievable by modifying the porphyrin backbone. Alternatively, this may include investigating other solid support platforms for MOFs as well as developing other MOF-polymer blends to tune the uptake kinetics of the material and overall increase the rate of ion accessibility to the blended MOF.

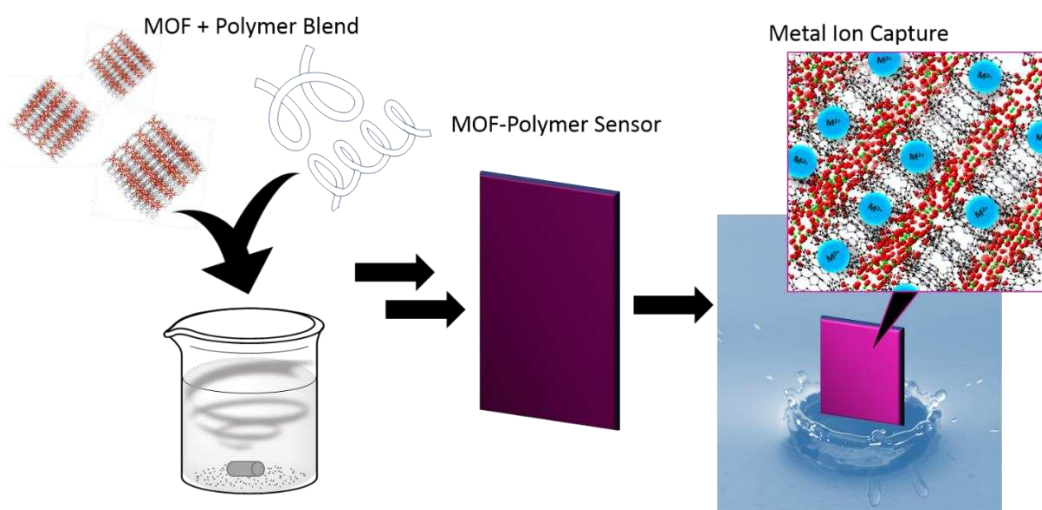


Figure 5.3. MOFs NU-902 PVC polymer blended composites for the removal and fluorescence sensing of divalent metal ions.

REFERENCES

1. Tchounwou, P. B.; Yedjou, C. G.; Patlolla, A. K.; Sutton, D. J. *EXS* **2012**, *101*, 133.
2. Samantara, M. K.; Padhi, R. K.; Sowmya, M.; Kumaran, P.; Satpathy, K. K. *Groundwater for Sustainable Development* **2017**, *5*, 49.
3. Jaishankar, M.; Tseten, T.; Anbalagan, N.; Mathew, B. B.; Beeregowda, K. N. *Interdisciplinary Toxicology* **2014**, *7*, 60.
4. Jayaswal, K.; Sahu, V.; Gurjar, B. R. In *Water Remediation*; Bhattacharya, S., Gupta, A. B., Gupta, A., Pandey, A., Eds.; Springer-Verlag Singapore Pte Ltd: Singapore, 2018, p 11.
5. Fang, X.; Zong, B.; Mao, S. *Nano-Micro Letters* **2018**, *10*, 64.
6. Kreno, L. E.; Leong, K.; Farha, O. K.; Allendorf, M.; Van Duyne, R. P.; Hupp, J. T. *Chemical Reviews* **2012**, *112*, 1105.
7. Lustig, W. P.; Mukherjee, S.; Rudd, N. D.; Desai, A. V.; Li, J.; Ghosh, S. K. *Chemical Society Reviews* **2017**, *46*, 3242.
8. Zhao, D.; Cui, Y.; Yang, Y.; Qian, G. *CrystEngComm* **2016**, *18*, 3746.
9. Yang, J.; Wang, Z.; Hu, K.; Li, Y.; Feng, J.; Shi, J.; Gu, J. *ACS Applied Materials & Interfaces* **2015**, *7*, 11956.
10. Bozkurt, S. S.; Cavdar, I. K.; Kurtbay, H. M.; Merdivan, M. *Journal of Liquid Chromatography & Related Technologies* **2010**, *33*, 748.
11. Burnham, B. F.; Zuckerman, J. J. *Journal of the American Chemical Society* **1970**, *92*, 1547.

12. Kilian, K.; Pyrzynska, K. *Tetrakis(p-carboxylphenyl)porphyrin as a complexing agent for solid phase extraction of metal ions*, 2002; Vol. 47.
13. Dhakshinamoorthy, A.; Asiri, A. M.; Alvaro, M.; Garcia, H. *Green Chemistry* **2018**, *20*, 86.
14. McKellar, S. C.; Graham, A. J.; Allan, D. R.; Mohideen, M. I. H.; Morris, R. E.; Moggach, S. A. *Nanoscale* **2014**, *6*, 4163.
15. Hintz, H.; Wuttke, S. *Chemistry of Materials* **2014**, *26*, 6722.
16. Deria, P.; Yu, J.; Balaraman, R. P.; Mashni, J.; White, S. N. *Chemical Communications* **2016**, *52*, 13031.
17. Deria, P.; Gómez-Gualdrón, D. A.; Hod, I.; Snurr, R. Q.; Hupp, J. T.; Farha, O. K. *Journal of the American Chemical Society* **2016**, *138*, 14449.
18. Sun, D. T.; Peng, L.; Reeder, W. S.; Moosavi, S. M.; Tiana, D.; Britt, D. K.; Oveisi, E.; Queen, W. L. *ACS Central Science* **2018**, *4*, 349.

CHAPTER 6

¹H NMR WITH SOLVENT SUPPRESSION TO DETERMINE STOICHIOMETRY, KINETICS, AND MECHANISM OF Cu²⁺ VS. WATER-STABLE METAL–ORGANIC FRAMEWORK (CuBTTri) HETEROGENOUS CATALYSIS IN WATER⁵

6.1 Summary

Metal-organic frameworks (MOFs) have emerged in recent years as versatile heterogeneous catalysts. However, few mechanistic studies with MOFs exist. A lack of fundamental mechanistic studies to fully understand how small molecules interact with MOFs is in part due to limited methods to analyze these complex systems. Moreover, having appropriate methods to study and elucidate the mechanism of catalysis with MOFs and small molecules would yield powerful intel towards the design of future, improved-by-design MOF catalysts. Herein, we report the first of the necessary experimental studies towards understanding these reaction mechanisms. A ¹H NMR spectroscopy method with solvent suppression was optimized and allows for the simultaneous quantification of multiple reaction components in water, which

⁵ This dissertation chapter was adapted from Tuttle, R. R.; Rubin, H. N.; Rithner, C. D.; Finke, R. G.; Reynolds, M. M. Direct ¹H NMR Monitoring of Copper Ion and Metal–Organic Framework Catalyzed Decomposition of Bioavailable *S*-Nitrosoglutathione in Water: The Balanced Reaction Stoichiometry and Variable Thiol Dependence *Currently in submission* **2018**. This work was supported by the National Science Foundation Division of Biomaterials (DMR-1352201) and Colorado State University for funding. Author Robert Tuttle contributed significantly to the mechanistic details of the findings and contributed to running chemical reactions, NMRs, and writing the resultant paper. The great majority of the details herein were discussed, implemented, and presented as combined efforts of Robert Tuttle and Heather Rubin. Author Christopher Rithner's contributions were towards the development and optimization of the NMR method. The authors thank Jim Self and Debbie Weddle in the CSU Soil, Water and Plant Testing Lab for ICP-AES analysis and the Central Instrument Facility at CSU for NMR and other analytical instrumentation access and assistance.

yields the complete, balanced reaction stoichiometry. Copper is known to catalyze the decomposition of bioavailable *S*-nitrosoglutathione (GSNO) to yield nitric oxide (NO) and glutathione disulfide (GSSG), an important biological reaction to achieve vasodilation, antibacterial activity, and other desirable physiological effects. This has first led to the strategic use of solvated copper ions, and more recently, copper-based MOFs en route to viable biomedical applications. CuBTri is a copper-containing MOF with thermodynamic stability due to the Cu-triazole coordination. The balanced reaction stoichiometry (a prerequisite for mechanistic development) remains poorly understood for both solvated Cu^{2+} and copper-MOF catalyzed GSNO decomposition, at least prior to the present study. The ^1H NMR method used herein reveals important similarities and differences for solvated Cu^{2+} vs copper-MOF catalyzed GSNO decomposition in water. Specifically, decomposition of two equivalents of GSNO yields a single equivalent of GSSG in both systems. After 16 h solvated Cu^{2+} catalyzes the complete decomposition of GSNO in water, both with *and* without GSH present. Conversely, the copper-MOF only catalyzes complete GSNO decomposition within 16 h if GSH is present as a reducing agent, and merely 10% over 16 h if no GSH is added to the reaction. Retention of [GSH] over the course of the copper-MOF catalyzed reaction indicates that GSH is *catalytic* in the copper-MOF system. The results provide a method to directly monitor both the solvated copper and copper-MOF systems in water in real time, establish the balanced reaction stoichiometry in both systems for the first time, and reveal variable thiol dependence of the two systems. The results yield initial kinetic and mechanistic insights which demonstrate that there is a fundamental difference in the reaction mechanisms of the two systems.

6.2 Introduction

Metal-organic frameworks (MOFs) are porous coordination networks that provide a unique platform for heterogeneous catalysis. The composition of repeating secondary binding units (SBUs) having metal ion or cluster nodes coordinated to bi- or multi-coordinating organic linkers offers near infinite opportunities to tailor the materials for reactivity with small molecules. The unmatched opportunity to tune the physical and chemical properties of the material, high surface area, and structural homogeneity coupled with the unique chemical environments in the pores of MOFs allows for substrate selective,¹ diastereoselective,² and regioselective catalysis.³ The heterogeneous nature of MOFs is advantageous for isolating and recycling the catalyst and provides a straightforward approach to flow catalysis.⁴ As more stable frameworks are realized, the applicability of MOF catalysis is rapidly expanding to include biological applications.⁵ MOFs have been implemented in catalytic biological applications to mimic natural occurring processes. Nevertheless, MOF catalysis is often less efficient than catalysis with homogeneous counterparts. A primary prerequisite to developing more efficient MOF catalysts, is establishing a fundamental understanding of how small molecules interact with MOFs during catalysis.

The intrinsic properties of MOFs introduces a level of complexity when attempting to study the kinetics and mechanism of MOF catalysis. Heterogeneity impedes the ability to isolate and define key reaction intermediates by classical solution-phase techniques like NMR and UV-Vis. Catalysis may occur at the surface of the MOF and/or the pores of the material which may have different rates based on diffusion limitations. Additionally, most frameworks are not stable to water or catalytic conditions. Thus, few studies exist to elucidate mechanistic aspects of MOF catalysis. Stoichiometric, kinetic, and ultimately mechanistic knowledge of MOF-catalyzed

reactions promise to be essential in guiding the directed design of future MOF catalysts with improved selectivity and turn-over.

Herein, we provide an ^1H NMR spectroscopy method with solvent suppression to investigate biologically relevant decomposition of *S*-nitrosoglutathione (GSNO), an endogenous source of nitric oxide (NO) present in human blood, with MOF $\text{H}_3[(\text{Cu}_4\text{Cl})_3\text{-(BTri)}_8]$, $\text{H}_3\text{BTri} = 1,3,5\text{-tris}(1H\text{-}1,2,3\text{-triazol-}5\text{-yl) benzene]$ (CuBTri).^{6,7} This reaction carries great importance in medicine as NO is a vital signaling molecule in the human nervous,^{8,9} immune,^{10,11} and cardiovascular systems^{12,13} as well as an effective antibacterial agent.^{14,15} Kinetic and mechanistic studies of Cu^{2+} and CuBTri catalyzed decomposition of GSNO to yield NO and glutathione disulfide (GSSG) have been reported but not the complete balanced reaction stoichiometry, likely due to difficulties monitoring the reaction directly in water.¹⁶⁻¹⁸ Solvated Cu^{2+} or copper-MOF catalyzed RSNO decomposition was previously monitored by ultraviolet-visible (UV-VIS) spectroscopy or with a nitric oxide analyzer (NOA). UV-VIS spectroscopy only yields RSNO concentration changes,^{19,20} while NOA experiments use a chemiluminescence scheme to quantify the amount of gaseous $\text{NO}\cdot$ generated.²¹ These two techniques provide only the concentration of one chemical species in the complex reaction mixture. Importantly, the NMR method detailed herein allows for the first simultaneous quantification of GSNO, GSSG, and glutathione (GSH) concentrations in water (a biologically relevant solvent), and yields the complete, balanced reaction stoichiometry. Each species is monitored as a function of time, thereby enabling subsequent kinetic studies for reliable reaction mechanism determination. In addition, a comparison between Cu^{2+} and CuBTri is reported as Cu^{2+} is currently the most efficient copper pre-catalyst known for RSNO decomposition. The differences between the two catalysts promises to instruct the design of future MOFs for enhanced catalytic activity towards

RSNO decomposition. This study ultimately represents a model for fundamental studies of MOF-catalyzed reactions in other highly complex, biologically relevant systems and aqueous environments.

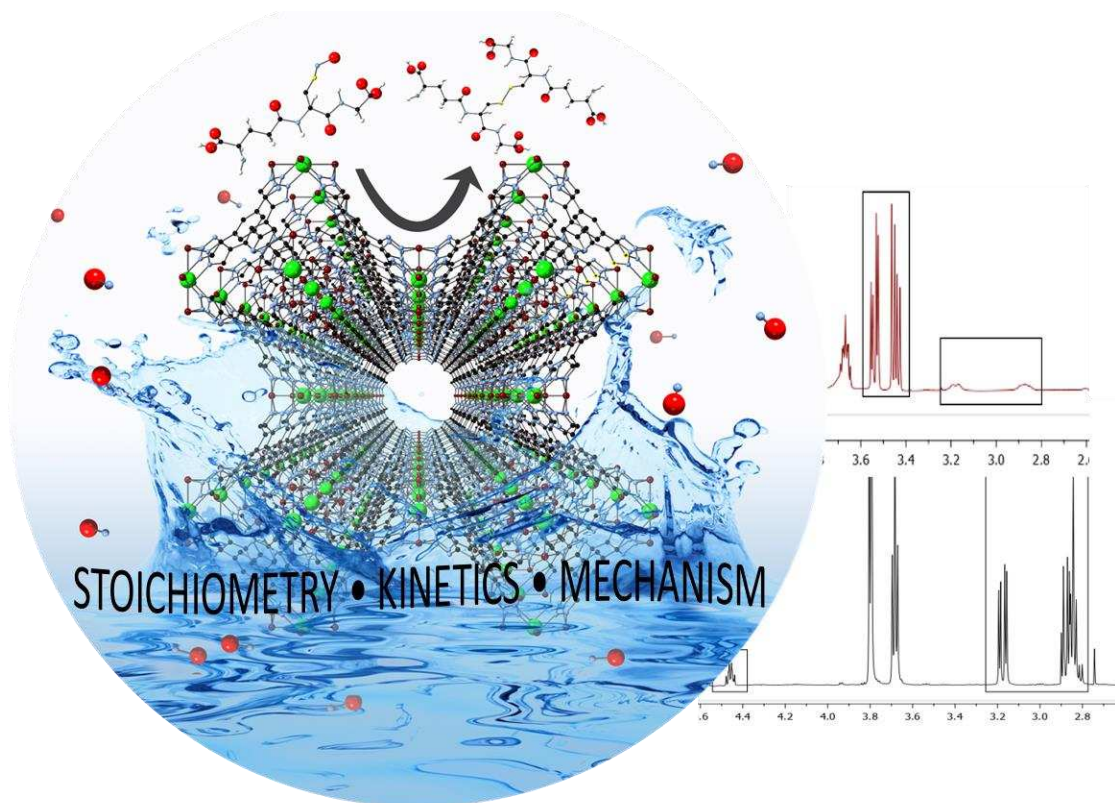


Figure 6.1. Summary image of chapter 6, whereby CuBTri and Cu^{2+} were studied using ^1H NMR to understand similarities and mechanism between MOFs and free ions. This study used the biologically relevant solvent water, to report the full reaction stoichiometry for biomedically relevant catalytic release of nitric oxide (NO) from *S*-nitrosoglutathione (GSNO).

6.3 Experimental

6.3.1 Reagents.

Diethylamine (99%), trimethylsilylacetylene (98%), trimethylsilylazide (94%), and 1,3,5-tribromobenzene (98%) were purchased from Alfa Aesar (Ward Hill, MA, USA). Glutathione (98%) was purchased from VWR (Radnor, PA, USA). Sodium nitrite (99.5%), oxidized glutathione (98%), copper (I) iodide (99.5%), bis(triphenylphosphine)palladium(II) dichloride

(99%), and dichloromethane (99%) were purchased from Sigma-Aldrich (St. Louis, MO, USA). HCl (1N), methanol (99%), and sodium hydroxide (98.9%) were purchased from Fisher Scientific (Hampton, NH, USA). Dimethylformamide (99%) and copper (II) chloride dihydrate (99%) were purchased from EMD Chemicals (Gibbstown, NJ, USA). Ultrahigh purity nitrogen gas was supplied by Airgas (Denver, CO, USA). Deionized water (18.2 M Ω ·cm) was obtained from a Millipore Direct-Q water purification system (EMD Millipore, Billerica, MA, USA). All materials were used as received without any further purification.

6.3.2 Water Suppression ¹H NMR Method.

All NMR experiments were performed using an Agilent Inova 500 equipped with a 5mm pulsed-field-gradient HCN probe. Samples were prepared in septa-capped Wilmad 528-PP 500 MHz tubes under inert atmosphere (N₂). For this, 0.5 mL of reaction supernatant was added into an NMR tube containing 0.1 mL of 20 mM NaH₂PO₄ buffered D₂O and mixed by hand, followed by 2 s of sonication to remove any air bubbles. Samples were kept dark, air-free, and analyzed as soon as possible. NMR experiments were run using PRESAT with PURGE solvent signal suppression available in VnmrJ version-4.2.²² The system was buffered with NaH₂PO₄ to a pH of 4 due to the sensitivity of the compounds of interest (GSNO, GSH, GSSG) to the pH of the solvent. 512 transients were acquired for all samples, which took 35 minutes to complete. A 2 s square presat with a bandwidth of 100 Hz on resonance at 4.67 ppm (water) was used, followed by the PURGE crusher sequence and a pi/2 excitation pulse of 5.7 μ s. Acquisition time was 2 s, so with the PRESAT delay the total time between transients was about 4 s.

6.3.3 Syntheses.

Syntheses were carried out by Robert Tuttle of GSNO, H₃BTTri ligand, and MOF H₃[(Cu₄Cl)₃(BTTri)₈(DMF)₁₂] \cdot 72H₂O (CuBTTri) following previously established literature procedures.²³

6.3.4 Reaction Setup.

GSNO and GSH solutions were prepared from millipore H₂O and solid GSNO or GSH powder under inert conditions (N₂) in a 200 mL round bottom flask. CuBTTri was weighed into a multi neck 100 mL round bottom flask and oven dried overnight at 110 °C. Following drying, the flask containing CuBTTri was placed under vacuum for 1 h on a Schlenk line and backfilled with N₂ (g) prior to reaction. GSNO and GSH solutions were then injected into the reaction flasks containing dry CuBTTri. Vigorous bubbling in the solution was established. Reaction flasks were wrapped in aluminum foil to prevent exposure to light and reactions proceeded for a predetermined time. To quench the reaction once the reaction time had been reached, the exit needle was removed to stop bubbling and the supernatant was carefully decanted via a syringe, leaving the MOF particles in the flask. The quenched reaction solution was then kept cool and dark in a Cu-free glass vial under inert atmosphere (N₂) or added directly to an NMR tube. The ¹H-NMR sample was prepared in a septa capped sample tube under inert atmosphere (N₂) by injecting 0.5 mL of reaction supernatant into the NMR tube along with 0.1 mL of 20 mM NaH₂PO₄ buffered D₂O. An identical procedure as described was carried out for the reaction between GSNO and CuCl₂. No major or unanticipated safety hazards were encountered over the course of all experiments.

6.4 Results and Discussion

6.4.1 Ex-Situ ^1H NMR Reaction Monitoring.

Each individual reaction component, GSNO, GSH, and GSSG, all contain distinguishable signals, despite structural similarities, in 20 mM NaH_2PO_4 buffered 90% H_2O 10% D_2O (Figure 1). GSSG displays two doublets of doublets at 3.15 – 3.19 ppm and 2.84 – 2.89 ppm identified as the protons on the carbon adjacent to the sulfur groups. GSH displays a multiplet at 4.40 – 4.48 ppm associated with the C-H two carbons away from the sulfur group and a multiplet at 2.80 – 2.88 ppm attributed to the protons adjacent to the sulfur group. The two protons on the carbon adjacent to the sulfur group in GSNO are present as two distinctly broad peaks occurring at 4.03 – 4.00 ppm and 3.89 – 3.85 ppm. All individual peaks that were used for determining the concentration of reaction components are identified with boxes in Figure 6.2.

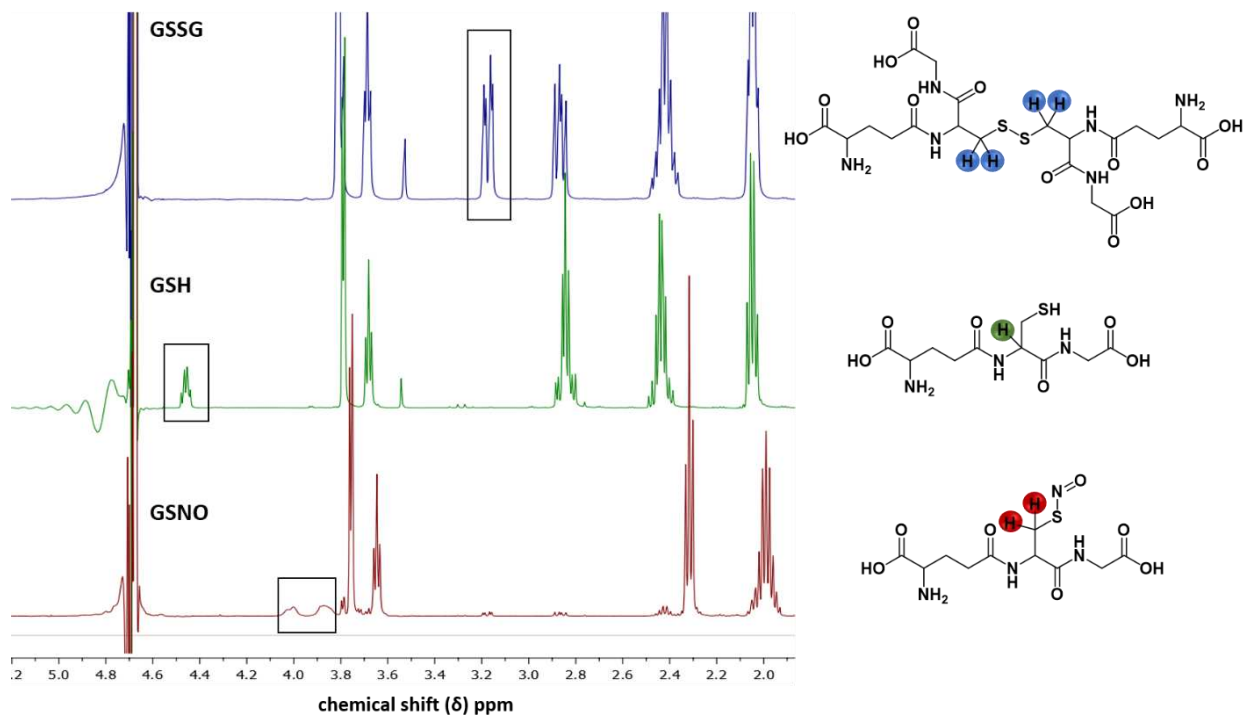


Figure 6.2: Structures and diagnostic peaks used for ^1H -NMR analysis of GSH (green), GSNO (red), and GSSG (blue) in 0.5 mL H_2O and 0.1 mL 20 mM NaH_2PO_4 buffered D_2O .

Initial attempts to determine reaction species concentration used benzene as an internal quantitative standard, but the significant difference in longitudinal relaxation time, T_1 , among various reaction components and benzene protons afforded a large error under the conditions necessary for data acquisition. In response, efforts were directed to quantify the individual reaction components in solution directly by developing an absolute calibration curve based on known concentrations of authentic GSNO, GSH, and GSSG. The intensity of the signals used to quantify GSH and GSNO were both affected by the solvent suppression method due to their proximity to the water peak. However, the magnitude of this error was stable and consistent from experiment to experiment over a concentration range from 500 μM to 3 mM. To generate the necessary calibration curves, 4 different concentrations were used for each component (500 μM , 1 mM, 2 mM, and 3mM). A calibration curve was constructed whereby the intensity of the highest peak within the boxed regions shown in Figure 6.2 were plotted on the y-axis and concentration plotted on the x-axis (Supporting Information, APPENDIX Figure D4). A linear fit was applied yielding the following where y is signal intensity and x is species concentration:

$$\text{GSNO: } y = 28.4x - 2.05 \quad (1a)$$

$$\text{GSH: } y = 138x - 17.5 \quad (1b)$$

$$\text{GSSG: } y = 368x + 223 \quad (1c)$$

The resultant equations of the linear fits, all having R^2 values greater than 0.99, were used to quantify the amount of each component in all reaction mixtures. Buffering the system with NaH_2PO_4 for NMR analysis was critical to prevent peak broadening and unwanted competing reaction pathways that could arise from minor differences in pH. DMSO was also examined as a possible solvent, but failed as it either stabilized GSNO preventing any decomposition or yielded unwanted oxidization of GSH to GSSG.²⁴ In short, an optimal method has been developed to

quantitatively analyze the heterogeneous reaction of CuBTTri and, separately, Cu^{2+} with GSNO, all in water as both a preferred and optimum solvent.

All free induction decay (FID) spectra were processed using MestraNova® software to examine peak intensities and integration values. Data analysis and calculations were performed using Microsoft Excel®.

The reaction scheme previously proposed²⁵ for copper catalyzed RSNO decomposition by Cu^{2+} or a copper-based MOF is shown in Scheme 6.1, in which one equivalent of RSNO decomposition yields one equivalent of NO.^{26,27} Given a central goal of this study, developing a quantitative method for the simultaneous detection of all aqueous reaction components, it is notable that determination of RSSR concentration in the reaction yields the balanced reaction stoichiometry for the disulfide and the RSNO for the first time.

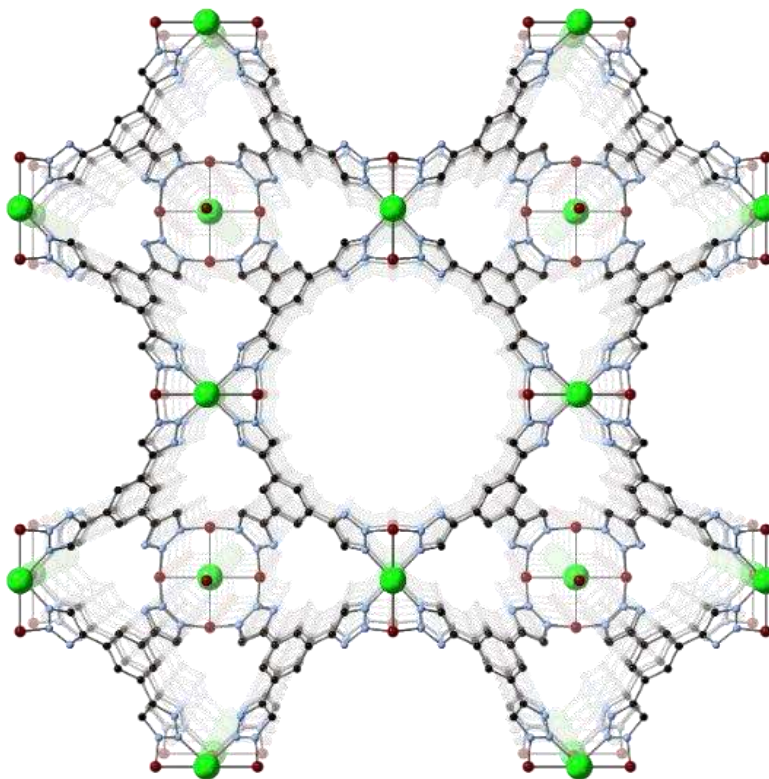
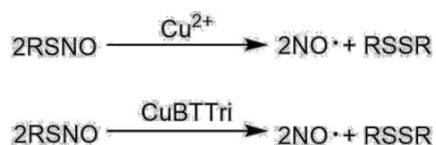


Figure 6.3. Repeating CuBTTri subunit. Shown are carbon (black), nitrogen (blue), chlorine (green), and copper (red).

Scheme 6.1. Previously proposed²⁵ reaction stoichiometry for copper catalyzed decomposition of GSNO.



Reaction systems were designed to maximize biological relevancy. As such, GSNO and water were selected as the substrate and solvent. Choosing a MOF catalyst required careful consideration, as many MOF species are not stable in water or biological media.²⁸⁻³⁰ Towards that end CuBTri, shown in Figure 6.3, was used based on prior evidence that the MOF is stable in both water and biological media.^{27,31} CuBTri contains open copper sites both at the surface and inside its pores to induce GSNO decomposition. Figure 2 shows the open channels formed in the CuBTri repeating subunit which allow for the diffusion of GSNO substrate into MOF pores. The H₃BTri ligand and CuBTri were synthesized by Robert Tuttle following a previously reported procedure.²³

6.4.2 Cu²⁺ Catalyzed GSNO Decomposition.

With a reliable, quantitative ¹H NMR technique to monitor GSNO, GSH, and GSSG concentrations in hand, the Cu²⁺ ion catalyzed decomposition of GSNO was investigated first. Complete decomposition of GSNO (1 mM) was observed upon exposure to both catalytic (0.2 mM) and stoichiometric (1 mM) Cu²⁺ in water under N₂ (g) after 16 h, as shown in Figure 3. The initial concentration of GSNO was chosen based upon the operating window of the NMR spectrometer where the relationship between signal intensity and concentration is linear for GSNO, GSH, and GSSG (0.5 – 3 mM). The only detectable products observed by ¹H NMR from this decomposition are GSSG and a GSSG-Cu²⁺ chelate complex, shown in boxes in Figure 6.4, right

and left respectively. The formation of a chelate complex between the disulfide functional group of GSSG and Cu^{2+} is supported by Noble et al and Kenche et al.^{32,33} Importantly, all ^1H NMR data collected indicates no detectable reaction products other than GSSG or the GSSG- Cu^{2+} chelate complex.

Cu^{2+} catalyzed decomposition in the presence of GSH was investigated as one hypothesis is that Cu^{2+} is reduced to Cu^+ to catalyze GSNO decomposition.³⁴ However, elevated levels of GSH (1:1, $[\text{GSH}]/[\text{Cu}^{2+}]$) in the reaction mixture led to incomplete GSNO decomposition after 16 h (Supporting Information, APPENDIX Figure D9). Elevated levels of GSH may prevent complete GSNO decomposition due to competitive complexation of Cu^{2+} ions by the carboxylate or thiol functional groups of GSH, rendering the ions inactive for GSNO decomposition.^{35,36} The necessity for low levels of GSH to allow for the complete decomposition of GSNO agrees well with previous reports that show a drastic decrease in the rate of RSNO decomposition at increasing levels of RSH.³⁷⁻³⁹ Complete GSNO decomposition only occurred within 16 h at low levels of GSH, as shown in Figure 4 (1:5, $[\text{GSH}]/[\text{Cu}^{2+}]$ or lower).

A low concentration of GSH (0.04 mM) and catalytic concentration of Cu^{2+} (0.2 mM) yields complete decomposition of GSNO (1 mM) in water under N_2 (g) in 16 h (Figure 6.5). The only products detectable by ^1H NMR were GSSG and the GSSG- Cu^{2+} chelate complex. The level of GSH (0.04 mM) required for the reaction to reach completion was below the limits of detection for the instrument. The fact that such a low concentration of GSH is required for the reaction to reach completion led us to two alternative mechanistic hypotheses. First, that GSH may act catalytically during Cu^{2+} catalyzed GSNO decomposition. Second, that GSH may not participate in the reaction at low levels for Cu^{2+} catalyzed GSNO decomposition.

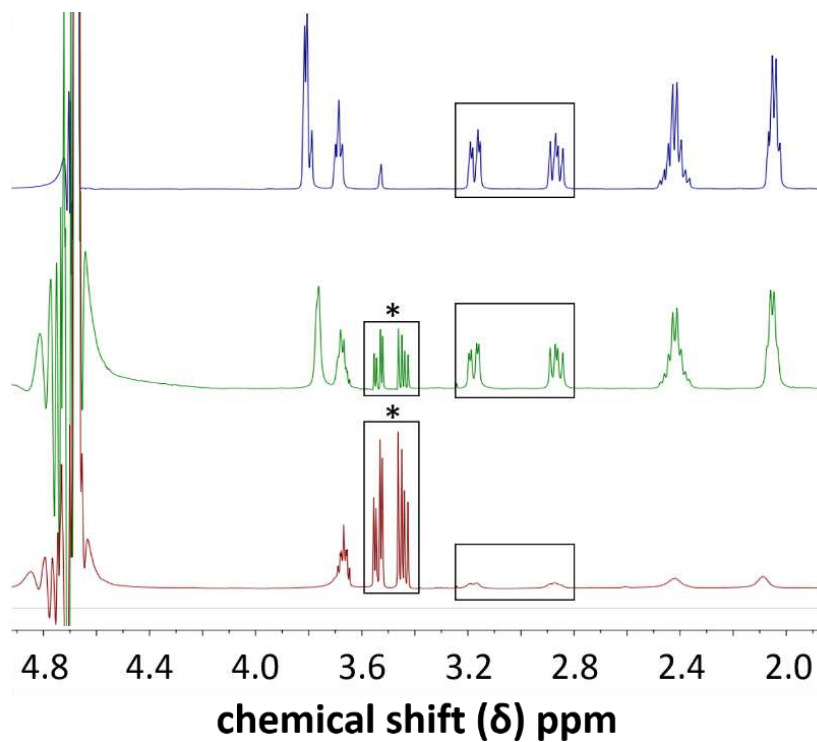


Figure 6.4. Blue: GSSG (2 mM) in H₂O. Decomposition of GSNO (1 mM) with Cu²⁺ (0.2 mM, green), (1 mM, red) in H₂O. *Indicates a GSSG-Cu²⁺ complex.

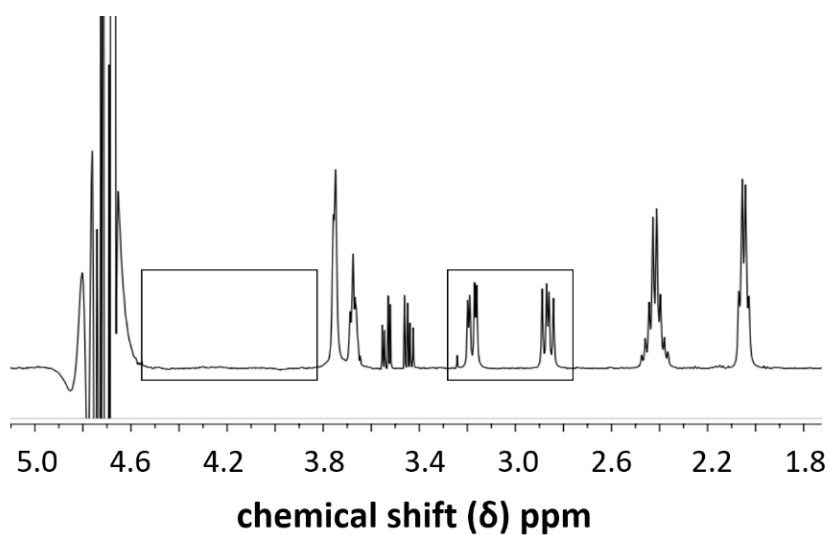


Figure 6.5. Decomposition of GSNO (1 mM) in the presence of Cu²⁺ ions (0.2 mM) and GSH (0.04 mM) in H₂O.

Table 6.1 summarizes the reaction status and GSSG concentration for Cu^{2+} catalyzed reactions with and without GSH after 16 h. Measured concentration values at 16 hours are reported as the average of three trials with standard deviation. As the only observed reaction products were GSSG and the GSSG- Cu^{2+} complex, the total amount of GSSG should equal half the initial amount of GSNO. Indeed, complete decomposition of 1 mM GSNO yielded 0.5 ± 0.1 mM GSSG and 0.4 ± 0.1 mM GSSG with and without GSH, respectively. Control experiments, summarized in Table 1, verified that GSH alone does not induce the observed decomposition of GSNO over 16 h. The data summarized in table 1 suggests that the Cu^{2+} catalyzed reaction yields one equivalent of GSSG per two equivalents of GSNO decomposed.

Table 6.1 Concentration values (expressed in mmol/L) for reactants and products in the Cu^{2+} catalyzed system at 0 h and 16 h.

| Entry | Initial Conditions, T=0h | | | T=16h | | | |
|-------|--------------------------|--------|---------------------|-------|----------------|-----------------|-------------------------|
| | [GSH] _{Added} | [GSNO] | [Cu ²⁺] | [GSH] | [GSNO] | [GSSG] Total | % GSNO Decomposition |
| 1 | 0 | 1.0 | 0.2 | 0 | 0 | 0.5 ± 0.1 | 100 |
| 2 | 0.04 | 1.0 | 0.2 | N/A | 0 | 0.4 ± 0.1 | 100 |
| 3 | 1.0 | 1.0 | 0.2 | 1.0 | 0.75 ± 0.1 | 0.2 ± 0.1 | 25 |
| 4 | 0.04 | 1.0 | 0 | N/A | 1.0 ± 0.01 | 0 ± 0.05 | 0 |

6.4.3 Cu-MOF Catalyzed GSNO Decomposition.

Copper-catalyzed GSNO decomposition in water may change when copper is bound in a solid framework and unable to move freely through solution or exchange ligands as easily as Cu^{2+} . Therefore, GSNO decomposition catalyzed by the *water stable MOF* CuBTTri was studied utilizing the detailed ¹H NMR method. Upon exposure of GSNO (2 mM) to CuBTTri (2:1

GSNO/Cu mol ratio) for 16 h in water under N₂ (g) the reaction did not reach completion, with only approximately 10% GSNO decomposition observed, as shown in Figure 6.6. This decomposition yields an experimental reaction rate of: $9.4 (\pm 3.1) \times 10^{-3} \text{ Mm} \cdot \text{h}^{-1}$.

Importantly, the only product detectable by ¹H NMR from the incomplete decomposition of GSNO is GSSG with no GSSG-Cu²⁺ complex observed for the CuBTTri catalysis. This observation, along with ICP-AES data collected for all CuBTTri catalyzed reactions (which corresponded to a less than 1% loss of the total copper from the MOF) discredit the possibility of GSNO decomposition by Cu²⁺ ions released from the MOF (data not shown). As such, efforts were directed towards understanding the reaction between GSNO and CuBTTri.

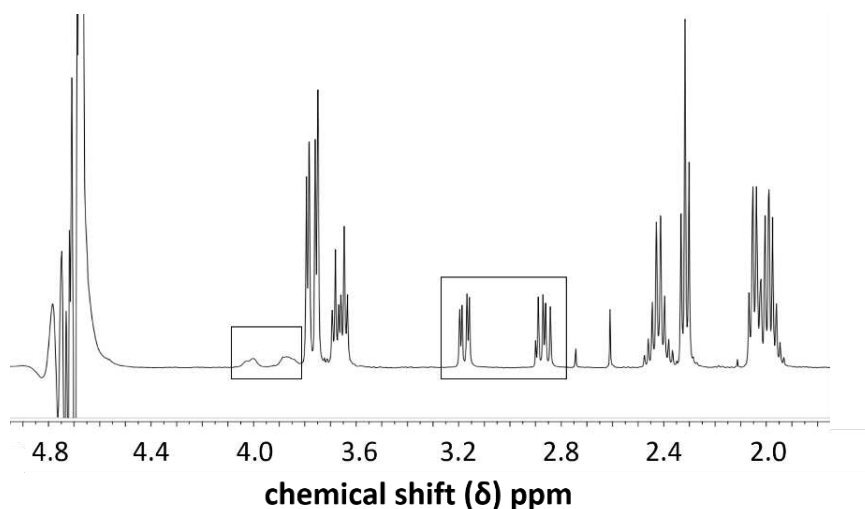


Figure 6.6. Decomposition of GSNO (2 mM) in the presence of CuBTTri in H₂O at a ratio of 2:1 mol GSNO:mol Cu atoms in the MOF sample.

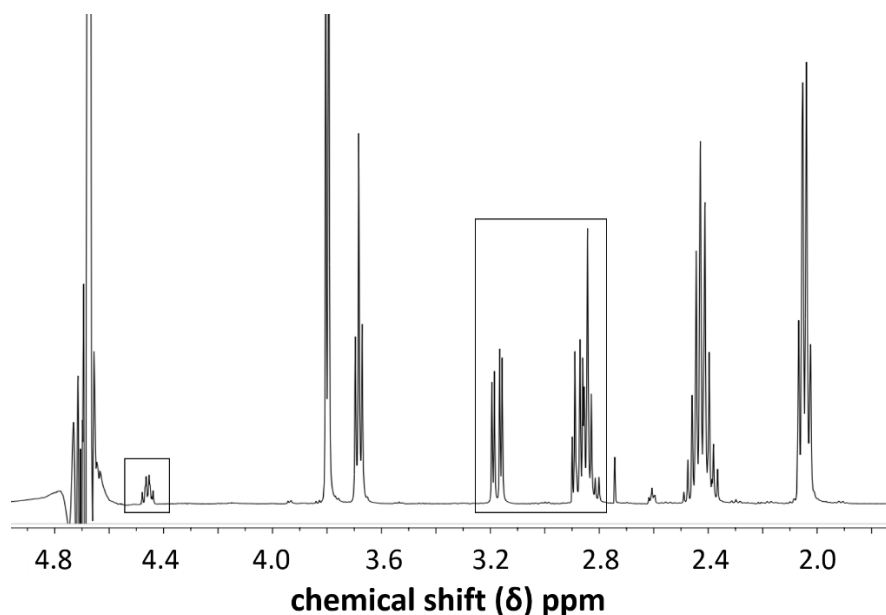


Figure 6.7. Decomposition of GSNO (2 mM) in the presence of GSH (2 mM) and CuBTTri in H₂O with 2:1 mol GSNO:mol Cu in the MOF sample.

Following the observation of incomplete GSNO decomposition efforts were made to drive the reaction to completion. The addition of a reducing agent may accelerate the CuBTTri catalyzed reaction if Cu⁺ is the active solvated ion catalyst for GSNO decomposition. Previous computational studies also suggest that RSH species may reduce Cu²⁺ centers to Cu⁺ in copper-based MOFs to create an active catalyst for RSNO decomposition or multiple GSNO/GSH molecules to adjacent copper centers may yield high free energy barriers to reaction.⁴⁰ Thus, GSH was added to activate the MOF pre-catalyst. GSH was chosen as the reducing agent because the ¹H NMR technique reported here is capable of tracking GSH concentration over time and GSH is a biologically relevant compound (GSNO is formed endogenously via nitrosation of thiyl radicals³⁷) potentially present during the endogenous decomposition of GSNO.^{37,38}

Complete GSNO decomposition was observed upon the introduction of an equivalent of GSH (2 mM) to a reaction mixture containing GSNO (2 mM) and CuBTTri (2:1, GSNO/Cu mol

ratio) in 16 h in H₂O under N₂ (g). Figure 6.7 illustrates that GSSG is the only product detectable by ¹H NMR. GSH may be catalytic in the CuBTTri system as the GSH peak centered on 4.454 ppm is also retained after complete GSNO decomposition. Control experiments to ensure that observed reactivity was not solely a result of GSH were performed with no CuBTTri present, demonstrating little to no reaction between GSNO (2 mM) and GSH (2 mM) over 14 h, further supporting that CuBTTri is the necessary pre-catalyst in the system (Supporting Information, APPENDIX Figure D7).

Table 6.2 summarizes the reaction status and GSSG concentration for CuBTTri catalyzed reactions with and without GSH after 16 h. Measured concentration values at 16 hours are reported as the average of three trials with associated standard deviation. The final observed GSH concentration is slightly decreased from its initial concentration (2 mM to 1.7 mM). However, the loss of GSH observed likely does not lead towards GSSG formation. This would lead to elevated levels of GSSG relative to the decomposition of GSNO, which are not observed. One current hypothesis to explain this small reduction in GSH concentration after 16 h of reaction time is the adsorption of GSH either onto the surface or into the pores of CuBTTri forming a [GSH-CuBTTri] species. This would result in a lower concentration of GSH present in the reaction supernatant, and thus a lower observed concentration of GSH by ¹H NMR. In response, after thoroughly rinsing the used MOF after reaction, ongoing X-ray photoelectron spectroscopy (XPS) is to be performed to further investigate this possible interaction between GSH and CuBTTri. The complete decomposition of 2 mM GSNO catalyzed by CuBTTri in the presence of GSH (2mM) yielded 0.9 ± 0.1 mM GSSG, as summarized in Table 2. This ultimately suggests that the CuBTTri catalyzed reaction yields one equivalent of GSSG per two equivalents of GSNO decomposed with GSH

present. GSH plays a key role in the CuBTri system in accelerating the reaction, hypothetically by chemically reducing copper (II) in the MOF pre-catalyst to copper (I).

Table 6.2. Concentration values (expressed in mmol/L) for reactants and products in the CuBTri catalyzed system at 0 h and 16 h. Reaction completion based on GSNO decomposition.

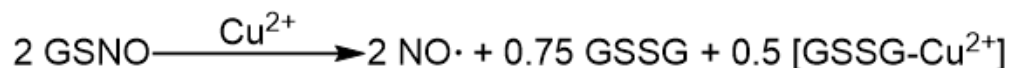
| Entry | Initial Conditions, T=0h | | | T=16h | | | |
|-------|--------------------------|--------|----------|-----------|-----------|-----------|----------------------|
| | [GSH] _{Added} | [GSNO] | CuBTri** | [GSH] | [GSNO] | [GSSG] | % GSNO Decomposition |
| 1 | 0 | 2.0 | 0.015 | 0 | 1.9 ± 0.1 | 0 ± 0.1 | 10 |
| 2 | 2.0 | 2.0 | 0.015 | 1.7 ± 0.1 | 0 | 0.9 ± 0.1 | 100 |

**Value expressed in mmol. Due to the heterogeneous nature of the MOF pre-catalyst the appropriate mass was added to achieve a 2:1 ratio of GSNO molecules to copper atoms present in the MOF sample. This was done to operate under catalytic conditions.

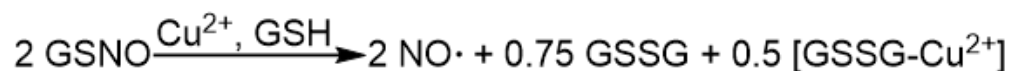
6.4.4 Balanced Reaction Stoichiometry.

The experimentally determined, balanced reaction stoichiometry is summarized in Schemes 6.2 through 6.6. Schemes 6.2 and 6.3 summarize the full stoichiometry for solvated Cu²⁺ catalyzed GSNO decomposition in water with and without GSH, respectively. Scheme 6.4 indicates that the reaction does not proceed to completion without a copper catalyst. Scheme 6.5 presents the stoichiometry for CuBTri catalyzed GSNO decomposition without added GSH. Scheme 6.6 summarizes the complete reaction stoichiometry when CuBTri catalyzes the decomposition of GSNO in the presence of stoichiometric GSH.

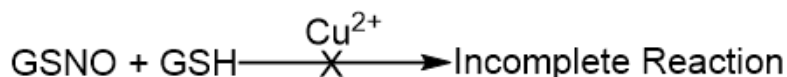
Scheme 6.2. Balanced reaction stoichiometry for Cu²⁺ (0.2 mM) catalyzed GSNO (1 mM) decomposition without added GSH.



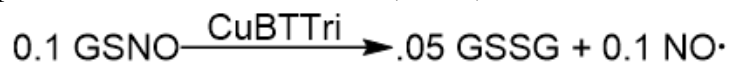
Scheme 6.3. Balanced reaction stoichiometry for Cu²⁺ (0.2 mM) catalyzed GSNO (1 mM) decomposition with added sub stoichiometric GSH (0.04 mM).



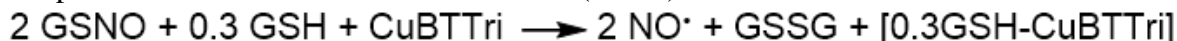
Scheme 6.4. Incomplete reaction between Cu²⁺ (0.2 mM) and GSNO (1 mM) with added stoichiometric GSH (1 mM).



Scheme 6.5. Incomplete reaction between GSNO (2 mM) and CuBTTri without added GSH.



Scheme 6.6. Balanced reaction stoichiometry for CuBTTri catalyzed GSNO (2 mM) decomposition with added stoichiometric GSH (2 mM).



The full and balanced reactions reported here improve upon the stoichiometry initially hypothesized for both systems, described in Scheme 6.1. Importantly, the full range and quantitative distribution of products were determined. The complete stoichiometry has been achieved in the Cu²⁺ system via quantification of the two main products, GSSG and a GSSG-Cu²⁺ chelate complex (this was achieved via ¹H NMR peak integration comparisons). Additionally, Scheme 2 again highlights the important result that the Cu²⁺ system does not require the presence of GSH to reach completion. This is in contrast to the CuBTTri system, which only reaches completion upon the introduction of GSH (Scheme 4). The product distribution of this system is

slightly more complex due to the previously hypothesized adsorption of GSH onto the CuBTTri. The 15% decrease in GSH concentration in the reaction supernatant over the course of the reaction did not result in elevated levels of GSSG, and as such the observation was ascribed to the formation of a [GSH-CuBTTri] species. This is indicated in Scheme 4 with 15% of the initial GSH bound in the [GSH-CuBTTri] species, with the remaining 85% free in the reaction supernatant. Scheme 4 shows the sum of two separate reactions, one major reaction where the CuBTTri and GSH act catalytically towards GSNO decomposition, and a second minor one where the GSH interacts with CuBTTri to form the [GSH-CuBTTri] species.

6.5 Conclusions

This work demonstrates that ^1H NMR with solvent suppression is a viable technique to track copper catalyzed GSNO decomposition in biologically relevant media, such as water. Additionally, our ^1H NMR method is preferred as it allows GSNO, GSH, and GSSG to be directly monitored by differentiable ^1H NMR signals in water. The use of an absolute calibration curve for each molecule allows for quantitative determination of each compound's concentration. The ability to track the concentration of each reaction component (other than NO (g)) in both systems allowed for identification of all reaction products and experimental determination of the complete and balanced reaction stoichiometry for the first time. These findings show that the previously proposed general reaction stoichiometry (Scheme 6.1) for copper catalyzed GSNO decomposition (by ions or a MOF catalyst) is ultimately inaccurate and over simplified. In the case of the copper ion catalyzed system, some portion of the GSSG product forms a GSSG-Cu^{2+} complex, with the relative ratio between the two dependent on the amount of Cu^{2+} present. In the CuBTTri system there is an interaction between GSH and CuBTTri, leading to the formation of a [GSH-CuBTTri]

species. One total equivalent of GSSG forms per two equivalents of GSNO decomposed in both systems, as experimentally verified herein for the first time. In all reactions that reached completion, the only products detectable by ^1H NMR in water are GSSG or a GSSG- Cu^{2+} chelate complex (the latter for copper-ion catalyzed systems only). Therefore, by the law of conservation of mass-energy, the total amount of GSSG formed cannot exceed one half of the GSNO decomposed, further supporting the reported reaction stoichiometry.

Copper ion and CuBTTri catalyzed systems show key differences in response towards the addition of GSH. Sub stoichiometric levels of GSH are sufficient for the complete decomposition of GSNO by copper ions (Table 1, entries 1 and 2), but not for CuBTTri (Table 2, entry 1). Complete decomposition of GSNO by CuBTTri was observed upon the introduction of a stoichiometric equivalent of GSH (Table 2, entry 2), while the introduction of stoichiometric GSH to the copper ion catalyzed system prevents reaction completion (Table 1, entry 3). Taken together, these observations support our hypothesis that the copper-ion and CuBTTri catalyzed reactions *must be operating through different mechanistic pathways*.

With an appropriate ^1H NMR methodology in hand, future kinetic and mechanistic studies of copper catalyzed GSNO decomposition become possible. The complete and balanced reaction stoichiometry is necessary initial mechanistic knowledge, as it allows for proposal of all possible reaction mechanisms in which the proposed steps sum to the experimentally determined reaction stoichiometries. Disproof-based studies utilizing kinetics and other experiments can now be used to determine the most likely, experimentally supported reaction mechanism for both copper ion and CuBTTri catalyzed GSNO decomposition in water. Accounting for the apparent variable thiol dependence of the two reactions promises to yield important mechanistic insight into the identity of the active catalyst in the CuBTTri system. Future studies aim to determine the exact amount of

GSH necessary to activate the CuBTTri for catalysis. Combining study of the homogeneous copper-ion pre-catalyst with the CuBTTri pre-catalyst promises to allow for the incorporation of findings related to their mechanisms into future MOF design to precisely tune activity towards GSNO decomposition. Future application of the ^1H NMR method detailed here for the same or other catalytic systems in physiological conditions/environments, such as blood, promise to prove necessary for understanding the reactivity in such biomedical systems. The feasibility of the techniques reported herein in water supports the viability of future fundamental mechanistic studies of the same or similar catalytic systems in blood, vital for biological applications of MOF catalysis. Thus, ultimately expanding the basic understanding of heterogeneous catalysis with MOFs.

REFERENCES

1. Metzger, E. D.; Brozek, C. K.; Comito, R. J.; Dincă, M. *ACS Central Science* **2016**, *2*, 148.
2. Karmakar, A.; Guedes da Silva, M. F. C.; Pombeiro, A. J. L. *Dalton Transactions* **2014**, *43*, 7795.
3. Beyzavi, M. H.; Stephenson, C. J.; Liu, Y.; Karagiari, O.; Hupp, J. T.; Farha, O. K. *Frontiers in Energy Research* **2015**, *2*.
4. Chen, X.; Jiang, H.; Hou, B.; Gong, W.; Liu, Y.; Cui, Y. *Journal of the American Chemical Society* **2017**, *139*, 13476.
5. Gu, Z.-Y.; Park, J.; Raiff, A.; Wei, Z.; Zhou, H.-C. *ChemCatChem* **2014**, *6*, 67.
6. Tsikas, D.; Schmidt, M.; Böhmer, A.; Zoerner, A. A.; Gutzki, F.-M.; Jordan, J. *Journal of Chromatography B* **2013**, *927*, 147.
7. Tsikas, D.; Hanff, E. In *Nitric Oxide: Methods and Protocols*; Mengel, A., Lindermayr, C., Eds.; Springer New York: New York, NY, 2018, p 113.
8. Williams, D. R.; Lee, M.-R.; Song, Y.-A.; Ko, S.-K.; Kim, G.-H.; Shin, I. *Journal of the American Chemical Society* **2007**, *129*, 9258.
9. Knott, A. B.; Bossy-Wetzel, E. *Antioxidants & Redox Signaling* **2009**, *11*, 541.
10. Bogdan, C. *Nature Immunology* **2001**, *2*, 907.
11. Coleman, J. W. *International Immunopharmacology* **2001**, *1*, 1397.
12. Palmer, R. M. J.; Ferrige, A. G.; Moncada, S. *Nature* **1987**, *327*, 524.
13. Marletta, M. A. *Trends in Biochemical Sciences* **1989**, *14*, 488.
14. Carpenter, A. W.; Schoenfisch, M. H. *Chemical Society reviews* **2012**, *41*, 3742.
15. Schairer, D. O.; Chouake, J. S.; Nosanchuk, J. D.; Friedman, A. J. *Virulence* **2012**, *3*, 271.

16. Dicks, A. P.; Swift, H. R.; Williams, D. L. H.; Butler, A. R.; Al-Sa'doni, H. H.; Cox, B. G. *Journal of the Chemical Society, Perkin Transactions 2* **1996**, 481.
17. Smith, J. N.; Dasgupta, T. P. *Nitric Oxide* **2000**, 4, 57.
18. Diers, A. R.; Keszler, A.; Hogg, N. *Biochimica et biophysica acta* **2014**, 1840, 892.
19. Williams, D. L. H. *Accounts of Chemical Research* **1999**, 32, 869.
20. Bartberger, M. D.; Houk, K. N.; Powell, S. C.; Mannion, J. D.; Lo, K. Y.; Stamler, J. S.; Toone, E. J. *Journal of the American Chemical Society* **2000**, 122, 5889.
21. Instruments, G. A. 2014.
22. Simpson, A. J.; Brown, S. A. *Journal of Magnetic Resonance* **2005**, 175, 340.
23. Demessence, A.; D'Alessandro, D. M.; Foo, M. L.; Long, J. R. *Journal of the American Chemical Society* **2009**, 131, 8784.
24. Homer, N. Z. M.; Reglinski, J.; Sowden, R.; Spickett, C. M.; Wilson, R.; Walker, J. J. *Cryobiology* **2005**, 50, 317.
25. Gorren, A. C. F.; Schrammel, A.; Schmidt, K.; Mayer, B. *Archives of Biochemistry and Biophysics* **1996**, 330, 219.
26. Harding, J. L.; Reynolds, M. M. *Journal of the American Chemical Society* **2012**, 134, 3330.
27. Harding Jacqueline, L.; Metz Jarid, M.; Reynolds Melissa, M. *Advanced Functional Materials* **2014**, 24, 7503.
28. Huang, L.; Wang, H.; Chen, J.; Wang, Z.; Sun, J.; Zhao, D.; Yan, Y. *Microporous and Mesoporous Materials* **2003**, 58, 105.
29. Schoenecker, P. M.; Carson, C. G.; Jasuja, H.; Flemming, C. J. J.; Walton, K. S. *Industrial & Engineering Chemistry Research* **2012**, 51, 6513.

30. Al-Janabi, N.; Hill, P.; Torrente-Murciano, L.; Garforth, A.; Gorgojo, P.; Siperstein, F.; Fan, X. *Chemical Engineering Journal* **2015**, *281*, 669.
31. Neufeld, M. J.; Ware, B. R.; Lutzke, A.; Khetani, S. R.; Reynolds, M. M. *ACS Applied Materials & Interfaces* **2016**, *8*, 19343.
32. R. Noble, D.; R. Swift, H.; Lyn H. Williams, D. *Chemical Communications* **1999**, 2317.
33. Kenche, V. B.; Zawisza, I.; Masters, C. L.; Bal, W.; Barnham, K. J.; Drew, S. C. *Inorganic Chemistry* **2013**, *52*, 4303.
34. Ngamchuea, K. B.-M., C.; Compton, R. G. *Chemistry: A European Journal* **2016**, *22*, 15545.
35. Taylor-Edinbyrd, K.; Li, T.; Kumar, R. *Physical Chemistry Chemical Physics* **2017**, *19*, 11947.
36. Li, T.; Taylor-Edinbyrd, K.; Kumar, R. *Physical Chemistry Chemical Physics* **2015**, *17*, 23403.
37. Broniowska, K. A.; Diers, A. R.; Hogg, N. *Biochimica et Biophysica Acta (BBA) - General Subjects* **2013**, *1830*, 3173.
38. Staab, C. A.; Ålander, J.; Morgenstern, R.; Grafström, R. C.; Höög, J.-O. *Chemico-Biological Interactions* **2009**, *178*, 29.
39. Hedberg, J. J. G., W. J.; Nilsson, S. J. F.; Hoog, J. *European Journal of Biochemistry* **2003**, *270*, 1249.
40. Pietraforte, D.; Mallozzi, C.; Scorza, G.; Minetti, M. *Biochemistry* **1995**, *34*, 7177.
41. Singh, S. P.; Wishnok, J. S.; Keshive, M.; Deen, W. M.; Tannenbaum, S. R. *Proceedings of the National Academy of Sciences of the United States of America* **1996**, *93*, 14428.

CHAPTER 7

SUMMARY AND FUTURE FOR MOFs

7.1 Summary

Metal-organic frameworks (MOFs) are versatile organic-inorganic hybrid materials having great potential for applications including in gas storage,^{1,2} chemosensing,^{3,4,5} biomimicry,^{6,7} and catalysis^{8,9} among others. A primary goal of this research was to address several of the challenges associated with the development, use, and application of MOFs. Such challenges include inefficient or expensive syntheses, instability to water, selectivity, and limited methods to understand heterogeneous catalysis.

Chapter 2 addresses both synthetic challenges associated with $\text{Cu}_2(\text{NH}_2\text{BTC})_3$ and stability of the MOF to water. The research goals for chapter 2 include addressing (a) if $\text{NH}_2\text{H}_3\text{BTC}$ can be accessed with a scalable, cost-effective synthesis to provide a tricarboxylate MOF for PSM, (b) if MOFs with sterically hindered constituents can undergo covalent PSM with long chained and branched hydrocarbons, and (c) if such PSM can expand functionality of the material by providing an isostructural system with improved hydrophobicity. Chapter 2 achieves covalent postsynthetic modification (PSM) of a metal-organic framework (MOF), $\text{Cu}_3(\text{NH}_2\text{BTC})_2$, to manipulate the degree of hydrophobic character and the kinetic stability to water of the MOF. The wettability of a material can be directly related to its practical applicability; however, the ability to control wettability is very challenging especially with regard to microporous materials. In chapter 2, the kinetic stability of tricarboxylate MOFs to water was enhanced for the first time via postsynthetic modification.¹⁰ Unmodified $\text{Cu}_2(\text{NH}_2\text{BTC})_3$ was determined to be highly unstable to water, losing crystallinity and undergoing structural collapse when submerged in water for just a few minutes.

However, when the material was modified by reacting the free-amine moiety with an anhydride, introducing new hydrophobic hydrocarbons via the formation of an amide, the wettability of the material was altered and the kinetic stability of the material to water was significantly enhanced (retaining crystallinity after 30 min submersed in room temperature water). This work facilitates reliable access to mixed-ligand frameworks with predictable, calculated wettability and tunable kinetic stability to water. This is also the first report to functionalize copper-MOFs as well as MOFs containing a benzene-1,3,5-tricarboxylate ligand to achieve hydrophobic characteristics. In addition, a new and efficient synthesis of the ligand $\text{H}_3\text{NH}_2\text{BTC}$ was developed which reduced the cost to produce the MOF by 120-fold and yields the ligand and MOF on multigram-scale, further supporting practical applicability of $\text{Cu}_2(\text{NH}_2\text{BTC})_3$. This study demonstrates the power of tuning the hydrophobicity of organic-inorganic hybrid materials, such as MOFs, and capitalizing on structural bias to finely tune such nanomaterials to broaden their usefulness for industrial, environmental, and biological applications.

Chapter 3 also addresses synthetic challenges of MOF surfaces and stability of the MOF $\text{Cu}_2(\text{NH}_2\text{BTC})_3$ to water. In chapter 3, the research goal was to develop a $\text{Cu}_2(\text{NH}_2\text{BTC})_3$ MOF-cotton material that could be tuned with PSM to deliver antibacterial copper. We hypothesized that by postsynthetically modifying the material, the resultant changes in kinetic stability of the MOF to water would result in variable release rates of Cu^{2+} ions in solution. We hypothesized that the presence of copper on the surface of the MOF-cotton material would yield an antibacterial surface and the release of Cu^{2+} ions into solution would kill planktonic bacteria in solution. With access to the MOF ligand on multi-gram scale described in chapter 2, in chapter 3 surface growth of $\text{Cu}_2(\text{NH}_2\text{BTC})_3$ and subsequent postsynthetic modification to alter kinetic stability of the MOF to aqueous environments was extended for a tunable antibacterial application.¹¹ Postsynthetic

modification of MOF $\text{Cu}_3(\text{NH}_2\text{BTC})_2$ achieves the first report of synthetically tunable Cu^{2+} ion release from the surface of a textile. The Cu^{2+} ions yield an antibacterial surface that is capable of tunable ion release to kill bacterial in solution and prevent the growth of bacteria on the surface of cotton. While the antibacterial results are exciting, this chapter showcases the ability to generate surface MOFs (SURMOFs) that can then undergo subsequent postsynthetic modification tuning. A newly applied carboxymethylation process was implemented, which led to the highest reported surface nucleation sites for MOF growth on cotton. Using a layer-by-layer dip-coating process optimized with dip-coating robotics, a uniform crystalline layer of MOF was synthesized on the surface of the modified cotton. The resultant MOF-cotton composites were thoroughly characterized using scanning and transmission electron microscopy and discovered to have attached MOF around each individual cotton fiber. The resultant materials are reproducible and demonstrated the potential for tunable decomposition rates to release Cu^{2+} from the surface of the materials. Notably, we demonstrate tunable kinetic stability in biologically relevant media (nutrient broth media) that exhibit slow Cu^{2+} ion release, an apparent surface phenomenon, as the remaining SURMOF retains crystallinity (determined by PXRD). This study not only will prove important for the development of future surface immobilized MOFs, but also opens up the possibility for MOFs in applications such as antibacterial wound dressings.

Chapter 4 was developed to test the hypothesis that $\text{Cu}_2(\text{NH}_2\text{BTC})_3$ may undergo a detectable change in emission spectra upon the introduction of metal-ion analytes, which would be suitable for sensing. The MOF $\text{Cu}_2(\text{NH}_2\text{BTC})_3$ was used once more in chapter 4 with the research goal to investigate the interaction of the MOF with small molecules. Specifically, the photophysical properties of $\text{Cu}_2(\text{NH}_2\text{BTC})_3$ were investigated. Sensing with the NH_2BTC ligand was studied and reveals ion-MOF interactions that, while they need to be better understood, should

help to guide future developments of MOFs for ion sensing. The ligand of the MOF was found to fluoresce in solution and also when embedded in the MOF structure. The ligand inherently has multiple potential modes of metal-ion – MOF interactions that could lead to a detectable photoluminescent response (fluorescence quenching or enhancement) in the presence of various metal ions, overall performing as a chemosensor. Consequently, various metal ion solutions were introduced to a solution of the MOF resulting in photoluminescent changes. Such changes, were probed (using postsynthetic modification of the material and isostructural CuBTC) to reveal significant insights as to how ions interact with the MOF. For instance, some anions like dichromate ($\text{Cr}_2\text{O}_7^{2-}$) are likely detected by direct interaction with the amine. Iron (Fe^{2+} and Fe^{3+}) on the other hand likely interacts with the ligand elsewhere, such as the carboxylate moiety. The results herein not only demonstrate high sensitivity and selectivity to detect M^{2+} ions, but also suggest how MOFs interact with ions.

While understanding the interactions of small molecules is important for the development of next-generation chemosensors, the instability of $\text{Cu}_2(\text{NH}_2\text{BTC})_3$ to water prevents any real-world application of the as-synthesized material in water. Thus, the research goal in chapter 5 is to strategically use a zirconium-carboxylate MOF, that is thermodynamically stable to water (100°C in aqueous 8M HCl) for divalent metal-ion detection and metal-ion removal from water. The MOF, NU-902, contains a porphyrin-containing ligand, tetrakis(4-carboxyphenyl)porphine (TCPP), which is a selective divalent metal ion chelator, known to selectively chelate Cd^{2+} and Cu^{2+} over other metal-ions. The open N-donor center of the porphyrin can capture metal ions to potentially remove metal ions from water. Additionally, the photoluminescent properties of the materials enables simultaneous fluorescence detection of metal ions. With a growing global concern of limited drinking water, the work in this thesis showcases the first application of a

strategically utilized MOF (-polymer composite), to both remove and detect metal ions in water. There are only two other studies in the prior literature using a MOF for heavy metal removal, one with the MOF LMOF-263 (selective for Hg^{2+}) and the other with the water sensitive MOF FeBTC in a polydopamine composite.^{12,13}

Chapter 6 of this dissertation investigates heterogeneous catalysis with thermodynamically stable MOF CuBTTri. A central research goal of this chapter was to develop a method that would allow for monitoring multiple reaction species to determine the true stoichiometry of the reaction. En route to better understand MOF catalysis in aqueous systems, a ^1H NMR method with solvent suppression was used to simultaneously monitor all relevant reaction components during the release of nitric oxide (NO), a vital signaling molecule of biological importance, from nitrosothiols (RSNOs). The reaction of Cu^{2+} ions as well as Cu^{2+} -containing MOFs with RSNOs is reported, yielding the full reaction stoichiometry for the first time. This study led to the determination of the reaction stoichiometry for both Cu^{2+} ions and copper-MOFs. Notably, this study revealed a difference in thiol dependence for free copper ions vs. Cu-MOF. This study provides the first necessary precedent for future studies of MOFs in biologically relevant media, and enables future studies in biologically relevant medias such as blood. Importantly, such studies are necessary en route to developing more efficient MOF catalysts for biomedical applications.

Taken together, the body of work presented as this Ph. D. dissertation addresses several key challenges facing the MOF community today including synthetic development, stability, and understanding the interacting of small molecules with MOFs. As such, the findings promise to have far reaching implications to biomedical, industrial, and environmental applications among others.

7.2 Postsynthetic Modification (PSM) and Future Design Principles

PSM of MOFs is, by definition, late stage chemical modification that does not compromise the integrity of the MOF crystal lattice.¹⁴⁻¹⁶ There are several advantages, as well as disadvantages, of postsynthetically modifying MOFs. PSM allows for fine tuning of these heterogeneous materials. Tunable kinetic stability to water for example is ideal for controlling potential drug delivery (release) kinetics,¹⁷ via the ligands, metal ions, or pre-loaded host molecules. PSM allows for late-stage optimization for various applications, can yield mechanistic insights of small molecule interactions with MOFs, and can be exploited for selective interactions with target molecules for chemosensing.^{18,19} The diversity of PSM literature available to date demonstrates the widespread impact this strategy holds on broadening the overall applicability of these materials.

When considering future uses of PSM of MOFs, it is currently important to consider the final application. While such modification can indeed be advantageous for enhancing the kinetic stability or rigidity of MOFs, this method is not a substitute for developing more thermodynamically stable and robust frameworks. In fact, by incorporating free and accessible functional handles into more structurally robust frameworks next-generation PSM will enable anchoring of new functionality into MOFs. Conceivably, these applications will include catalysis (where perhaps a necessary co-catalyst or reductant is present), biomimicry (where enzymes and proteins are incorporated), among other complex systems.

7.3 Emerging Real-World Applications of MOFs

The development of MOFs is still in its infancy. For several decades, despite thousands of MOF structures, the fundamental lack of stability associated with MOFs significantly stifled any

potential use of these materials for practical applications. However, recent advances in fundamental design principles has yielded access to highly robust materials that have kinetic and/or thermodynamic stability. Postsynthetic modification to enhance hydrophobicity and increase steric hindrance of water to the metal sites of the MOF allows one to increase the kinetic stability of MOFs. By simply following hard/soft acid base theory and synthesizing MOFs whereby, high-valent harder metal cations are paired with hard ligands such as, oxo-donors, or low-valent soft metal cations are paired with softer N- or P- donors, more thermodynamically stable frameworks are developed.²⁰ Additionally, recent syntheses have focused on reducing synthetic temperature and efficiency, thereby lowering costs necessary to generate MOFs on practical, industrial scales.^{21,22} Several MOFs are now commercially available such as Basolites A100, C300, F300, Z373 and Z1200 via Sigma Aldrich. Queen's University Belfast spin-off MOF Technologies (founded 2012) sells a MOF that is used by fruit packaging and storage firm Decco to slow the ripening of fruit with the slow release of gas 1-methylcyclopropene.²³ Start-up NuMat Technologies (founded 2011), markets research from Northwestern University chemistry Professors Omar Farha and Joseph Hupp, focused primarily on gas storage applications including safe storage of gases for the semiconductor industry.²⁴ Seminal work from the laboratories of Professors Mircea Dincă, Jeffrey Long, and Melissa Reynolds all indicate that commercialization of MOFs is rapidly escalating with the increased availability of more stable structures. Professor Dincă's research has demonstrated the use of MOFs to achieve record atmospheric fresh water capture,²⁵ a process that may prove key for capturing drinking water (a scarce resource). Professor Long's research has led to the start-up Mosaic Materials, focused on selectively capturing CO₂ with higher efficiency and lower costs than previously reported.²⁶ Professor Reynolds' research uses MOFs for biomedical applications, notably the incorporation of CuBTri into polymeric

composites to yield antibacterial materials that can prevent thrombosis and hence lessen device failure of blood-contacting devices.²⁷ In short, the application of MOFs is intensifying and the possibility of practical applications has just begun.

7.4 Final Comments

It is exciting to be a part of metal-organic framework research, a rapidly expanding field of chemistry attracting significant attention from the scientific community. The development of MOFs has begun to change the way the world thinks about materials for industrial, biological, and environmental applications. As the population on earth continues to rise at exponential rates, it is vital to engineer new materials that can help meet the demands associated with limited resources. MOFs offer an opportunity through catalysis and storage to capture and remove greenhouse gases from the atmosphere in a critical response to slowing climate change.²⁸ These materials show unprecedented capabilities to purify contaminated water.²⁹ MOFs offer a new solution to combat the recent threat of superbugs, having antimicrobial properties which do not contribute to antibiotic resistance.³⁰ While the potential for MOFs is clear, the widespread use of these materials is still underdeveloped. Affordable access to the ligands and robust MOFs requires immediate synthetic attention. With useful, scalable MOFs in-hand the scientific community is then tasked with further understanding and optimizing the application of these materials. For instance, while MOFs display great potential as chemosensors, much work is needed to understand and improve upon signal transduction.³¹ Additionally, while MOFs may have a favorable future in biological applications including drug delivery systems³² and blood contacting device coatings,³³ further studies to understand long term thermodynamic stability in biological mediums and overall compatibility, are necessary. In conclusion, MOFs are unique materials that upon necessary further development

of accessible, stable structures, the systemic design to generate more selective, stable, and efficient systems can reach their full potential in diverse applications.

REFERENCES

1. Li, H.; Wang, K.; Sun, Y.; Lollar, C. T.; Li, J.; Zhou, H.-C. *Materials Today* **2018**, *21*, 108.
2. Li, J.-R.; Kuppler, R. J.; Zhou, H.-C. *Chemical Society Reviews* **2009**, *38*, 1477.
3. Fang, X.; Zong, B.; Mao, S. *Nano-Micro Letters* **2018**, *10*, 64.
4. Lustig, W. P.; Mukherjee, S.; Rudd, N. D.; Desai, A. V.; Li, J.; Ghosh, S. K. *Chemical Society Reviews* **2017**, *46*, 3242.
5. Zhao, D.; Cui, Y.; Yang, Y.; Qian, G. *CrystEngComm* **2016**, *18*, 3746.
6. Wu, X. Q.; Ma, J. G.; Li, H.; Chen, D. M.; Gu, W.; Yang, G. M.; Cheng, P. *Chem Commun (Camb)* **2015**, *51*, 9161.
7. Gu, Z.-Y.; Park, J.; Raiff, A.; Wei, Z.; Zhou, H.-C. *ChemCatChem* **2014**, *6*, 67.
8. Hu, Z.; Zhao, D. *CrystEngComm* **2017**, *19*, 4066.
9. Beyzavi, M. H.; Stephenson, C. J.; Liu, Y.; Karagiari, O.; Hupp, J. T.; Farha, O. K. *Frontiers in Energy Research* **2015**, *2*.
10. Rubin, H. N.; Reynolds, M. M. *Inorganic Chemistry* **2017**, *56*, 5266.
11. Rubin, H. N.; Neufeld, B. H.; Reynolds, M. M. *ACS Applied Materials & Interfaces* **2018**.
12. Rudd, N. D.; Wang, H.; Fuentes-Fernandez, E. M. A.; Teat, S. J.; Chen, F.; Hall, G.; Chabal, Y. J.; Li, J. *ACS Applied Materials & Interfaces* **2016**, *8*, 30294-30303.
13. Sun, D. T.; Peng, L.; Reeder, W. S.; Moosavi, S. M.; Tiana, D.; Britt, D. K.; Oveisi, E.; Queen, W. L. *ACS Central Science* **2018**, *4*, 349-356.
14. Tanabe, K. K.; Cohen, S. M. *Chem Soc Rev* **2011**, *40*, 498.
15. Wang, Z.; Cohen, S. M. *Chemical Society Reviews* **2009**, *38*, 1315.
16. Tanabe, K. K. Z., W., and Cohen, S. M. *JACS* **2008**, 8508.

17. Faust, T. *Nature Chemistry* **2015**, 7, 270.
18. Islamoglu, T.; Goswami, S.; Li, Z.; Howarth, A. J.; Farha, O. K.; Hupp, J. T. *Accounts of Chemical Research* **2017**, 50, 805.
19. Du, Y.; Li, X.; Lv, X.; Jia, Q. *ACS Applied Materials & Interfaces* **2017**, 9, 30925.
20. Pearson, R. G. *Journal of the American Chemical Society* **1963**, 85, 3533.
21. Butova, V. V.; Soldatov, M. A.; Guda, A. A.; Lomachenko, K. A.; Lamberti, C. *Russian Chemical Reviews* **2016**, 85, 280.
22. Julien, P. A.; Mottillo, C.; Frišćić, T. *Green Chemistry* **2017**, 19, 2729.
23. In *MOF Technologies About*; Vol. 2018.
24. **2018**.
25. Rieth, A. J.; Yang, S.; Wang, E. N.; Dincă, M. *ACS Central Science* **2017**, 3, 668.
26. McDonald, T. M.; Mason, J. A.; Kong, X.; Bloch, E. D.; Gygi, D.; Dani, A.; Crocellà, V.; Giordanino, F.; Odoh, S. O.; Drisdell, W. S.; Vlasisavljevich, B.; Dzubak, A. L.; Poloni, R.; Schnell, S. K.; Planas, N.; Lee, K.; Pascal, T.; Wan, L. F.; Prendergast, D.; Neaton, J. B.; Smit, B.; Kortright, J. B.; Gagliardi, L.; Bordiga, S.; Reimer, J. A.; Long, J. R. *Nature* **2015**, 519, 303.
27. Neufeld, M. J.; Lutzke, A.; Jones, W. M.; Reynolds, M. M. *ACS Applied Materials & Interfaces* **2017**, 9, 35628.
28. Li, S.; Chen, Y.; Pei, X.; Zhang, S.; Feng, X.; Zhou, J.; Wang, B. *Chinese Journal of Chemistry* **2016**, 34, 175.
29. Neufeld, B. H.; Neufeld, M. J.; Lutzke, A.; Schweickart, S. M.; Reynolds, M. M. *Advanced Functional Materials* **2017**, 27, 1702255.
30. Liu, L.; Zhou, Y.; Liu, S.; Xu, M. *ChemElectroChem* **2018**, 5, 6.

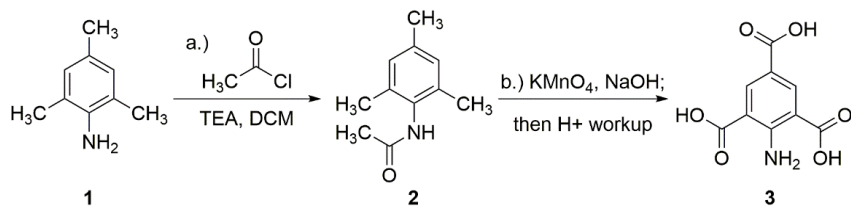
31. Wu, M.-X.; Yang, Y.-W. *Advanced Materials* **2017**, 29, 1606134.

APPENDIX A

SUPPORTING INFORMATION FOR CHAPTER 2

A.1. Synthesis and Characterization

Scheme A1. NH₂H₃BTC Synthesis



A.1.1 *N*-mesitylacetamide A2.

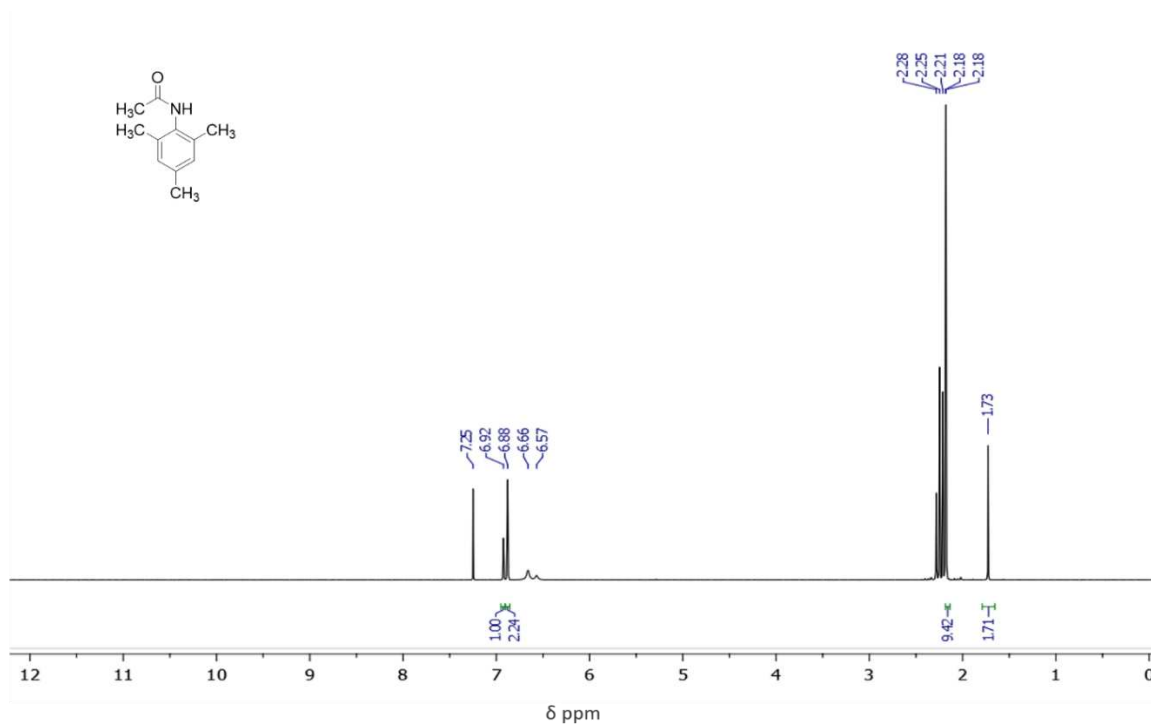


Figure A1. ¹H NMR spectra of *N*-mesitylacetamide **2** in CDCl₃.

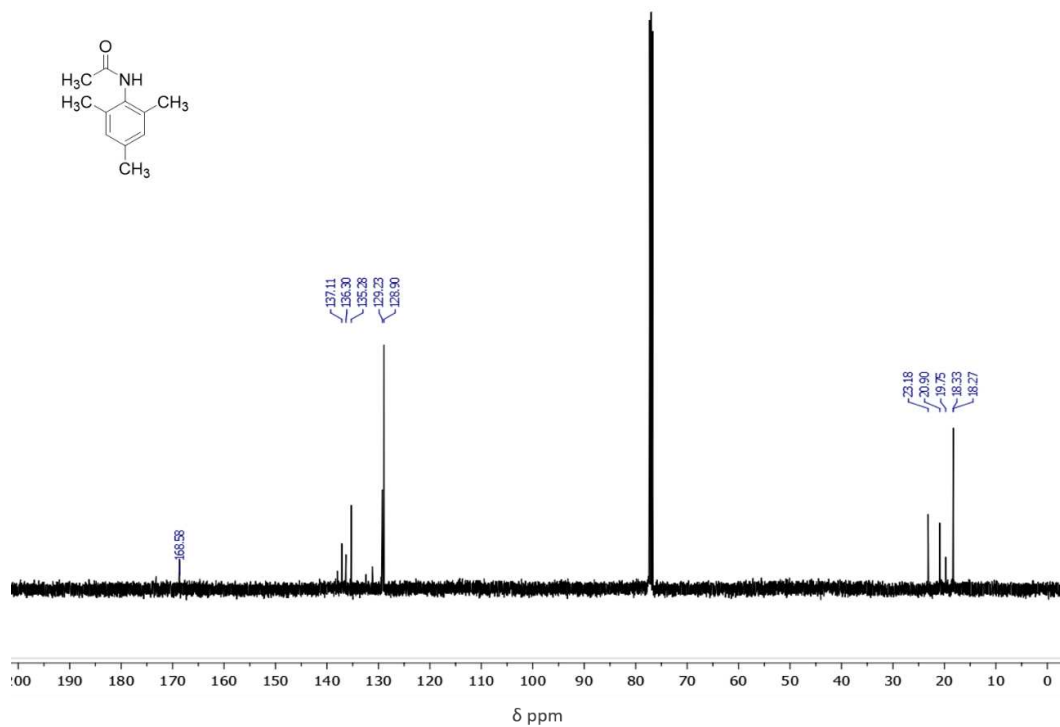


Figure A2. ¹³CNMR spectra of *N*-mesitylacetamide **2** in CDCl₃.

A.1.2. Characterization of 2-aminobenzene-1,3,5-tricarboxylic acid **3**.

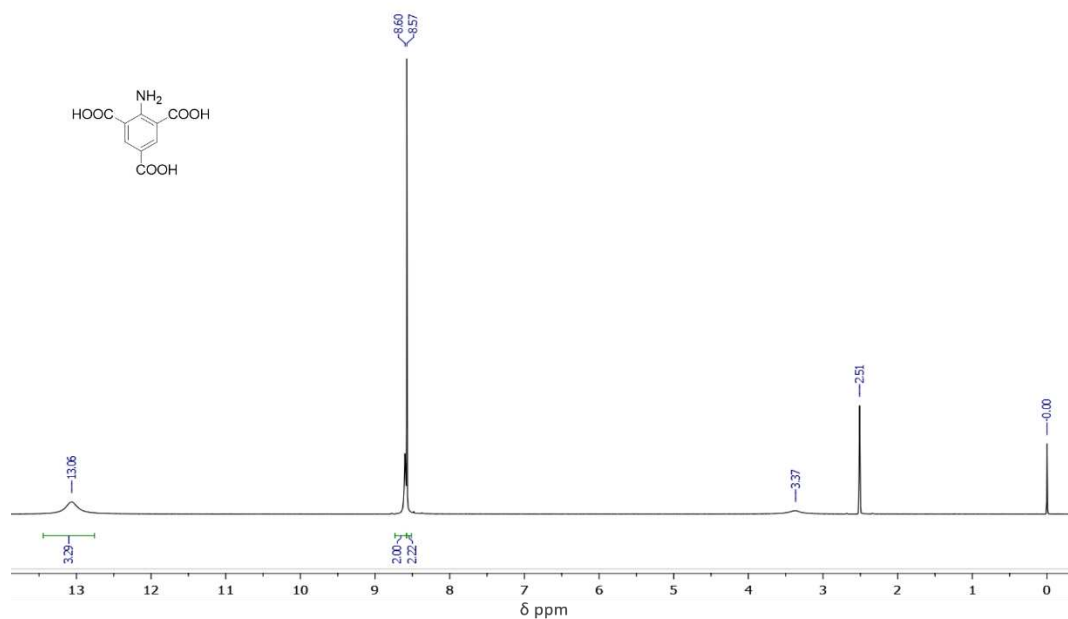


Figure A3. ¹HNMR spectra of 2-aminobenzene-1,3,5-tricarboxylic acid **3** in DMSO-d₆.

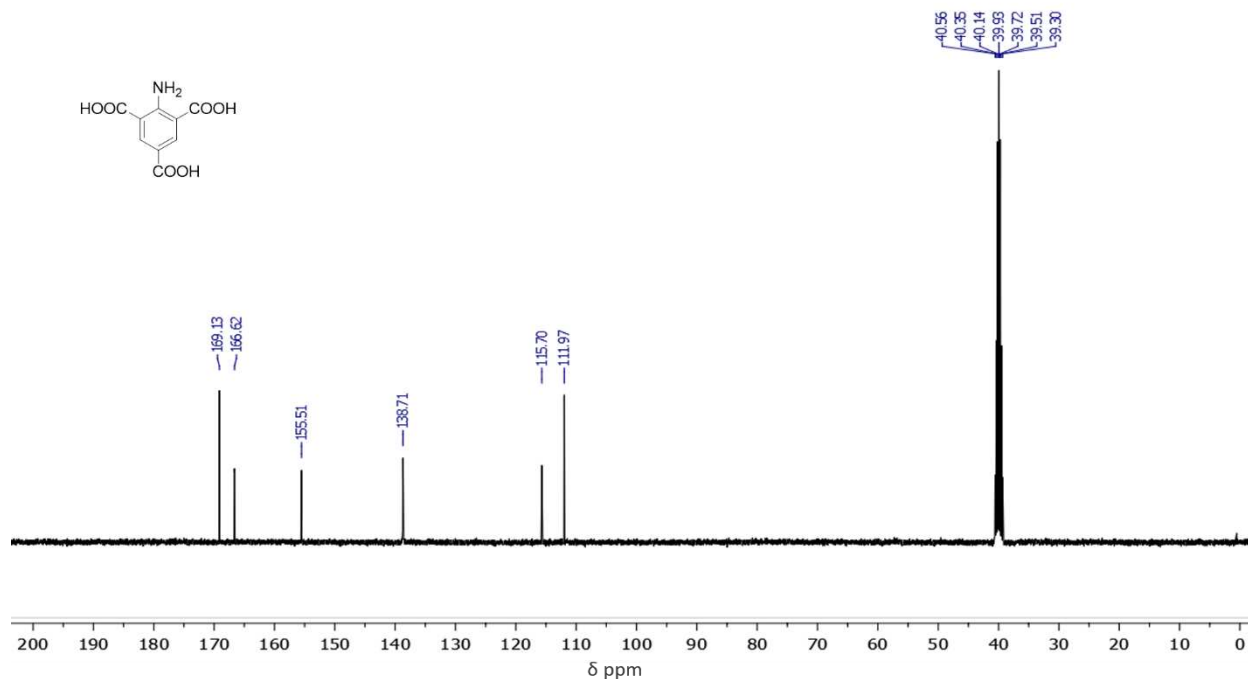
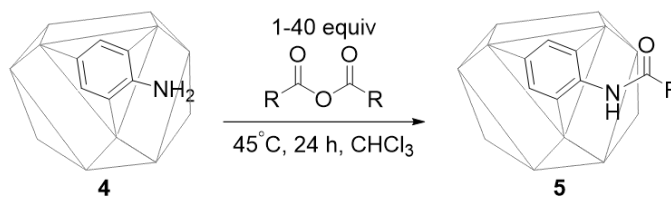


Figure A4. ^{13}C NMR spectra of 2-aminobenzene-1,3,5-tricarboxylic acid **3** in $\text{DMSO-}d_6$.

A.2. Post-synthetic modification

Scheme A2. Amide Functionalization of $\text{Cu}_3(\text{NH}_2\text{BTC})_2$



A.2.1. ^1H NMR spectra of modified ligands

The unmodified ligand peaks are denoted with a black square and appear slightly downfield of the modified ligands denoted with red circles. The appearance and intensity of a chemical shift within the ^1H NMR spectra of the digested MOF samples at 8.39 ppm, indicative of the aromatic protons on the modified amino tricarboxylate ligands was identified. Aromatic region (8 ppm – 9 ppm) was used to quantify percent conversion to the desired amides. As the equivalents of anhydride

increases, so does the percentage of modification, denoted by the peak in the aromatic region with the red circle. All modifications were performed in triplicate, and the three independent studies were averaged and summarized in Table 1.

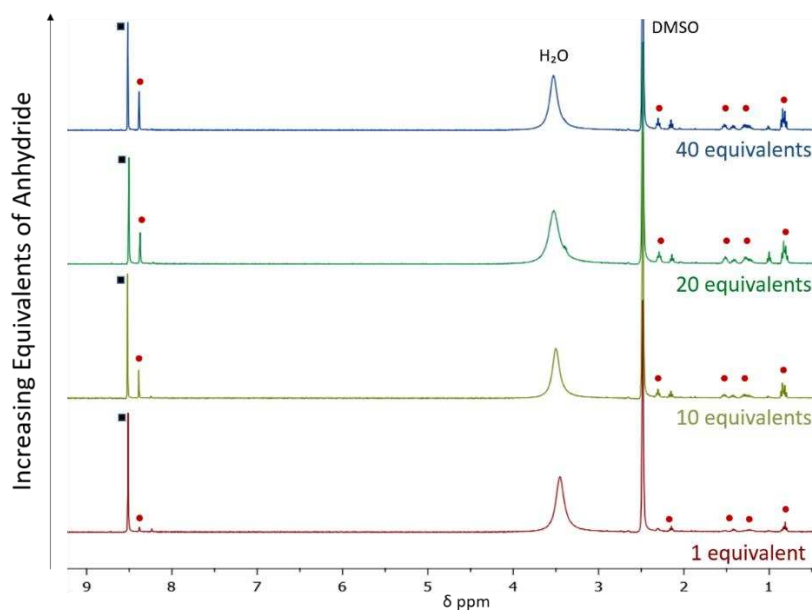


Figure A5. ¹H NMR spectra of digested $\text{Cu}_3(\text{NH-AM5-BTC})_2$ in CDCl_3 , showing the increase in modified ligand to unmodified ligand as the equivalents of anhydride increases.

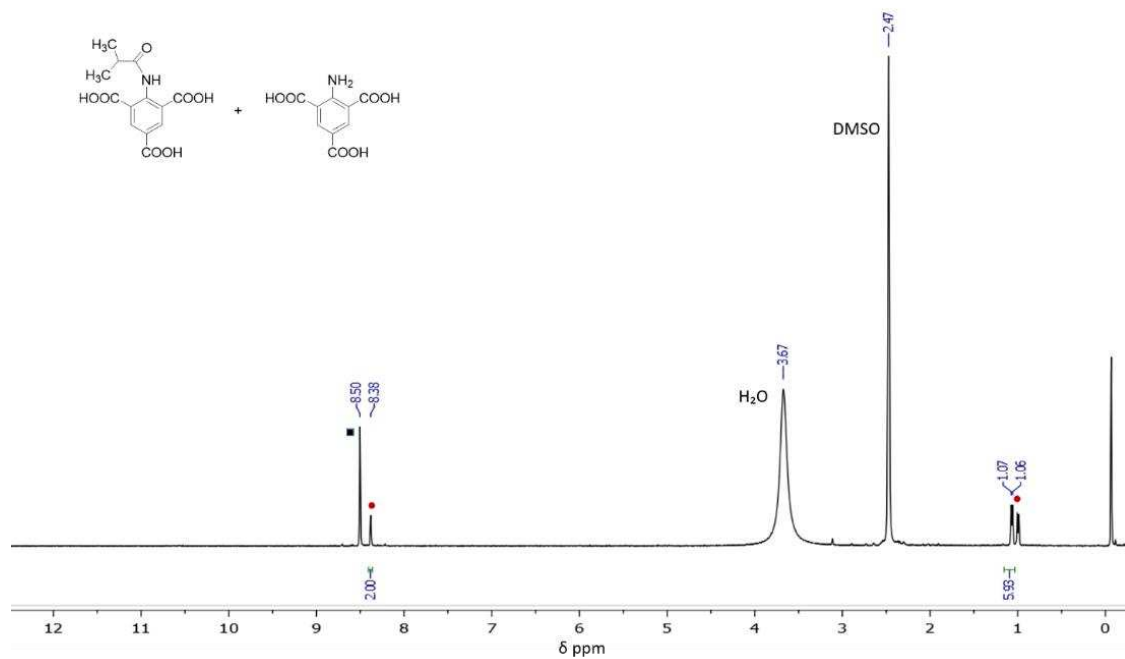


Figure A6. ^1H NMR spectra of digested $\text{Cu}_3(\text{NH-AMiPr-BTC})_2$ in CDCl_3 .

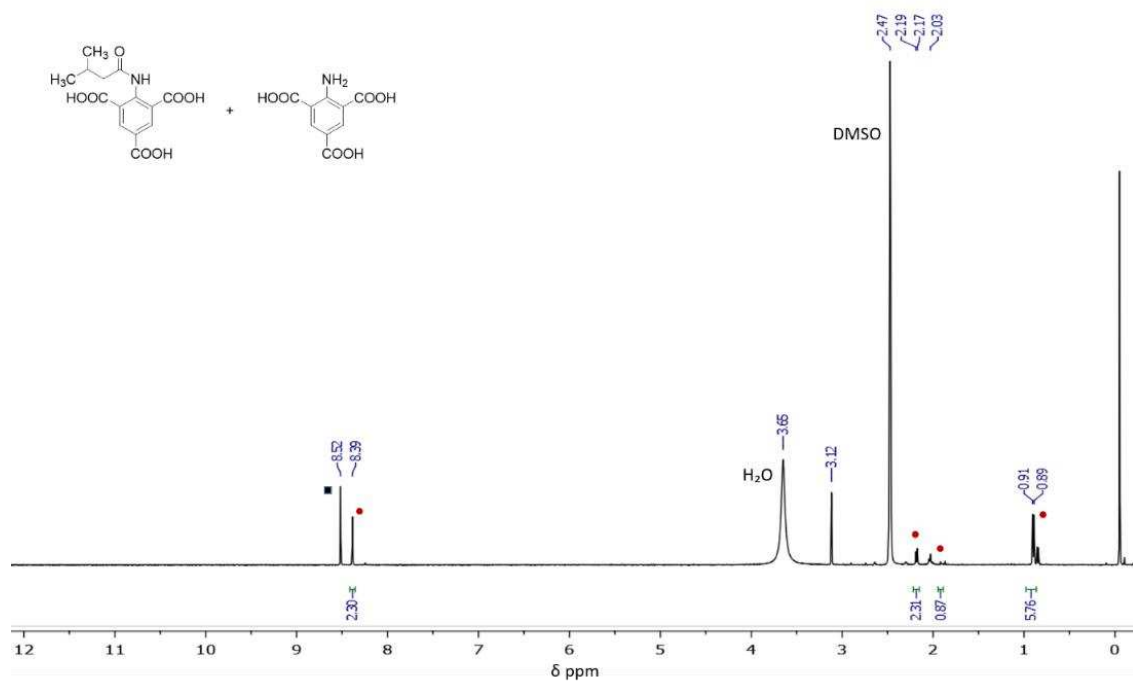


Figure A7. ^1H NMR spectra of digested $\text{Cu}_3(\text{NH-AMiBu-BTC})_2$ in CDCl_3 .

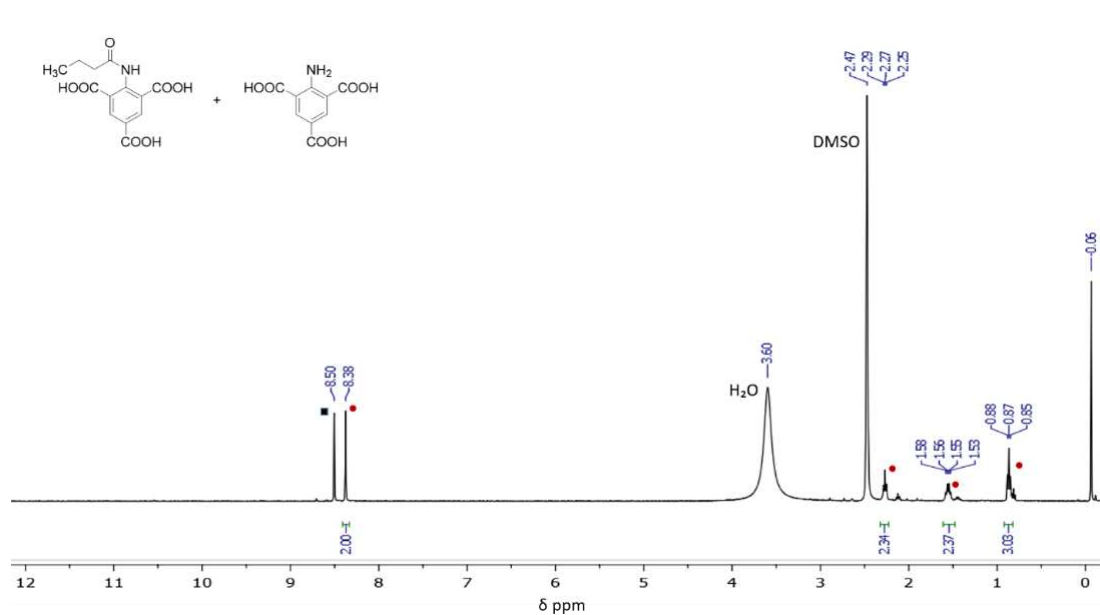


Figure A8. ¹H NMR spectra of digested $\text{Cu}_3(\text{NH-AM4-BTC})_2$ in DMSO-D₆.

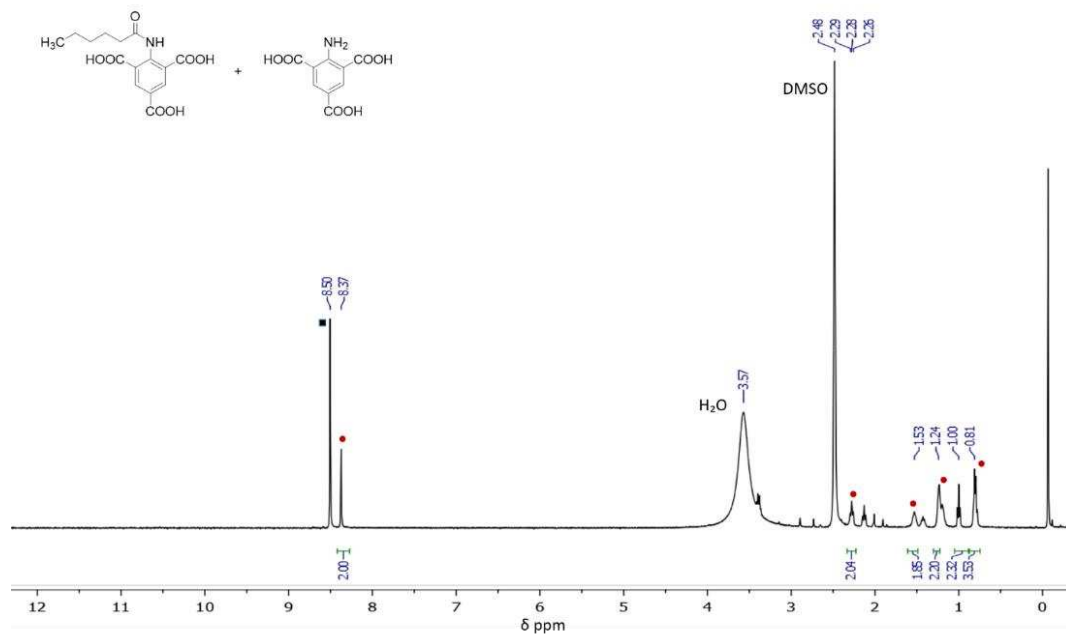


Figure A9. ¹H NMR spectra of digested $\text{Cu}_3(\text{NH-AM6-BTC})_2$ in DMSO-D₆.

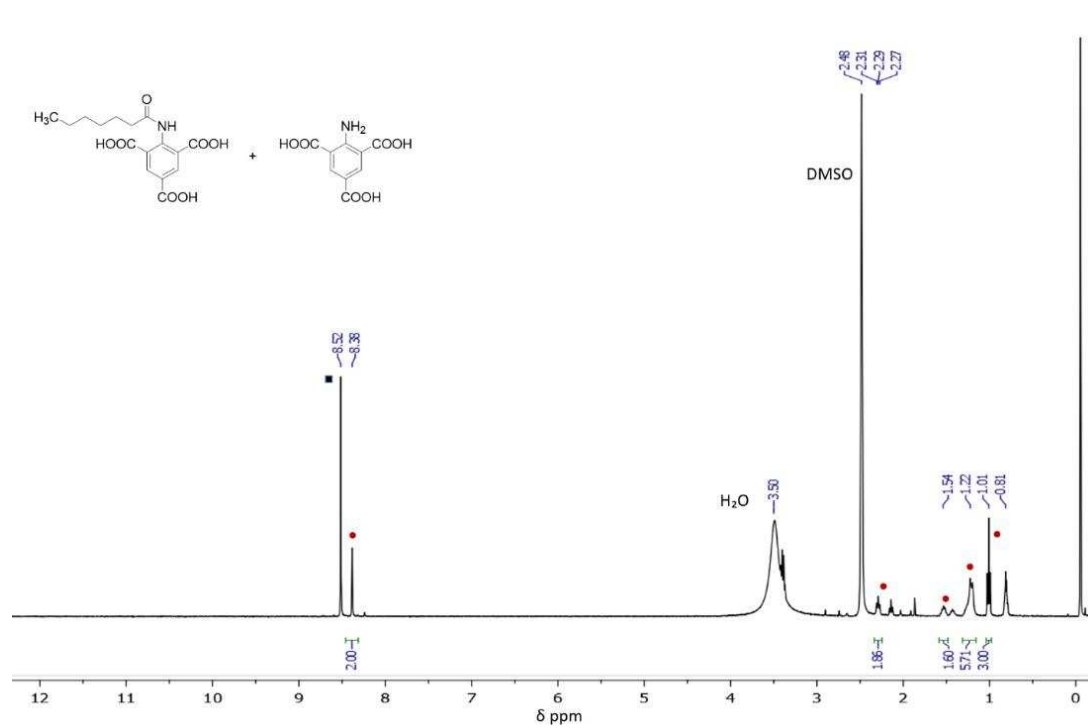


Figure A10. ¹H NMR spectra of digested Cu₃(NH-AM7-BTC)₂ in DMSO-D₆.

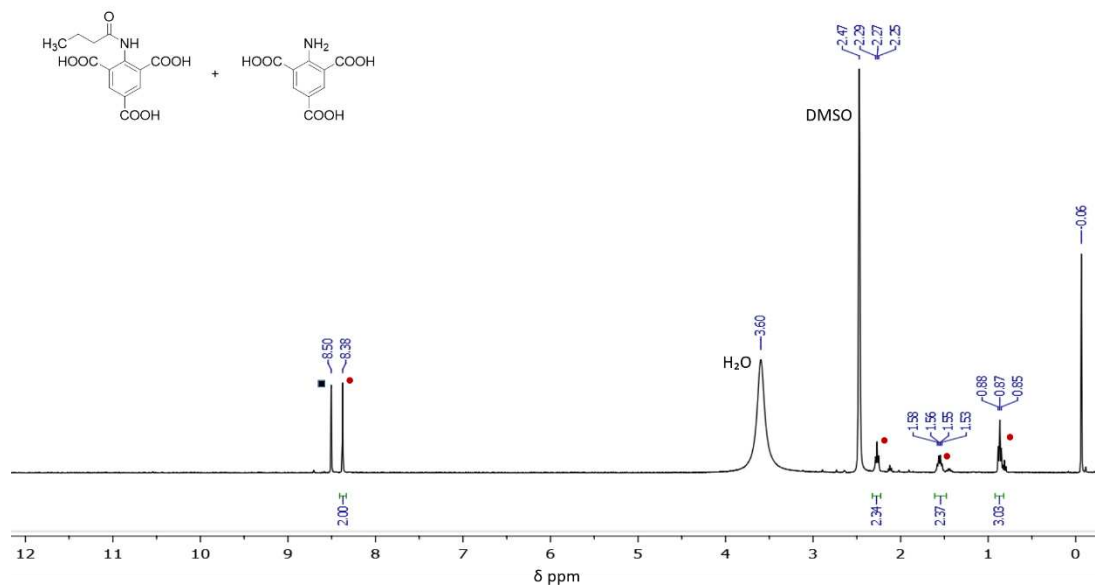


Figure A11. ¹H NMR spectra of digested Cu₃(NH-AM10-BTC)₂ in DMSO-D₆.

A.2.2. Mass spectrometry of acid digested modified ligands.

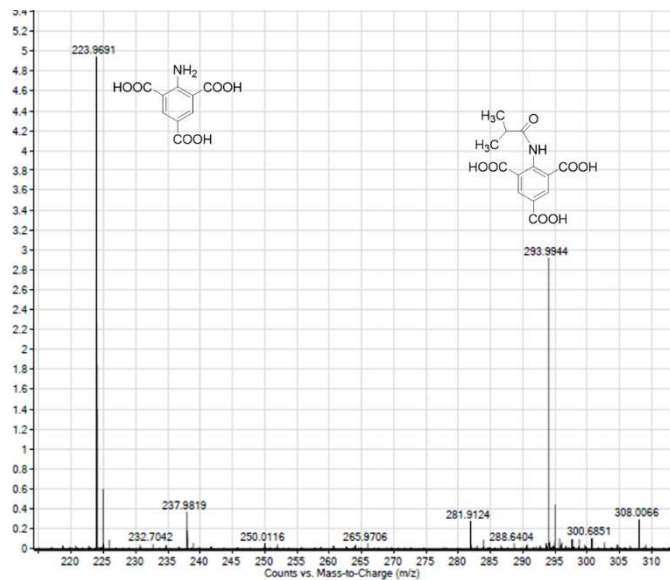


Figure A12. Digested $\text{Cu}_3(\text{NH-AM/Pr-BTC})_2$ ESI/APCI-MS.

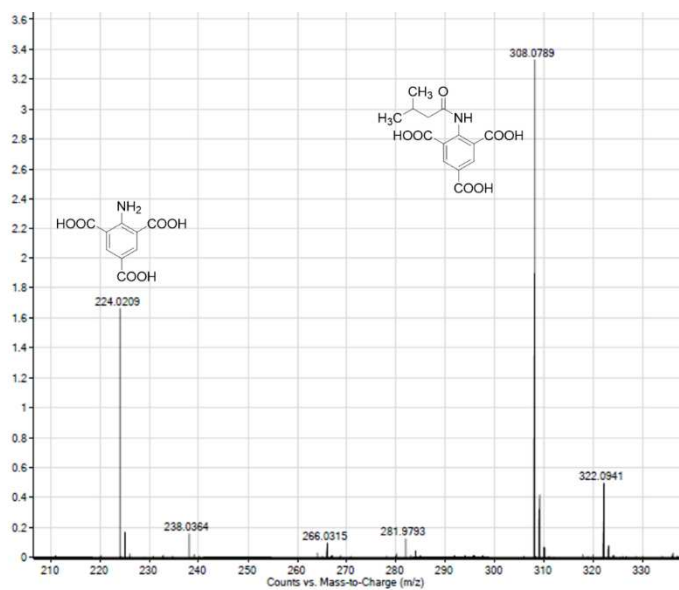


Figure A13. Digested $\text{Cu}_3(\text{NH-AM/Bu-BTC})_2$ ESI/APCI-MS.

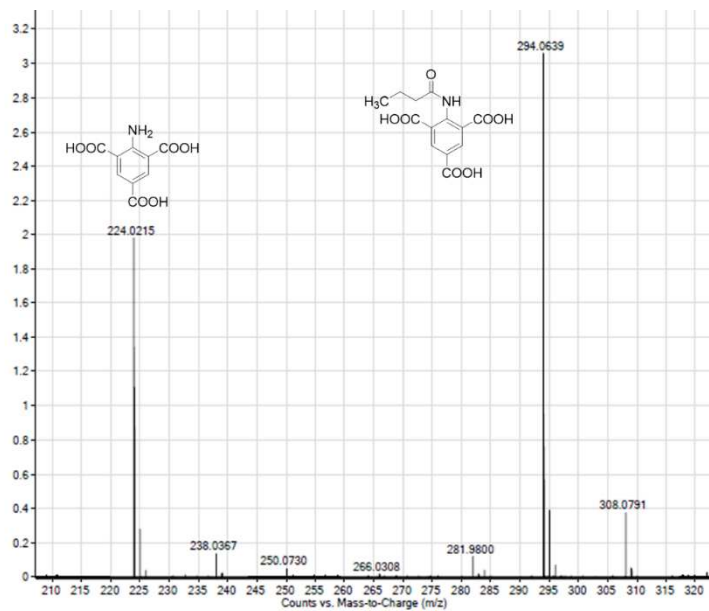


Figure A14. Digested $\text{Cu}_3(\text{NH-AM4-BTC})_2$ ESI/APCI-MS.

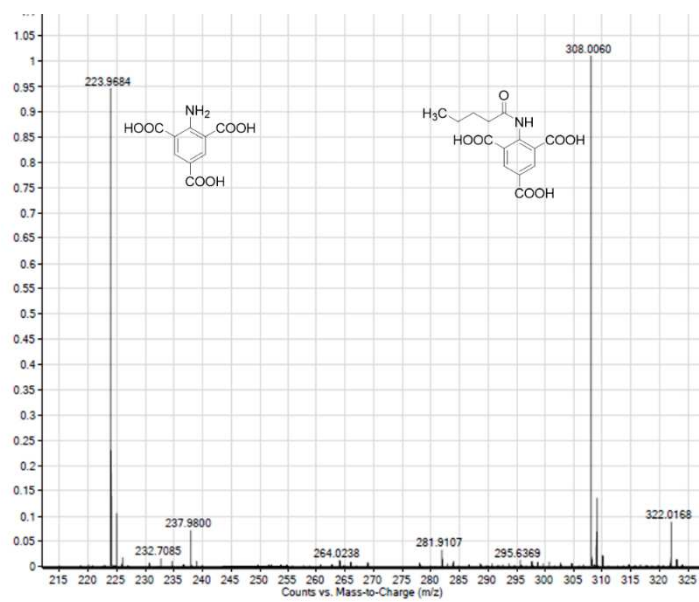


Figure A15. Digested $\text{Cu}_3(\text{NH-AM5-BTC})_2$ ESI/APCI-MS.

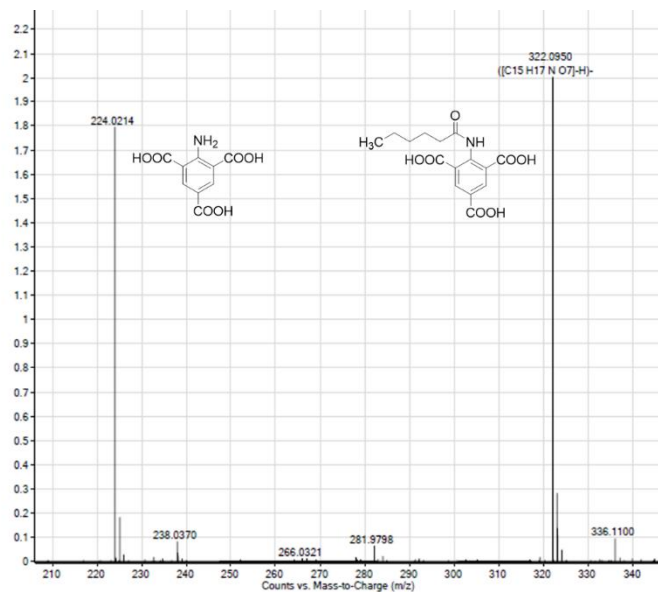


Figure A16. Digested $\text{Cu}_3(\text{NH-AM6-BTC})_2$ ESI/APCI-MS.

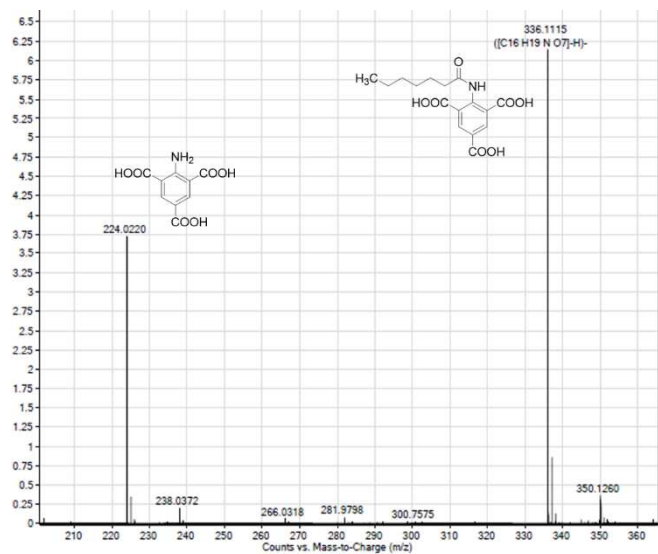


Figure A17. $\text{Cu}_3(\text{NH-AM7-BTC})_2$ ESI/APCI-MS.

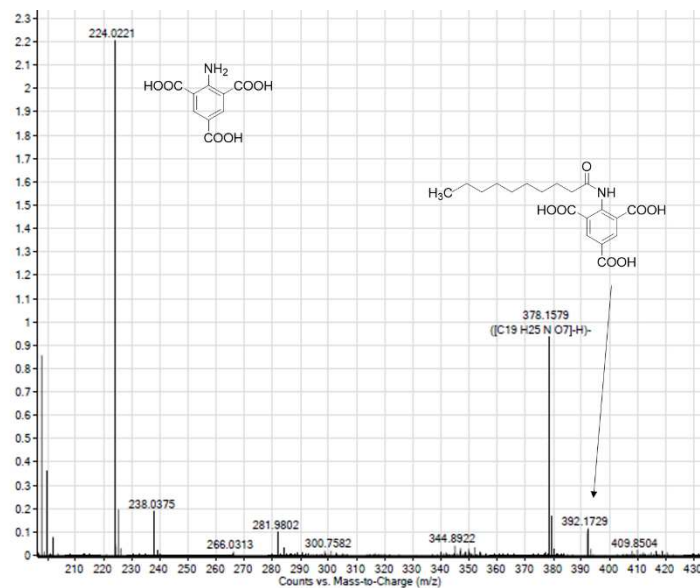


Figure A18. Digested $\text{Cu}_3(\text{NH-AM10-BTC})_2$ ESI/APCI-MS.

A.3. Thermal gravimetric analysis (TGA)

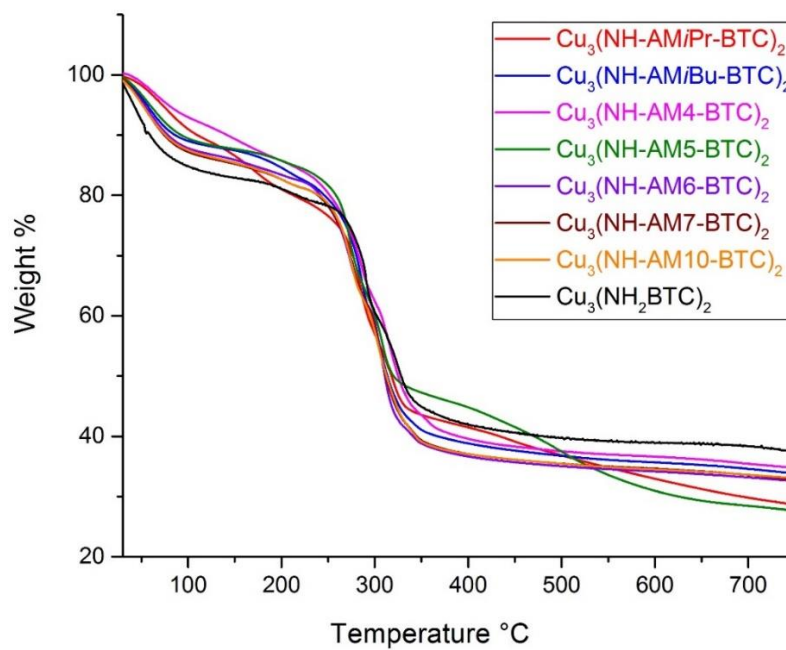


Figure A19. Thermal gravimetric analysis (TGA) of $\text{Cu}_3(\text{NH}_2\text{BTC})_2$ and all modified materials. TGA shows that the modified materials retain thermal stability.

A.4. IR

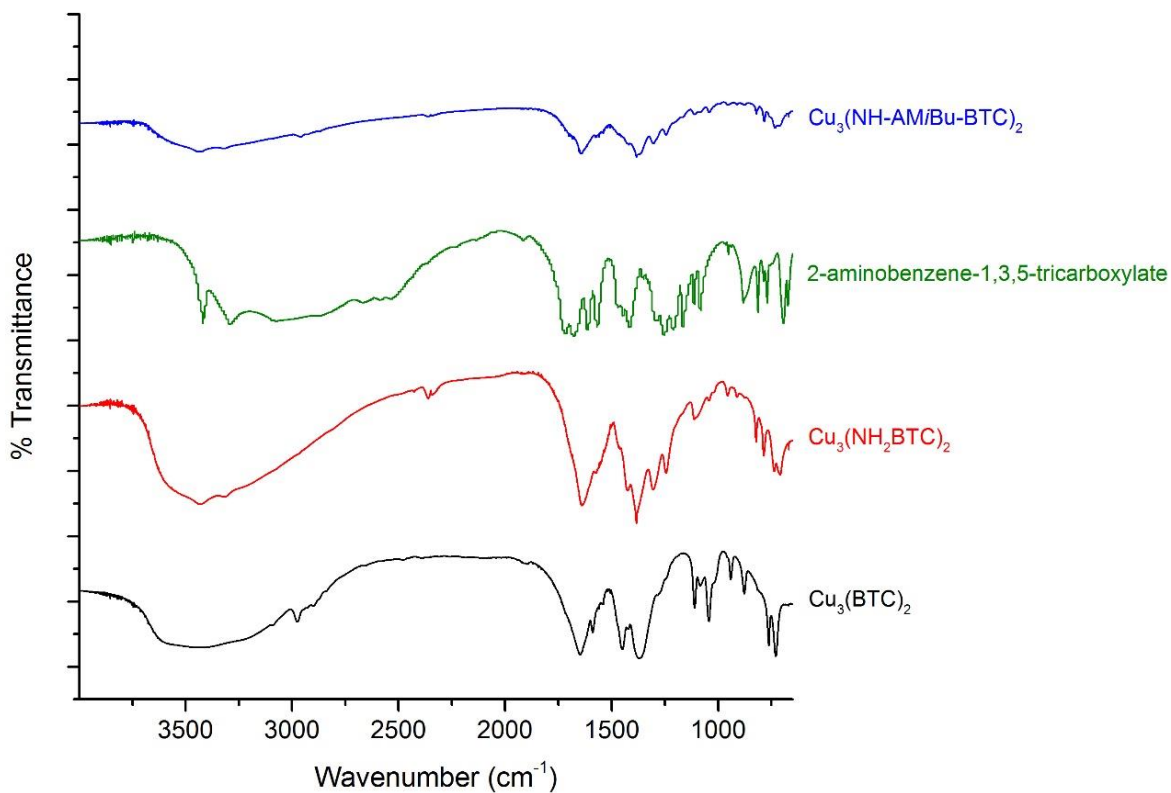


Figure A20. IR spectroscopy from bottom to top of $\text{Cu}_3(\text{BTC})_2$, $\text{Cu}_3(\text{NH}_2\text{BTC})_2$, preligand $\text{NH}_2\text{H}_3\text{BTC}$ and modified MOF $\text{Cu}_3(\text{NH-AMiBu-BTC})_2$. The MOF samples do not appear to contain any free-ligand (little to no decomposition). All modified spectra are consistent with that of $\text{Cu}_3(\text{NH-AMiBu-BTC})_2$ (shown).

A.5. Wettability

A.5.1 Water Contact Angles (WCA)

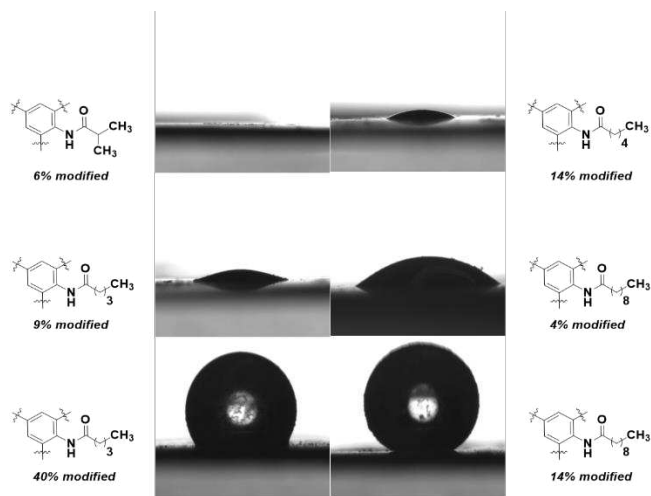


Figure A21. Water contact angle and sorption study images highlighting the ability to select different modifications and percent of functionalization to obtain different amounts of hydrophobicity.

A.5.2. WCA vs Number of Carbons in Amide

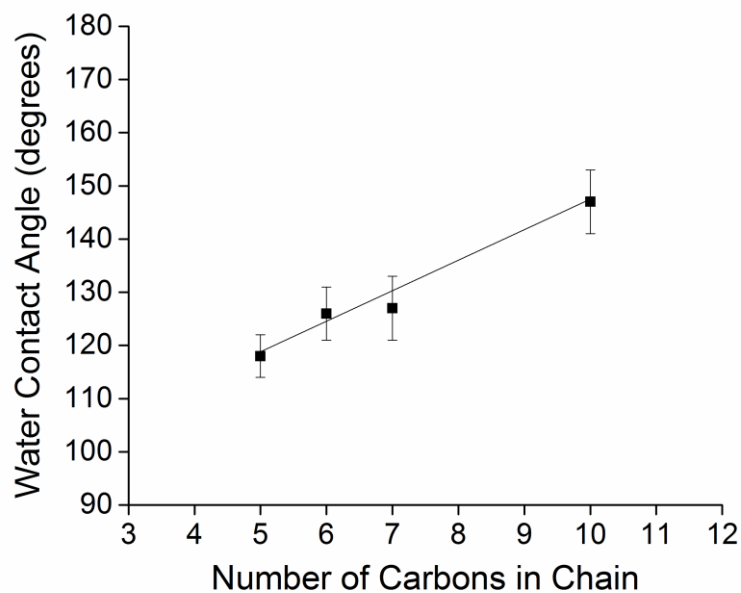


Figure A22. Relationship where the observed water contact angle in degrees (y) increases as the number of carbons (x) increases (when maximum modification is performed) with linear alkyl chains from 5–10 carbons. $y = 5.7x + 89.5$, $R^2 = 0.97$. Each data point represents the average of three trials. Error bars represent the standard deviation of 3 water droplets on the material after 1 second.

A.6. Water Stability PXRD

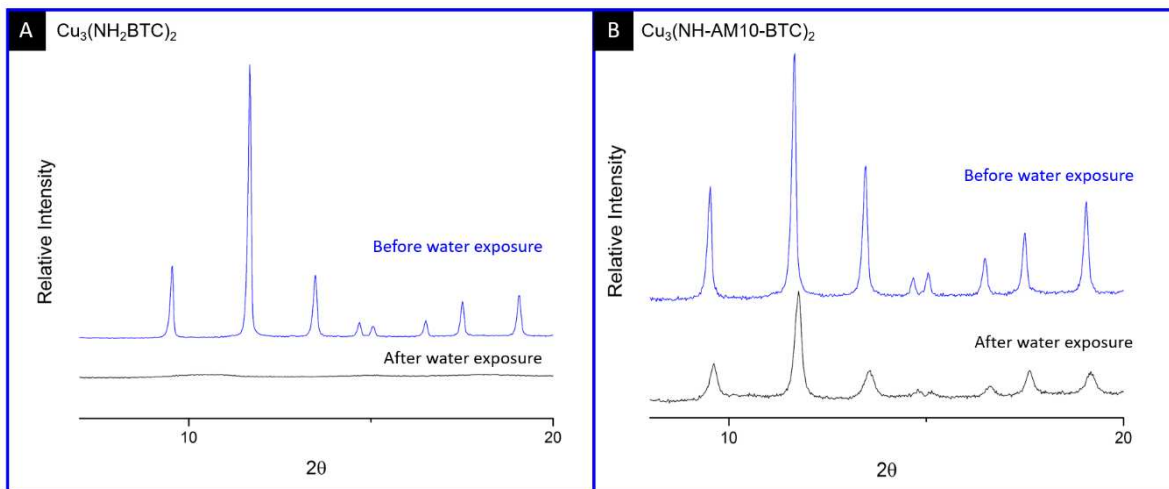


Figure A23. Powder X-ray diffraction data before (top, shown in blue) and after (bottom, shown in black) water submersion. (A) $\text{Cu}_3(\text{NH}_2\text{BTC})_2$ before water exposure. Little to no diffraction pattern is observed after water exposure with the unmodified material. (B) $\text{Cu}_3(\text{NH-AM10-BTC})_2$. The result shown is with 14% conversion and minor changes in intensity and slight shift in the 2θ diffraction pattern is observed after water exposure with the unmodified material. To our knowledge, this increased amount of water stability has never been observed for copper MOFs via synthetic functionalization of the ligand, and foreshadows exciting possibilities for applications of $\text{Cu}_3(\text{NH}_2\text{BTC})_2$ in place of $\text{Cu}_3(\text{BTC})_2$.

A.7. 3-D Crystal Drawings

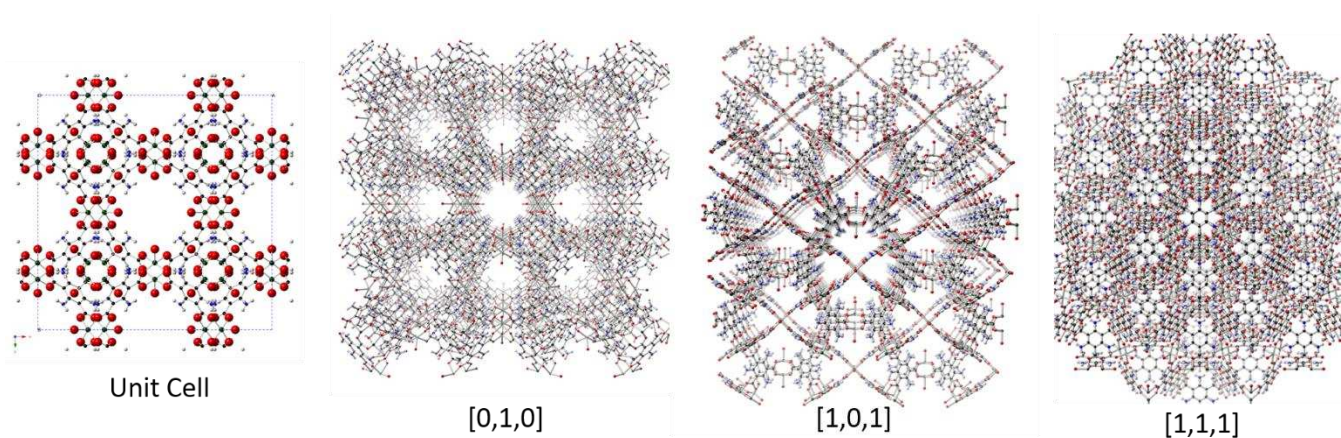


Figure A24. $\text{Cu}_3(\text{NH}_2\text{BTC})_2$ 3-dimensional drawings showing potential access views of the amino functional handle. Oxygen is highlighted in red, nitrogen in blue, copper in green, hydrogen in grey, and carbon in black.

A.8. SEM of MOF

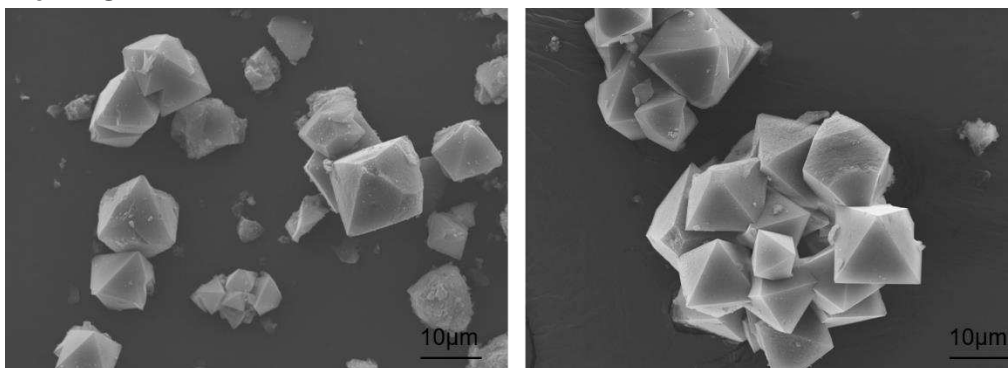


Figure A25. $\text{Cu}_3(\text{NH}_2\text{BTC})_2$ and $\text{Cu}_3(\text{NH-AM5-BTC})_2$ (left to right) SEM images after gentle grinding taken at 1400X.

REFERENCES

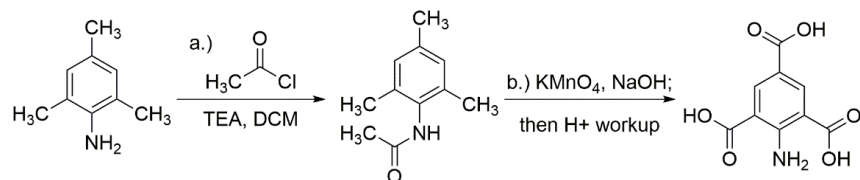
1. Peikert, K.; Hoffmann, F.; Froba, M. *Chem. Commun.* **2012**, *48*, 11196-11198.
2. Cai, Y.; Kulkarni, A.; Huang, Y.-G.; Sholl, D.; Walton, K. *Crystal Growth & Design* **2014**, *14*, 6122-6128.

APPENDIX B

SUPPORTING INFORMATION FOR CHAPTER 3

B.1. Ligand Details

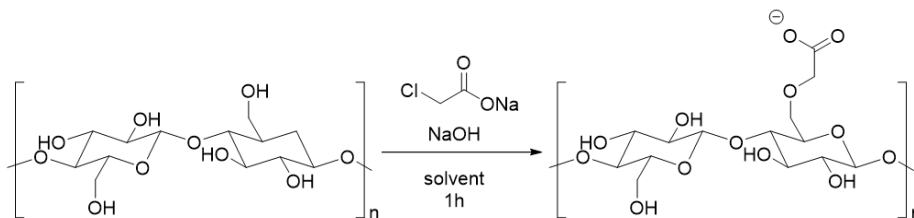
Scheme B1. NH₂H₃BTC Synthesis



The ligand was synthesized as previously reported. All NMR and MS characterization was consistent with that previously published.⁴⁶

B.2. Carboxymethylation of natural cotton

Scheme B2. Carboxymethylation of cotton



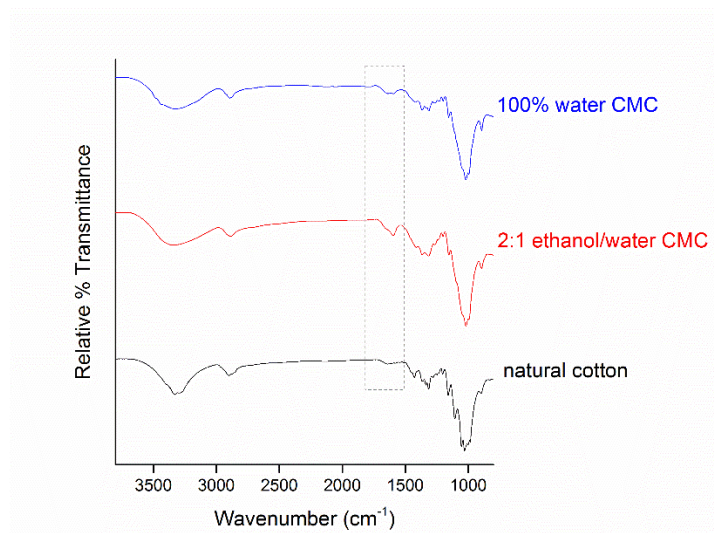


Figure B1. IR of carboxymethylated cotton with 100% water solvent and 2:1 ethanol/water solvent. The modified material with alcohol shows an enhanced intensity around 1640 cm⁻¹ representing the C=O addition from modification.

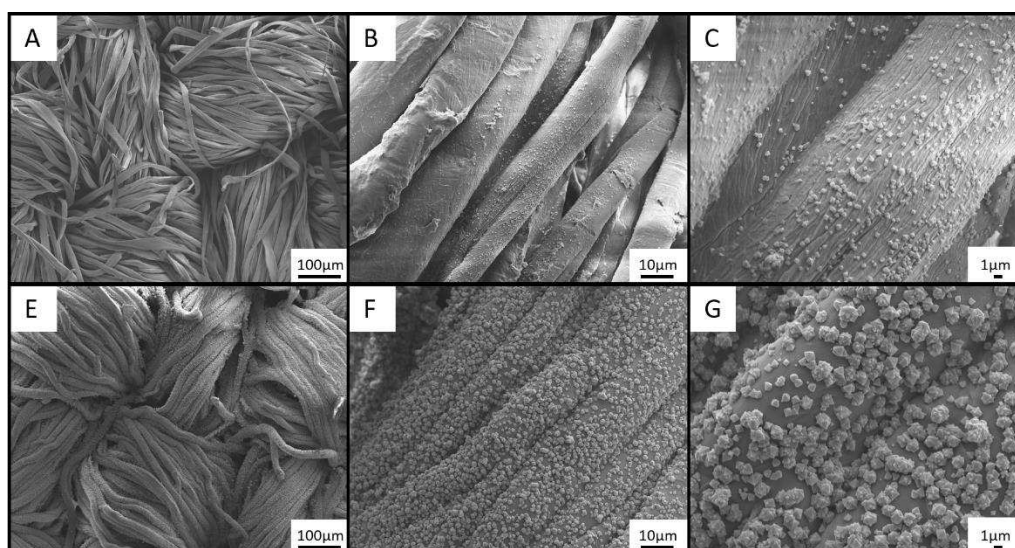


Figure B2. $\text{Cu}_3(\text{NH}_2\text{BTC})_2$ grown with 10 layers onto carboxymethylated cotton, whereby 100% water (A-C) was used as the solvent or 2:1 ethanol/water was used as solvent (E-F). These images indicate coverage is significantly enhanced by carboxymethylation with alcohol. Thus, 2:1 ethanol/water was used for future optimization.

B.3. Layer-by-layer MOF growth

Scheme B3. MOF growth

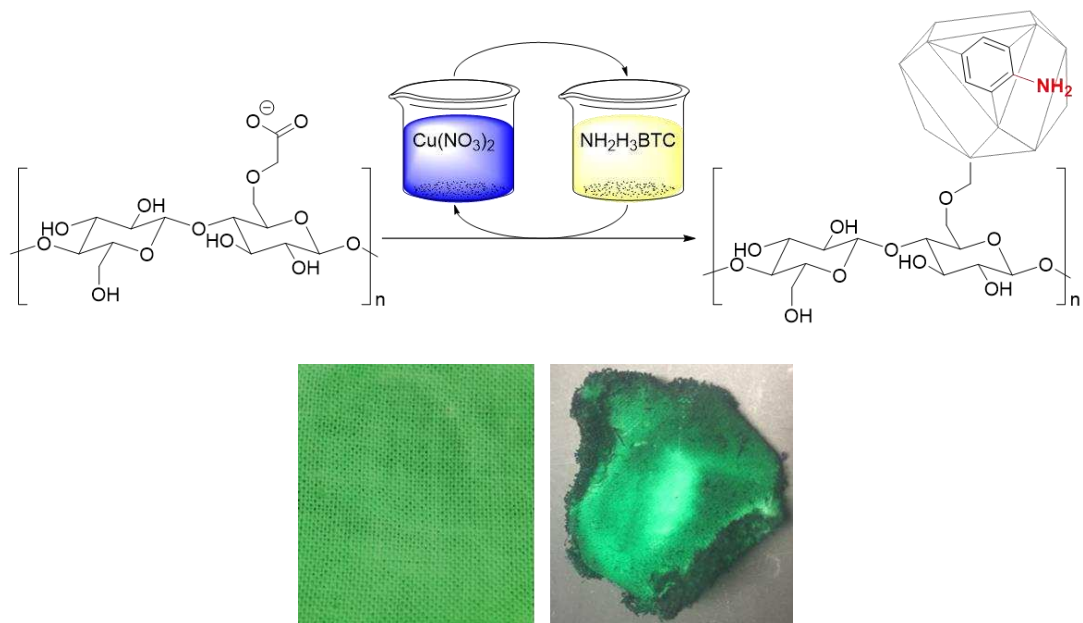
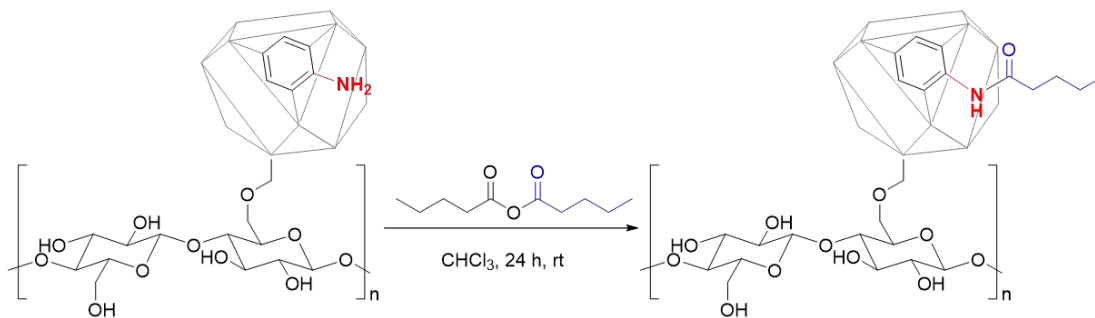


Figure B3. Cu₃(NH₂BTC)₂ grown on cotton using layer-by-layer methodology (left) yields uniform coverage of MOF, unlike self-assembly (right), whereby the MOF was grown by traditional hydrothermal conditions soaking carboxymethylated cotton in a sonicated solution containing both the MOF ligand and copper (II) nitrate at 85 °C for 42 hours.

B.4. Modified MOF-cotton AM-5

Scheme B4. PSM of MOF on cotton



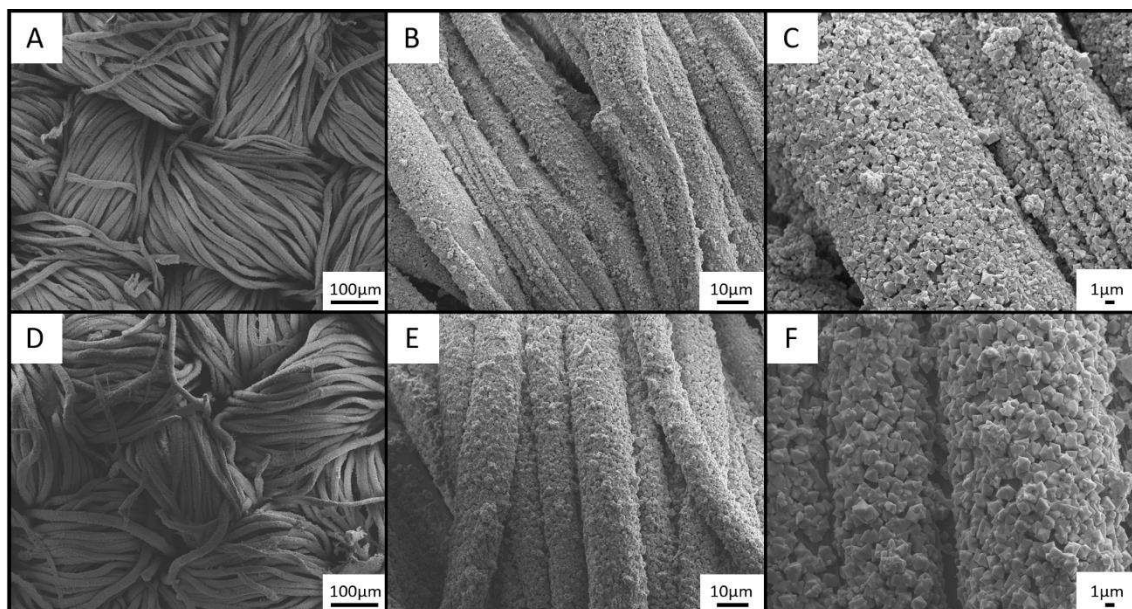


Figure B4. Images A-C are MOF on cotton. Images D-F are of postsynthetically modified MOF-cotton (AM-5). These images suggest that the modification process does not yield detectable degradation of the MOF as the MOF crystallites display similar size and morphology to the unmodified MOF-cotton materials.

B.5. PXRD after NBM exposure

For these experiments a swatch 0.7 cm x 0.7 cm was added to a 2 dram vial followed by 1 mL of room temperature nutrient broth media (NBM). After 1 h the solution was decanted and the material rinsed thoroughly with ethanol. The materials were transferred to a clean vial and soaked in ethanol for 5 minutes, and removed to dry at room temperature.

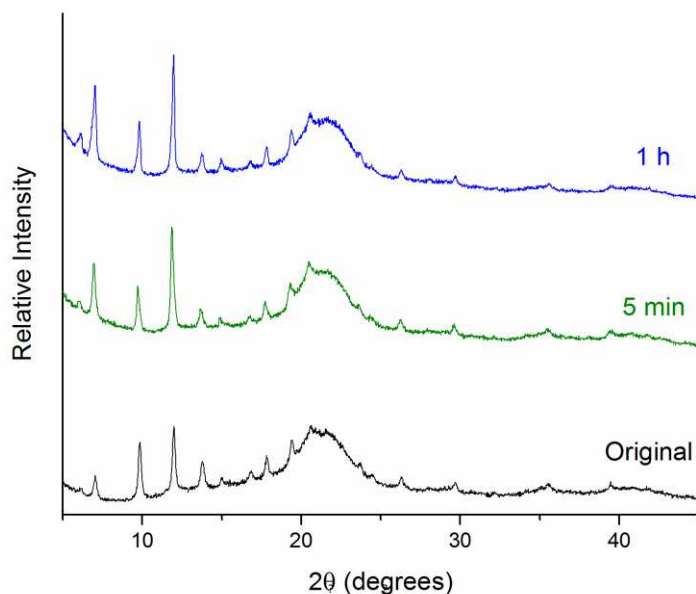


Figure B5. PXRD of the MOF-cotton materials (black) after being submerged at room temperature in NBM after 5 min (green) and 1 h (blue). Importantly, the MOF on cotton retain crystallinity after 1 h in NBM.

REFERENCES

1. Rubin, H. N.; Reynolds, M. M. *Inorg. Chem.* **2017**, *56* (9), 5266-5274.

APPENDIX C

SUPPORTING INFORMATION FOR CHAPTER 4

C.1 PXRD Characterization of $\text{Cu}_3(\text{NH}_2\text{BTC})_2$ used in Metal Ion Detection

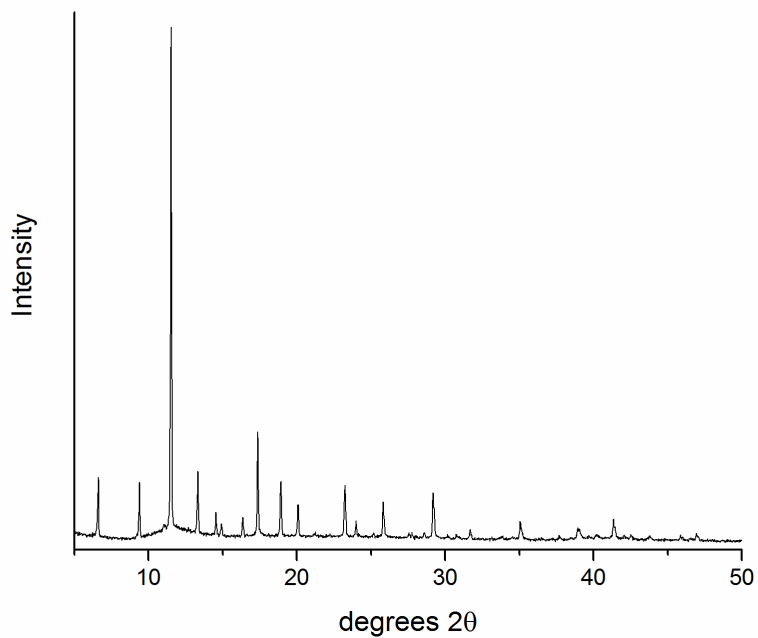


Figure C1. PXRD of synthesized $\text{Cu}_3(\text{NH}_2\text{BTC})_2$ used in photoluminescent ion detection studies.

APPENDIX D

SUPPORTING INFORMATION FOR CHAPTER 6⁶

D.1. Additional Characterization Methods

Elemental analysis was performed using ICP-AES provided by the Colorado State University Soil, Water and Plant Testing Laboratory. Powder X-Ray diffraction (PXRD) patterns were obtained using a Bruker D8 Discover DaVinci Powder X-ray Diffractometer with CuK α radiation operated at 40 kV and 40 mA. A typical scan rate was 0.3 sec/step with a step size of 0.02 deg. Ligand characterization ¹H NMR spectra was acquired using an Agilent (Inova) 400MHz spectrometer.

D.2. PXRD Characterization of CuBTTri

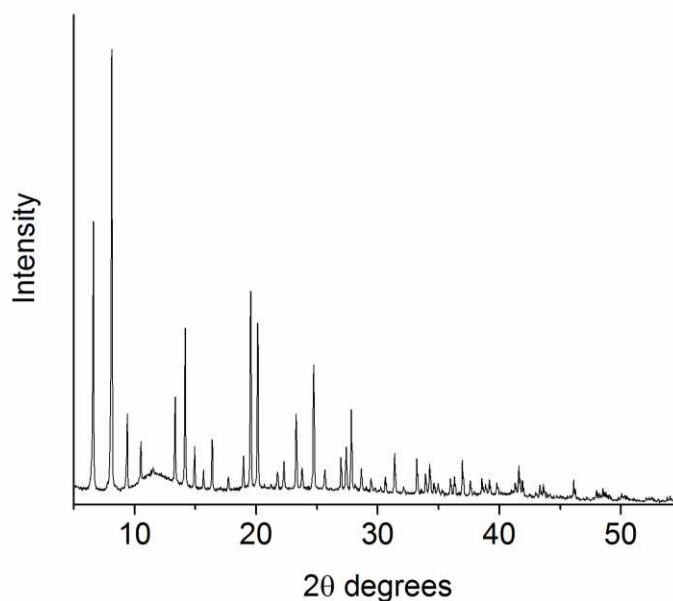


Figure D1. PXRD of synthesized CuBTTri.

⁶ This supporting information was compiled in collaboration with Robert Tuttle. Robert Tuttle synthesized GSNO (97% pure by UV-Vis) and CuBTTri (those details are omitted), organized the tables and graphs, while my contributions were focused more on the ¹H NMR spectra provided and labeled as well as PXRD and MOF drawings.

D.3. ^1H NMR Peak Assignments of GSH

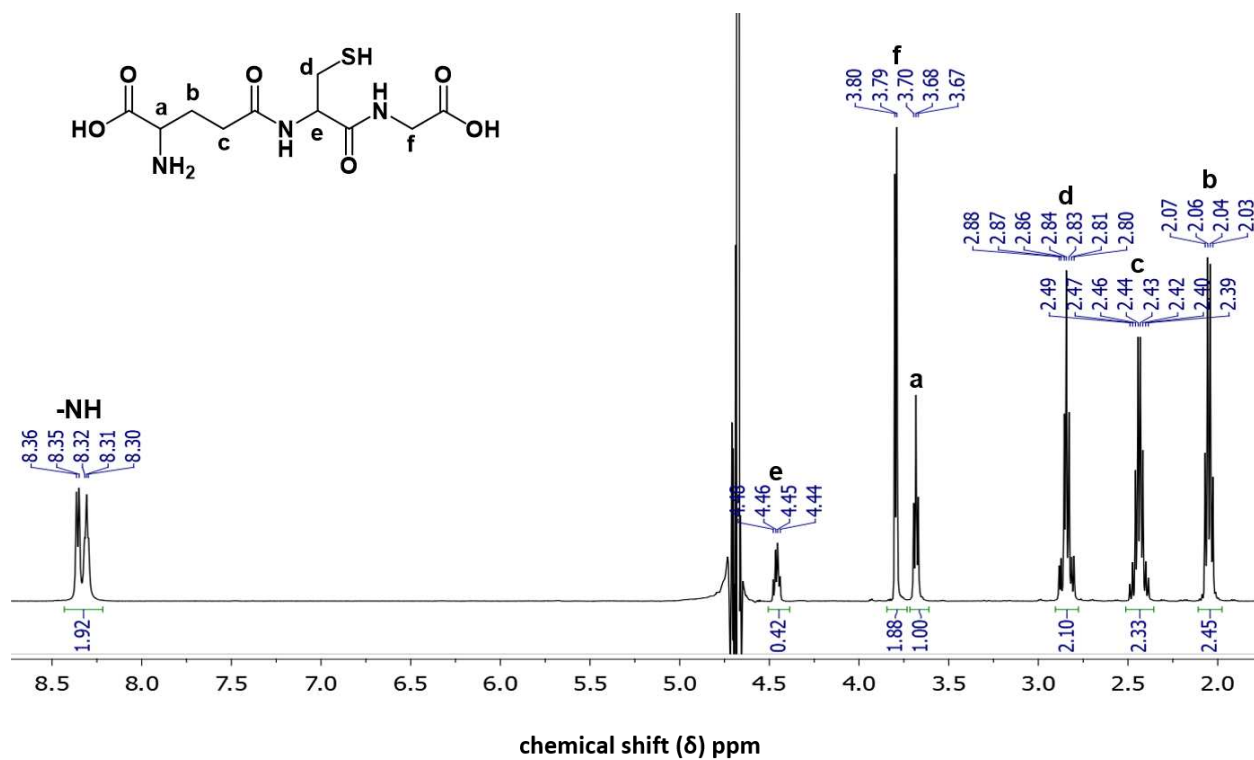


Figure D2. ^1H NMR peak assigned spectra of GSH.

D.4. CuBTTri Drawings.

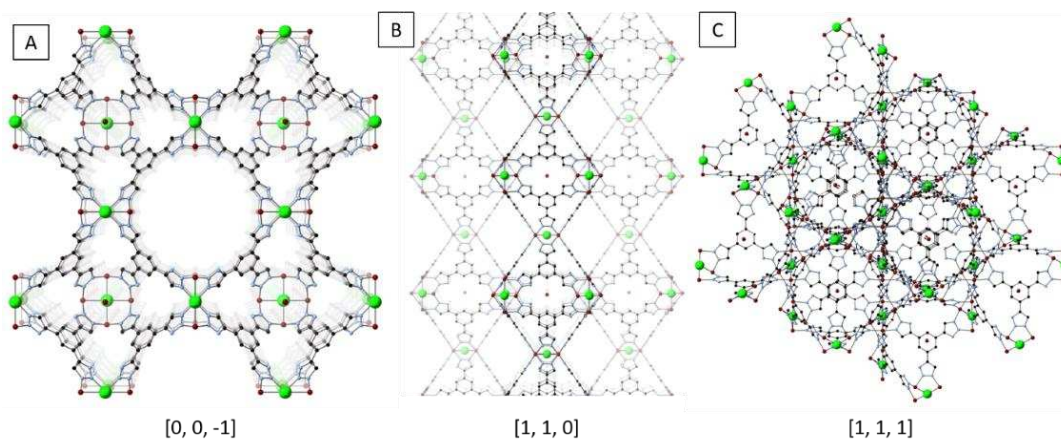


Figure D3. CrystalMaker drawings of CuBTTri along the (A) $[0, 0, -1]$, (B) $[1, 1, 0]$, and (C) $[1, 1, 1]$ planes.

D.5. Calibration ^1H NMR Spectra and Resulting Calibration Curves

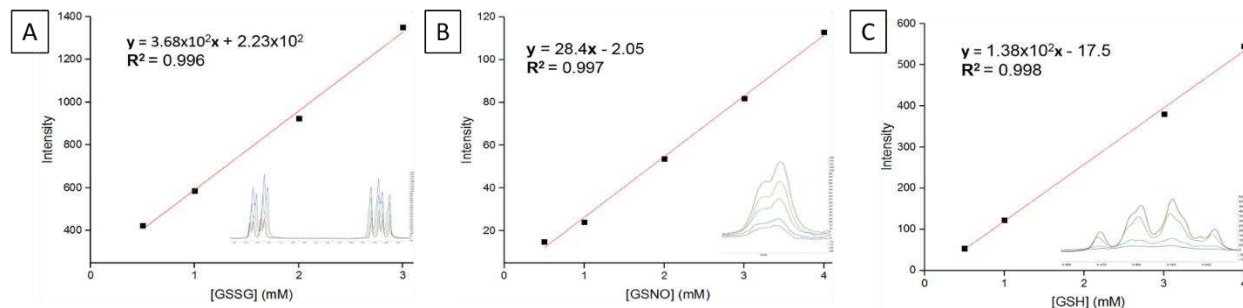


Figure D4. Calibration curves used to calculate (A) [GSSG] (Inset: Purple = 3 mM, Blue = 2mM, Green = 1 mM, Red = 0.5 mM), (B) [GSNO] (Inset: Red = 4 mM, Yellow = 3mM, Green = 2mM, Blue = 1 mM, Purple = 0.5 mM), and (C) [GSH] (Inset: Red = 4 mM, Yellow = 3mM, Blue = 1 mM, Purple = 0.5 mM) in reaction samples.

D.6. GSNO after 16 h (no catalyst)

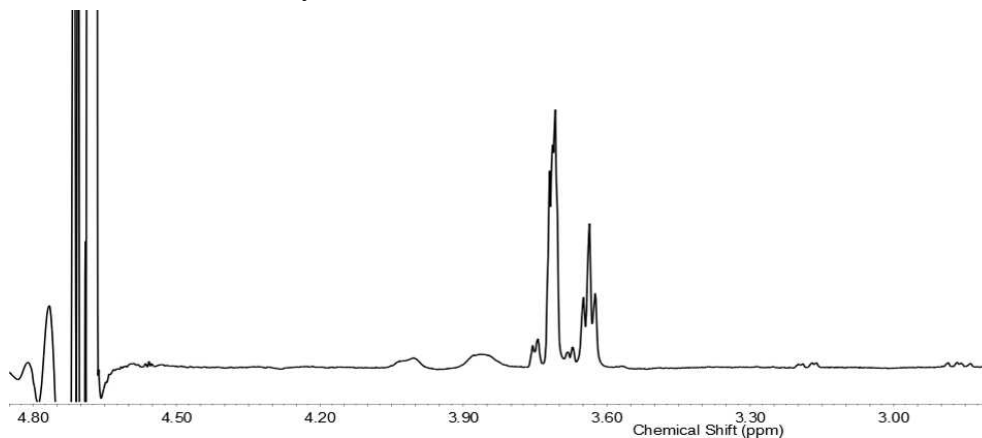


Figure D5. Resulting ^1H NMR spectra of GSNO (1 mM) alone without Cu^{2+} or Cu-BTtri present after 16 h. Spectra provided supports GSNO alone (no copper containing catalytic species) under experimental conditions does not yield decomposition of GSNO.

D.7. GSNO and GSH (no catalytic copper species)

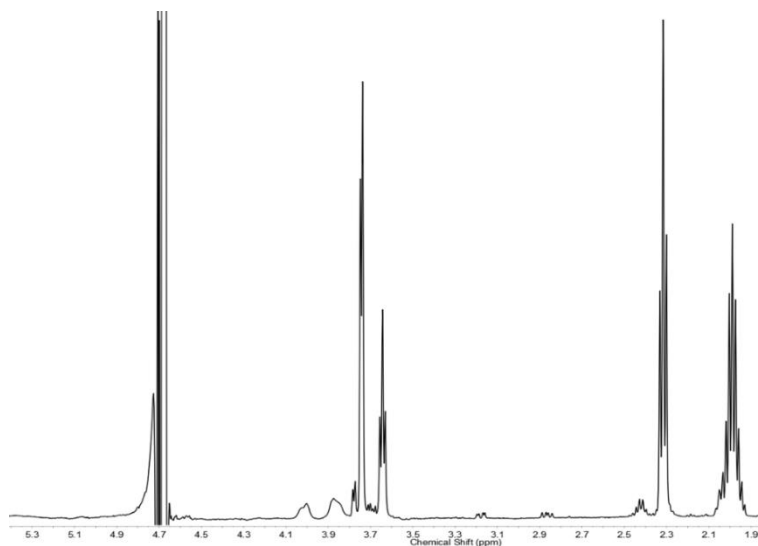


Figure D6. ¹H NMR spectra of GSNO (1 mM) and GSH (0.04 mM) after 16 h (no copper-containing catalytic species present). Observed GSNO decomposition does not take place due to low levels of GSH alone.

D.8. GSNO (2 mM) and GSH (2 mM)

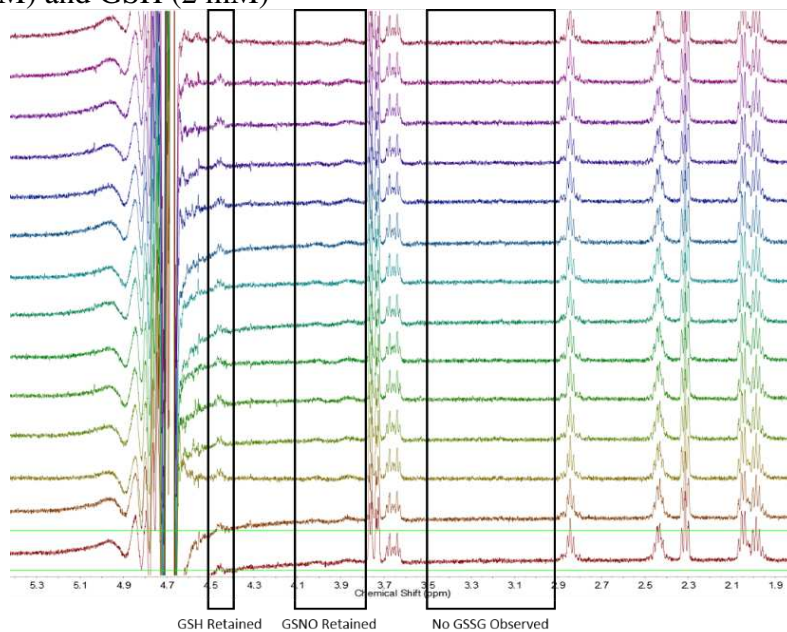


Figure D7. Reaction between GSNO (2 mM) and GSH (2 mM) over the course of 14 h. Spectra were collected at 1 h intervals. Each spectrum was collected with 8 transients. Spectra provided to support the need for CuBTtri to observe GSNO decomposition. GSH alone does not induce significant GSNO decomposition without CuBTtri present.

D.9. Cu-BTtri Reactions Under Open Atmospheric Conditions

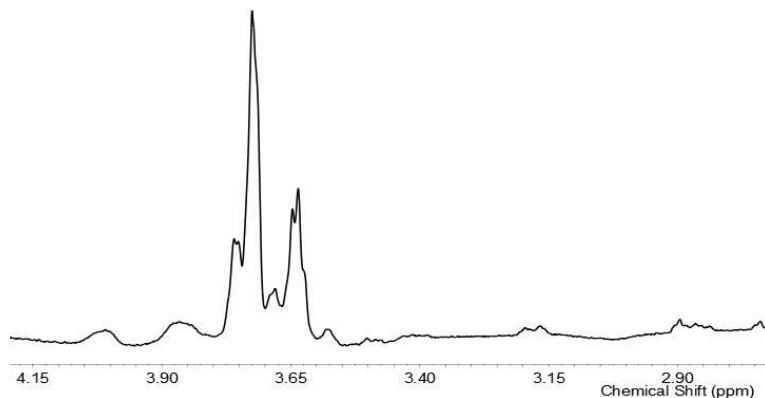


Figure D8. ^1H NMR spectra of reaction between GSNO (2mM) and Cu-BTtri (2:1 mol ratio GSNO:Cu) bubbled with house air after 1 h. Spectra shows that by introducing a chemical oxidant (O_2) into the reaction system, little to no GSNO decomposition occurs. Conversely, introduction of a chemical reductant (GSH) into the reaction (not shown).

D. 10. Incomplete Cu^{2+} Reactions with Excess GSH

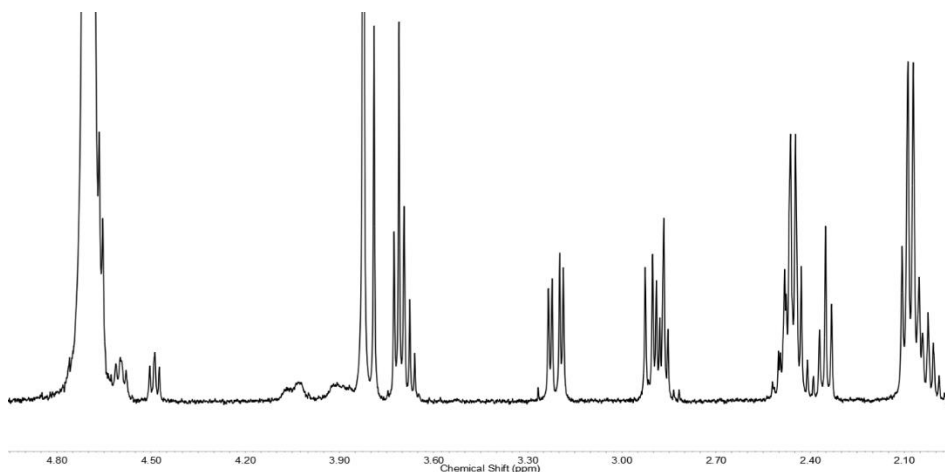


Figure D9. Resulting ^1H NMR spectra of reaction between GSNO (1 mM) and Cu^{2+} (0.2 mM) in the presence of GSH (1 mM) after 12 h. The reaction reaches 50% completion after approximately 1 h, and then does not proceed further (over additional 11 h monitored).

APPENDIX E

Nitric Oxide Donors in Nerve Regeneration⁷

Nitric oxide (NO) is a key signaling molecule involved in various critical activities related to nervous system functioning such as intracellular and intercellular messaging. Experimentation that aids in understanding the particular role of NO in such pathways has become increasingly popular in recent years. While recovery of the nervous system after trauma is still not entirely understood, many believe NO may be an important factor for regulating fundamental processes associated with such traumas.¹ However, various studies showed that NO signaling provides a switching mechanism between the degenerative and regenerative states of neuronal remodeling mediated by the available NO concentration *in situ*.^{2,3} In brief, according to Rabinovich et al. high NO levels promote the neurodegeneration while low levels support the neuroregeneration. Given the dual nature of NO, a detailed description of the role and mechanism of NO in both neuroregeneration and neurodegeneration is crucial for the proper design of an NO-releasing pro-drug or device for the desired application. A comprehensive narration of these aspects is provided in the first section of this chapter. Subsequently, a detailed and complete summary of various NO donors evaluated for nerve regenerations is presented.

⁷ This work was adapted with permission from Vinod B. Damodaran, Divya Bhatnagar, Heather Rubin, Melissa M. Reynolds, Chapter 6 - Nitric Oxide Donors in Nerve Regeneration, Editors Amedea Barozzi Seabra, Nitric Oxide Donors, Academic Press, 2017, Pages 141 - 168. Copyright 2017 Elsevier Inc. All rights reserved. Vinod B. Damodaran and Divya Bhatnagar contributed to the overall editing of the work, finding of references, and writing portions of the introduction. All other work was researched and written by Heather Rubin (primarily section labeled “Examples of NO donors evaluated for nerve regeneration” until the section “Conclusion”).

NO in neuroregeneration

Neurotransmission

Nitric oxide functions as a critical neurotransmitter in both central nervous system (CNS) and peripheral nervous system (PNS) by cyclic guanosine monophosphate (cGMP) dependent mechanisms. Garthwaite et al. were the first to report the role of NO as a neurotransmitter.⁴ They observed activation of brain NMDA (N-methyl-D-aspartate) receptors by glutamate resulted in the release of NO, which had similar properties as endothelium-derived relaxing factor (EDRF), a local hormone that causes smooth muscle relaxation through a cGMP dependent pathway. NO is a free radical gas which simply diffuses from nerve terminals into adjacent cells and forms covalent linkages to a soluble guanylyl cyclase (sGC) enzyme or other protein to stimulate their activity.^{5,6} Figure E1 presents a schematic illustration of the signaling mechanism of NO through cGMP-pathway.⁷

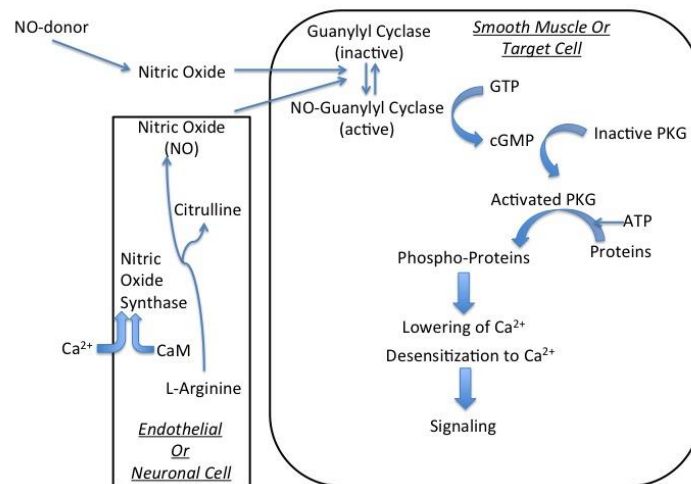


Figure E1. Nitric oxide signaling through cGMP pathway. NO is synthesized from L-arginine by nitric oxide synthases (NOS) through an increase in the cellular Ca^{2+} concentration or through the binding of Ca^{2+} /calmodulin (CaM) complex. NO then diffuses into the extracellular space and vascular smooth muscle cell and activates guanylyl cyclase to synthesize cGMP from GTP. The increase in the cGMP level enables the PKG phosphotransferase activity and leads to the signaling activity. Adapted from Francis, S.H., Corbin, J.D., 2005. *Phosphodiesterase-5 inhibition: the molecular biology of erectile function and dysfunction*. *Urol. Clin. North Am.* 32, 419–429, Elsevier. ⁴ © Elsevier.

The covalent binding of NO to sGC causes 100 to 200- fold activation of the enzyme, which increases the conversion of GTP to cGMP, resulting in increased production of cGMP and initiation of a cGMP-signaling pathway.⁸ Elevation in cGMP can further activate cGMP dependent protein kinase (PKG), other phosphodiesterases, cGMP regulated ion channels and transcription factors through which NO influences smooth muscle relaxation, synaptic plasticity, neurotransmission and neurosecretion.^{9,10}

NO donors can further stimulate the release of classical neurotransmitters such as acetylcholine. In the nucleus accumbens (NAc), the glutamatergic neurons can release glutamate where cGMP mediates the NO-induced release of acetylcholine by enhancing the glutamate outflow.¹¹ Lorraine et al. showed that NO can increase the release of dopamine and serotonin in the rat medial preoptic area by an sGC-cGMP dependent pathway.¹² N-methyl-D-aspartate (NMDA) receptors and NO donors have also proved to stimulate the noradrenaline (NE) release in the hippocampus, both *in vivo* and *in vitro*, whereas NOS inhibitors have shown to decrease NE levels.¹³

Neuronal growth and synaptic plasticity

The increases in NOS expression during development play a role in synapse formation and maturation. Disruption of the NO signaling during the development phase can introduce changes in synapse morphology and interfere with neuronal growth.¹⁴⁻¹⁶ Long-term potentiation (LTP) and long-term depression (LTD) are the two mechanisms, which affect the efficacy of a synapse and synaptic plasticity is important for recognition memory. NO that is produced in the postsynaptic cell and acts on the presynaptic sites is recognized as a retrograde diffusible messenger. Tamagnini et al. showed that NO dependent signaling is critical in perirhinal cortex-dependent visual

recognition memory in the rats.¹⁷ Cooke et al. studied the role of endogenous NO signaling in neuronal growth and synaptic remodeling after nerve injury in CNS.¹⁸ They demonstrated that blocking sGC activity completely suppresses neurite extension and synaptic remodeling after nerve crush, showing the importance of cGMP in these processes. However, they concluded that the effects of cGMP-dependent protein kinase inhibition on neurite growth and synaptic remodeling were mediated by separate signaling pathways.

Neuroprotectant

Nitric oxide can have beneficial effects on recovery from nerve injury. Yuan et al. used NOS blocker, *N*_ω-nitro-l-arginine methyl ester (l-NAME) after hypophysectomy in the adult Sprague–Dawley (SD) rats.¹⁹ They found that the l-NAME treatment effectively blocked the regeneration of magnocellular neurons of the rodent hypothalamus suggesting that the induced increase of nNOS expression enhances the regenerative ability of magnocellular neurons following hypophysectomy. NO also plays a role in axonal elongation.^{20,21} NO-cGMP transduction pathway is known to play a vital role in regulating axonal growth and neuronal migration. Stern et al.²² showed that NO/cGMP promotes axonal regeneration in an insect embryo, whereas inhibiting NO or sGC delays regeneration. NO-induced cGMP immunostaining shown in Figure E2 confirms the serotonergic neurons as direct targets of NO.

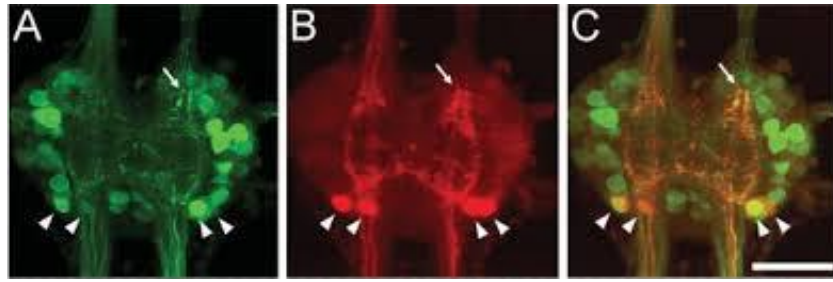
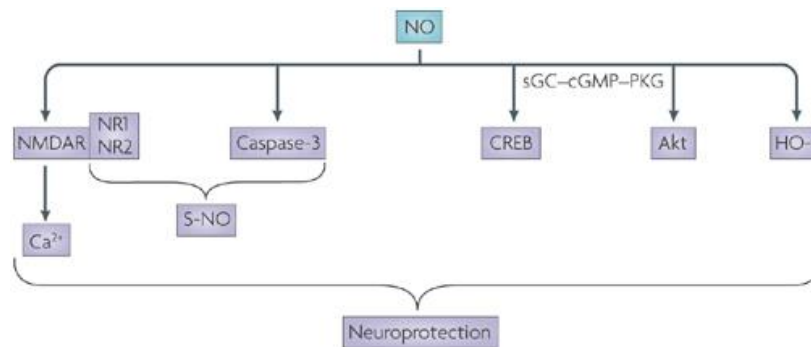


Figure E2. Nitric oxide-induced cGMP immunoreactivity in serotonergic and other neurons. (A) Confocal image of an abdominal ganglion A6 of a 65% embryo stained for NO-induced cyclic GMP, 2 h post crush. Severed axons have already retreated into the ganglion (arrow). (B) Confocal image of serotonin immunoreactivity in the same preparation as in (A). Arrowheads point to the four serotonergic cells. (C) Superimposed images of (A) and (B), revealing colocalization of serotonin and NO-induced cGMP in cell bodies (arrowheads) and axon stumps (small arrow). Scale bar: 100 μ m, anterior is to the top. Reproduced with permission from *Reproduced with permission from Stern, M., Bicker, G., 2008a. Nitric oxide regulates axonal regeneration in an insect embryonic CNS. Dev. Neurobiol. 68, 295–308, John Wiley & Sons.*²² © John Wiley and Sons.



Nature Reviews | Neuroscience

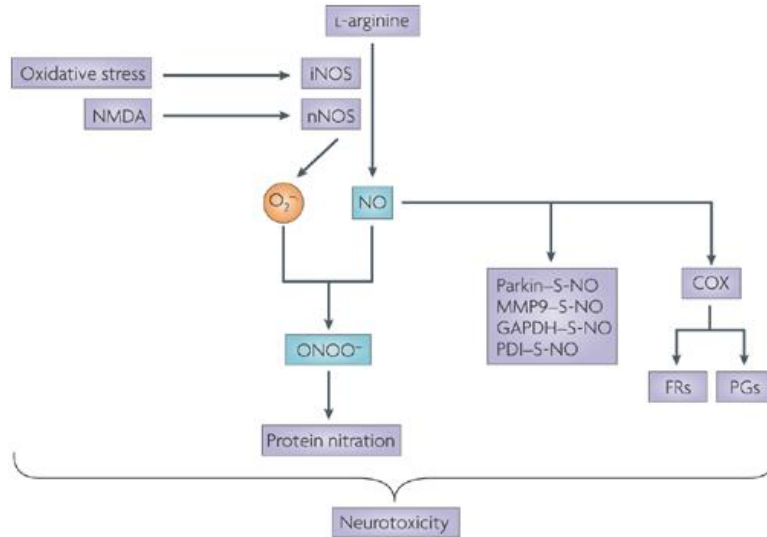
Figure E3. Neuroprotective effects of nitric oxide. nNOS, neuronal nitrogen oxide synthase; S-NO, S-nitrosylation. *Reproduced with permission from Calabrese, V., Mancuso, C., Calvani, M., Rizzarelli, E., Butterfield, D.A., Stella, A.M.G., 2007. Nitric oxide in the central nervous system: neuroprotection versus neurotoxicity. Nat. Rev. Neurosci. 8, 766–775, Nature Publishing Group.* © Nature Publishing Group.

In the peripheral nervous system, the three isoforms of NOS are overexpressed after transection of the nerve. High levels of NO are maintained at the lesion site by different cellular sources that act on different targets to benefiting peripheral nerve regeneration.²³ nNOS further is colocalized with growth associated protein-43 (GAP-43) in growth cones, thus indicating its

involvement in nerve regeneration.²⁴ It has been shown that the local release of NO following peripheral nerve injury is a crucial factor that can cause regenerative delay and delayed Wallerian degeneration in nNOS knockout mice after peripheral nerve injury.²⁵

Nitric oxide promotes cell survival and neuroprotection by different pathways as shown in Figure E3.²⁶ NO activates cyclic AMP-responsive-element-binding protein (CREB) and Akt, two proteins that are mainly involved in neuroprotection through the stimulation of the soluble guanylate cyclase (sGC)–cyclic GMP (cGMP)–protein kinase G (PKG) pathway.^{27,28} It is known that prolonged stimulation of *N*-methyl-d-aspartate receptor (NMDAR) causes toxic cell death.²⁹ By *S*-nitrosylation of thiols from cysteines such as caspase 3 and the NR1 and NR2 subunits of the NMDAR receptor, the intracellular Ca²⁺ influx responsible for cell death is inhibited thus leading to a decrease in cell death.³⁰ Under pro-oxidative conditions, excess NO and RNS can be formed. As a secondary mechanism, in the brain, NO induces the activity of hemeoxygenase 1 (HO-1) that is known to have a neuroprotective function. The upregulation of HO-1 is followed by an increase in biliverdin, the precursor of the powerful antioxidant and antinitrosative molecule bilirubin.³¹⁻³³

NO in neurodegeneration



Nature Reviews | Neuroscience

Figure E4. Neurotoxic effects of nitric oxide. If it is produced in excess, or if a cell is in a pro-oxidant state, nitric oxide (NO) has cytotoxic effects. It is well established that NO can react with superoxide anions (O_2^- ; produced by inducible nitric oxide synthase (iNOS) under inflammatory conditions or neuronal nitric oxide synthase (nNOS), as in the case of excitotoxicity) to form peroxynitrite ($ONOO^-$), an anion with strong oxidant properties. As a consequence of the interaction between peroxynitrite and cellular components, protein nitration takes place, resulting in damage to cellular components. The NO-mediated S-nitrosylation (S-NO) of certain substrates, such as matrix metalloproteinase 9 (MMP9), parkin, GAPDH and protein-disulphide isomerase (PDI), has been proposed to be a novel mechanism through which NO becomes neurotoxic. NO also activates the haemoprotein cyclooxygenase (COX). During its catalytic cycle, COX generates free radicals (FRs) and prostaglandins (PGs), both of which have strong pro-inflammatory features. NMDA, N-methyl-D-aspartate. Reproduced with permission from Ref.²² © Nature Publishing Group.

When produced in excess, NO can become toxic.²⁹ In peripheral nerve regeneration, localized increase of NO may be toxic to the regenerating axons.³⁰ At a higher concentration, NO can lead to cell death by increasing peroxynitrite ($ONOO^-$) concentrations. NO can react with oxygen in an oxidative-reductive reaction to form toxic compounds that belong to reactive nitrogen species (RNS) family. Peroxynitrite is formed by one such reaction between NO and superoxide anion and has been known to cause 'nitrosative stress' or cellular damage.^{34,35} These nitrosative

stresses have been known to be involved in many neurodegenerative disorders such as Parkinson's disease (PD), Huntington's disease (HD), Alzheimer's disease (AD), amyotrophic lateral sclerosis (ALS), multiple sclerosis (MS) and ischemia since all these diseases exhibit oxidative stress. Nitrotyrosination that alters the normal activity of proteins by inducing conformational changes has also been indicated in several neurodegenerative disorders.²⁹ Figure E4 illustrates the various mechanisms demonstrating the neurotoxic effects of nitric oxide.²⁶

Alzheimer's disease

Proteins such as α -enolase have been shown to being specifically oxidized in the brains of people with Alzheimer's disease.³⁶ α -enolase together with the increased nitration of triosephosphate isomerase causes altered glucose tolerance and metabolism, a possible mechanism exhibited in patients with Alzheimer's disease. Acetylcholinesterase inhibitors and *N*-methyl-D-aspartate (NMDA) receptor antagonists are the few available treatments to manage the cognitive deficit functions in AD. AD is a neurodegenerative disorder correlated with oxidative stress, and it has been shown that NO plays a role in the progression of the disease. AD patients have been found to have amyloid beta-peptide ($A\beta$) in their brains, which is characterized to form intracellular neurofibrillary tangles. $A\beta$ fibrils on their reaction with NO can induce ROS formation that can have toxic effects due to the production of peroxynitrite.³⁷ Amyloid β ($A\beta$) is a critical factor involved in the pathogenesis of Alzheimer's disease. Continuous infusion of intracerebroventricular $A\beta$ ¹⁻⁴⁰ induces iNOS leading to peroxynitrite formation followed by tyrosine nitration of proteins in the hippocampus. This can result in an impairment of nicotine-evoked acetylcholine (ACh) release and memory deficits. To achieve a delay in AD progression,

reducing A β production, cholinergic deficit and targeting NOS isoforms that damage the brain cells are an important consideration.

Parkinson's disease

PD is a neurodegenerative disorder associated with aging resulting from progressive loss of dopamine-producing brain cells within the substantia nigra. Several studies have indicated that oxidative damage in PD is mediated by the formation of peroxynitrite.³⁰ Dopamine (DA) release is modulated by NMDA receptor stimulation. Higher NO concentrations can decrease NMDA-induced DA levels.³⁸ Tyrosine hydroxylase is an enzyme that promotes the conversion of tyramine to dopamine. This enzyme can be inhibited by peroxynitrite through nitrotyrosination.³⁹ Peroxynitrite can also contribute to the depletion of major cellular antioxidant defense and has also been implicated in the apoptosis of dopaminergic neurons in PD.⁴⁰ Another pathway of PD involves Parkin, an enzyme protein that plays an important role in the ubiquitin-proteasome system and acts as a regulator of protein breakdown. It has been shown that *S*-nitrosocysteine derived NO can nitrosylate parkin. Parkin mutation has been acknowledged as a common pathway of sporadic and hereditary Parkinson's disease.⁴¹

Nitric oxide derived from the endogenous nitrosothiol *S*-nitrosocysteine can *S*-nitrosylate matrix metalloproteinase 9 (MMP9), causing neuronal apoptosis. MMP9s are implicated in the pathogenesis of neurodegenerative disorders (stroke, AD, multiple sclerosis).⁴² A similar mechanism has been proposed for Parkinson's disease. The GAPDH–SIAH1 (E3 ubiquitin ligase) complex is formed when NO *S*-nitrosylates GAPDH, thereby inducing apoptosis.⁴³ During the neurodegenerative diseases such as cerebral ischemia, denatured proteins generated by protein-disulphide isomerase (PDI) can accumulate and be toxic to neurons. In the brains of AD and PD

patients, *S*-nitrosylation of cysteines and the inhibition of PDI enzymatic activity has been observed.⁴⁴

Huntington's disease

Huntington's disease is another neurodegenerative disease that causes progressive breakdown of nerve cells in the brain, particularly in the striatum and cerebral cortex. It is a genetic disorder that can cause dementia. Researchers have reported that oxidative and nitrosative damage in the basal ganglia could be the trigger for HD.⁴⁵ Development of HD is also affected by an excessive production of NO that can result in the oxidative fragmentation of DNA in striatal neurons.⁴⁶ Other studies have also implicated the increased production of oxidative stress products in HD patients.^{47,48}

In brief, NO can have both neuroprotective and neurotoxic effects. Here we have reviewed the role of NO in neuroregeneration as well as in neurodegeneration especially under oxidation and nitrotyrosination of functional proteins. Peroxynitrite formation is the primary reason underlining all the neurodegenerative diseases. Therefore, prevention of peroxynitrite formation without modifying the activity of NOS is one possible way to counter neurodegenerative disorders.

Examples of NO donors evaluated for nerve regeneration

NO donors have demonstrated the ability to increase NO bioavailability, which may yield desirable effects with regard to angiogenesis, vasodilation, neurogenesis and synaptic plasticity – all of which are central for neurorepair. Consequently, various NO donors (Figure E5) have been explored along with other important NO regulators to probe the pathways and provide mechanistic

insight surrounding NO influence on the recovery of the central, peripheral, and autonomic nervous systems. Herein, results and discussions of such findings are highlighted.

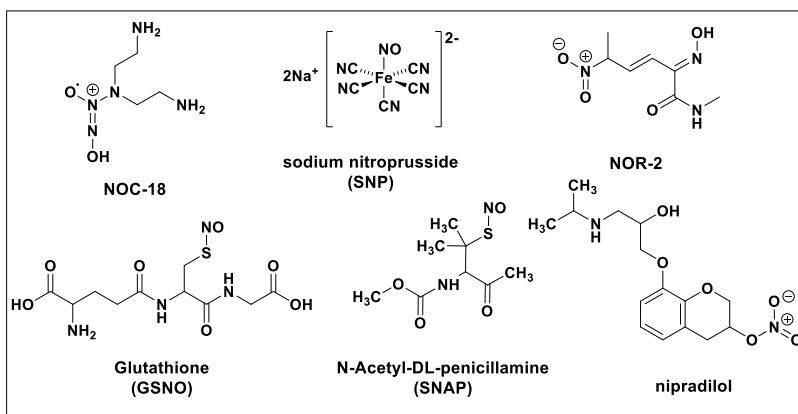


Figure E5 Various NO donors evaluated for nerve regeneration. *Adapted with permission from Nitric Oxide Donors: Novel Biomedical Applications and Perspectives; Vinod B. Damodaran, Divya Bhatnagar, Heather Rubin, Melissa M. Reynolds, Chapter 6 - Nitric Oxide Donors in Nerve Regeneration, Editors Amedea Barozzi Seabra, Academic Press, 2017, Pages 141 - 168. Copyright 2017 Elsevier Inc. All rights reserved.*

Hydra regeneration studies on the NO-cGMP pathway with NOC-18

NO has been recognized as vital to activating soluble guanylyl cyclase (sGC).⁴⁹ The resultant increase in intracellular cGMP affects many biochemical processes including activation of protein kinase G (PKG), notorious for regulating cellular processes.⁵⁰ Notably, the NO-cGMP pathway may be initiated during the differentiation of embryonic stem cells. To probe the potential for the NO-cGMP pathway to influence proliferation and differentiation events during development and regeneration, the involvement of NO in the regeneration of *Hydra vulgaris* was evaluated.⁵¹ An archaic invertebrate with a nervous system, known as the *Hydra*, possesses an impressive capability to regenerate. A *Hydra* body is comparable to an early-stage embryo containing ectodermal, endodermal, and interstitial stem cells. Together, the three stem cell body and the ability to rapidly regenerate makes *Hydra* an ideal system for studying morphogenetic processes including development and regeneration. An initial control study with regenerating

Hydra found NO concentrations steadily increased during *Hydra* regeneration, peaking 36 h after damage, as determined by the Griess Assay. The Griess Assay estimates NO concentrations based on nitrite ions in solution, however, this method has proven inaccurate for measuring NO.⁵² Although the exact amount of NO may not be accurate, the outcomes still suggest NO release plays a vital role in regeneration. Expanding upon this study, the heads of the specimen, consisting of the hyposome and tentacles, were removed under a microscope and placed in culture plates for observation. Samples were dosed daily with either the NO donor 3, 3-bis (aminoethyl)-1-hydroxy-2-oxo-1-triazene (NOC-18); the NOS inhibitor L-nitroarginine methyl ester (L-NAME); the guanylate cyclase inhibitor 1H [1,2,4]oxadiazolo-[4,3-a]quinoxalin-1-one (ODQ); or the protein kinase G inhibitor KT-5823. Nitric oxide synthase (NOS) encompasses a set of enzymes that catalyze the release of NO from endogenous sources like L-arginine; therefore, areas with high concentrations of these enzymes are believed to be more active with regard to NO release. Under a microscope, tentacles per head were monitored for growth. The decapitated *Hydra* treated with NOC-18 showed significantly increased growth rates in comparison to the control and L-NAME treated samples (Figure E6). After just two days, NOC-18 remarkably showed tentacle growth, whereas, no tentacles were visible in the control and L-NAME treated samples. Similarly, the diminished growth rate was observed when samples were treated with ODQ or KT-5823, suggesting that sGC and PKG are both involved in the NO pathway of *Hydra* regeneration.

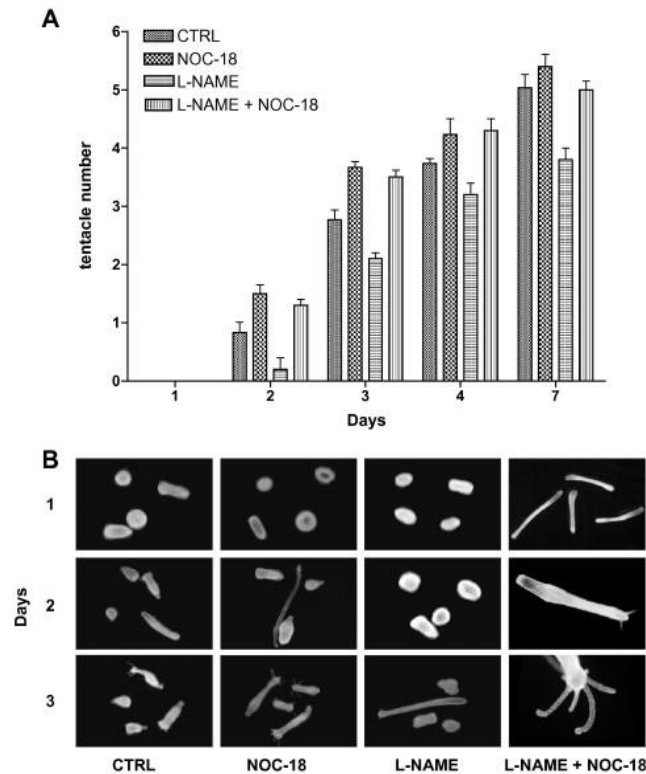


Figure E6 NO donor and NOS inhibitor affect Hydra regeneration. Hydra were treated with the NO donor NOC-18, the NOS inhibitor L-NAME, or both. NOC-18-treated samples enhanced regenerative rate, whereas L-NAME treatment inhibited the regeneration process. *Reproduced with permission from Colasanti, M., Mazzone, V., Mancinelli, L., Leone, S., Venturini, G., 2009. Involvement of nitric oxide in the head regeneration of Hydra vulgaris. Nitric Oxide 21, 164–170, Elsevier. © Elsevier.*

The authors also demonstrated the impact of NO on cell proliferation and discovered that DNA synthesis was accelerated in the presence of NOC-18 and impeded when treated with L-NAME. These results demonstrate NO also plays an important role in cell proliferation of *Hydra* regeneration. NOC-18 is a slow releasing (20 h half-life) NO donor where the rate of release is attributed to the structure. NOC-18 is an ideal NO donor since the amine byproduct formed has no known interferences with cellular activities; however, since NO release is spontaneous and the donor is reported to rapidly degrade it is uncertain as to how much NO was administered in the *Hydra* regeneration experiments. Even though effective NO concentrations are not conveyed in this study, it is clear that the NO-cGMP/PKG pathway is vital to cnidarian *Hydra* regeneration, in

turn supporting the apparent involvement of this pathway in early embryogenesis, likely translatable to more complex animals.

Locust studies on NO-cGMP with NOC-18 and SNP

Insects are acknowledged as invertebrates with complex nervous systems, many of which capable of regeneration in both the peripheral and central nervous systems. Since regeneration of the central nervous system (CNS) in advanced vertebrates following axonal injury has been observed with minimal success, insects present a unique opportunity to study these processes. The locust has displayed axonal regeneration subsequent to nerve crush injury and the mechanism of such regeneration has been explored by Stern and coworkers in an attempt to evaluate how the NO-cGMP system is integrated into this physiological event.^{53,54} The foremost goal was to determine if the locust embryo exemplifies an appropriate model system for investigating factors that manipulate CNS regeneration. In one study, the connective tissues on the right side were carefully crushed with forceps without affecting the neural sheath of the locust embryos (mostly 65-70% developed). The researchers focused on Serotonergic neurons of the *Locusta*, where typically neurons reform around 40% embryogenesis. The expression of SERT, serotonin reuptake transporter, as well as physiological serotonin synthesis allowed for developmental tracking of neurons via staining. In the crushed region there were four serotonin-immunoreactive axons. Typically, after a few hours, neurons began to appear. In most cases after 24 h minor serotonin-immunoreactive processes were noticeable, and after 96 h immunofiber regeneration was achieved, many of which reaching the adjacent ganglia. Regenerated fibers were visually obvious due to thinner appearance and abnormal growth directions and configuration (not as straight) compared to normal neurons. The number of regenerated serotonin-immunoreactive neurites in

the connective tissue that grew beyond the crush site were counted and compared to those on the un-crushed control side. In culture post-crush, an average of 44.5% regeneration occurred in the first 48 h. Meaning, 48 h post-crush a great degree of nerve regeneration in the locust was achieved, rendering this system an ideal model on which to investigate the uncertainties surrounding how an increase in NOC-18 can influence such CNS regeneration events.

As described previously with the *Hydra* studies, the NO-cGMP pathway is involved in regeneration of the nervous system in cnidarian invertebrates. To assess if a similar mechanism was at play in the CNS regeneration event of locusts, NO and cGMP concentrations were methodically manipulated. When NOC-18 was employed as an NO donor, a significant increase in regeneration was observed. Concentrations of cGMP within the crushed samples were increased when incubated with membrane-permeable 8Br-cGMP. This ultimately led to a significant increase in the rate of regeneration. When the NO scavenger carboxy-PTIO was employed, significantly less axons displayed axonal regrowth over 48 h. Furthermore, utilizing the inhibitor of guanylyl cyclase, ODQ, regeneration was significantly inhibited; however, the coincubation with ODQ and 8Br-cGMP resulted in a restoration of regrowth to near normal levels. This data indicates NO-cGMP regulation is pertinent to axon regeneration in insect embryos. Using fluorescence labeling, the authors observed colocalization of NO initiated cGMP and serotonin in the cell bodies and neurites of S1 and S2 neurons, signifying NO likely directly targets serotonergic neurons. These results distinguish the NO donor NOC-18 as both a positive initiator of neurite outgrowth during development and beneficial in axonal regeneration after locust nerve crush, but once again the amount of NO required necessitates further investigation.

Sodium nitroprusside (SNP) is recognized as an NO donating drug often used as a vasodilator. Building upon the above study, SNP was used to determine if NOS is indeed localized

to the aforementioned areas proposed for NO activity after nervous system injury. SNP also aided in investigating what markers are most helpful for identifying this activity. The mechanism of NO release, however, appears to vary widely based on other small molecules present and can lead to a variety of byproducts.⁵⁵ Therefore, it is not surprising that unlike NOC-18, SNP had little to no effect on regeneration rates.

In another study, nervous systems of the *Locusta* were carefully dissected and subjected to abdominal ganglia nerve crush, without damaging the local sheath.⁵⁶ NADPH disphosphorase (NADPHd) staining and immunostaining against universal nitric oxide synthase (uNOS), citrulline, and NO-induced cGMP were used to assess components of the NO-cGMP pathway. NADPHd staining has been used to indicate NOS presence, however, it does not necessarily indicate NOS activity, ergo a byproduct of NO release known as citrulline was monitored to better represent the physiological activity of the existing NOS. Since all citrulline-immunoreactive cells also stained with NADPHd, and immunostained for NOS, it was determined NADPHd staining is an adequate method to detect nitrenergic cells. At 30% embryo development, NOS was detected with NADPHd, suggesting the NO-cGMP pathway may be engaged early-on during the development and formation of the locust CNS. On the other hand, NO activity and appearance as determined by the citrulline and NOS expression did not appear until late stages of the neuropil regeneration. This suggests that NO is unlikely to contribute to the formation in the neuropil region but may, however, be active during synapse formation or plasticity in later stages of development. Additional testing with NO donors may once again aid in a better understanding of the role of NO involved versus the impact of the specified chosen donor.

Goldfish optic nerve regeneration studied with NOR2 and SNAP

In the search to better understand the mechanism of NO in nerve regeneration, more complex vertebrate systems are being investigated. The NO-cGMP pathway impacts nerve regeneration following injury in both the *Hydra* and the *Locusta*. Primary studies in more advanced vertebrate systems would necessitate the ability to monitor the NO related influence in an isolable system capable of regeneration. Unlike mammalian retina, fish retinal ganglion cells (RGCs) can survive and regrow axons post nerve damage. Axonal regrowth begins 5-6 days after damage, tectum reinnervation occurs within 5-6 weeks, and visual functions are restored within 5-6 months. Therefore, axonal elongation during nerve regeneration in goldfish both *in vitro* and *in vivo* warranted investigation. In this study, performed by Koriyama and coworkers, the authors attempted to elucidate the role of the NO-cGMP pathway in goldfish RGCs and to clarify the specific mode of action.⁵⁷ Since NADPH activity is directly and proportionally associated with NO activity, NADPHd staining was performed and revealed intense staining in the photoreceptor cells and horizontal cells, with mild staining in the inner nuclear layer. Positive cells significantly increased within five days following axotomy and peaked after 20 days, while normal levels were restored after 40 days. Nitrite concentration was also assessed as an indicator of NO production using the Griess method. Nitrite production in the retina echoed the NADPH findings, showing a significant increase after 5 days, peaking around 20 days. The addition of an NOS inhibitor reduced nitrite concentration by nearly 24%, indicating that NO production was uniquely regulated during optic nerve regeneration. Following similar patterns as observed before, nNOS in the ganglion cell layer (GCL) also exhibited increased concentrations noticeable around 5 days, and peaking after 20 days following nerve lesion.

The regulatory effect of NO influence was manipulated using a series of NO donors and inhibitors (Figure E7). As monitored via positive staining with anti-GAP43 immunocytochemistry, retinal explant control cultures having spontaneous neurite outgrowth were quantified and designated as 100% regrowth. Employing the nitric oxide donor NOR2 at doses between 50-100 μ M, increased neurite outgrowth by 150% was achieved. Similar effects were observed when the NO donor *S*-nitroso-*N*-acetyl penicillamine (SNAP) was dosed at a slightly higher level of 500 μ M. On the other hand, NOS inhibitors like L-NAME, significantly reduced neurite outgrowth by 40-60% at doses of 200-400 μ M. By adding an NO donor back to a culture containing L-NAME, outgrowth rates could be restored to nearly 80-90% outgrowth. The NO scavenger c-PTIO was added at varying time points following NOR2 stimulation in order to highlight optimal NO bioavailability. When added at the same time as NOR2, neurite growth was entirely blocked. After 3 hours, outgrowth was moderately blocked, and after 6 hours c-PTIO had little to no effect on neurite outgrowth. Plainly, NO surges seem most crucial to neurite regeneration within the first few hours post nerve injury. This also suggests that NO bioavailability in the central nervous system can be increased to promote neurite outgrowth after damage using exogenous sources of NO from NOR2 and SNAP, however it is not clear, what the concentrations of NO available were with each donor, as NO donor concentration is not directly correlated with NO availability. Additionally, the four analogs of NOR, have varying effects on cell toxicity even at very low doses. Depending on the length of exposure to these donors, adverse effects can arise.⁵⁸ As a result, time scale studies shown may not be entirely accurate, and could be strengthened by verification with another NO donor like SNAP.

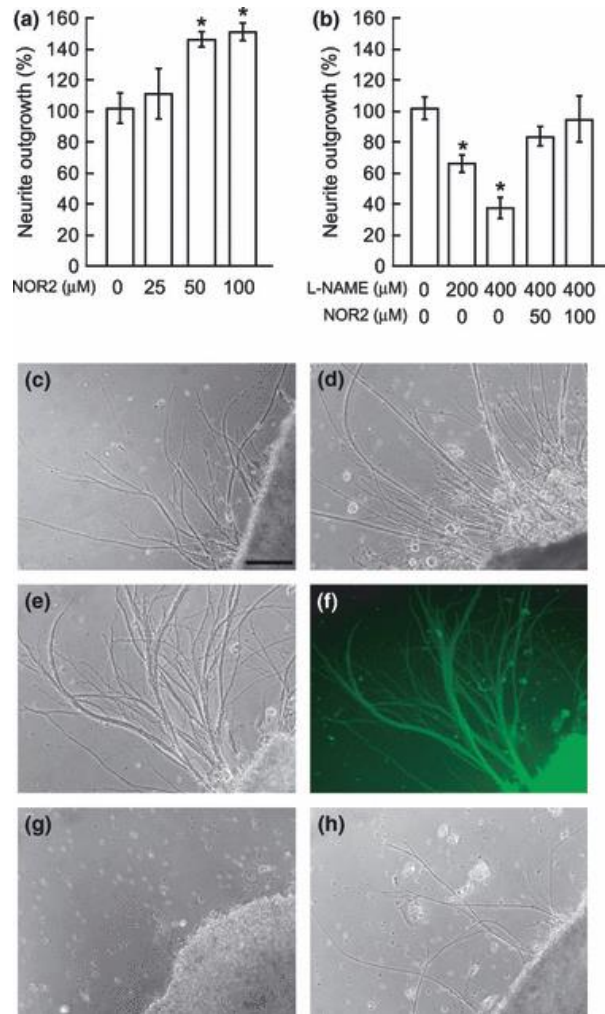


Figure E7. Regulatory effect of NOS-NO related molecules upon neurite outgrowth in the goldfish retinal explant culture. (a,b) Quantitative data for NOS-NO related drugs on neurite outgrowth were obtained from axotomized goldfish retinal explant culture relative to the control (no treatment, 100%). (a) NO generator, NOR2 induced the neurite outgrowth. $*p < 0.05$ versus control. ($n = 4$). (b) Universal NOS inhibitor, l-NAME inhibited the neurite outgrowth. $*p < 0.05$ versus control. ($n = 4$). (c–h) Photomicrographs of neurite outgrowth under various conditions: (c) control, (d) NOR2, (e) SNAP, (f) immunohistochemistry of anti-GAP43 antibody in (e), (g) L-NAME, (h) L-NAME plus NOR2. *Reproduced with permission from Koriyama, Y., Yasuda, R., Homma, K., Mawatari, K., Nagashima, M., Sugitani, K., et al., 2009. Nitric oxide-cGMP signaling regulates axonal elongation during optic nerve regeneration in the goldfish in vitro and in vivo. J. Neurochem. 110, 890–901, John Wiley & Sons. © John Wiley and Sons.*

In goldfish retina, nNOS is at least in part responsible for NO production following axotomy to promote neurite outgrowth. Concentrations of nNOS specific inhibitor ETPI as low as 10 μM suppressed neurite outgrowth by 40-60%. Samples treated with small interfering RNS

(siRNA), shown to specifically target region of goldfish nNOS mRNA, resulted in a 60% decrease in outgrowth. Whether NO acting via the NO-cGMP pathway was directly responsible for neurite outgrowth here remained unclear thus far, meriting further exploration. The selective sGC inhibitor ODQ was added and found to decrease neurite outgrowth. When, however, membrane permeable dbcGMP was added, ODQ effects were reversed. Additionally, the PKG specific inhibitor Rp-cGMPS dose-dependently inhibited neurite outgrowth. It was found, that dbcGMP dosed samples showed significantly increased rates of regeneration (70%) after injury compared to controls (40%), suggesting that dbcGMP undoubtedly facilitates goldfish optic nerve regeneration *in vivo*. In all, these results strongly suggest that the NO-cGMP pathway plays a penultimate role in optic nerve regeneration in goldfish, and that an increase in NO or NO targeted receptors during the first few hours following nerve injury may lead to enhanced regeneration to the optic nerve.

Regenerating RGCs of cats with nipradilol

Nipradilol (8-[2-Hydroxy-3-(isopropylamino)propoxy]-3-chromanol,3-nitrate) is a nitric oxide donor as well as a selective beta adrenergic receptor blocker, commonly administered to treat cardiovascular hypertension conditions.^{59,60} It is used clinically in eastern Asia as an anti-glaucoma drug. Following axotomization of the optic nerve (OpN) in adult cats, RGCs are capable of just 2-5% regeneration. These levels are too low to recover visual function, for this reason a method to enhance RGC regeneration after OpN transection could lead to a restoration of lost functionalities, including acute vision. Preliminary studies investigating neurotropic effects, found nipradilol to be neuroprotective for axotomized RGCs in adult cats.⁶¹ Hence, neuroprotection for axotomized RGCs in adult cats was reaffirmed and the connection between the donor's potential to release NO and the blockage of adrenoceptors with nipradilol was investigated by Watanabe

and colleagues.⁶¹ The drug was injected into the vitreous humor at concentrations of 10 μM , 0.1 μM , and 0.01 μM to determine the optimal dosage. Injection concentrations of 10 μM and 0.01 μM yielded a subtle increase in survival ratios compared to controls. Consequently, injections were carried out at 0.1 μM , with mean survival ratios after 7 days of 1.4-fold, and at 14 days 2.6 -fold compared to controls. The increase in survival ratios with the nipradilol treated samples exemplifies the drugs ability to overall enhance RGC regeneration.

RGCs in cats can be classified into one of 3 categories: alpha, beta, or NAB based on soma size and dendrite morphology. Having confirmed nipradilol's ability to induce RGC generation, it was next explored as to which specific RGCs were increasing. Cells with large somas and thick primary dendrites branching in wide fields were classified as alpha, while cells containing medium-sized somas and bushy dendrites in small fields were classified as beta. All others were termed NAB. Using systematic LY (Lucifer Yellow) injections into RGCs in three patches, the ratio of alpha, beta, and NAB cells was attained. While alpha cell counts matched controls in nipradilol injected retinae, the drug appeared to promote the survival of both beta and NAB cells, as evidenced by a 5.1-fold increase and a 2.0-fold increase respectively observed after 14 days.

Next, whether nipradilol was capable of enhancing the regeneration of cat RGCs including the elongation of cat RGCs after transplanting a segment of PN into the stump of transected cat OpN was explored. The number of RGCs having regenerated axons 10 mm or longer as well as the ratio of RGCs with 20 mm or longer axons verses RGCs having axons 10-20 mm was calculated. Initial experimentation showed the mean number of regenerating RGCs after 6 weeks could be enhanced when 0.1 μM nipradilol was injected; however, no increase compared to controls was observed when 1 μM was used. Showing once again that concentration seems to be vital for regeneration capabilities with nipradilol. Timing was also deemed critical to regeneration,

as injections immediately before transection did not influence regeneration, rather injections 30 minutes prior to transection was ideal. Increased numbers of RGCs were observed in the nipradilol-injected retina than the controls with generally smaller somal sizes, indicating the survival population consisted mostly of beta cells or NAB cells. Targeted LY injections found that after 4 weeks the number of alpha, beta, and NAB cells all increased 3.4-fold, 4.1-fold, and 6.8 fold respectively, raising the possibility the nipradilol is capable of increasing all three cell types in cat RGCs. After 4 weeks, the 20R/10R ratio increased 2.2-fold compared to controls. By 6 weeks, ratios matched that of controls. Taken together, these results suggest nipradilol-injected retinae elongated faster within 4 weeks compared to controls and nipradilol increases the number of regenerating alpha, beta, and NAB RGCs.

It was evident that nipradilol effectively promoted RGC regeneration in adult cats, therefore an effort to elucidate the mechanism by which nipradilol promoted axonal regeneration in adult cat RGCs including the contribution from NO donation was investigated. Firstly, an additional NO donor, SNP (100 μ M) was evaluated and found to increase regenerating RGCs 3.2-fold in 6 weeks, but the 20R/10R ratio was not enhanced as observed with nipradilol. This suggests that NO was involved in the increase in a number of RGC cells, but is not likely the only contributing factor for axonal elongation. Additionally, cPTIO, an NO-scavenger, was added followed by nipradilol prior to transplantation of a PN to the cut optic nerve to reduce NO concentrations potentially donated by nipradilol and an insignificant increase in RGCs was described. Lastly, denitro-nipradilol in place of nipradilol was used, effectively reducing the NO release ability that nipradilol exploits. These studies revealed a significant decrease in the efficacy of regeneration. In conclusion, nipradilol at specific doses benefits regenerating RGC rates in cat retina including alpha, beta, and NAB cells while also enhancing axonal elongation. NO release

also proves quintessential to the overall mechanism in conjunction with other contributing factors of RGC regrowth in cat retina. NO release from nipradilol is not observed in the absence of cells, and has been linked to dependency on glutathione-S-transferase.⁶² Therefore, it seems that both NO release and nipradilol are important for regeneration in these studies.

RGCs can also be classified as ON-center or OFF-center based on the depth ratio. Following the results of the aforementioned study, nipradilol effects on survival and axonal regeneration of OFF-center retinal ganglion cells in adult cats was also investigated.⁶³ NeuroLucida analysis, using three-dimensional imaging, was used to identify ON cells and OFF cells based on dendritic ramification. RGCs with dendrites spreading 0-26% were classified as OFF cells, while those spreading dendrites 30-78% in depth were classified as ON cells. OFF cells regenerate axons less efficiently than ON cells. When RGCs underwent intravitreal injection of brain-derived neurotrophic factor (BDNF) + ciliary neurotrophic factor (CNTF) + forskolin (BCF), BCF influenced the axonal regeneration of ON cells, but not OFF cells. Nipradilol promotes RGC regeneration fourfold, but retains ON/OFF ratios consistent with saline; 61% ON cells and 38% OFF cells. The ON cells increased 5.4 fold, while OFF cells increased 8.2 fold, suggesting that Nipradilol is capable of promoting both ON and OFF cell regeneration. NO donor nipradilol enhances ON and OFF RGCs in both alpha and beta cell types, whereas BCF increased only ON RGCs in both cell types. Additionally, 14 days after OPN transection, fewer OFF RGCs were observed in the OpN-transected retina than the intact, suggesting that OFF RGCs are more vulnerable than ON to transection. This may result in lower survival, however, it was found that nipradilol promotes neuroprotection, as indicated by proportions consistent with controls after transection as well as axonal regeneration resulting in an overall increase in RGCs including alpha,

beta, and NAB cells. These studies show nipradilol is a distinctive donor that may offer a potential for recovering the function of acute vision.

Reinnervation after penile nerve crush studies with SNP in rats

There remains a poor understanding of how the parasympathetic nervous system (PSNS) responds physiologically to injury. Often neurons of the parasympathetic nervous system are isolated to target organs making selective damage experimentally challenging. To investigate penile nerve injury regeneration, penile nerves in rats were either isolated and manually crushed or cut completely on one side.⁶⁴ The ability of the erectile tissue to recover following nerve injury when SNP was added, found noradrenergic and nitrenergic axons became widely prevalent in proximal regions to injury. As such, their results suggest that vasodilator therapies employed early after penile nerve injury may be quintessential to expediting functional recovery following trauma. A subsequent study examined the response to NO using SNP following penile nerve crush.⁶⁵ By assessing contractile responses of the tissues and analyzing nerve morphology, SNP sensitivity was reduced in samples containing metabolic syndrome. Metabolic syndrome is associated with aging conditions leading to erectile dysfunction. These studies suggest that NO sensitivity remains fairly consistent during nerve injury; however, rats that had a decreased sensitivity to NO were significantly less likely to recover erectile function. In conclusion, NO regulation arises as a strategic aspect in penile nerve recovery after trauma.

Exogenous SNAC on motor functional recovery in rats

Nerve injuries that do not completely transect the nerve, encompass the most commonly observed peripheral nerve injuries. Traditionally, steroids have been widely administered to treat

nervous system injury; although, it has been hypothesized that supplementation of NO may enhance peripheral nerve regeneration.⁶⁶ Since Ischemia/reperfusion (I/R) appears to downregulate eNOS and nNOS in the rat sciatic nerve, it seems likely that NO production is hindered. Thus, an exogenous source of NO may influence motor functional recovery of the reperfused rat sciatic nerve. I/R injury was achieved invoking a 100-g load over 2 hours. The effects of the steroid methylprednisolone (MP) versus nitric oxide via *S*-nitroso-*N*-acetylcysteine (SNAC) were then evaluated in rats by means of a walking track test, muscle contractile test, muscle weight analysis, and histology. Each rat was continuously infused intravenously with MP, SNAC, or PBS. The material blood pressure only slightly decreased in all animals and the heart rate remained stable for both the PBS and SNAC treated groups; although significant bradycardia was found in the MP-treated group. The walking track test in brief allowed the animals to walk down a corridor leaving behind blue footprints, where the distance between toes and overall print length could be attained and used to calculate an overall quantification of the sciatic functional index (SFI). A score of 0 represented normal nerve function, while -100 indicated complete dysfunction. SNAC-treated rats began to show signs of recovery at day 7 with an SFI of -84.2 ± 13.8 , while the MP and PBS treated rats remained paralyzed. The muscle contractile test involved removal of the extensor digitorum longus (EDL) muscle, then attached by suture to an isometric force transducer on one end and attached to a glass hook at the bottom of a field-stimulating electrode on the distal end. Maximal twitch force was measured and the resultant contractile force was expressed as a percentage of the normal contralateral muscle contractile force. In SNAC-treated rats maximal twitch force was 80% as early as day 21 and 94% by day 42, while the MP- and PBS- treated rats recovered twitch force at 76% and 60% respectively. The SNAC-treated rats demonstrated a significantly greater isometric force produced at all frequencies attained. In each

experimental limb muscle atrophy was apparent, hence the weight of the muscle was recorded and expressed as a percentage of the normal contralateral muscle. The wet weight for the SNAC-treated rats once again was continuously higher, while MP- and PBS-treated rats progressively exhibited degenerated muscle weight until day 21, and showed weight gains near 10% less than the SNAC-treated samples by day 42. In all, the results of the walking track test, muscle contractile test, and muscle weight analysis indicate that although MP marginally aids in reducing the damaging effects of I/R injury in rats, the NO donor SNAC shows greater potential for maximizing recovery.

Histologic examinations corroborated SNAC's potential to enhance recovery after I/R injury in rats. The blind histologic examinations indicated more Wallerian degeneration, myelin debris, and acute inflammatory responses were present in MP- and PBS- treated rats than in SNAC-treated specimen at day 5. Uniquely, the SNAC-treated rats also appeared to have near normal myelin sheath thickness and regenerated axons at day 42. Taken together, these results show improved early regeneration of axons in the reperfused peripheral nerve as well as improved axonal regeneration due to exogenous NO. In conclusion, NO is preferential in the early stages of recovery from peripheral nerve I/R injury. NO may assist by scavenging superoxide free radicals, which can be detrimental to early stages of reperfusion or by inducing necessary vasodilation. Unfortunately, the concentrations of NO release were once again overlooked. Stability among different *S*-nitrosothiols in solution must take the concentration effect carefully into account since half-lives of primary RSNOs found *in vivo* can vary widely by their intrinsic structural properties.⁶⁷ Moreover, peripheral nerve I/R injury may result in undesirable inhibition of NO production, vital to the recovery of the nervous system during this type of injury, and *S*-nitrosothiol NO donors like SNAC may aid in countering the resultant deleterious effects.

GSNO effects after I/R injury in rats

Traumatic brain injury (TBI) often results in adverse neurobehavioral dysfunctions attributed to oxidative injury of neurogenic vasculature.⁶⁸ Such dysfunctions lead to an undesirable progression of damage. Reactive oxygen and nitrogen species in brain and endothelial cells complicate studies of the mechanistic pathways invoking such damage. Peroxynitrite is a highly reactive oxidative species formed rapidly from superoxide and nitric oxide. It is associated with a series of unwanted effects including oxidatively uncoupling endothelial NOS causing a depletion of L-arginine. Increasing peroxynitrite concentrations increase tetrahydrobiopterin up regulation of ICAM-1 compromising the BBB and increasing edema. Additionally, resultant nitration of tyrosine in proteins can be physiologically problematic. The formation of peroxynitrite during TBI significantly depletes bioavailability of NO vital to initiating angiogenic processes. Since the NO donor S-nitroso glutathione (GSNO) has shown potential to protect the central nervous system through decreasing reactive oxygen species, the ability for GSNO to influence both short and long term neurorepair following TBI in rats was explored.⁶⁹

The rat controlled cortical impact (CCI) model used mimics contusion type injury, representative of near 40% of all TBIs. It mirrors effects of human brain injuries such as inflammation, BBB deviations, neuron loss, motor control loss, and memory degradation. The direct interaction between GSNO and peroxynitrite was explored by monitoring 3-nitrotyrosine (3-NT) expression using dot blot analysis and immunohistochemistry (IHC), 4 h after TBI in the injured penumbra region (Figure E8). Moreover, brain tissues were stained for 4-hydroxynonenal (4-HNE) – a consequence of lipid peroxidation, as well as ferritin – capable of catalyzing the formation of a highly reactive hydroxyl radical with peroxynitrite. TBI induced expression of 3-NT was significantly hindered in the GSNO treated samples. After two weeks, 3-NT expression

was markedly increased in the injured penumbra. The GSNO treated samples, however, once again displayed a reduction in 3-NT expression. Samples treated with peroxyntirite forming 3-morpholino sydnonimine (SIN-1) on the other hand displayed significantly increased 3-NT expression compared to the TBI group. Plasma analyses echoed these findings. Concurrently, plasma NO levels were monitored indirectly by way of nitrate/nitrite concentration with a nitric oxide fluorometric assay kit from Biovison. As expected, peroxyntirite concentrations exhibited an inverse relationship with NO. A significant drop in NO concentration was observed with SIN-1 treated samples as compared to the TBI plasma. The lipid peroxidation product, 4-HNE, levels in plasma were significantly lower in the GSNO-treated samples, while SIN-1 treated samples displayed an increased expression of 4-HNE. Once again, traumatic penumbra resonated these results. It appears by increasing NO through implementing GSNO it is possible to decrease peroxyntirite concentrations after TBI in both brain tissue and plasma.

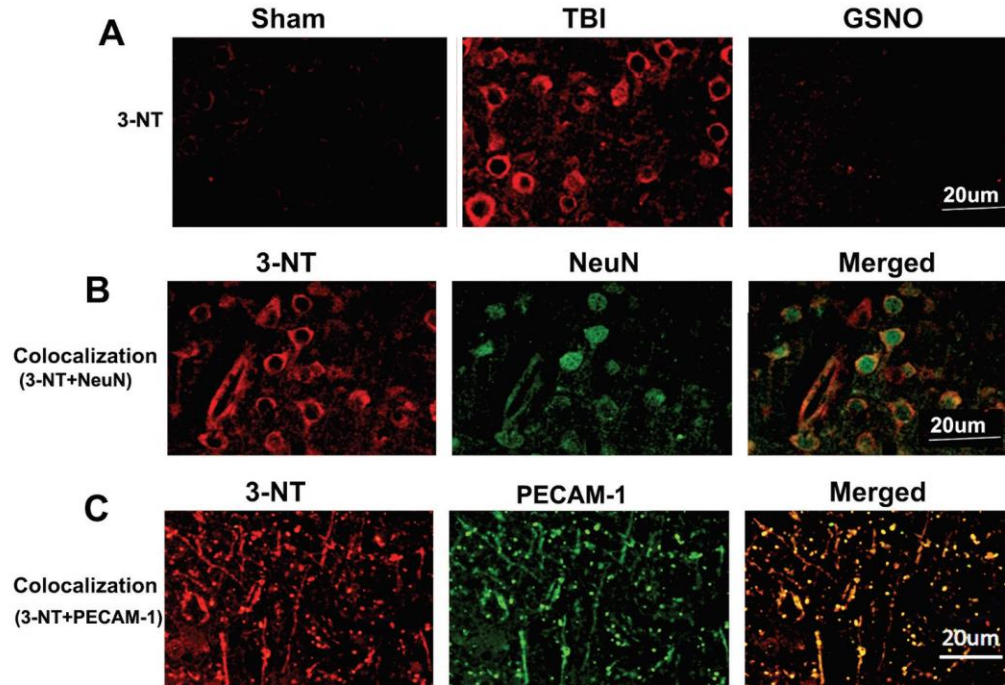


Figure E8. Photomicrographs of IHC show (A) reduced 3-NT (red) in the traumatic penumbra region in the presence of GSNO. Sham brain does not show 3-NT-positive cells. Colocalization (yellowish, merged) of 3-NT (red color) with either neuronal marker NeuN (green) (B) or endothelial cell marker PECAM-1 (green) (C) indicates that both neurons and endothelial cells have increased expression of 3-NT. *Reproduced from Khan, M., Sakakima, H., Dhammu, T.S., Shunmugavel, A., Im, W.-B., Gilg, A.G., et al., 2011. S-nitrosoglutathione reduces oxidative injury and promotes mechanisms of neurorepair following traumatic brain injury in rats. J. Neuroinflamm. 8, 78; licensee BioMed Central Ltd. © Khan et al; licensee BioMed Central Ltd.*

If peroxynitrite was responsible for damage after TBI, an increase in brain water content (edema) would be expected. BBB leakage evaluated by edema was determined 24 hours after CCI and extravasations of Evan's blue dye were highest in SIN-1 treated samples as compared to TBI and much lower still in GSNO treated. Indicating, peroxynitrite did cause neurovascular oxidative injury during TBI. In the TBI group brain tissue water content increased. In the SIN-1 treated sample water content was further increased. Conversely, GSNO treated samples contained less edema than the TBI samples. Therefore, while a boost in peroxynitrite increases edema, greater GSNO concentrations protect neurovascular tissues during TBI.

An increase in edema may concur with BBB damage. BBB leakage is influenced by a surge in mRNA levels of ICAM-1; therefore, one-way to assess damage to the BBB and potential for GSNO to induce neurorepair is to monitor ICAM-1 levels in the traumatic penumbra area. GSNO-treating samples prevented the increase of ICAM-1 levels, suggesting GSNO may stimulate neurorepair and reduce inflammation.

GSH is a precursor to GSNO and an endogenous antioxidant to peroxynitrite involved in endothelial function. To better understand the relationship between peroxynitrite and GSH, GSH levels were monitored. The TBI brain had significantly depleted levels of GSH compared to the controls and GSNO samples. SIN-1 levels were significantly lower than the TBI control levels. Peroxynitrite reduces the concentration of GSH, which in turn may be partially responsible for its damaging effects.

Histopathology, demyelination, and axonal integrity were assessed using hematoxylin and eosin (H&E), luxol fast blue (LFB) and Bielschowsky silver impregnation respectively 14 days after the TBI. H&E studies revealed that GSNO prevented TBI-induced tissue deformation and immune cell infiltration. While controls showed a decline in myelin, the GSNO-treated samples did not have nearly the same degree of declination, which supports that GSNO may induce the neurorepair process. The Bielschowsky silver staining, marking axonal integrity, showed enhanced staining over the TBI sample, indicating GSNO also plays a role in the protection of axonal integrity following TBI.

BDNF, TrkB, and synaptophysin are important factors associated with neurorepair. Expression of BDNF and its receptor TrkB promotes neuronal survival and axonal growth, while synaptophysin facilitates synaptogenesis. A significant decrease in synaptophysin, BDNF, and TrkB was witnessed in TBI versus Sham control groups. GSNO-treated samples displayed a

significant increase in expression of all three factors compared to the TBI samples. Hence, GSNO contributes to the neurorepair process at least in part by inducing these vital neurotropic factors following TBI. In all, treatment with GSNO after TBI depletes peroxynitrite levels, increases NO and GSH bioavailability, and safeguards the BBB, while simultaneously supporting neurorepair. Overall, this evidence suggests that GSNO can be effective at protecting the central nervous system by reducing reactive oxygen species and enhancing both short and long term neurorepair.

GSNO influences angiogenesis in rats

Stroke is amongst the top five leading causes of death both in the United States and globally. A stroke leads to neuronal damage that can ultimately cause irreversible neuronal death. As such, a better understanding of factors central to neurorepair associated with stroke is a necessary step towards enabling the therapeutic design to minimize disabilities and enhance recovery for stroke victims. It is generally accepted that NO induces vasodilation as well as regulates several angiogenic and potential neurorepair factors such as hypoxia-inducible factor-1 alpha (HIF-1 α). Limited data identifies the specific mechanisms of such neurorepair processes. In response, Khan and coworkers investigated the mechanism by which the NO-donor GSNO may influence neurorepair specifically through the HIF-1 α /VEGF/angiogenesis pathway.⁷⁰ HIF-1 is a regulatory nuclear transcription factor, capable of invoking tissue survival by inducing GLUT, a cellular metabolism enzyme, as well as influencing angiogenic enzymes like VEGF, VEGFR1, and angiopoietin. Stabilizers of HIF-1 α , like GSNO, may promote neuroprotection, angiogenesis, and neurotrophins. In rats, cerebral ischemia and reperfusion (stroke) was induced by left middle cerebral artery occlusion (MCAO). Animals were sacrificed either 7 or 14 days later and brain tissue was prepared for histological and immunohistochemical analyses. Shortly after reperfusion,

the GSNO group was injected with GSNO, followed by feeding of GSNO daily until the time of sacrifice. Some animals were also treated with 2-methoxyestradiol (2-ME), an inhibitor of HIF-1 α .

Analyses were performed to assess the weight, neurological state, and motor behavior of the rats. Animals showing paralysis 1 hour after MCAO were graded on a scale of 0-4, where a 0 was awarded for normal functionality and 4 awarded when leaning continuously to the contralateral side or when simply no spontaneous motor activity was observed. Modified neurological severity scores (mNSS) were determined to reflect asymmetries. A body swing test was also used where the animals were held vertical and a swing recorded whenever the rat moved its head out of vertical alignment. A normal healthy rat tends to have an equal number of swings on both sides. Furthermore, motor coordination and balance were evaluated on an accelerating rotarod task. Each rat was placed on the rotarod cylinder and speed was increased. The mean speed which the animal fell off out of the drum was noted. After 14 days of GSNO treatments, tolerated rotation speed, body swing behavior, mNSS, as well as body weights significantly improved compared to controls. As a result, the NO donor GSNO can be associated with improving motor function after stroke in rats.

The physiological impact of GSNO following induced stroke was also assessed. Immunohistochemical and histological studies entailed brain tissue stained for HIF-1 α , VEGF, and PECAM-1; cell proliferation, examined using Ki67; cell counting, and immunostained sections. The degree of neuronal damage was determined by cresyl violet (Nissl) staining, which highlights key structural features of the neurons. Both immunohistochemical staining and Western blot analyses were performed to determine protein concentrations. 14 days following injury, angiogenic mediators HIF-1 α , VEGF, and PECAM-1 increased in the injured areas.

Advantageously to neurorepair, treatment with GSNO significantly increased the expression of these mediators and promoted new vessel formation, as evidenced by a substantial increase in expression of vessel density markers, including laminin and GSL-1. Additionally, Ki67 expression was also significantly enhanced in GSNO-treated samples compared to controls, suggesting a possible increase in angiogenic processes including cell proliferation was being induced.

When the inhibitor of HIF-1 α , 2-ME, was administered, the previously mentioned beneficial effect on brain infarctions due to GSNO, was blocked, rotorod performances mimicked controls, and neurological scores were impeded. These results suggest that the interaction between GSNO and HIF-1 α is vital for recovery following cerebral IR. Cell transfection with siRNAs, known to silence HIF-1 α , reduced the expression of angiogenic factor VEGF, compared with untreated cells, and inhibited GSNOs capillary-like structure. These results support the hypothesis that HIF-1 α proangiogenic activity is stimulated by GSNO. Consequently, GSNO-mediated stabilization of HIF-1 α may be an effective approach to enhance neurorepair processes, ultimately reducing stroke-induced disabilities.

Conclusion

A review of the recent literature suggests that NO appears to be involved in the process of nerve regeneration. NOC-18 was found to directly target serotonergic neurons and initiate the cGMP/PKG pathway early on in *Hydra* regeneration. In the *Locusta*, both NOC-18 and SNP endorse axonal regrowth and neurite outgrowth, but perhaps in later stages of development after the initial reformation. SNP was used to discover that after penile nerve injury, recovery was hindered by insensitivity to NO, suggesting NO was in some way necessary for the recovery of penile function after injury. Nipradilol was determined an effective drug only when nitrosated, indicating it was most likely the NO release that was responsible for nipradilol's ability to enhance

RCG recovery in cats following optic nerve trauma. SNAC was capable of inducing motor functional recovery in rats following damage to the sciatic nerve. Following induced stroke, GSNO was determined an appropriate source of additional NO to reduce the effects of superoxide peroxynitrite, minimizing damaging effects after TBI. It was also found that GSNO could stabilize HIF-1 α , consequently enhancing neurorepair. These studies provide interesting precedence for further investigating NO influence on neuronal regeneration.

Zochodne and coworkers investigated the effect of nitric oxide synthase (NOS) on the peripheral nerve regeneration of a transected sciatic nerve in mice.³⁰ Based on aforementioned observations during CNS regeneration, researchers anticipated when dosed with L-NAME, a NOS inhibitor, antagonistic impression on nerve regeneration of myelinated fibers from the proximal stump would occur. The results however, reflected the contrary. Both electrophysiological and morphometric evaluations illustrate PNS regeneration in mice benefits from inhibition of NOS. It is possible that local levels of NO release in these studies may have been excessively high, leading to toxic adverse effects. NO concentrations can be crucial to efficacy, therefore, in order to fully understand the implications of using each NO donor above, a direct method to determine NO concentration in these instances is of utmost importance. As seen in the GSNO experimentation, other reactive species like peroxynitrite or proteins can succumb to rapid reaction with NO, effectively depleting detectable NO. Additionally, each type of NO donor yields different byproducts, as seen with SNP and nipradilol that may be at least in part responsible for the present results, not necessarily solely caused by NO. NO drugs are constantly expanding, leading to a greater understanding of the difference in NO loading, release kinetics and mechanisms associated with each.⁷¹⁻⁷³ Although the studies mentioned reveal NO is a vital signaling molecule undoubtedly involved in nerve regeneration, thus far research has just begun to shed light on NO donor potential

in this field. Each NO donor exhibits unique physical and chemical properties resulting in differentiated physiological consequences. Additional consideration of NO release rates and concentration dependent pathways warrants further exploration and may led to original specialized therapeutic methods better adept to promote nerve regeneration.

REFERENCES

1. Zochodne, D. W.; Levy, D. *Cellular and Molecular Biology* **2005**, *51*, 225-267.
2. Rabinovich, D., Yaniv, Shiri p., Alyagor, I. & Schuldiner, O. *Cell*, *164*, 170-182.
3. Awasaki, T.; Ito, K. *Nature* **2016**, *531*, 182-183.
4. Garthwaite, J., Charles, S. L. & Chess-Williams, R. 1988. Endothelium-derived relaxing factor release on activation of NMDA receptors suggests role as intercellular messenger in the brain.
5. Cary, S. P., Winger, J. A., Derbyshire, E. R. & Marletta, M. A. *Trends in Biochemical Sciences* **2016**, *31*, 231-239.
6. Garthwaite, J. *Molecular and Cellular Biochemistry* **2010**, *334*, 221-232.
7. Francis, S. H.; Corbin, J. D. *Urologic Clinics of North America* **2005**, *32*, 419-429.
8. Francis, S. H.; Busch, J. L.; Corbin, J. D. *Pharmacological Reviews* **2010**, *62*, 525-563.
9. Krumenacker, J. S.; Hanafy, K. A.; Murad, F. *Brain Research Bulletin* **2004**, *62*, 505-515.
10. Arnold, W. P.; Mittal, C. K.; Katsuki, S.; Murad, F. *Proceedings of the National Academy of Sciences*, **1977**, *74*, 3203-3207.
11. Prast, H.; Tran, M.; Fischer, H.; Philippu, A. *Journal of neurochemistry* **1998**, *71*, 266-273.
12. Lorrain, D. S.; Hull, E. M. *Neuroreport* **1993**, *5*, 87-89.
13. Lonart, G.; Wang, J.; Johnson, K. M. *European Journal of Pharmacology* **1992**, *220*, 271-272.
14. Gibbs, S. M.; Becker, A.; Hardy, R. W.; Truman, J. W. *The Journal of Neuroscience* **2001**, *21*, 7705-7714.
15. Godfrey, E. W.; Schwarte, R. C. *Experimental Cell Research* **2010**, *316*, 1935-1945

16. Seidel, C.; Bicker, G. *Development* **2000**, *127*, 4541-4549.
17. Tamagnini, F.; Barker, G.; Warburton, E.; Burattini, C.; Aicardi, G.; Bashir, Z. I. *The Journal of Physiology*, **2013**, *591*, 3963-3979.
18. Cooke, R. M.; Mistry, R.; Challiss, R. J.; Straub, V. A. *The Journal of Neuroscience* **2013**, *33*, 5626-5637.
19. Yuan, Q.; Scott, D. E.; So, K.-F.; Lin, Z.; Wu, W. *Neurochemical Research* **2009**, *34*, 1907-1913.
20. Rentería, R. C.; Constantine-Paton, M. *The Journal of Neuroscience* **1999**, *19*, 7066-7076.
21. Van Wagenen, S.; Rehder, V. *Journal of Neurobiology* **1999**, *39*, 168-185.
22. Stern, M.; Bicker, G. *Developmental Neurobiology* **2008**, *68*, 295-308.
23. González-Hernández, T.; Rustioni, A. *Journal of Neuroscience Research* **1999**, *55*, 198-207.
24. González-Hernández, T.; Rustioni, A. *Journal of Comparative Neurology* **1999**, *404*, 64-74.
25. Keilhoff, G.; Fansa, H.; Wolf, G. *Journal of Neuroscience Research* **2002**, *68*, 432-441.
26. Calabrese, V.; Mancuso, C.; Calvani, M.; Rizzarelli, E.; Butterfield, D. A.; Stella, A. M. *Nature Reviews Neuroscience* **2007**, *8*, 766-775.
27. Contestabile, A.; Ciani, E. *Neurochemistry International* **2004**, *45*, 903-914.
28. Riccio, A.; Alvania, R. S.; Lonze, B. E.; Ramanan, N.; Kim, T.; Huang, Y.; Dawson, T. M.; Snyder, H.; Ginty, D. D. *Molecular Cell* **2006**, *21*, 283-294.
29. Guix, F.; Uribealago, I.; Coma, M.; Munoz, F. *Progress in Neurobiology* **2005**, *76*, 126-152.
30. Zochodne, D. W.; Misra, M.; Cheng, C.; Sun, H. *Neuroscience Letters*, **1997**, *228*, 71-74.

31. Mancuso, C.; Bonsignore, A.; Di Stasio, E.; Mordente, A.; Motterlini, R. *Biochemical Pharmacology* **2003**, *66*, 2355-2363.
32. Mancuso, C. *Antioxidants & Redox Signaling*, **2004**, *6*, 878-887.
33. Motterlini, R.; Green, C. J.; Foresti, R. *Antioxidants and Redox Signaling* **2002**, *4*, 615-624.
34. Pacher, P.; Beckman, J. S.; Liaudet, L. *Physiological Reviews* **2007**, *87*, 315-424.
35. Ridnour, L. A.; Thomas, D. D.; Mancardi, D.; Espey, M. G.; Miranda, K. M.; Paolocci, N.; Feelisch, M.; Fukuto, J.; Wink, D. A. *Biological Chemistry* **2004**, *385*, 1-10.
36. Castegna, A.; Aksenov, M.; Aksenova, M.; Thongboonkerd, V.; Klein, J. B.; Pierce, W. M.; Booze, R.; Markesbery, W. R.; Butterfield, D. A. *Free Radical Biology and Medicine*, **2002**, *33*, 562-571.
37. Miranda, S.; Opazo, C.; Larrondo, L. F.; Muñoz, F. J.; Ruiz, F.; Leighton, F.; Inestrosa, N. *Progress in Neurobiology* **2000**, *62*, 633-648.
38. Kegeles, L. S.; Martinez, D.; Kochan, L. D.; Hwang, D. R.; Huang, Y.; Mawlawi, O.; Suckow, R.; Van Heertum, R. L.; Laruelle, M. *Synapse* **2002**, *43*, 19-29.
39. Kuhn, D. M.; Geddes, T. J. *Brain Research* **2002**, *933*, 85-89.
40. Naoi, M.; Maruyama, W. *Parkinsonism & Related Disorders* **2001**, *8*, 139-145.
41. Miklya, I.; Göttl, P.; Hafenscher, F.; Pencz, N. *Neuropsychopharmacologia Hungarica: a Magyar Pszichofarmakologiai Egyesület lapja= official journal of the Hungarian Association of Psychopharmacology* **2014**, *16*, 67-76.
42. Gu, Z.; Kaul, M.; Yan, B.; Kridel, S. J.; Cui, J.; Strongin, A.; Smith, J. W.; Liddington, R. C.; Lipton, S. A. *Science* **2002**, *297*, 1186-1190.

43. Hara, M. R.; Thomas, B.; Cascio, M. B.; Bae, B.-I.; Hester, L. D.; Dawson, V. L.; Dawson, T. M.; Sawa, A.; Snyder, S. H. *Proceedings of the National Academy of Sciences of the United States of America* **2006**, *103*, 3887-3889.
44. Uehara, T.; Nakamura, T.; Yao, D.; Shi, Z.-Q.; Gu, Z.; Ma, Y.; Masliah, E.; Nomura, Y.; Lipton, S. A. *Nature* **2006**, *441*, 513-517.
45. Browne, S. E.; Beal, M. F. *Antioxidants & Redox Signaling* **2006**, *8*, 2061-2073.
46. Butterfield, D.; Howard, B. J. Lafontaine, M. A. *Current Medicinal Chemistry* **2001**, *8*, 815-828.
47. Sorolla, M. A.; Reverter-Branchat, G.; Tamarit, J.; Ferrer, I.; Ros, J.; Cabiscol, E. *Free Radical Biology and Medicine* **2008**, *45*, 667-678.
48. Lin, M. T. & Beal, M. F. *Nature* **2006**, *443*, 787-795.
49. Beuve, A.; Wu, C. G.; Cui, C. L.; Liu, T.; Jain, M. R.; Huang, C.; Yan, L.; Kholodovych, V.; Li, H. *J. Proteomics* **2016**, *138*, 40-47.
50. Sellak, H.; Choi, C. S.; Dey, N. B.; Lincoln, T. M. *Cardiovasc. Res.* **2013**, *97*, 200-207.
51. Colasanti, M.; Mazzone, V.; Mancinelli, L.; Leone, S.; Venturini, G. *Nitric Oxide* **2009**, *21*, 164-70.
52. Hunter, R. A.; Storm, W. L.; Coneski, P. N.; Schoenfisch, M. H. *Analytical Chemistry* **2013**, *85*, 1957-1963.
53. Patschke, A.; Bicker, G.; Stern, M. *Dev. Brain Res.* **2004**, *150*, 73-76.
54. Stern, M.; Bicker, G. *Dev Neurobiol* **2008**, *68*, 295-308.
55. Grossi, L.; D'angelo, S. *Journal of Medicinal Chemistry* **2005**, *48*, 2622-2626.
56. Stern, M.; Boger, N.; Eickhoff, R.; Lorbeer, C.; Kerksen, U.; Ziegler, M.; Martinelli, G. P.; Holstein, G. R.; Bicker, G. *J Comp Neurol*, **2010**, *518*, 1157-75.

57. Koriyama, Y.; Yasuda, R.; Homma, K.; Mawatari, K.; Nagashima, M.; Sugitani, K.; Matsukawa, T.; Kato, S. *J Neurochem* **2009**, *110*, 890-901.
58. Yamamoto, T.; Yuyama, K.; Nakamura, K.; Kato, T.; Yamamoto, H. *Eur J Pharmacol* **2000**, *397*, 25-33.
59. Imai, S.; Nakahara, H.; Nakazawa, M.; Takeda, K. *Drugs* **1988**, *36*, 10-19.
60. Toshio, H.; Iguchi, A. *Cardiovascular Drug Reviews* **1998**, *16*, 212-235.
61. Watanabe, M.; Tokita, Y.; Yata, T. *Neuroscience* **2006**, *140*, 517-28.
62. Hayashi, T.; Iguchi, A. *Cardiovascular Drug Reviews* **1998**, *16*, 212-235.
63. Yata, T.; Nakamura, M.; Sagawa, H.; Tokita, Y.; Terasaki, H.; Watanabe, M. *Neuroscience* **2007**, *148*, 53-64.
64. Nangle, M. R.; Keast, J. R. *Exp Neurol* **2007**, *207*, 30-41.
65. Nangle, M. R.; Proietto, J.; Keast, J. R. *J Sex Med* **2009**, *6*, 3032-44.
66. Park, J. W.; Qi, W. N.; Cai, Y.; Nunley, J. A.; Urbaniak, J. R.; Chen, L. E. *J Hand Surg Am* **2005**, *30*, 519-27.
67. De Oliveira, M. G.; Shishido, S. M.; Seabra, A. B.; Morgon, N. H. *The Journal of Physical Chemistry A* **2002**, *106*, 8963-8970.
68. Cornelius, C.; Crupi, R.; Calabrese, V.; Graziano, A.; Milone, P.; Pennisi, G.; Radak, Z.; Calabrese, E. J.; Cuzzocrea, S. *Antioxidants & Redox Signaling* **2013**, *19*, 836-53.
69. Khan, M.; Sakakima, H.; Dhammu, T. S.; Shunmugavel, A.; Im, W.-B.; Gilg, A. G.; Singh, A. K.; Singh, I. *Journal of Neuroinflammation*, **2011**, *8*.
70. Khan, M.; Dhammu, T. S.; Matsuda, F.; Baarine, M.; Dhindsa, T. S.; Singh, I.; Singh, A. K. *Drug Des Devel Ther* **2015**, *9*, 2233-47.
71. Miller, M. R.; Megson, I. L. *British Journal of Pharmacology* **2007**, *151*, 305-321.

72. Joslin, J. M.; Damodaran, V. B.; Reynolds, M. M. *RSC Advances* **2013**, *3*, 15035-15043.
73. Damodaran, V. B.; Place, L. W.; Kipper, M. J.; Reynolds, M. M. *Journal of Materials Chemistry* **2012**, *22*, 23038-23048.